HYBRIDISATION OF SELF-REINFORCED COMPOSITES:

MODELLING AND VERIFYING A NOVEL HYBRID CONCEPT

Yentl SWOLFS

Supervisor:
Prof. I. Verpoest
Dr. L. Gorbatikh

Members of the Examination Committee:
Prof. S.V. Lomov
Prof. B. Goderis
Prof. M. Seefeldt
Prof. J.W. Seo
Prof. M.R. Wisnom
Dr. P.J. Hine
Prof. J. Berlamont, chairman

Dissertation presented in
partial fulfilment of the
requirements for the
degree of Doctor in
Engineering Science

January 2015

Uitgegeven in eigen beheer, Yentl Swolfs, Leuven

ISBN: 978-94-6018-954-8
D/2015/7515/10

Acknowledgements

Welcome to the most read part of this PhD thesis. This is the part where I get to say thank you to all the people who directly or indirectly contributed to my PhD. They all have, in one way or the other, contributed to paving my life path in the past four years.

First of all, I would like to thank my promoters. My promoter, Ignaas Verpoest, sparked my interest into the field of composites in my third bachelor year at KU Leuven. Ever since, I have been fascinated by this field. Many of the achievements presented in this PhD thesis would not have been possible without his mentoring. The best way to describe his contribution is with the following expression: "*If I have seen further it is by standing on the shoulders of giants (Isaac Newton, 1676).*" Ignaas' enthusiasm, passion and knowledge certainly make him qualified to be a "*giant*".

My co-promoter, Larissa Gorbatikh, also made indispensable contributions to this PhD thesis. She always kept me on the right track and her background in solid and fracture mechanics was very useful during my thesis. She continuously pushed my research to a higher level by challenging me to do better. These challenges were crucial for my development as a researcher and for my future career.

I am also grateful to the members of my supervisory and examination committee: Prof. Marc Seefeldt, Prof. Bart Goderis, Prof. Stepan Lomov, Prof. Maria Seo, Dr. Peter Hine, and Prof. Michael Wisnom. Their input and feedback was indispensable in increasing the quality of this PhD thesis.

I would also like to acknowledge my funding. My initial funding came from the EU-FP7 project HIVOCOMP. I am very proud to have obtained an IWT grant later on. This allowed me to work more independently and focus more on fundamental understanding. The Samsonite and Propex people are gratefully acknowledged for providing guidance, context and industrial relevance.

As a researcher, one of the great pleasures of the job is working together with other people. I have always thoroughly enjoyed working with thesis students, which is why I had so many. The work of Xiaoming Sun, Pieter De Cuyper, Winke van den Fonteyne, Liesbet Crauwels, Hans Van Der Velpen, Eline Van Breda, Yannick Meerten, Qingcheng Zhang, Jia Shi, Koen Michielsen, Haoran Wu, Xiaoshi Jia, Kathleen Schuurbiers, Jonas Claus, Mengdie Yang, Yoran Geboes and Gilles Cleeren inspired me to investigate interesting topics which may not always have been possible within my PhD. A selection of their results will also appear in various parts of this thesis.

My colleagues within the Composite Materials Group were also very helpful in many ways. They helped me to fine-tune my own way of doing research.

Their feedback and friendly chats are highly appreciated. I need to and would like to thank Yannick in particular. I need to, because I promised him a while ago. I want to, because it was a great experience for me to see a master thesis student being so passionate that he wants to continue doing a PhD on the same subject. Ichiro also deserves to be mentioned. Our time in the group only overlapped for a few months, but he continued to provide guidance on all carbon fibre related enquiries. I would like to thank Kris, Bart, Manuël and Marc for preparing experimental setups, maintaining the equipment in good shape and opening the Big Hall so early.

Working in an environment such as the MTM department was very stimulating. Interacting with researchers from other groups helped me to put things in perspective. They also provided fun and laughter at various activities, such as cheese & wine evenings and departmental dinners. Many of them are not just colleagues but have become friends.

I have also had many interactions with researchers outside of our department. Through the HIVOCOMP-project, I closely collaborated with Ian Ward, Peter Hine, Paul Unwin and Mark Bonner from the University of Leeds. Ian's never-ending work spirit, even at the age of 86, was a major motivation for my own research. The frequent interactions with Peter were very fruitful and contributed to the success of HIVOCOMP. The 1-month research stay in their group was very useful in developing a deeper understanding of the hot compaction process.

During my PhD, I also set up collaborations with Hannah Morton from the University of Southampton, Soraia Pimenta and Hele Diao from Imperial College London and Gergely Czél, Meisam Jalalvand and Hana Yu from the University of Bristol. These collaborations were very rewarding and useful, in particular in the validation of my models. Interactions with these people also influenced the content of this PhD thesis. The different perspective on hybrid composites offered by the HiPerDuCT project was in many ways complementary to this thesis. One of these interactions also resulted in the experimental validation on hybrid composites.

I had a very fruitful and productive time during my 4-month research stay at the University of California, Santa Barbara. I would like to thank Bob McMeeking for hosting me and for providing me with new insights in my model. He was crucial in creating a highly stimulating environment, and advancing my model to a higher level. The interactions with Frank Zok and Varun Rajan were very useful and allowed me to develop a new model, which would not have been possible without them. More on a personal note, I would like to thank Natalie, Wennie, Mattia, Eunhee, Patrick and Mirko, for all the jogging, surfing and other cool things we did in Santa Barbara.

My friends Jeroen, Lian, Lies, Martijn, Sam, Stef, Steven en Tinne were also crucial in my personal development and my PhD. The discussions we had in the past 15 years were often intellectually challenging and were an excellent preparation for a scientific career. They also provided plenty of fun, leisure and laughter along the way.

My parents also deserve to be acknowledged. Over the years, I have realised that how they raised me has been a large benefit in all areas of my life. They taught me the importance of a good work-life balance and allowed me to gradually develop my own independence. These qualities have been crucial in my personal development as well as in my PhD.

Finally, my sincerest gratitude goes to my girlfriend Annelies. She corrected numerous papers, this thesis and even these acknowledgments for linguistic errors. However, she did not know that I changed this paragraph the last day before printing this thesis. She deserves the longest acknowledgment. One day, I hope she will gain the ability to see herself through my eyes, because only then would she realise how special she is to me. Having someone nearby going through the same PhD process was invaluable. She has always supported me during my PhD. The best of luck with your own PhD, I will always be there for you!

To conclude, I have some advice for other PhD students and young people in general: always (yes, always!) prioritise your personal development over your research. Johan D'Haeseleer, David Allen and other productivity gurus have been instrumental in my personal development. I am convinced that their seminars and books increased my output by at least 100%. They also changed my perspective on life, which is summarised in the following quotes:

"Infinite striving to be the best is man's duty; it is its own reward" - Mahatma Ghandi

"Plans are worthless; planning is everything" – Dwight D. Eisenhower

"Obstacles are those frightful things you see when you take your eyes off your goal" – Henry Ford

"Amateurs sit and wait for inspiration, the rest of us just get up and go to work." – Stephen King

"You can do anything, but not everything" – David Allen

Whenever you find yourself on the side of the majority, it is time to pause and reflect – Mark Twain (adapted)

"*Work on yourself before you work on your work." – Yentl Swolfs*

Abstract

The use of carbon fibre-reinforced composites has been growing exponentially in the past few decades. They offer excellent mechanical properties in combination with a low density, making them an ideal solution for many lightweight applications. However, they often suffer from a lack of toughness. In contrast with carbon fibre composites, self-reinforced composites have an excellent toughness, but a relatively low stiffness and strength. They consist of a polymer fibre in a matrix made from the same polymer. This thesis aims to break through the typical stiffness-toughness dilemma by hybridising carbon fibres with self-reinforced polypropylene (SRPP) and to design a material that is both stiff and tough. The focus lies on optimising the tensile properties and impact resistance of these novel hybrid composites.

Before hybridising SRPP, it is vital that the influence of the process parameters on the mechanical properties of SRPP is understood. Hot compaction uses oriented monocomponent polymer tapes, and melts their outer surface to create the matrix. This process has a narrow processing window and is therefore inherently sensitive to the process parameters. It was shown that increasing the temperature or dwell time increased the matrix fraction and molecular relaxation of the oriented polymer tapes. This leads to improved interlayer bonding, which has a small effect on the tensile properties, but a large effect on the impact resistance. The compaction pressure was even more important, as too low of a pressure can strongly reduce the penetration impact resistance. The impact resistance is a key advantage of SRPP, and therefore potential issues with traditional testing techniques were identified.

Hybridisation of SRPP with carbon fibres resulted in a novel class of hybrid composites with a unique combination of stiffness, strength, ultimate failure strain and impact resistance. Inter- and intralayer hybrids were developed and optimised. For interlayer hybrids, it was revealed how the damage development in tension can be controlled by changing the carbon fibre volume fraction, the carbon fibre and SRPP orientation, and the relative layer thickness. An appropriate choice of these parameters leads to pseudo-ductility, where the carbon fibre layers are able to fracture multiple times. For intralayer hybrids, the importance of intralayer bonding was highlighted. This parameter is crucial as a strong intralayer bonding reduces the ultimate failure strain and impact resistance, but improves the flexural properties. Improving the adhesion between carbon fibre and polypropylene has a similar, but more pronounced effect.

The experimental work was supported by extensive modelling studies. A novel and versatile strength model for unidirectional hybrid composites was developed. This model was first elaborated for non-hybrid composites, and

its strengths and limitations were identified. An in-depth experimental validation was performed for carbon fibre composites by comparing fibre failure predictions with synchrotron computed tomography data. This led to vital recommendations for future model developments. This model was then extended to hybrid composites and an extensive parametric study was performed. This study focused on the hybrid effect, which is a synergistic effect that increases the failure strain of carbon fibres through hybridisation with a more ductile fibre. The hybrid effect was shown to increase by reducing the carbon fibre volume fraction and by improving the dispersion of both fibre types. The mechanical properties of the ductile fibre were not crucial for the hybrid effect, provided its failure strain is at least twice as high as the carbon fibre failure strain. Using very ductile polypropylene fibres instead of the traditional glass fibres hence does not lead to a larger hybrid effect in carbon fibre hybrid composites. The main advantage of polypropylene fibres is its potential of achieving a larger ultimate failure strain. The predictions of the hybrid effect were also compared to experimental measurements. This validation was the first of its kind to achieve a good agreement, which indicates that the model captures the main phenomena of the hybrid effect.

Finally, a road map for optimising hybrid self-reinforced composites was set up by combining the experimental results with the modelling insights. This road map can also be used to optimise other hybrid self-reinforced composites. The presented results revealed the potential benefits of hybrid composites. They should provide a driving force for future work on hybrid composites and for improvements in processing technologies for manufacturing well-dispersed hybrid composites.

Samenvatting

Het gebruik van koolstofvezelversterkte composieten is sterk gegroeid in de laatste decennia. Zij bieden uitstekende mechanische eigenschappen in combinatie met een lage densiteit, wat hen een ideale oplossing maakt voor lichtgewicht toepassingen. Hun grootste nadeel is echter hun lage taaiheid. In tegenstelling tot koolstofvezelcomposieten hebben zelfversterkte composieten een uitstekende taaiheid, maar een relatief lage stijfheid en sterkte. Deze composieten bestaan uit een polymeervezel in een matrix, waarbij beiden van hetzelfde polymeer gemaakt zijn. Deze thesis heeft als doel om door het klassieke taaiheid-stijfheidsdilemma te breken. Dit gebeurt door het hybridiseren van koolstofvezels met zelfversterkt polypropyleen (SRPP) om zo een nieuw materiaal te ontwikkelen dat zowel taai als stijf is. De nadruk ligt op het optimaliseren van de trekeigenschappen en impactweerstand van deze nieuwe hybride composieten.

Vooraleer SRPP te hybridiseren is het belangrijk om de invloed van de procesparameters op de mechanische eigenschappen van SRPP te begrijpen. Warmcompactie gebruikt georiënteerde monocomponent tapes en smelt hun buitenkant om de matrix te vormen. Dit proces heeft een nauw procesvenster, waardoor het inherent gevoelig is aan de procesparameters. Deze thesis toonde aan dat een verhoging van de procestemperatuur of –tijd zowel de hoeveelheid matrix als de moleculaire relaxatie van georiënteerde polymeertapes verhoogt. Dit versterkte de binding tussen de lagen, wat een klein effect heeft op de trekeigenschappen maar een groot effect op de impactweerstand. De druk was nog belangrijker omdat een te lage druk de penetratie-impactweerstand sterk verlaagde. Deze impactweerstand is het belangrijkste voordeel van SRPP en daarom zijn ook potentiële problemen met het testen hiervan onderzocht.

Hybridisatie van SRPP met koolstofvezels leidde tot de ontwikkeling van een nieuwe familie van hybride composieten met een unieke combinatie van stijfheid, sterkte, finale breukrek en impactweerstand. Inter- en intralaag hybrides werden ontwikkeld en geoptimaliseerd. Voor interlaag hybrides werd aangetoond hoe de schade ontwikkeling in trekbelasting gecontroleerd kan worden door het veranderen van de koolstofvezelvolumefractie, de koolstofvezel- en SRPP-oriëntatie en de relatieve laagdikte. Een geschikte keuze van deze parameters kan leiden tot pseudoductiel gedrag, waarbij de koolstofvezellagen meerdere keren kunnen falen. Voor intralaag hybrides is het belang van de intralaaghechting aangetoond. Deze parameter is cruciaal aangezien een sterke intralaaghechting de finale breukrek en impactweerstand verlaagt, maar wel de buigeigenschappen verbetert. Een sterkere hechting tussen koolstofvezel en polypropyleen had een gelijkaardig, maar sterker effect.

Het experimentele werk werd ondersteund door een uitgebreide modelleerstudie. Een nieuw en flexibel model voor unidirectionele hybride composieten werd ontwikkeld. Dit model werd eerst uitgewerkt voor niet-hybride composieten en de voordelen en beperkingen werden aan het licht gebracht. Een diepgaande experimentele validatie werd uitgevoerd door de modelvoorspellingen te vergelijken met synchrotron computertomografie. Dit leidde tot uiterst belangrijke aanbevelingen voor verdere model-ontwikkelingen. Het model werd dan uitgebreid naar hybride composieten en een uitgebreide parametrische studie werd uitgevoerd. Deze studie bestudeerde vooral het hybride effect, wat een synergistisch effect is dat voor een verhoging van de koolstofvezelbreukrek zorgt door hybridisatie met een ductielere vezel. Het hybride effect werd kan vergroot worden door de volumefractie aan koolstofvezel te verlagen of door beide vezels goed te dispergeren. De mechanische eigenschappen van de ductiele vezel zijn niet cruciaal, zolang zijn breukrek minstens twee maal groter is dan die van koolstofvezel. Het gebruik van polypropyleenvezel in plaats van glasvezel zou dus niet leiden tot een groter hybride effect. Het belangrijkste voordeel van de ductiele polypropyleenvezels ligt daarom in zijn potentieel voor het bekomen van een grotere finale breukrek in hybride koolstofvezel-composieten. De voorspelde hybride effecten werden ook vergeleken met experimentele metingen. Deze validatie was de eerste in zijn soort waarbij een goede overeenkomst gevonden werd. Dit toont aan dat het model de belangrijkste aspecten van het hybride effect kan vatten.

Uiteindelijk werden de experimentele resultaten gecombineerd met de modelleerinzichten om zo een road map op te stellen voor het optimaliseren van hybride zelfversterkte composieten. Deze road map kan ook gebruikt worden voor het optimaliseren van andere hybride zelfversterkte composieten. Dit onderzoek toont de potentiële voordelen van hybride composieten aan. Dit zou een drijvende kracht moeten vormen voor verder onderzoek naar hybride composieten en verbeteringen in procestechnologieën voor het maken van goed gedispergeerde hybride composieten.

Table of contents – at a glance

Table of contents – detailed

List of abbreviations

ANOVA	Analysis of variance
ASTM	American Society for Testing and Materials
C	Carbon fibre ply
CF	Carbon fibre
CFRP	Carbon fibre-reinforced plastic
CFRPP	Carbon fibre-reinforced polypropylene
CLT	Classical laminate theory
CTE	Coefficients of thermal expansion
DSC	Differential scanning calorimetry
EC	European Commission
FE	Finite Element(s)
G	Glass fibre ply
HE	High elongation
ISO	International organization for standardization
LE	Low elongation
microCT	Micro computed tomography
MA	Maleic anhydride
MAPP	Maleic anhydride polypropylene
OF	Overfed
OF-F	Overfed with films
PA	Polyamide
PE	Polyethylene
PEEK	Polyether ether ketone
PET	Polyethylene theraphthalate
PLA	Polylactic acid
PMMA	Poly(methyl methacrylate)
PP	Polypropylene
PPS	Polyphenylene sulphide
PVA	Polyvinyl alcohol
RVE	Representative volume element
SCF	Stress concentration factor
SF	Standard fed
SLM	Shear-lag model
SRC	Self-reinforced composite
SRPE	Self-reinforced polyethylene
SRPP	Self-reinforced polypropylene
UD	Unidirectional

List of symbols

α	Exponent for the gauge length dependence of the Weibull distribution [-]
δ_{LE}	Ineffective length of an LE fibre composite [µm]
δ_h	Ineffective length of a hybrid composite [µm]
ε	Strain [-] or [%]
ε^*_{CFRPP}	Failure strain of the CFRPP layers [-]
ε_{full}	Strain at which the delamination reaches its final length [-]
$\bar{\varepsilon}_{h,c}$	Average failure strain of the hybrid composite [-]
$\bar{\varepsilon}_{HE,f}$	Average failure strain of the HE fibres [-]
$\bar{\varepsilon}_{LE,c}$	Average failure strain of the LE fibre composite [-]
$\bar{\varepsilon}_{LE,\mathrm{f}}$	Average failure strain of the LE fibres [-]
ε_D	Strain in the delaminated region [-]
ε_U	Strain in the undelaminated region [-]
ϕ_0	Tape cross-sectional area prior to drawing [m²]
ϕ_f	Tape cross-sectional area after drawing [m²]
$\varnothing$	Outer diameter of the clamp of an impactor [mm]
$\varnothing_{RVE}$	Diameter of the RVE [µm]
λ	Draw ratio [-]
λ_{high}	High draw ratio during overdrawing [-]
λ_{low}	Low draw ratio during overdrawing [-]
ν_{12}	Longitudinal Poisson’s ratio (in 12 direction) [-]
ν_{13}	Longitudinal Poisson’s ratio (in 13 direction) [-]
ν_{23}	Transverse Poisson’s ratio (in 23 direction) [-]
θ	Slope of the sample for C-scan [°]
ρ_{CF}	Carbon fibre density [kg/m³]
ρ_{high}	High density [kg/m³]
ρ_{low}	Low density [kg/m³]
ρ_{PP}	Polypropylene density [kg/m³]

σ	Stress [MPa]
σ_0	Weibull scale parameter [MPa]
σ_{01}	Weibull scale parameter of the first flaw population [MPa]
σ_{02}	Weibull scale parameter of the second flaw population [MPa]
σ_{CFRPP}	Strength of the CFRPP layer [MPa]
σ_D	Stress in the delaminated region [MPa]
σ_f	Fibre strength [MPa]
σ_U	Stress in the undelaminated region [MPa]
$\sigma_{z,avg}$	Average fibre stress at distance z from fibre break [MPa]
ΔH	Enthalpy change [J]
ΔP	Pressure change [bar]
ΔS	Entropy change [J/K]
ΔT_m	Melting temperature change [K or °C]
A	Cross-sectional area of a fibre [μm^2]
A_D	Cross-sectional area of the delaminated region [m^2]
A_{HE}	Cross-sectional area of the high elongation fibre [μm^2]
A_{LE}	Cross-sectional area of the low elongation fibre [μm^2]
A_U	Cross-sectional area of the undelaminated region [m^2]
C^u	Unidirectional carbon fibre layer [-]
C^w	Woven carbon fibre layer [-]
d	Surface-to-surface distance between two fibres [μm]
D	Fibre diameter [μm]
E	Young’s modulus [GPa]
E_{11}	Longitudinal Young’s modulus (in 11 direction) [GPa]
E_{22}	Transverse Young’s modulus (in 22 direction) [GPa]
E_{33}	Transverse Young’s modulus (in 33 direction) [GPa]
E_{CFRPP}	Tensile modulus of CFRPP layer [GPa]
E_{HE}	Young’s modulus of the high elongation fibre [GPa]
E_{LE}	Young’s modulus of the low elongation fibre [GPa]
E_{SRPP}	Tensile modulus of SRPP layer [GPa]
F	Applied force [N]
F_0	Force required for overdrawing [N]

F_D	Force in the delaminated region [N]
$\mathrm{F}_{\mathrm{max}}$	Maximum force during impact [N]
F_U	Force in the undelaminated region [N]
G	Shear modulus of an isotropic material [GPa]
G_{12}	Longitudinal shear modulus (in 12 direction) [GPa]
G_{13}	Transverse shear modulus (in 13 direction) [GPa]
G_{23}	Transverse shear modulus (in 23 direction) [GPa]
$G_{II,\mathrm{C}}$	Mode II fracture toughness [kJ/m²]
G_{ratio}	Geometric ratio [-]
h_1	Height of the first support of a C-scan [mm]
h_2	Height of the second support of a C-scan [mm]
h_{trans}	Distance between transducer and the glass plate [mm]
k_h	Stress concentration factor in a hybrid composite in Zweben's model [-]
k_{LE}	Stress concentration factor in an LE fibre composite in Zweben's model [-]
$k^{overheating}$	Phenomenological constant defining the increase in melting temperature with increased pressure [°C/bar]
L	Characteristic gauge length in the Weibull distribution [mm]
L_0	Reference gauge length in the Weibull distribution [mm]
L_D	Length of the delaminated region [mm]
$L_{D,\mathrm{full}}$	Final length of the delaminated region [mm]
$L_{D,init}$	Initial length of the delaminated region [mm]
L_{edge}	Edge length of an impact sample [mm]
L_{RVE}	Length of the RVE [µm]
L_{tot}	Total sample length [mm]
L_U	Length of the undelaminated region [mm]
m	Weibull modulus [-]
m_1	Weibull modulus of the first flaw population [-]
m_2	Weibull modulus of the second flaw population [-]
n_{crit}	Critical cluster size [-]
N_{EA}	Factor in Zweben's model which only depends on $E \cdot A$ [-]

P	Probability of fibre failure [-]
R	Fibre radius [µm]
R^2	Coefficient of determination in linear regression [-]
R_{CF}	Carbon fibre radius [µm]
R_{EA}	Ratio of the normalised stiffnesses of both fibre types [-]
R_{GF}	Glass fibre radius [µm]
R^{hybrid}	Hybrid effect [-]
S^{U}	Unidirectional SRPP layer [-]
S^{W}	Woven SRPP layer [-]
t	Sample thickness [mm]
t^{c}_{CFRPP}	Critical layer thickness of the CFRPP [mm]
t_m	Thickness of the matrix region in Zweben's model [µm]
T_g	Glass transition temperature [K or °C]
T_m	Melting temperature [K or °C]
V_f	Fibre volume fraction [%]
V_H	Ratio of delaminated cross-sectional area over undelaminated cross-sectional area [-]
w_{CF}	Carbon fibre weight [kg]
w_m	Width of the matrix region in Zweben's model [µm]
w_{PP}	Polypropylene weight [kg]
z	Distance along a fibre [µm]
z^*	A specific distance along fibre [µm]

List of figures

List of tables

Chapter 1:

Introduction

The framework of this thesis is placed in a broader context. The benefits of carbon fibre composites as well as self-reinforced composites are introduced and their drawbacks are assessed. The concept of hybrid self-reinforced composites is introduced and the strengths and limitations of this novel material combination are discussed. The objectives of this thesis are stated. Finally, the structure of this thesis is outlined and the relationship between the chapters is explained.

1.1 General introduction

Fibre-reinforced polymer composites consist of reinforcing fibres in a polymeric matrix. The reinforcing fibres impart stiffness and strength to the composite, but do not provide structural integrity on their own. This integrity is provided by the matrix, which binds the fibres together and forces them to deform as a whole. The two most common fibres are carbon and glass due to their high stiffness and strength. These properties combined with a low density matrix lead to excellent mechanical performance, both in absolute terms and on a weight basis.

Fibre-reinforced polymer composites are increasingly used in a growing number of applications [1]. This is especially true for carbon fibre-reinforced polymer composites (CFRP). Early CFRP applications were mainly in sports equipment and aerospace, where its excellent properties fulfilled the lightweight and performance requirements [2-4]. These areas continue to be major markets for composites. In the past decade however, CFRPs have also been introduced in more cost-driven markets of which the automotive industry is the most prominent example [1,5]. Currently, extensive use of CFRPs is mainly found in expensive cars that are produced in limited volumes. Popular examples include McLaren’s MP4 [4], Lamborghini’s Aventador [6] and Tesla’s Roadster [7,8].

The use of CFRP in automotive industry is gradually shifting into higher volume cars [1]. The BMW i3 is claimed to be the first high volume car with its load carrying structure and body made of CFRP [9]. Figure 1-1 shows this load carrying structure. The BMW i3 is an electric vehicle and hence requires a large and heavy battery pack [10]. The main drawback of these cars is their limited driving range [11,12]. This range strongly depends on the vehicle weight, making the use of lightweight materials critical for their success. Lowering the weight and thereby increasing driving range is the main driver for the use of CFRP in electric cars.

Figure 1-1: The load carrying structure of a BMW i3 made in CFRP [13].

A low manufacturing cycle time is also critical for composites if they want to be successful in high volume applications. If the aim is to produce more than 100.000 pieces per year, then the cycle time needs to be below 5 min. Most traditional manufacturing technologies use thermoset matrices that normally require longer cycle times for curing of the resin [14]. This is not a problem in the aerospace industry, where the number of parts produced per day is relatively low. The automotive industry, however, requires improvements in processing technology for thermoset resins to reach high volumes in a cost-efficient manner [15-18]. An alternative strategy to reduce cycle times is to switch to thermoplastic composites. Common thermoplastics do not require curing and can hence be produced in short cycle times. Thermoplastic composites have the additional benefit of better recyclability than their thermoset counterparts. This recyclability became crucial for new materials in automotive applications due to the European directive on end-of-life vehicle 2000/53/EC [19].

Most thermoplastics have a better impact resistance than their thermoset counterparts [18,20-22]. Nevertheless, even thermoplastic composites are generally considered to be brittle materials. The failure strain of long fibre thermoplastic CFRP is similar to that of thermoset CFRP and does not exceed 2% in the fibre direction [18,23].

Thermoplastic composites are of great interest to the automotive industry, but do have some disadvantages. Firstly, the impregnation is more difficult due to the high viscosity of thermoplastic resins [24-26]. Typically, high pressures are needed for impregnation, which necessitates the use of expensive equipment. Secondly, melting thermoplastics only creates new physical bonds and no new chemical bonds. Creating a strong bond between fibre and matrix is hence a common problem in traditional fibre-reinforced composites. A weak fibre/matrix bond may initiate damage earlier than in composites with a strong bond [27]. Interfacial bonding issues also arise in thermoset composites due to the inherent chemical differences between fibre and matrix. These issues are, however, more pronounced for thermoplastic composites.

The impregnation and interfacial bonding issues in thermoplastic composites can be solved by self-reinforced composites (SRCs). These composites consist of a fibre and a matrix that are made from the same polymer. The matrix is created in situ around each individual fibre, which strongly reduces the impregnation length. Unlike traditional thermoplastic composites, SRCs hence do not suffer from impregnation issues. Moreover, fibre and matrix are made from the same polymer and are hence chemically compatible. This creates a strong interface, which will be difficult to break [28,29]. Finally, SRCs are also tougher than carbon and glass fibre composites [30-32]. This is true for toughness in terms of impact resistance, but also in terms of ultimate failure strain. Currently, self-reinforced polypropylene (SRPP) is not only the toughest SRC [32-34], but also commercially the most important one [32,35,36].

1.2 Problem statement

Most materials follow the stiffness-toughness dilemma, meaning they are either stiff and strong but lacking toughness or tough but compliant and weak [37-40]. SRPP and CFRP do not escape this dilemma. SRPP combines a low density with a high toughness. Its relatively low stiffness and strength unfortunately make SRPP unsuitable for structural and semi-structural applications. In contrast, carbon fibre-reinforced composites possess an excellent stiffness and strength, but often suffer from their lack of toughness.

By hybridising SRPP with carbon fibre, the aim is to achieve a better balance in stiffness, strength and toughness. These hybrid self-reinforced composites, however, also create new scientific challenges. Nearly all research on hybrid composites deals with combinations of two brittle fibre types. Carbon fibre is for example often hybridised with glass or aramid fibres, but only rarely with polymer or metal fibres. In hybrid self-reinforced composites, the failure strain of both fibre types differs by a factor of 10, compared to a factor of 2 in traditional hybrid composites. Similarly, the stiffness differs by a factor of more than 20 compared to a factor of 3 in traditional hybrid composites. Drawing conclusions from the available literature is difficult due to these large differences.

A major difficulty in hybrid composites is to understand how the failure of the CFRP affects the ductile fibres. CFRP fails in an explosive manner, releasing a large amount of energy almost instantaneously. The ductile fibres may immediately break when this occurs, or they may be able to absorb this energy without significant damage. The parameters that govern these phenomena in hybrid composites are currently unknown.

Models that are capable of predicting the strength of hybrid composites would allow an efficient investigation of many of these parameters. As will be shown later, these types of models are lagging behind on the state-of-the-art models for non-hybrid composites. The understanding of the failure development in hybrid composites is therefore mainly limited to qualitative instead of quantitative statements. The state of the art in hybrid composites would greatly benefit from the development of suitable and reliable strength models.

SRCs are inherently difficult to manufacture, as the polymer fibres are sensitive to temperature. This requires an accurate process control and a proper understanding of the influence of the processing parameters. The optimal processing conditions strongly depend on the type of polymer fibre, and hence need to be optimised separately for each SRC.

Apart from these challenges, hybrid self-reinforced composites also create new opportunities. The increase in composite failure strain that can potentially be achieved is much larger in hybrid SRCs. The failure strain of the least brittle fibre is typically set as a theoretical upper limit for the failure strain of hybrid composites. In case of hybrid SRPP, this can be up to 20%, while this is only 3-4% for carbon/glass hybrid composites. Whether and under which conditions such large failure strains can actually be achieved in practice is currently unknown in literature.

1.3 Objective and thesis outline

The overall research objective is to **develop a novel class of hybrid SRCs with optimised mechanical performance**. The research focuses on tensile behaviour and impact resistance, as these are the two key mechanical properties for potential applications of hybrid SRCs. Ideally, the tensile stiffness and strength of SRCs should be improved without large losses in toughness and impact resistance. To maximise the impact resistance, SRPP is chosen, as this is currently the toughest SRC. SRPP will be hybridised with carbon fibre to maximise the stiffness and strength and increase competitiveness with traditional automotive materials, such as aluminium and steel.

To successfully achieve the overall objective, this thesis is divided into four chapters of results, each with their own research objective. Table 1-1 summarises the objectives of each of these four chapters.

Table 1-1: Summary of the objectives of the four chapters of results.

Chapter #	Objective
2	Understanding the tensile behaviour and impact resistance of SRCs and how they are affected by processing parameters.
3	Understanding how the addition of carbon fibre affects the mechanical properties of SRCs and how the material and processing parameters can be optimised in practice.
4	Developing a reliable and versatile model for tensile behaviour of unidirectional fibre-reinforced composites
5	Extending the strength model to hybrid composites and understanding how failure develops. This leads to further guidelines for optimising tensile behaviour of hybrid composites.

Figure 1-2 presents a schematic overview of how the different chapters are linked together and how they jointly lead to the overall research objective. Each of these chapters deals with a different topic that has its own challenges. Therefore, each chapter begins with a description of the state of the art for that specific topic.

Chapter 2 is a prerequisite for studying hybrid SRCs and reaching the overall goal. This chapter develops an in-depth understanding of the tensile behaviour and impact resistance of SRCs. The objectives of chapter 2 will help to understand the more complex situation in hybrid SRCs.

Chapter 3 is most closely linked to the overall research goal of optimising hybrid SRCs. This chapter focuses on experimentally optimising the mechanical properties of hybrid SRCs. To succeed in the overall goal however, experiments alone are insufficient. Some parameters cannot be changed experimentally due to practical limitations. These limitations can be overcome through modelling. Strength models for hybrid composites are hence required. Such models facilitate parametric studies and are more efficient than trial-and-error experiments.

Unfortunately, appropriate strength models for hybrid composites are not available in literature. Therefore, a novel and versatile strength model for UD hybrid composites is developed. Chapter 4 sets up this strength model for non-hybrid composites and analyses the issues that may occur in these types of models. Chapter 5 then extends this strength model to hybrid composites and performs an extensive parametric study. Chapter 3 and 5 are linked together, as some conclusions of one chapter will be used in the other.

In the end, a road map will be developed that describes how the processing and material parameters affect the mechanical properties. This map will be established based on both experimental and modelling evidence. The goal of such a map is to be able to tailor hybrid SRCs to specific requirements for application.

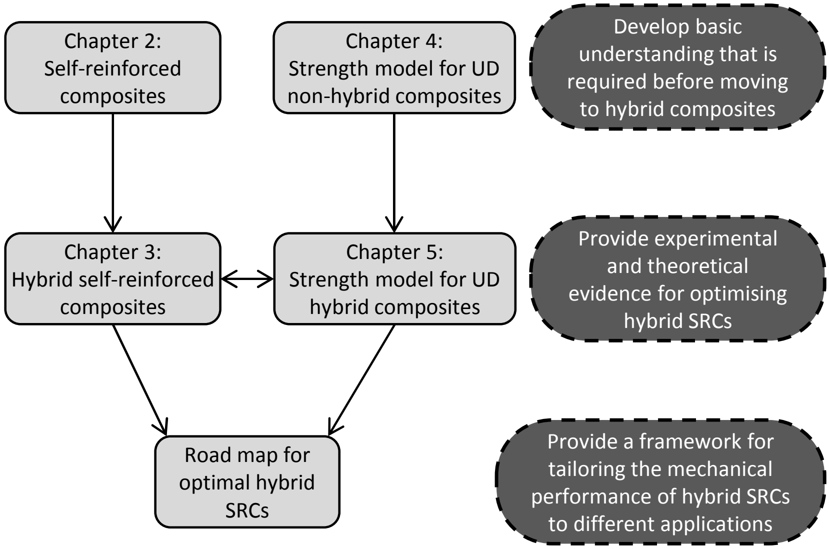

Figure 1-2: Schematic overview of how the four chapters of results are linked together and lead to the overall research objective.

Chapter 2:

Self-reinforced composites

Self-reinforced composites have interesting mechanical properties, but do pose some additional challenges compared to traditional fibre-reinforced composites. These challenges need to be understood before moving into the hybrid self-reinforced composites. This chapter therefore analyses three of these difficulties. Firstly, the relationship between process parameters and mechanical properties of self-reinforced composites is revealed. Secondly, impact testing methodologies are introduced and their potential issues for testing self-reinforced composites are highlighted. Finally, it is shown how the weave architecture affects the mechanical properties as well as the processing window.

This chapter describes the mechanical properties of SRCs and has two objectives. The first objective is to optimise the hot compaction process. Such optimisation is required for making high-quality and consistent SRCs, as hot compaction is sensitive to its process parameters. The second objective is to understand the tensile behaviour and impact resistance of SRCs. These two aspects of mechanical behaviour are chosen, as both are vital in practical applications and in optimising hybrid SRCs.

The state of the art and materials and methods sections are followed by three sections of results. Figure 2-1 gives an overview of these sections and the type of properties that are investigated in each section.

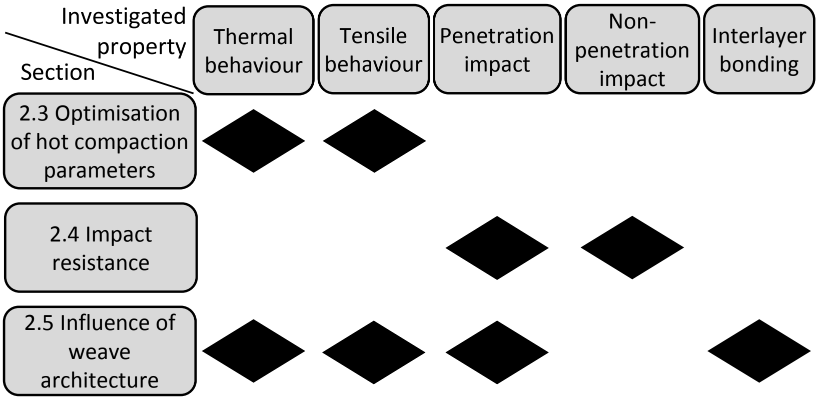

Investigated property / Section	Thermal behaviour	Tensile behaviour	Penetration impact	Non-penetration impact	Interlayer bonding
2.3 Optimisation of hot compaction parameters	◆	◆			
2.4 Impact resistance			◆	◆	
2.5 Influence of weave architecture	◆	◆	◆		◆

Figure 2-1: Schematic overview of the material behaviour that will be investigated in three sections of results in this chapter.

2.1 State of the art

Thermoplastic polymers combine a low density with excellent processability. These polymers cannot be used in structural applications due to their low stiffness and strength as well as their creep sensitivity. These drawbacks can be mitigated by adding traditional reinforcement fibres, such as carbon and glass fibres. The nature of the chemical bonds in these fibres and the matrix are often different. This difference hinders the development of a strong bond. A weak fibre-matrix interface can lead to reduced compressive strength [41] and fatigue resistance. While sizings can improve the bond strength [42], this interface issue remains troublesome in composites.

In search for composites with strong fibre-matrix interfaces, Capiati and Porter [28] combined polyethylene (PE) fibres with a PE matrix. The PE fibres have a high molecular orientation, which leads to excellent mechanical properties. This will be explained in more detail in “2.1.1 Oriented polymers". The PE matrix was unoriented and its main function is to hold the fibres together. Capiati and Porter used the small difference in melting points of both PEs to make "one polymer composites", also known as single polymer, all-polymer or self-reinforced composites (SRC). The terminology of self-reinforced composites or SRCs will be consistently used throughout this thesis.

SRCs have several interesting properties:

- low density,
- good recyclability,
- easy impregnation,
- excellent toughness.

The low density is derived from the lack of any fillers. The recyclability also stems from this lack of fillers. Since SRCs contain only one polymer, melting and re-using is possible without significant property degradation. Such degradation is inevitable in recycling of carbon or glass fibre-reinforced composites. Impregnation is often a problem in thermoplastic composites due to the high melt viscosity of thermoplastics. SRCs, however, create the matrix in situ, which avoids any impregnation problems. The reasons for the excellent toughness will be explored further in "2.1.3 Mechanical properties".

The initial research on SRCs focused on self-reinforced PE (SRPE). The flexible PE backbone leads to an excellent drawability, allowing high molecular orientation and high stiffnesses of up to 200 GPa [43,44]. This seemed promising as woven SRCs with a stiffness of up to 40 GPa were achieved [45]. This means SRCs can outperform glass fibre composites in stiffness at a much lower density. SRPE, however, had some serious drawbacks [32,36]:

- low maximum service temperature,
- high creep sensitivity,
- low toughness,
- high price.

In the middle of the nineties, these drawbacks caused a shift to other SRCs. Various polymers have been investigated: polypropylene (PP) [46-49], polyethylene terephthalate (PET) [50-52], polyamide (PA) [34,53], poly(methyl methacrylate) (PMMA) [54-56], polyvinyl alcohol (PVA) [57], polylactic acid (PLA) [58] and liquid crystalline polymers [33]. The largest commercial potential was found in self-reinforced PP (SRPP). The benefits of SRPP compared to SRPE include [32,36]:

- increased maximum service temperature,
- higher toughness,
- wider processing window,
- lower price.

Various processing methods have been devised to produce SRCs, such as hot compaction [32,45-48,59], bi-component tapes [60-62], film stacking [28,63,64], exploiting polymorphism [65,66], and powder impregnation [67]. These will be discussed in more detail in "2.1.2 Production of self-reinforced composites". Most processing methods start off with highly oriented polymers. The production process and properties of these oriented polymers will first be described in the next subsection.

2.1.1 Oriented polymers

Oriented polymers are of great importance in nature. Orientation indicates whether a material is aligned and anisotropic. In contrast with isotropic materials, the mechanical properties of anisotropic materials depend on the measurement direction. Nature has perfected the use of oriented polymers. Silk spiders pull on their silk fibres during spinning. This increases the molecular orientation inside the fibres and increases their stiffness and strength. The cellulose microfibrils in the flax plant are mainly oriented in the direction of the stem to maximise rigidity of the stem. Similarly, coconut or coir fibres have much less oriented microfibrils, as nature builds them to absorb energy when the coconut falls from the tree.

Oriented polymers are popular in many industrial applications, such as packaging, tapestry and rope industries. Every production process inevitably induces some local orientation in polymers. The discussion here will focus on solid state drawing, as this is the key technology for the fibres and tapes used in SRCs.

Solid-state drawing

Solid-state drawing takes place between the glass transition temperature T_g and melting temperature T_m of the polymer. Before drawing, the polymer can be considered to be isotropic, with large and randomly oriented spherulites [68,69]. A spherulite is a stack of densely packed lamellae, which consist of folded chains. Figure 2-2 depicts three of these lamellae. Each molecule is mainly part of a single lamellae. At some locations however, molecules can be part of more than one lamella. The parts of the molecules that interconnect the lamellae are called tie molecules. These molecules are crucial during the drawing process.

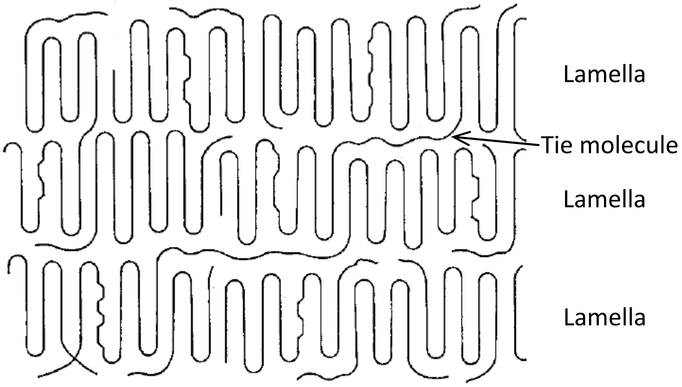

Figure 2-2: Stack of three lamellae containing folded chains. The parts of the molecules that connect two lamellae together are called tie molecules (adapted from [68], with permission from Springer).

These lamellae are highly oriented in itself, but all of them are oriented in different directions. This leads to behaviour that is more or less isotropic. Solid state drawing is then applied to orient the molecules and increase the mechanical performance in the drawing direction. Typically, the polymer is guided over two rollers with a different rotation speed. This elongates the polymer, thereby stretching, rotating and breaking up crystal lamellae [68,70]. This molecular process of chain reorientation during drawing is illustrated in Figure 2-3. This process results in small but highly oriented crystal lamellae, with tie molecules in between. Some authors prefer the terminology of microfibrils instead of lamellae [69], as they are small and narrow. The orientation of the tie molecules is not as strong as for the crystals. Nevertheless, the orientation of these tie molecules is known to determine the tensile modulus [71].

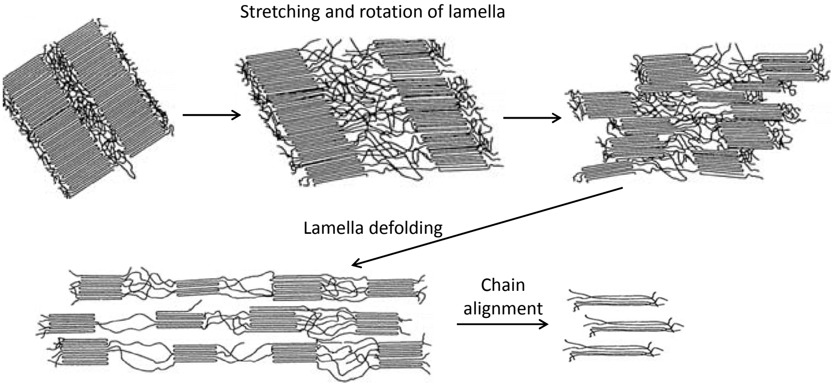

Figure 2-3: Scheme of chain reorientation during solid state drawing (adapted from [70], with permission from Elsevier).

The drawability of a polymer is determined by the flexibility of the backbone and the molecular weight [72-74]. Polymers containing aromatic rings have stiff backbones and are hence difficult to draw. PE has a flexible backbone, as it consists of only carbon-carbon bonds in the main chain. Depending on the specific grade, PE can not only have many but also large side chains. These side chains are typically kept to a minimum to achieve a good drawability.

Just like PE, PP belongs to the group of olefinic polymers. Figure 2-4 presents the PP backbone. This backbone has three steric configurations: isotactic, syndiotactic and atactic. The CH_3 side chain can be accommodated in crystals by forming a helical structure. Such structure is only possible for isotactic and syndiotactic PP. The different crystal structure in syndiotactic PP may have potential to yield a higher stiffness [75]. To date, however, this potential has not been achieved yet, mainly due to difficulties in achieving high degrees of syndiotacticity. Therefore, the focus here is on isotactic PP.

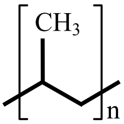

Figure 2-4: Molecular structure of PP.

The draw ratio, λ, is a crucial parameter to characterise oriented polymers. λ is defined as the ratio of the initial cross-sectional area ϕ_0 of the tape over the final cross-sectional area ϕ_f:

$$\lambda = \frac{\phi_0}{\phi_f} \tag{2-1}$$

Overdrawing

Overdrawing is a peculiar regime in drawing of polymers. This occurs when a certain draw ratio is exceeded. For PP, this can be visually observed by a change in appearance from transparent to white (see Figure 2-5). The whitening occurs due to the formation of crazes and voids inside the polymer [76]. In industry, this regime is often avoided due to the increased number of fractures during the drawing process. Only recently, there has been significant interest in literature in the overdrawing regime [75,77]. For SRCs, this regime is of particular interest, as all the commercial manufacturing processes for SRCs use overdrawn tapes.

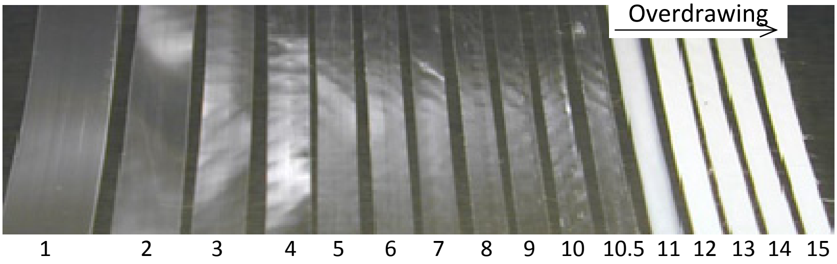

Figure 2-5: Optical appearance of tapes drawn at various draw ratios. The number below each tape indicates the draw ratio (adapted from [75], with permission from the author).

In PP, overdrawing leads to the development of a peculiar microstructure. This microstructure is crucial in understanding the tape behaviour. Figure 2-6 schematises its microstructure, consisting of regions with a higher (grey) and lower (black) draw ratio. The reason for the development of these regions was explained by El Maaty [78]. Overdrawing starts when the draw ratio λ_{low} in Figure 2-7 is reached. To achieve a draw ratio in between λ_{low} and λ_{high}, the force F_0 is required. This causes the tape to split up into regions with a low draw ratio λ_{low} and regions with a high draw ratio λ_{high}. The tape is hence simultaneously drawn at both draw ratios.

This phenomenon is similar to necking, where the cross-section decreases to maintain the density of the material. In the case of overdrawing however, the cross-section is maintained, which means that the density needs to decrease [78]. The high draw ratio regions would like to contract, but the low draw ratio regions prevent this contraction. This can also be observed in Figure 2-5, where the width of the overdrawn tapes does not decrease in the overdrawing regime. A biaxial stress state is created in the high draw ratio regions. Due to the high draw ratio, the transverse strength was reduced in those regions. The combination of biaxial stress state and low transverse strength creates regions with low densities by creating voids or crazing in the material [78]. These regions further reduce the transverse strength of tapes, which is crucial in the behaviour of SRCs.

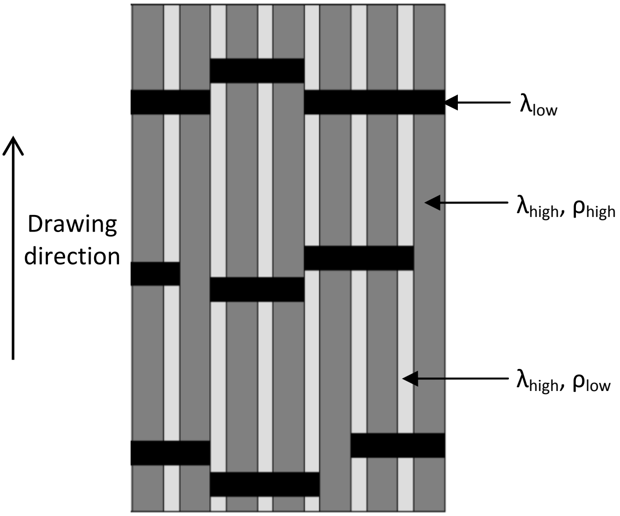

Figure 2-6: The microstructure of a drawn PP tape, containing regions with different draw ratios and densities (adapted from [75]).

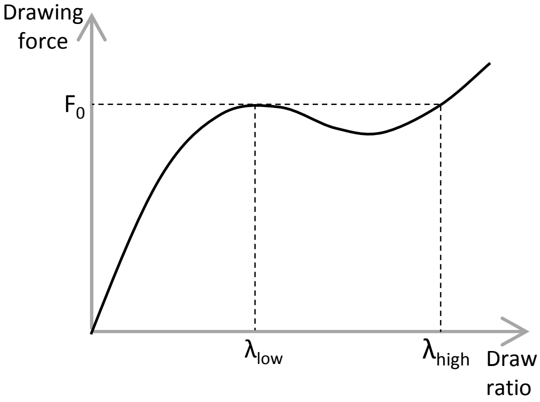

Figure 2-7: Drawing force as a function of draw ratio, to illustrate the high and low draw ratio regions in overdrawn PP tapes (based on [78]).

The low density regions should also lead to a reduction in the overall density of the tape. Alcock et al. [72] confirmed this by measuring the tape density as a function of the draw ratio, see Figure 2-8. The density is constant until a draw ratio of about 11, after which the density rapidly drops. This draw ratio also corresponded to the change from transparent to opaque tapes.

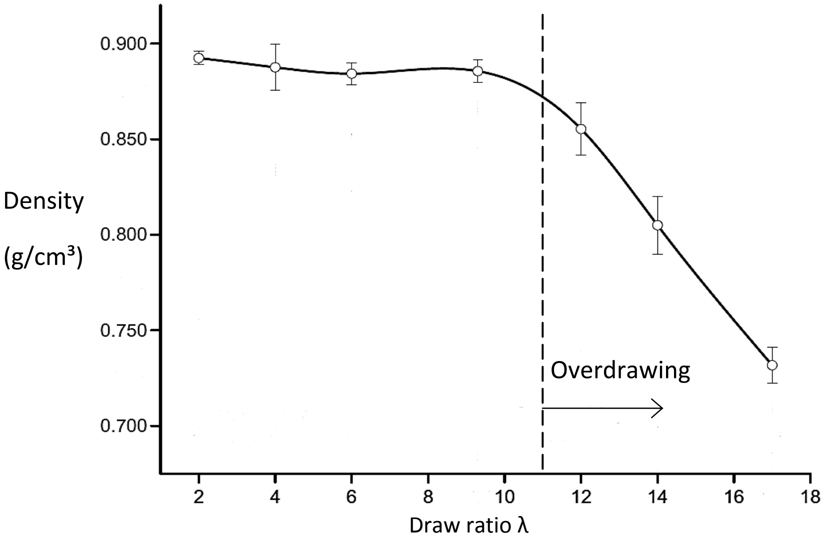

Figure 2-8: Density as a function of draw ratio, illustrating the onset of overdrawing (adapted from [72], with permission from Elsevier).

Mechanical behaviour

The tensile modulus of drawn polymers strongly depends on the draw ratio. Figure 2-9 illustrates this for PP tapes. A typical tensile modulus for isotropic PP is 1-1.5 GPa, while a tensile modulus of about 15 GPa is achieved for λ=17. Yamada et al. [71] proved that the tensile modulus keeps on increasing even though crystal orientation levels off for draw ratios above 9. In contrast, the orientation of the tie molecules keeps increasing. This correlates well with the increase in tensile modulus. This proves that the tensile modulus is determined by the orientation of the tie molecules instead of by the orientation of the crystals.

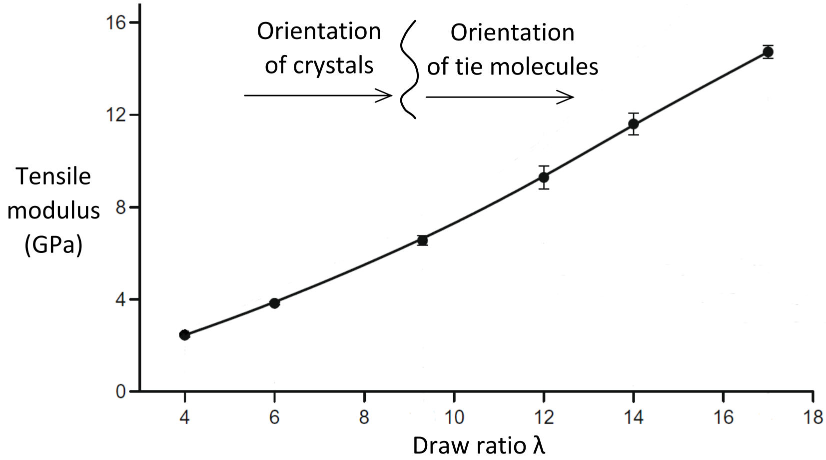

Figure 2-9: Tensile modulus as a function of draw ratio (adapted from [72], with permission from Elsevier).

Figure 2-10 plots the tensile strength and failure strain as a function of draw ratio. Tensile strength is known to be governed by the orientation of the crystals [79]. This orientation increases by the drawing process but levels off for draw ratios above 9 [71]. This correlates well with the observed plateau in tensile strength, indicating that crystal orientation determines the tensile strength.

The increase in tensile strength also causes a large reduction of the failure strain. If the tape was linear elastic, then this reduction is expected as the tensile modulus keeps increasing, while the tensile strength levels off. As will be shown in Figure 2-16, the tape behaviour is not completely linear, but it is nevertheless a reasonable approximation. For the highest draw ratio, this failure strain is about 10%, which is still significantly higher than the 1.5-2% for carbon fibre.

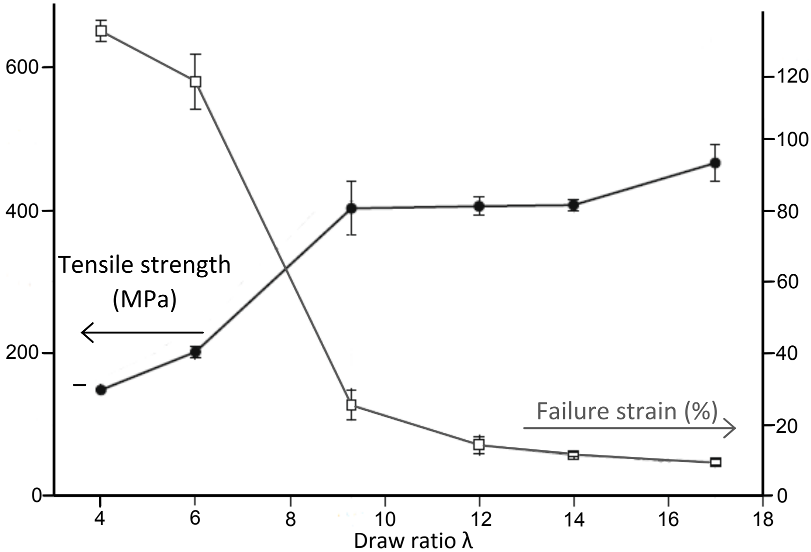

Figure 2-10: Tensile strength and failure strain as a function of draw ratio (adapted from [72], with permission from Elsevier).

Defining a typical draw ratio for the tapes used in SRPP is difficult, as this value is often not mentioned in literature. Alcock et al. [60,61] and Abraham et al. [80] are notable exceptions. Alcock et al. used tapes with a draw ratio of 8 and 17, while Abraham et al. used a PP tape which coincidentally had a draw ratio of 8 as well. The draw ratio however does not uniquely determine the mechanical properties, as those also strongly depend on the PP grade and the drawing conditions. Some authors used geotextiles, in which the tapes are typically not overdrawn [81,82]. The properties of these tapes typically are: a tensile modulus of 5-8 GPa, a tensile strength of 350-450 MPa and a failure strain of 15-20% [81-83]. For overdrawn tapes, typical reported values are: a tensile modulus of 10-15 GPa, a tensile strength of 350-600 MPa and a failure strain of 5-15% [72,75,77,82].

2.1.2 Production of self-reinforced composites

The subsection describes the production of SRCs. First, the two most important production processes are compared. Then, it is shown how these processes can be optimised and how the process parameters affect the mechanical properties. Finally, the morphology of SRCs is discussed, as this is closely linked with the process parameters.

Hot compaction versus bi-component tape technology

Two processes for making SRPP have been commercially developed: CURV® and PURE®/Tegris®. The technical name for the CURV®-process is hot compaction. This process was developed at the University of Leeds by Hine, Ward and co-workers [32]. PURE® and Tegris® are based on bi-component tape technology and was developed by Peijs and co-workers. Sometimes, this technology is referred to as “co-extrusion”, but this terminology is misleading. Co-extrusion refers to the process of making bi-component tapes, instead of that of making SRCs. Therefore, the terminology co-extrusion will be avoided in this thesis.

The crucial difference between both processes is that hot compaction uses a mono-component material, while bi-component tape technology implies two components in the starting material. Other processes for SRCs include film stacking [28,63,64], powder impregnation [67] and exploiting polymorphisms [53,65,66]. Polymorphism indicates that a polymer can exist in different crystal structures. Each crystal structure typically has a different melting temperature, which can hence be exploited to make SRCs. The properties of SRCs made with these alternative processes resemble SRCs made with either hot compaction or bi-component tape technology. Which process they resemble depends on a combination of the applied pressure and temperature and whether copolymers are used. The focus here will be on the two most common processes: hot compaction and bi-component tape technology.

The differences between hot compaction and bi-component tape technology are schematised in Figure 2-11. Hot compaction starts off with mono-component oriented fibres or tapes. These fibres are brought to the compaction temperature, which melts their outer sheath, but maintains the orientation in the inner core. Pressure is applied throughout the process to prevent shrinkage and to aid in the impregnation [46].

The bi-component tape technology process starts with bi-component tapes, made by co-extrusion. These tapes consist of a homopolymer core, covered by a thin copolymer layer. The process exploits the difference in melting temperature between the homopolymer and copolymer. By applying a temperature in between both melting temperatures, the outer layer melts and binds the homopolymer cores together.

Hot compaction and bi-component tape technology are essentially similar processes. Both processes melt the outer layer of the fibres or tapes by applying pressure and temperature (see Figure 2-11). The main difference is the temperature required to do so. In hot compaction, the temperature needs to be close to the melting temperature of the tape to allow selective melting of the surface. In bi-component tape technology on the other hand, the temperature can be significantly lower as the outer layer consists of copolymer with a lower melting temperature.

(a) Hot compaction

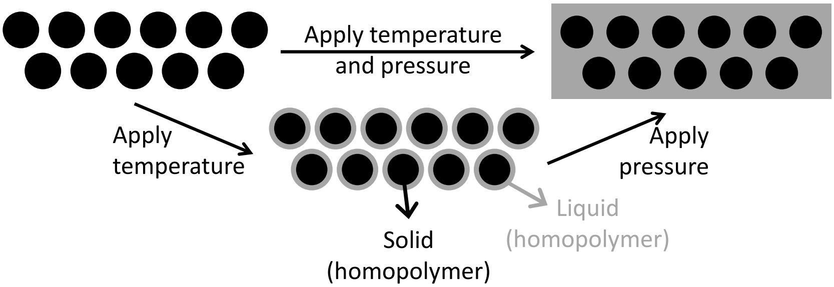

(b) Bi-component tape technology

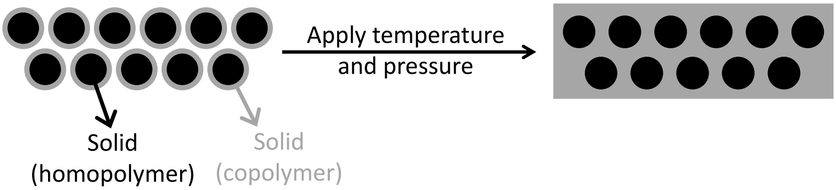

Figure 2-11: Comparison between (a) hot compaction and (b) bi-component tape technology as manufacturing methods for SRCs.

Both processes lead to high volume fraction of tapes in the range of 70 to 90%. A crucial difference between both processes is the way this fibre volume fraction is controlled. Bi-component tape technology determines the fibre volume fraction by changing the layer thickness of the copolymer. In contrast, the applied temperature, pressure and dwell time determine the fibre volume fraction during hot compaction [33,46]. The hot compaction process is therefore more sensitive to small variations in the process parameters.

The advantages of both processes are summarised in Table 2-1. The higher interlayer bonding and better thermoformability of hot compacted SRCs are mainly caused by the mono-component nature. The main advantage of the bi-component tape technology is the wider process window. This also leads to the possibility to directly form woven preforms, thereby avoiding the need for pre-compaction. Slightly higher stiffnesses are possible due to the lower molecular relaxation at lower processing temperatures. It should be noted that the sheet stiffness strongly depends on the stiffness of the starting tapes. These tapes have a higher draw ratio and are hence stiffer for bi-component tape technology. This higher draw ratio also limits the failure strain and affects the thermoformability in a negative way.

Table 2-1: Comparison between hot compaction and bi-component tape technology.

Hot compaction	Bi-component tape technology
Higher interlayer bonding [29,60,81,84-86]	Wider process window [32,36,61]
Better thermoformability [32,87]	Possibility to directly form woven preforms [87]
	Higher stiffness [88,89]

Some other advantages of one process over the other have been mentioned in literature. These were not added to Table 2-1, as they are either incorrect or have not been proven yet.

Molecular continuity is often mentioned as an advantage of hot compaction [34,82,90]. While molecular continuity is inevitable due to the mono-component nature of the process, this continuity also occurs in bi-component tape technology [36]. There is currently no direct proof for this molecular continuity nor is there any measure to quantify it.

The higher interlayer bonding for hot compaction could also have an effect on the penetration impact resistance. There is, however, no proof of this statement in literature. When comparing data in literature, most values lie in the range of 20-40 J/mm [32,60,91]. Comparing the data sheets from the commercial products is also inconclusive [88,89]. Furthermore, all data were gathered for SRCs with different polymer grades, draw ratios and weave architectures. One-to-one comparisons are currently not available, making it impossible to draw strong conclusions for impact resistance.

The rest of this state-of-the-art review will focus on hot compaction. In some cases, comparisons with bi-component tape technology will be made, to highlight some crucial differences.

Process optimisation

Optimising the process parameters for SRCs is not straightforward, as it requires an accurate process control. This is mainly due to the nature of oriented polymers, which are thermodynamically unstable. At increased temperatures, the driving force to return to their isotropic state increases. The four key process parameters are: temperature, pressure, dwell time and cooling rate.

From these four parameters, **temperature** is the most important one. The temperature window for bi-component tape technology is supposed to be about 30°C [61], while this window is only a few °C for hot compaction. One can of course argue how this process window should be defined, as the properties of SRCs change gradually with processing temperature. It is often stated that the temperature for hot compaction should be near the melting temperature T_m of the fibres or tapes. Despite the fact that this statement is correct, it is not helpful. T_m is strongly linked with the applied **pressure** through the superheating effect [32,34,35,92-95]. In general, superheating implies that a transition does not happen even though the temperature is sufficiently high. This can be explained using the concepts of thermodynamics. Using the Gibbs free energy, the melting temperature T_m can be calculated as the ratio of enthalpy change ΔH over entropy change ΔS. Since the nature of the molecular bonds and hence ΔH remains unchanged, the entropy change must be responsible for the T_m increase [94]. The applied pressure limits the mobility of the molecules, which decreases ΔS and hence increases T_m.

The increase in melting temperature ΔT_m with increased pressure ΔP has been used to define a phenomenological constant $k^{overheating}$ [93], defined as:

$$k^{overheating} = \frac{\Delta T_m}{\Delta P}. \tag{2-2}$$

For PE, a value of 0.0356°C/bar has been measured [93]. Typical hot compaction pressures of 40 bar would hence increase the melting temperature of PE by 1.4°C. The superheating effect is more prominent in PP than in PE [32]. Tensile forces can have the same effect, but is less important for SRCs. Furthermore, the T_m of oriented polymers increases with increasing draw ratio [96]. These two effects can lead to the optimum compaction temperature being more than 20°C higher than the T_m of the isotropic polymer.

Selective melting of the outer layer of the oriented tapes would not be possible if the entire tape had the same melting temperature. Instead, it is hypothesised that molecules in the outer layer have more mobility and hence more entropy. This decreases their melting temperature, and allows them to melt at a lower temperature than the inner core of the tape.

Pressure is also vital to restrain the fibre shrinkage. Oriented polymers are inherently unstable from a thermodynamical point of view [83]. At high temperatures, molecular relaxation is inevitable, but can be limited by a high pressure [46]. This pressure increases friction with the mould, which limits the tape shrinkage. Alcock et al. [61] demonstrated that SRPP stiffness and strength decreased by a factor of two by lowering the pressure from 124 bar to 1 bar. Higher pressure also leads to more intimate contact between tapes and can hence have a beneficial influence on the interfacial strength [61]. Simultaneously, this ensures a more homogeneous through-the-thickness temperature distribution.

Dwell time is the time spent at the compaction temperature. This may be an important parameter for hot compaction, but has received little attention in literature. Typical dwell times in literature are 2-10 min [66,86,90,97-100]. Longer dwell times are expected to lead to more surface melting and molecular relaxation of the tapes. Literature does not provide any insight into the importance of dwell time for the amount of surface melting. If additional matrix is created, then the interlayer bonding should increase and the impact performance should be affected. Unfortunately, there is no literature available to back up such claims. Hine and Ward [51] did recommend using short dwell times for hot compaction of PET fibres, but that was to avoid hydrolytic PET degradation.

The **cooling rate** is important mainly due to its influence on the mechanical properties of the matrix. Increased cooling rate tends to lead to lower crystallinity [82,85], and hence lower matrix modulus [101]. This also promotes higher ductility, which is important to hold the fibres together [51,82,85].

These four process parameters are crucial in determining the mechanical performance of SRCs. Nevertheless, most authors have focused solely on the temperature for their process optimisations. The pressure, dwell time and cooling rate have hardly been investigated in literature. Apart from these four key process parameters, three other approaches are used to widen the processing window for hot compaction.

The first approach adds **films** in between the layers. This creates additional matrix, and increases the interlayer bonding [81,100]. Alternatively, this can be considered as a combination of hot compaction and film stacking. Most importantly, these films widen the temperature window for hot compaction [81,100]. This may be of particular interest for SRPE, which has a smaller temperature window than SRPP [32]. The influence of films on impact resistance has not been investigated yet. This is surprising, as impact resistance is one of the key benefits in most SRC applications.

The second approach uses **tapes instead of fibres**. The flat geometry of tapes reduces the crimp compared to fibres and thus improves mechanical performance [82,85,102]. Tapes also require less matrix as they can be packed more efficiently than fibres. This effectively widens the processing window compared to hot compaction of fibres. Hine et al. [82] also reported an increased interlayer bonding for weaves composed of tapes instead of fibres.

The final approach is to **optimise the weave architecture**. Flat, low-crimp weave architectures have less empty spaces that need to be filled with matrix. Such architectures could potentially help to widen the processing window. Unfortunately, the efforts in this area are scarce. Houshyar et al. [103] compared different weave patterns and found a decrease in tensile modulus with increased crimp. Houshyar et al., however, did not find any differences in impregnation quality. Most likely, this is because Houshyar et al. used film stacking with a low viscosity copolymer film. Hot compaction can be expected to be more sensitive to changes in the weave architecture.

Morphology

The morphology of SRPP after production was already described in the very first paper on SRPP. Capiati and Porter [28] found epitaxial crystal growth onto the oriented polymer fibres. Epitaxial growth refers to growth of a crystal with the same orientation as the existing crystal on which it grows. The existing crystal provides nucleation sites for crystal growth of the melted polymer. Figure 2-12 illustrates this epitaxial growth in between two oriented fibres. Epitaxial growth has several advantages. Firstly, this type of crystal growth reduces the number of defects compared to bulk crystallisation [28]. Secondly, the presence of a morphology gradient is thought to be beneficial for the interfacial strength [59].

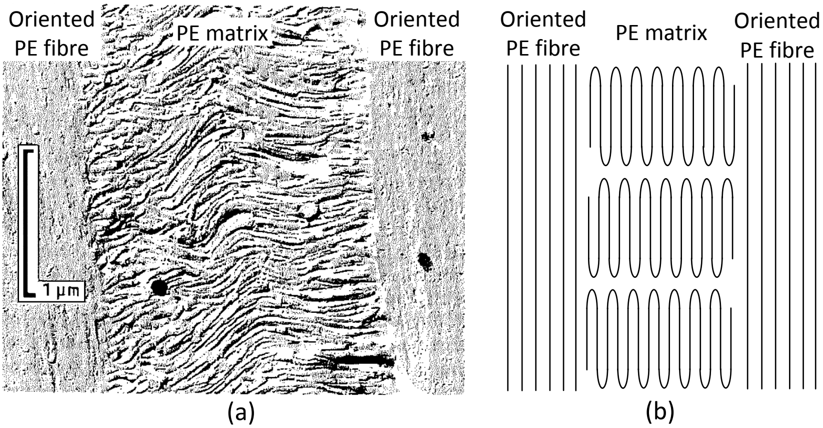

Figure 2-12: Two oriented PE fibres on the left- and righthand side, with epitaxially grown PE matrix in between: (a) real microstructure (adapted from [59], with permission from Springer), and (b) schematic microstructure. The PE fibre is oriented upwards.

Figure 2-13 reveals how three epitaxial growth fronts come together. The growth fronts are incompatible with each other due to the difference in crystal orientation. The melting front will push out low molecular weight PP as well as PP with lower stereoregularity [49,82,104]. This migration creates a weak interface between the epitaxial regions and may lead to damage initiation. Such migration has previously been observed in PE as well [105,106]. This issue is even worse for PP as for PE [104]. Choosing the right PP grade is hence crucial for achieving optimal SRPP performance.

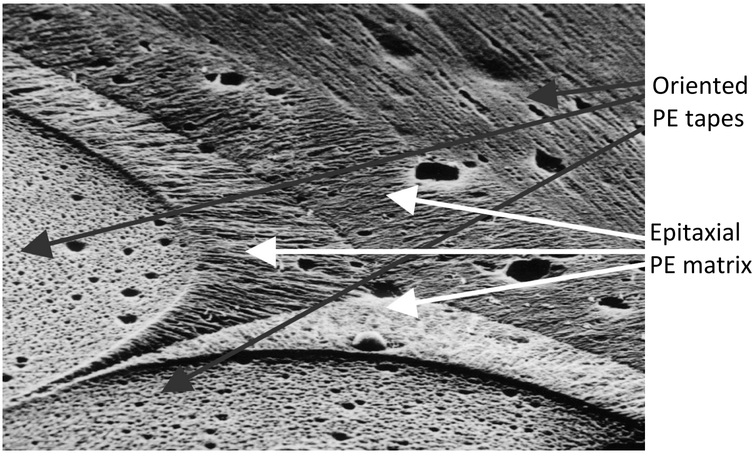

Figure 2-13: Microstructure with three epitaxial growth fronts in between three oriented PP tapes (adapted from [31], with permission from SPE).

2.1.3 Mechanical properties

This subsection analyses the mechanical properties of SRCs. First, different SRCs are compared to each other as well as to other material families. Then, the impact resistance and tensile behaviour of SRCs are described. Finally, the interlayer bonding is analysed, as this is a crucial parameter for SRCs.

Comparison with other materials

The mechanical properties of SRCs strongly depend on the polymer type. Table 2-2 summarises densities and mechanical properties of five different hot compacted SRCs.

SRPP has the highest impact resistance of all SRCs. SRPP is more than twice as impact resistant as other SRCs, but the reason is unclear from literature. The ductility of the PP matrix [82,85] and the relatively high matrix/fibre stiffness ratio [32] have been identified as possible reasons.

Table 2-2: Comparison of mechanical properties of various hot compacted woven SRCs [32-34].

	PE	PP	PET	PA
Density (kg/m^3)	970	920	1400	1140
Tensile modulus (GPa)	28	5	5.82	4.1
Tensile strength (MPa)	370	180	130	150
Edgewise notched Izod impact strength at 20°C (J/m)	1340	4750	2020	n/a

For real-life applications, the values in Table 2-2 should be compared to the values for competing material families. Table 2-3 compares SRPP to isotropic PP, random mat short glass fibre/PP and unidirectional glass/PP. SRPP and isotropic PP have a low density compared to glass fibre composites. The tensile properties and impact performance of SRPP are, however, much higher than for isotropic PP.

SRPP also has a high toughness. This toughness is attributed to: (1) the high stiffness and strength of the drawn fibres, (2) the ductility of the recrystallised matrix, and (3) the perfect bonding of the fibres to the matrix [32]. For SRPP, this leads to failure strains of about 20% and notched Izod impact strength of 4750 J/m [31,32]. At -40°C, most PP materials will embrittle, but SRPP becomes even tougher. This remarkable material behaviour will be discussed in more detail later in this subsection.

For structural applications, SRPP has a major disadvantage. The stiffness of woven SRPP is low compared to the 15-80 GPa typically found in woven glass and carbon fibre composites.

Table 2-3: Comparison of hot compacted SRPP with isotropic PP and glass fibre-reinforced PP [30-32].

		SRPP	Isotropic PP	Random mat 40 wt% short glass/PP	Continuous UD 60 wt% glass/PP
Density (kg/m³)		920	900	1185	1500
Tensile modulus (GPa)		5	1.12	3.5-5.8	25
Tensile strength (MPa)		180	27	99	420
Edgewise notched Izod impact strength (J/m)	+20°C	4750	200	672	1600
	-40°C	7500	brittle	brittle	n/a

Impact resistance

The impact resistance is one of the key advantages of SRCs compared to other materials. Nevertheless, the number of studies on impact resistance of SRCs is rather limited. Several of those studies focused on the Izod impact resistance [31,51,99,107]. Table 2-2 summarises some of these results.

Izod impact tests may be suitable for polymer applications, but not for composite applications. Figure 2-14a illustrates the setup for notched Izod tests. The notch introduces a local triaxial stress state upon impact, which rarely occurs in real-life composite applications.

Falling weight impact tests are more suitable for real-life composite applications. In this test, a striker falls down on a flat specimen, while load and displacement are measured. Figure 2-14b illustrates the setup for this test.

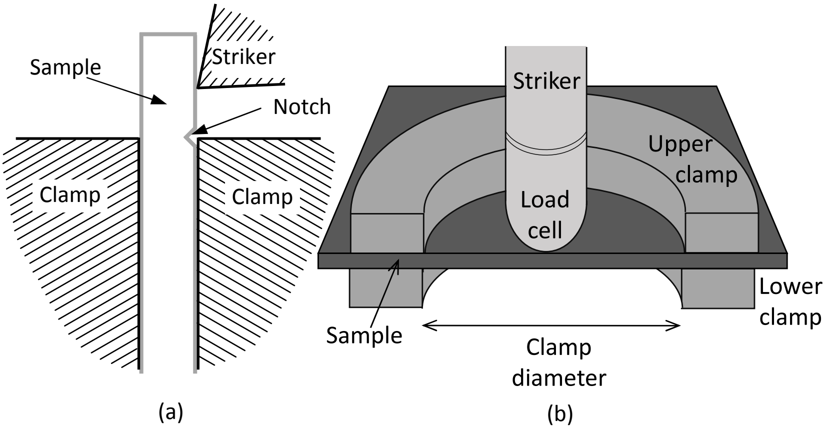

Figure 2-14: Schematic of the two common impact tests for SRCs: (a) notched Izod impact, and (b) falling weight impact tests.

Three types of impact resistance are of interest in falling weight impact tests: penetration resistance, damage resistance and residual properties. Penetration resistance measures the energy that is required to fully penetrate a sample. For measuring damage resistance and residual properties, the chosen impact energy is typically insufficient for penetration. In case of damage resistance, the degree of damage after an impact event is assessed. Alternatively, the residual properties after impact can be measured by performing a mechanical test on impacted samples. Compression-after-impact is a popular technique to measure the residual properties of carbon fibre-reinforced composites. Unfortunately, that technique is not suitable for ductile and relatively compliant materials. Residual properties after impact have not yet been reported for SRCs.

Up to now, most impact studies for SRCs focused on penetration impact [60,62,66,80,108,109]. Several damage mechanisms have been mentioned:

- Tape failure [60,62,91]
- Plastic deformation of tape and matrix [60,91]
- Matrix-tape debonding [60,62]
- Delamination [60,62,66,109]

Direct observations of these damage mechanisms are limited to macroscopic observations of tape failure and delamination. Microscopic observations of these mechanisms have not been reported yet. Furthermore, two failure mechanisms have not been listed here: matrix cracks and tape damage. Matrix cracks can occur due to the high strain rates in impact tests, while tape damage occurs due to their low transverse strength. Overdrawn tapes are inherently weak in the transverse direction, facilitating the development of transverse cracks in the tapes under transverse loading. So far, this has not been identified in literature as a possible damage mechanism.

Table 2-3 indicated that the Izod impact strength increased at lower temperatures. Alcock et al. [62] also confirmed this trend for falling weight and ballistic impact. Literature does not offer an explanation for this remarkable material behaviour. Alcock et al. [62] mention that SRPP, unlike isotropic PP, does not have a glass transition T_g around -10°C. The fundamental mechanism for the occurrence of the T_g is a change in the mobility of the amorphous chains. The high orientation of these chains, which are tie molecules in this case, limits the molecular mobility. This prevents a change in mobility and hence the T_g does not occur. The reasoning of Alcock et al. [62] unfortunately contains one vital flaw: the absence of a T_g only explains a constant impact resistance at lower temperatures, but fails to explain the observed increase in impact resistance. This increase has to be related to a change in the damage mechanisms, but this has not yet been investigated in literature.

The bonding strength is crucial for the mechanisms of matrix-tape debonding and delamination. The link between impact resistance and bonding strength, however, has not been established yet. The interlayer bonding strength is commonly assessed by peel tests [81,85,86,100]. Literature describes three parameters that affect this peel strength. Firstly, Hine et al. [47,110] proved that the peel strength increases with compaction temperature. Secondly, the peel strength is improved by adding matrix films [81,100]. Finally, Jordan et al. [85] proved that the interlayer bonding in tape weaves is much stronger than in multifilament weaves. Jordan et al. also mention that the weave architecture can affect the peel strength. In their study, the compaction temperature was different for all the tested configurations. Unfortunately, the compaction temperature strongly influences peel strength [110]. This prevents the establishment of a link between peel strength and weave architecture in Jordan et al. [85].

Some limited information on non-penetration impact is available [60,91]. Aurrekoetxea et al. [91] performed repeated impact tests on hot compacted SRPP. For 2.2 mm thick samples, Aurrekoetxea et al. found that no plastic deformation occurred below 5 J. For energies below 13 J, the impact test could be repeated more than 500 times without penetration. For higher energies, the number of tests required for penetration drops sharply. This sharp drop indicates a transition from plastic deformation to tape damage.

Alcock et al. [60] used 3D digital image correlation to find a transition from high deformation in the ±45° directions (see Figure 2-15) to a more isotropic deformation with increased compaction temperature. This was attributed to the low 45° tensile modulus of woven composites, allowing more deformation than in the 0° and 90° directions. The fact that the strains differ depending on the direction may seem surprising at first. Circumferential clamping should in principle lead to the same strains in all directions. The anisotropy of the woven SRPP however, significantly complicates the strain distribution. Furthermore, the layers can also debond and shear over each other. At higher compaction temperatures for example, the increased interlayer bonding transfers the load more efficiently to the tapes, which causes a more isotropic deformation.

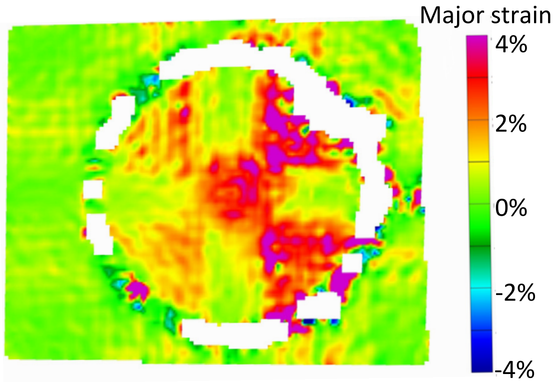

Figure 2-15: Surface strains of an SRPP samples after a 20 J impact event. The poor consolidation of the sample leads to larger strains in the ±45° directions (taken from [60], with permission from Elsevier).

Alcock et al. [60] also highlighted a crucial difference between penetration and non-penetration impact. Weak interlayer bonding allows large delaminations, which increases the energy required for penetration. These delaminations, however, also increase the indentation depth [60] and the damaged area. This leads to differences in optimal processing conditions for both types of impact. Stronger interlayer bonding improves non-penetration impact resistance, but reduces the penetration impact resistance.

Clearly, the optimal processing conditions depend on the application. This indicates the versatility of SRCs to be optimised for various applications. This versatility also necessitates a thorough understanding of the relationship between processing parameters and interlayer bonding, impact resistance and other mechanical properties.

Tensile behaviour

The tensile behaviour of SRCs depends on the mechanical properties of the tapes and the matrix. Figure 2-16 compares the stress-strain behaviour of hot compacted woven SRPP with that of its constituents. A simple rule of mixtures behaviour seemed suitable to predict the initial SRPP stiffness [32,82]. These calculations took into account the 0/90 orientations of the tapes in the weave, but neglected crimp. It should also be kept in mind that the tape and matrix properties are likely to change after they have been processed into SRPP. These changes are, however, difficult to measure, as the tapes cannot be extracted from SRPP.

The compacted woven sheet as well as the oriented tapes display a non-linear tensile behaviour. This non-linearity has been explained in literature based on the microstructure of oriented polymers [69]. In the initial part, the tie molecules in the oriented tapes are entangled and do not slide over each other. At the onset of non-linearity, the tie molecules start to slide over each other and disentangle. This causes a reduction in the stiffness at a strain of about 1%. Simultaneously, the tie molecules become more and more oriented. This increases the stress required for further deformation and is referred to as strain hardening. At some point, the tie molecules are highly oriented and further orientation becomes difficult. At that point, microscale damage starts to occur and leads to final failure. The non-linearity can be reduced by increasing the draw ratio, as illustrated by Loos et al. [95]. The increased draw ratio leads to a better tie molecule orientation [71], and hence less disentanglement.

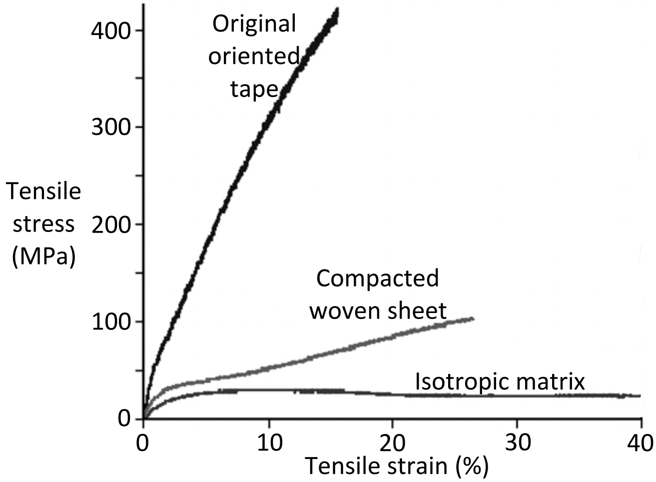

Figure 2-16: Comparison of the stress-strain behaviour of the compacted woven SRPP sheets with its constituent materials (adapted from [82], with permission from Elsevier).

A similar non-linear behaviour is observed in self-reinforced PET [52] (see Figure 2-17). In this case, however, the non-linearity was caused by the onset of failure of the PET matrix and the fibre-matrix interface. Due to the high ductility of the PP matrix, this early matrix failure will not occur in SRPP.

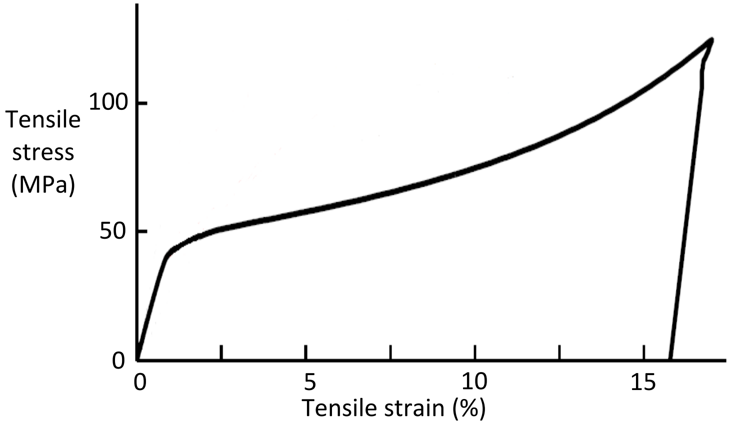

Figure 2-17: Tensile diagram of self-reinforced PET made by weaving of commingled yarns (adapted from [52], with permission from Elsevier).

In contrast with traditional fibre-reinforced polymer composites, the mechanical properties of SRCs depend on the processing conditions. The properties of the oriented fibres or tapes change during the production process. The tensile behaviour has often been analysed as a function of the process temperature. Many authors have reported an initial increase of tensile modulus and strength, followed by a decrease at even higher temperatures [65,100]. A similar trend has been observed for flexural modulus and strength [45,47,104]. For example, Izer et al. [65] found an initial increase in flexural modulus of a woven SRPP from 2.3 GPa to 3.5 GPa, after which it decreases down to 3.1 GPa. These changes occurred in less than 20°C variation in process temperature. The initial increase is attributed to increased bonding, leading to better load transfer between the tapes. The decrease is caused by a combination of molecular relaxation in the tapes and excessive tape melting [45,65].

In contrast with these results, Bárány et al. [109] reported a monotonic increase in the tensile modulus and strength with increased process temperature. Bárány et al. used SRPP where the polymorphism of PP was exploited. A similar monotonic increase was found in El Maaty et al. [46] for hot compacted SRPP. This may be attributed to two causes. Firstly, Bárány et al. used a random mat of PP fibres. This leads to relatively low modulus for the oriented reinforcement and hence a significant matrix contribution to the modulus. Secondly, the highest process temperatures were 170°C [109] and 174°C [46], which are both low for SRPP compared to the 190°C used in other studies [47,65,104].

The maximum of tensile modulus and strength as a function of process temperature is an indication of the temperature window. This window is crucial for hot compaction, but less critical for other processes. Hine et al. [81,100] describe that adding films leads to a broader maximum, which effectively widens the temperature window for hot compaction. For polyethylene, the processing window was increased from about 1°C to 5°C by adding films. The widening of the processing window in SRPP is more difficult to quantify, as it is less sensitive to the processing temperature than SRPE. In general, the hot compaction temperature of SRPP could be reduced by about 2°C by adding films.

The transverse tensile modulus and strength of UD SRPE increase monotonically with increased compaction temperature, even if longitudinal properties decrease [45]. A similar monotonic increase was found for the transverse flexural strength for UD SRPP [46]. The low transverse properties of UD SRCs are attributed to the high orientation in the fibre or tape. Increased temperature causes some molecules to reorient towards the transverse direction. This creates primary bonds in the transverse direction, which increases modulus and remediates the transverse weakness of oriented polymers.

Despite the hydrophobicity of PP, SRPP made with bi-component tape technology absorbed 10% of moisture at room temperature [111]. This occurred through open voids at the edge of the material. The tensile strength and modulus were, however, not affected. Sample conditioning is hence not necessary prior to testing.

Interlayer bonding

The interlaminar fracture toughness is a vital mechanical property of SRCs. In literature on SRCs, however, this is often called interlayer bonding. While this terminology is not entirely correct, it will be used throughout this text to maintain consistency with SRC literature. For traditional composites, this bonding is often quantified by mode I and mode II fracture toughness. Figure 2-18a and b depicts the test setups to determine these values. Both tests require a high stiffness of the composite to minimise deflections. The low stiffness of SRPP hence makes these tests unsuitable, unless the legs are stiffened externally. An alternative to fracture toughness tests are T-peel strength tests. Figure 2-18 illustrates the setup for peel tests. This test resembles a mode I fracture toughness, but with compliant instead of stiff legs. The peel test was originally developed for comparing adhesives, but has now been widely adopted for SRCs [29,60,64,85,86,110].

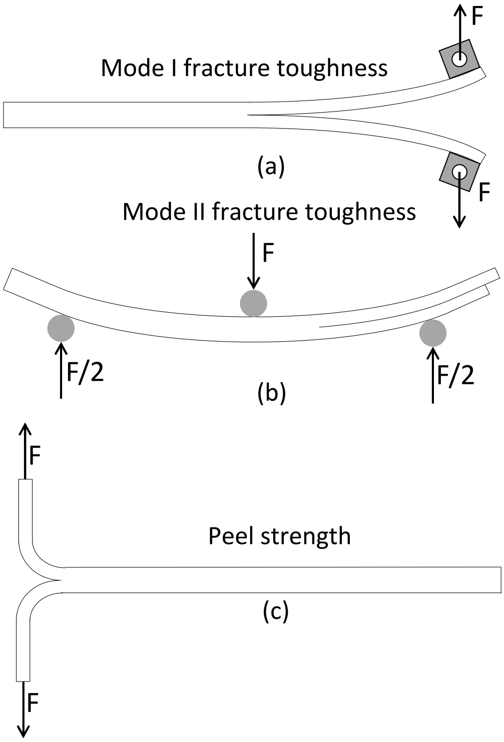

Figure 2-18: Schematic illustration of three tests for interlayer bonding in composites: (a) mode I fracture toughness, (b) mode II fracture toughness, and (c) T-peel strength test.

As mentioned in Table 2-1, the interlayer bonding is higher for hot compaction than for bi-component technology. SRPP made with bi-component tapes has been extensively investigated in literature. Cabrera et al. [84] quote an increased peel strength from 50 to 350 N/m when increasing the processing temperature from 120 to 170°C. Alcock et al. [60] found a similar peel strength increase from 0 to either 250 or 600 N/m, depending on the type of tape. In another study, Alcock et al. [29] also report peel strengths of up to 1100 N/m. These values were found for tapes with a draw ratio of 4 and 6. Such tapes are less relevant for SRCs due to their relatively low stiffness and strength (see “2.1.1 Oriented polymers”). The increase in peel strength at low draw ratios is proven in Alcock et al. [29].

For hot compacted SRPP, Foster et al. [86] found peel strengths between 500 and 750 N/m. The addition of PP films increased this to 850-1100 N/m.

Further improvements of up to 1500 N/m were achieved by adding talc powder or carbon black in the PP film. Hine et al. [81] reported similar values for without and with films.

From this data, hot compaction without films seems to yield a stronger interlayer bond than bi-component tape technology. The advantage of hot compaction becomes even larger by adding films. This conclusion should be interpreted with caution, as the peel strength also depends on the weave architecture [82,85] and the tape draw ratio [29]. Many authors have proven that increased process temperature increases the peel strength [29,64,65,81,86,100,112]. The higher process temperature facilitates welding of the layers, leading to a higher peel strength. The higher process temperature of hot compaction is thus likely the main reason for its higher peel strength compared to bi-component tape technology. The better compatibility between fibre and matrix may be another reason, but this has not been proven yet in literature.

2.1.4 Conclusion

SRCs have been extensively studied in literature. Many studies report on the optimal process parameters, but those unfortunately strongly depend on the materials used. Deriving optimal process parameters from literature is however not possible, especially with respect to temperature. These parameters need to be optimised separately for every material. There have been no systematic studies on the effects of weave architecture and how the architecture affects the processing and mechanical properties. Since the next chapter will weave carbon fibre prepregs together with PP tapes, an in-depth understanding of the influence of the weave architecture is crucial. The carbon fibre prepregs will also add additional matrix, which increases the bonding. The effect of this increased bonding can be studied in non-hybrid SRPP by interleaving with films or changing the processing parameters. Such a study is required in non-hybrid SRPP first before moving into the more complex situation in hybrid SRPP.

The high impact resistance and low density are clearly the main advantages of SRPP compared to others SRCs and other material families. Nevertheless, relatively little information is available in literature on the impact resistance. This is especially true for hot compacted SRPP and for non-penetration impact resistance. Most authors have adopted the typical brittle fibre testing methodologies for impact testing of SRPP. Proper testing and analysis procedures have not been set up for composites with such high ductility.

Finally, relatively little is known on the failure behaviour of SRPP or SRCs in general. Some generic damage mechanisms have been identified, but direct identification of those mechanisms is lacking in literature. This is also the reason why there is currently no satisfactory explanation for the increase in impact resistance at low temperatures.

2.2 Materials and methods

2.2.1 Materials

All pure PP materials were kindly provided by Propex Fabrics GmbH. They all consist of the same PP grade, namely Ineos 100-GA02. The melting temperature of this grade is 163°C in its isotropic state.

Two types of drawn PP tapes were used: tape A and tape B. The draw ratio is the same for both tapes and is between 10 and 15. The drawing conditions are confidential. The tapes have a rectangular cross-section with a width of about 2.4 mm. The thickness of tape A and B are 50 and 85 μm respectively. Tape A is always used, unless otherwise mentioned. Tape A has a linear density of 110 tex, which is lower than the 190 tex for tape B. The stiffness, strength and failure strain of both tapes prior to hot compaction are 10 GPa, 500 MPa and 9% respectively [113].

Propex Fabrics GmbH used these tapes to produce weaves on a pilot scale loom. A crucial aspect of tape weaving is the feeding: standard fed (SF) or overfed (OF). The difference between both feeding types is illustrated in Figure 2-19. When a new weft yarn is inserted in between the warp yarns, the weaving loom battens the weft yarn to move it towards the previously inserted weft yarn. Since tapes have a high width/thickness ratio, they have a tendency to fold along their length during battening. On industrial looms, the battening is performed so fast that tape folding is unavoidable. This fast battening is beneficial, as it increases the production rate. In the warp direction, overfeeding can be achieved by having more tapes than would normally fit in. The overfeeding is calculated as the ratio of the number of tapes per metre to 1000 divided by the width in millimetre:

$$overfeeding = \frac{\#tapes/m}{1000/width(mm)}.100\% \qquad (2\text{-}3)$$

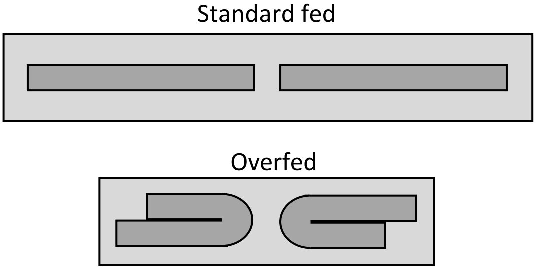

Figure 2-19: Schematic illustration of the difference between standard fed and overfed weaves. The overfed weaves contain tapes, which are folded along their length.

Propex Fabrics GmbH produced weaves in two patterns: plain and twill 2/2 patterns. The unit cells of these weave patterns are illustrated in Figure 2-20a and b. The overfeeding can be different in both directions, but this was not the case here. The twill OF and plain OF weave both have an overfeeding of

150% in the warp and weft direction. Folding increases the average or apparent tape thickness. This results in an increased crimp, which is a measure of the out-of-plane orientation of the tapes. The lower crimp of twill weaves can be seen from the larger amount of straight sections in Figure 2-20b compared to Figure 2-20a. To assess the influence of the overfeeding, a twill weave with standard feed was woven. To reduce the probability of folded tapes and maintain the same areal density, the standard fed weave uses the thicker tape B. The areal density of the twill SF weave is 125 g/m², which is close to the 130 g/m² for the twill OF and 140 g/m² for the plain OF weave. The twill OF is the default weave and is always used, unless otherwise mentioned. The twill SF and plain OF architectures are only used in the section “2.5 Influence of weave architecture”.

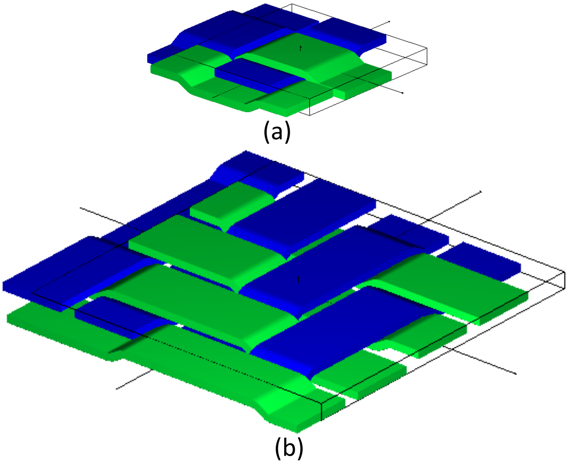
(a)

(b)

Figure 2-20: 3D illustration of weave patterns without overfeeding: (a) plain, and (b) twill 2/2. Black/blue tapes are weft yarns, while grey/green tapes are warp yarns.

Propex Fabrics GmbH also provided 20 μm and 50 μm thick films of the same PP grade.

2.2.2 Hot compaction

For the tensile and impact samples, woven layers of 320 x 320 mm were stacked onto each other. The default number of layers was 8. In section “2.5 Influence of weave architecture”, the number layers was increased to 12 layers. In some cases, a single 20 μm PP film was inserted between each woven layer.

The lay-up was placed in between two 1 mm thick aluminium cover plates without any spacers. The hot press was preheated at 188°C for 10 min to ensure a homogeneous temperature distribution over the press platens. The assembly was then inserted into the hot press at 188°C. This temperature was based on thermocouple measurements just below the surface of the press platens. After a dwell time of 5 min, the press was cooled to 40° in about 5 min. The hot press applied a pressure of 39 bar during the entire cycle. These are the default compaction conditions, but will be varied to analyse the influence of the process parameters (see Table 2-4).

Table 2-4: Summary of processing parameters and sample thickness for optimising the hot compaction parameters of the overfed twill weave.

Temperature (°C)	Dwell time (min)	Pressure (bar)	Films	Thickness (mm)
180	5	39	No	1.31 ± 0.03
	5	39	Yes	1.39 ± 0.03
	15	39	Yes	1.38 ± 0.02
184	5	39	No	1.26 ± 0.03
	5	39	Yes	1.35 ± 0.02
	15	39	Yes	1.38 ± 0.02
186	5	39	No	1.25 ± 0.02
	5	39	Yes	1.32 ± 0.02
	15	39	Yes	1.36 ± 0.02
188	2	39	Yes	1.38 ± 0.02
	5	10	No	1.60 + 0.03
	5	10	Yes	1.70 + 0.06
	5	39	No	1.24 ± 0.05
	5	39	Yes	1.34 ± 0.04
	15	39	Yes	1.33 ± 0.03
191	2	39	Yes	1.33 ± 0.03
	5	39	No	1.20 ± 0.04
	5	39	Yes	1.28 ± 0.03
194	2	39	Yes	1.31 ± 0.02
	5	39	No	1.09 ± 0.04
	5	39	Yes	1.28 ± 0.05

A similar procedure was used to prepare peel strength samples. A 12 µm polyimide release film was put in the middle of four woven layers. The film was placed over the entire length of the weaves and over a depth of 90 mm. This stack was hot compacted under the same processing conditions.

2.2.3 Tensile tests

Specimens for tensile tests were water jet cut from the hot compacted sheets. Tensile tests were performed according to ASTM D3039. At least five samples were tested for each configuration. Tests were conducted on an Instron 4505 tensile machine equipped with a 100 kN load cell and hydraulic clamps. Rectangular samples of 250 x 25 mm were tested at a gauge length of 150 mm. Sandpaper was used as end-tabs to avoid slippage in the clamps. The strain rate was 5%/min.

A speckle pattern was applied to the surface. This speckle pattern was tracked by a camera throughout the tensile test. Digital image correlation of the images was then performed to calculate the average surface strain.

The tensile modulus was calculated as the slope of the stress-strain diagram between 0.1 and 0.3% strain. The strength was calculated as the highest stress and the corresponding strain is defined as the failure strain. The area underneath the stress-strain diagram was calculated by integrating the stress-strain diagram, resulting in a measure of the energy absorption per volume of material. This integration was interrupted when the stress dropped below 10 MPa.

2.2.4 Falling weight impact tests

Two types of falling weight impact tests were performed: penetration and non-penetration. This terminology is used throughout, as it reflects the difference between both types more directly than the terminology high and low energy impact.

Falling weight impact tests were performed on a Fractovis CEAST 6789 machine, according to ISO 6603-2. The setup and its dimensions are displayed in Figure 2-21. A hemispherical striker with a 20 mm diameter was used. All samples were clamped at the maximum pressure of 9 bar, which corresponds to a force of 5600 N. The clamps were roughened to increase friction. Sample sizes were typically 100x100 mm, but the influence of this size will be investigated in “2.4.1 Penetration impact resistance”. At least six samples were tested for each combination of temperature and impact energy. The load was registered by a 20 kN load cell in the striker tip, while the displacement was measured using a laser.

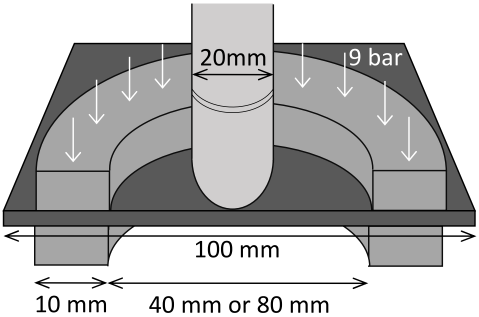

Figure 2-21: Schematic illustration of the falling weight impact setup. The dimensions are not to scale.

For penetration impact tests, the striker was set to a height of 1 m. The inner diameter of the clamp was 40 mm, while the outer diameter was 60 mm. The mass of the striker was 26.17 kg, corresponding to a total energy of 257 J. The energy absorption was calculated by integrating the load-displacement curve, until the load dropped to half of the peak load. This is the method recommended by the ISO standard.

The non-penetration impact tests were performed using a larger clamp. This clamp had an inner and outer diameter of 80 and 100 mm respectively. The larger diameter compared to penetration tests facilitates the registration of damaged area. The mass of the striker was 3.17 kg and the impact energy was varied by changing the height from 0.08 m to 1 m.

The plastic indentation depth after a non-penetration impact event was measured using a measuring clock. The sample was placed on a flat table with its indentation upwards. The height of the indentation was measured and the sample thickness was subtracted from this value. The dynamic indentation depth was measured by taking two points from the force displacement diagram. The first point is the displacement when the force starts to increase, as this corresponds to the displacement when the striker hits the sample. The second point is the minimum displacement. The difference between both displacements is the dynamic indentation depth.

2.2.5 Ultrasonic C-scan

The compaction quality and damaged areas were evaluated by ultrasonic C-scans. This was either performed on the 320 x 320 mm plates or on smaller impact samples. The samples were immersed in demineralised water. The scans were performed with an Olympus Panametrics V309SU transducer at a 5 MHz frequency and 13 mm nominal diameter. The reflections from the glass plate were analysed. The transducer was placed 25 mm above the glass plate or 10 mm above the bottom surface of the sample. The step size was either 1 or 2 mm at a scan rate of 0.2 mm/s. The result is a greyscale value ranging from 0 to 255 for each point in the scanned samples.

For impacted samples, the obtained greyscale values were converted into black and white by choosing a certain threshold. This threshold is an arbitrary parameter, which also depends on the equipment settings. Its value will determine the apparent size of the damaged area, making it crucial to fix it for a given comparison. To calculate the damaged area, the number of black pixels after thresholding were counted. This number is multiplied by the area of one pixel. Damage near the clamp or dark areas due to the supports in the corners were not taken into account. Only the central damage was taken into account.

2.2.6 Transmitted light imaging

The semi-transparent nature of SRPP allows the detection of damage by shining light through it. Since light scatters on damaged surfaces, it is possible to differentiate between damaged and undamaged areas with a high resolution. This technique will be referred to as transmitted light imaging, and will be used to detect damage in impacted SRPP. The samples were placed in front of a lightbox to achieve a strong and constant backlight. A Nikon 3200 reflex camera was mounted on a tripod to take photographs. The aperture was 1/3.5 with a shutter time of 10 ms. Image processing was applied to photographs in the raw format, as that format comes directly from the image sensors and is minimally processed. The raw images were processed in Adobe Lightroom to achieve a better visualisation of the damage. The processing parameters are summarised in Table 2-5.

Table 2-5: Processing parameters for transmitted light imaging.

Filter parameter		Value
White balance	Temp	5200
	Tint	44
Tone	Exposure	-0.2
	Contrast	100
	Highlights	25
	Shadows	-100
	Whites	-100
	Blacks	-60
Presence	Vibrancy	15
	Saturation	50
Color-Yellow	Saturation	100
	Luminance	-75

2.2.7 Peel strength tests

To assess the interlayer bonding, T-peel tests were performed according to ASTM D1876. The samples were cut down to a width of 20 mm using a sharp knife. The nominal sample thickness was 0.6 mm. The samples were cut in such a way that the length of the insert film, which is equivalent to the unbonded length, was 76 mm. The two unbonded ends were pulled apart at a rate of 254 mm/min. The samples were tested at room temperature on an Instron 5943 tensile machine with a 1 kN load cell.

The peel strength was defined as the average peel load per mm width of the sample. The average was calculated over the first 127 mm displacement after the initial load peak, as prescribed by the standard. At least 10 samples were tested for each configuration. The samples were always tested in random order to minimise systematic errors.

2.2.8 Differential scanning calorimetry

Differential scanning calorimetry (DSC) samples were cut from the middle of the plates for tensile and impact tests. The samples, with a nominal weight of 2 mg, were tested in TA instruments Q2000. A 50/50 helium/nitrogen flow of 50 ml/min was used. At least four samples were tested for each configuration.

The melting temperature was determined at the maximum of the heat capacity versus temperature.

The standard DSC measurements are unconstrained, meaning they do not prevent shrinkage inside the DSC pan. This shrinkage is known to have a significant effect on the thermal behaviour of oriented polymers. Therefore, constrained DSC measurements were also performed. This is achieved by tearing off a 0.5 mm wide strip of a PP tape, and wrapping it around a folded piece of aluminium. The ends are tied together to prevent shrinkage.

2.2.9 Areal density measurements

Areal densities of the PP tape cloths were measured by cutting a rectangular specimen of at least 100 cm^2. These specimens were weighed to an accuracy of 0.1 mg. Dividing the weight by the area of the specimen yields the areal density. Testing three specimens was found to be sufficient to get an accurate value for the areal density.

2.2.10 X-ray microtomography

X-ray microtomography or microCT is based on the interaction of X-rays with matter. As X-rays pass through different materials, they are attenuated differently. When an X-ray beam passes through a material, it creates a projection on a detector. Each point in the projection is the sum of all the attenuations along the paths of an X-ray. The sample is therefore placed on a rotation stage and scanned at various rotation angles. At each angle, a transmission X-ray image is taken and saved. By combining projections at different rotation angles, a virtual 3D representation of the internal material structure can be created.

All samples were scanned using a Skyscan 1172 system. A tungsten target was used and the X-rays were filtered using a 0.5 mm thick aluminium filter to compensate for beam hardening. The voltage was 94 kV and the current was 106 µA, leading to a power of 10 W. The sample rotated over 360° with intervals of 0.3°. The samples were 20x40 mm in size, but the imaged zone was typically 12x18 mm. This leads to a voxel size of 5.9 µm. The samples were taken either from unimpacted plates or from the middle of the impact area.

2.3 Optimisation of process parameters

As mentioned in “2.1.2 Production of self-reinforced composites”, the hot compaction process is highly sensitive to the production parameters. Understanding the influence of these processing parameters is crucial to develop an optimal processing route for hybrid SRCs.

The compaction temperature is the most crucial production parameter and has already been extensively studied. The dwell time, compaction pressure and cooling rate have received less attention in literature. Unfortunately, the available equipment is not capable of accurately controlling the cooling rate. Therefore, the cooling rate is kept constant, whereas compaction temperature, pressure and dwell time will be varied. The influence of adding matrix films is also investigated, as this increases the processing window and interlayer bonding strength.

The focus is on how these four process parameters affect the tensile properties of SRPP. But first, the thermal behaviour will be analysed, as this will help in understanding the processing conditions and the trends in the tensile properties.

2.3.1 Processing window

As mentioned in “2.1.2 Production of self-reinforced composites”, the selective surface melting that occurs during hot compaction is a complicated process. This subsection therefore first provides some background knowledge on the processing window and the thermal behaviour of the PP tapes.

A vital aspect of hot compaction is the melting behaviour of the oriented PP tapes. The high crystal orientation and perfection increase the melting temperature of oriented tapes compared to the isotropic polymer (see Figure 2-22). The situation in a standard, unconstrained DSC measurement however, does not correspond to the actual situation during hot compaction. The applied pressure constrains the tapes from shrinking, which increases their thermal stability and melting temperature (see “2.1.2 Production of self-reinforced composites”). In a DSC experiment, this can be simulated by wrapping a part of the tape around a small piece of aluminium and tying together the ends. This leads to the “constrained PP tape” curve in Figure 2-22, which has a significantly higher melting temperature than its unconstrained counterpart.

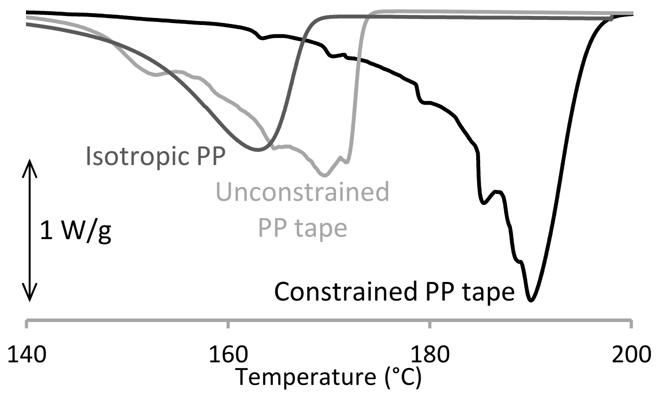

Figure 2-22: DSC thermograms of isotropic PP, unconstrained and constrained PP tapes.

While the thermal behaviour in Figure 2-22 is vital information for understanding the basic concept of hot compaction, it does not reveal the optimal temperature. This optimum should not exceed the melting temperature of the constrained tapes. The temperature should also be at least 180°C to allow sufficient surface melting. Therefore, the optimal temperature is expected to lie somewhere in the range between 180 and 190°C. It should be emphasised that the constraint in DSC differs from the constraint from the applied pressure during hot compaction.

2.3.2 Thermal behaviour

The drawn tapes typically have a high crystallinity, while the degree of crystallinity is much lower in the films [73]. DSC is performed on hot compacted samples with and without films to analyse how the crystal structure is influenced by the hot compaction process. The DSC thermograms are plotted in Figure 2-23, while the melting temperature and enthalpy values are summarised in Figure 2-24.

With increased compaction temperature, the melting temperature increases (see Figure 2-24a) by annealing of the crystals in the tapes during the compaction process. These crystals grow in size and become closer to perfect. The melting temperature of the tapes is not influenced by the presence of the films, as illustrated in Figure 2-24a. The additional matrix from the films has a lower melting temperature and appears either as a shoulder or as a small melting peak at about 160°C (see Figure 2-23b). This shoulder or peak corresponds to the melting peak found in the thermogram of the films. The shoulder or peak is less pronounced for samples without films, in which case the matrix originates only from surface melting of the tapes. In the thermograms for samples without films, however, these shoulders are only present at a compaction temperatures of 194°C. At lower temperatures, the surface melting of the tapes is insufficient to cause the appearance of a matrix peak or shoulder.

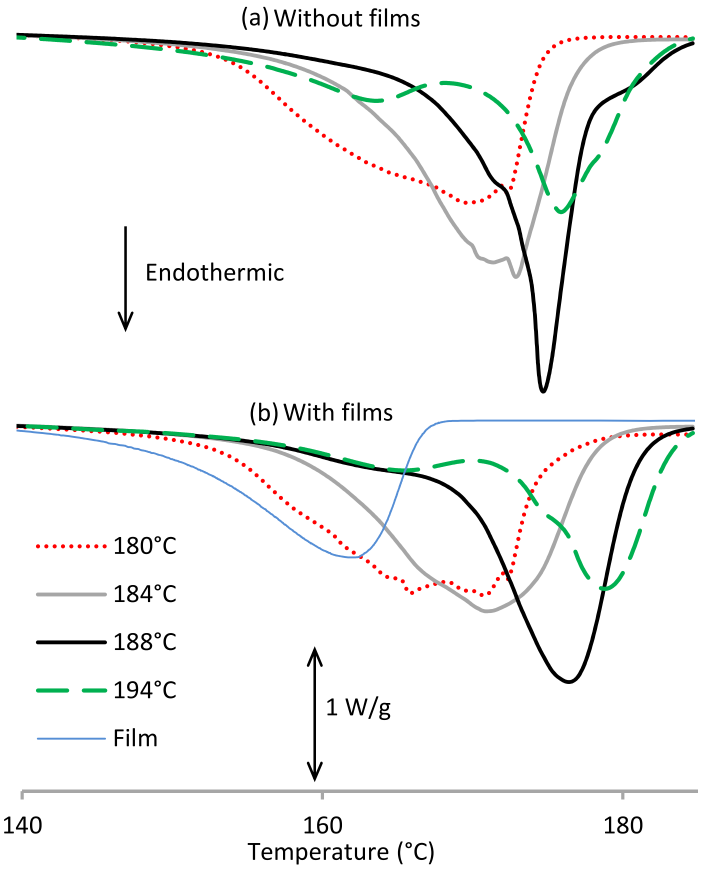

Figure 2-23: DSC thermograms for samples compacted for 5 min at 39 bar: (a) without films, and (b) with films. Each line represents the average of four DSC thermograms. The thermogram of the PP films is added as a reference, while the thermograms of 186°C and 191°C are omitted for clarity.

A larger difference is observed for the melting enthalpy in Figure 2-24b. The samples with films have a lower melting enthalpy, as these samples contain a lower fraction of highly crystalline tapes. The tapes have a higher melting enthalpy than the corresponding isotropic matrix. This difference reflects the higher degree of crystallinity and more perfect crystals in the tapes [94,102]. A reduction in the volume fraction of tapes hence causes a decrease in the overall melting enthalpy. The decreasing trend with increasing compaction temperature is caused by melting of the tape surface, which creates more matrix. This matrix has a lower crystallinity and less perfect crystals.

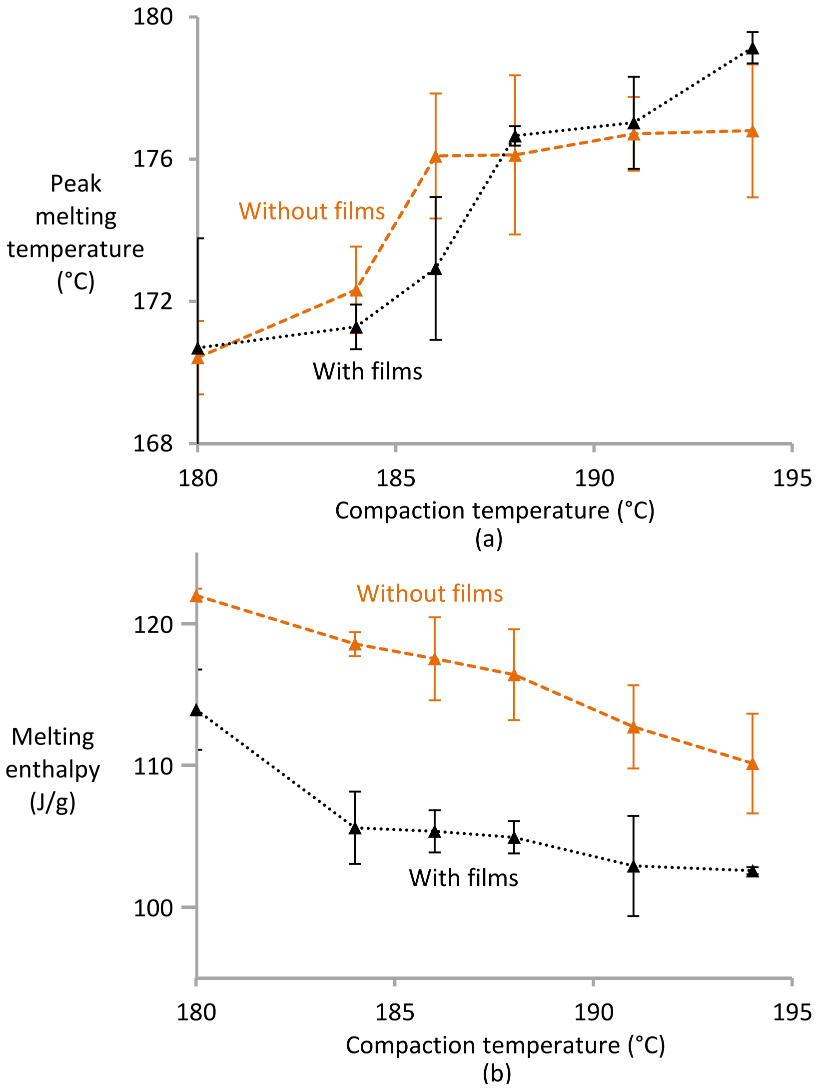

Figure 2-24: DSC results for samples compacted for 5 min at 39 bar without and with films: (a) melting temperature, and (b) melting enthalpy.

The influence of dwell time on melting temperature and enthalpy is summarised in Figure 2-25. Figure 2-25a demonstrates that dwell time does not have a clear influence on the melting temperature. Figure 2-25b indicates that a dwell time of 5 min leads to the lowest melting enthalpy. In principle, the dwell time should cause similar effects as an increased compaction temperature: more molecular relaxation and more melting of the tapes. The large scatter combined with the small differences indicate that DSC is not sensitive enough to draw clear conclusions with respect to dwell time.

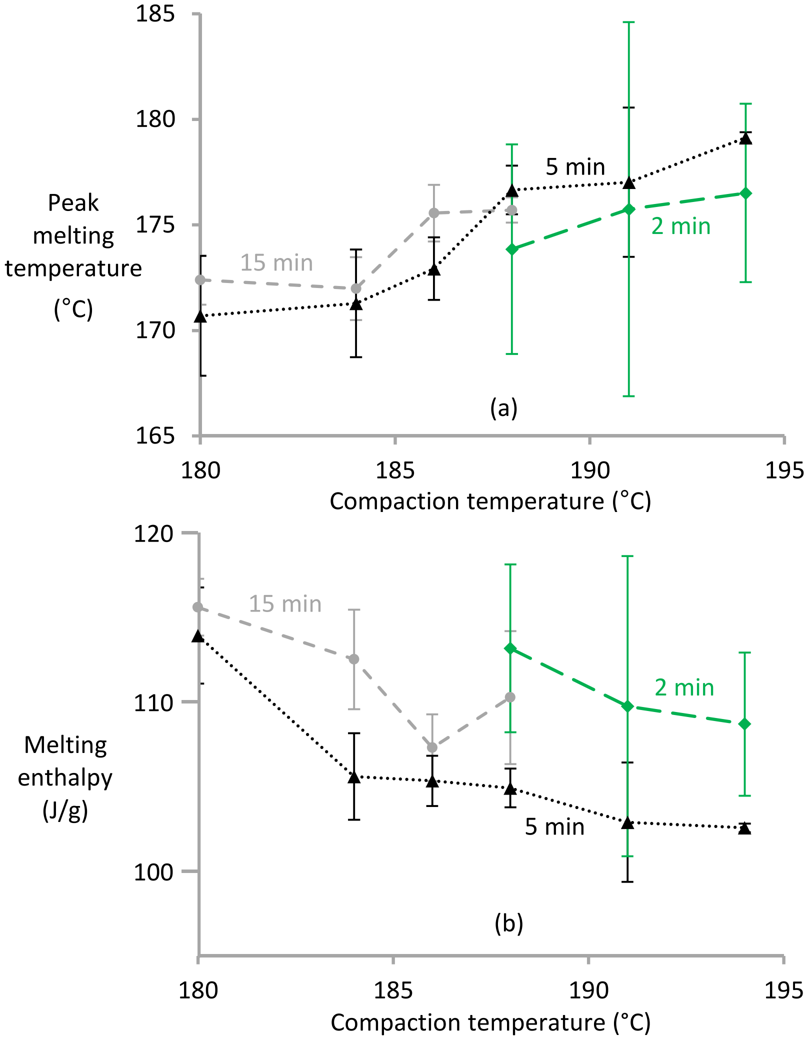

Figure 2-25: Influence of dwell time on DSC results for samples compacted with films at 39 bar: (a) melting temperature, and (b) melting enthalpy.

Figure 2-26 summarises the DSC results for two different compaction pressures in samples compacted at 188°C. The low compaction pressure leads to a higher melting temperature, but a lower melting enthalpy. The lower melting enthalpy is attributed to more molecular relaxation, as the lower pressure leads to less constraints against shrinkage. This causes the melting temperature of the tape during hot compaction to decrease, moving from the constrained closer to the unconstrained DSC thermogram in Figure 2-22. The processing temperature of 188°C is hence much closer to the melting temperature of the tapes, which hence melts more.

The higher melting temperature at low compaction pressure seems surprising at first, but the thermograms in Figure 2-27 explain this feature. The lower compaction pressure reduces the melting temperature of the tapes, which in turn causes more surface melting. The crystals that melt first are those with a slightly lower melting temperature. The melting peak is hence sharpened (see Figure 2-27), which leads to a slightly higher melting temperature.

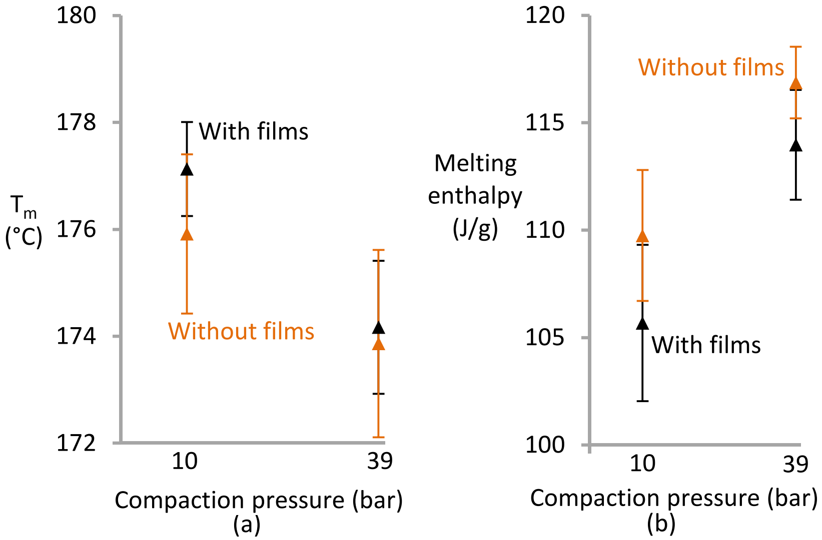

Figure 2-26: Influence of compaction pressure on DSC results for samples compacted for 5 min at 188°C: (a) melting temperature, and (b) melting enthalpy.

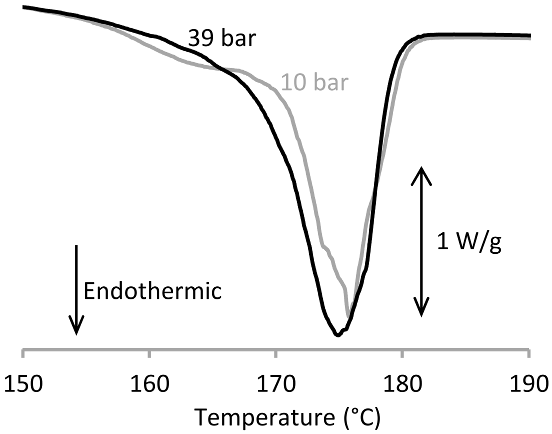

Figure 2-27: Influence of compaction pressure on DSC thermograms for samples without films compacted for 5 min at 188°C.

The DSC results indicate that a lower compaction temperature will have a large influence on the mechanical properties. This is a consequence of the increased molecular relaxation of the highly oriented crystalline structure in the tapes, and of the decreased tape fraction for lower pressures. The dwell time has a smaller influence and may not affect the mechanical properties. Increasing the compaction pressure increases the melting temperature of the tapes, and therefore reduces the molecular relaxation and surface melting.

2.3.3 Tensile properties

Figure 2-28 summarises the 0° tensile properties with and without films. For compaction temperatures above 180°C, the tensile modulus is not affected by the films (see Figure 2-28a). Firstly, films create additional matrix, but the stiffness difference between matrix and tape is small compared to the difference in traditional fibre-reinforced composites. Secondly, the amount of additional matrix material only increases the sample thickness by 12%, as the films are only 20 µm thick. At a compaction temperature of 180°C, however, the samples with films are significantly stiffer than the samples without films. This is caused by the poor compaction quality of the samples without films. A dwell time of 5 min at 180°C melts insufficient matrix material to fill up all the voids in between the tapes and layers. In fibre-based SRCs, a matrix volume fraction of 20-30% is typically needed to fill all these voids and achieve proper interlayer bonding [110]. In tape-based SRCs, the optimal matrix volume fraction is most likely lower. The voids contribute to the sample thickness, but do not contribute to the stress transfer in the 0° direction, which results in a lower modulus.

Figure 2-28a reveals a strongly decreasing modulus if the compaction temperature is increased from 180°C to 186°C. This can be attributed to two phenomena. Firstly, the amorphous, but oriented tie molecules between the crystals will relax [114]. Secondly, the volume fraction of tapes decreases with increased compaction temperature. At higher compaction temperatures, a small increase is observed, which might be attributed to an annealing effect on the matrix crystals. These crystals will grow in size and become more perfect [99], which can cause an increase in their tensile modulus. This annealing effect seems to be larger than the effect of increased molecular relaxation and decreased tape fraction. To confirm this hypothesis, the 45° modulus will also be investigated in Figure 2-29.

Figure 2-28b proves that the tensile strength of samples with films is higher at low compaction temperatures than for samples without films. At higher compaction temperatures, this difference decreases and then disappears. It is hypothesised that the low interlayer bonding at low compaction temperatures causes early tape and interlayer debonding in the samples without films. These damage phenomena cause a less efficient load transfer between tapes or layers and thereby prevents the samples from reaching high strengths. The samples with films have better interlayer bonding, which results in a clean and sudden failure, without much prior visible damage. While this remains a hypothesis, it was confirmed by visual observation during the tensile tests.

Figure 2-28c plots the failure strain, which is calculated as the strain when the maximum stress is reached. The failure strain increases until 188°C, after which a plateau is reached. Low compaction temperatures lead to low interlayer bonding, which causes early debonding and delamination. Also, molecular relaxation is more pronounced at high compaction temperatures. Both effects can cause the failure strain to increase. Above 188°C, the interlayer bonding is strong enough to prevent significant debonding, causing the failure strain increase to level off.

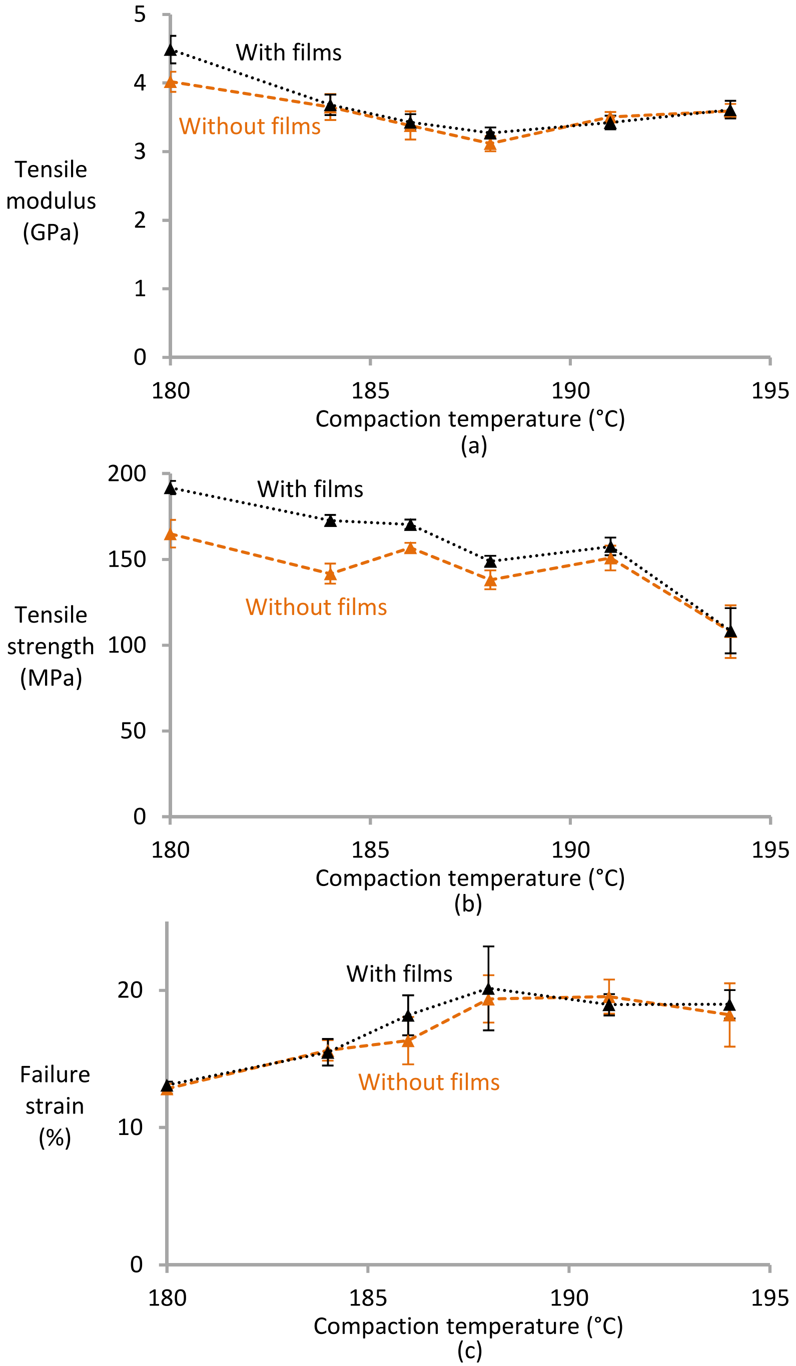

Figure 2-28: The 0° tensile properties for samples compacted at 39 bar for 5 min without and with films: (a) tensile modulus, (b) tensile strength, and (c) failure strain.

Tensile tests for different dwell times are performed in the 0° and 45° direction, and the results are summarised in Figure 2-29. Figure 2-29a demonstrates that the dwell time only has a small influence on the 0° modulus. The 0° modulus is lower when the dwell time is increased to 15 min, allowing more molecular relaxation and reducing the tape fraction.

The 45° modulus is mainly dominated by the matrix, causing it to be hardly affected by compaction temperature and dwell time. Since the slight increase in 0° modulus was attributed to annealing of the matrix crystals, a similar increase would be expected for the 45° modulus as well. This hypothesis thus cannot be valid. Another hypothesis would be the creation of additional crystallinity in the tapes. The melting temperature of the tapes is indeed further increased at high compaction temperatures (see Figure 2-24a), but at the same time the melting enthalpy is reduced (see Figure 2-24b). In conclusion, the hypotheses for increased matrix or tape crystallinity are not supported by experimental evidence. Therefore, insufficient evidence is available to explain the small increases observed above 188°C in Figure 2-28a and Figure 2-29a.

Figure 2-29b presents the results for tensile strength. The 0° tensile strength displays a strong decrease with increased compaction temperature, as the oriented tape fraction and molecular orientation are reduced. The 45° tensile strength increases with increased compaction temperature, as this decreases tape fraction and increases the matrix fraction. This matrix bonds the layers and tapes together, allowing the tapes to remain bonded during shear deformation. At 180°C, the tapes are poorly bonded and the in-plane shear stresses rapidly caused debonding of the tapes, leading to final failure. The increased bonding at higher temperatures allows the tapes to reorient themselves towards the tensile direction without causing shear failure until high strains. They can thus also fully exploit the tensile strength of the tapes. At 194°C, both diagrams seem to converge, meaning that the strength of the SRPP becomes nearly isotropic. Longer dwell time tends to slightly reduce the 0° tensile strength, although this reduction is small and not clear at all compaction temperatures. This confirms the DSC conclusions, which stated that dwell time has only a small influence on the relaxation, melting and recrystallisation of the PP tapes.

The failure strain results in Figure 2-29c confirm the previous conclusions. Longer dwell times create more matrix and hence better interlayer bonding. This stronger bonding can delay the onset of debonding during the tensile test and hence increase the failure strain. Simultaneously, longer dwell time also allows more molecular relaxation, which contributes to the increased failure strain with increased dwell time. Nevertheless, the influence of dwell time is relatively small in the 0° direction. The effects in the 45° direction are similar but more pronounced. This direction is more sensitive to the interlayer bonding and hence to the amount of matrix.

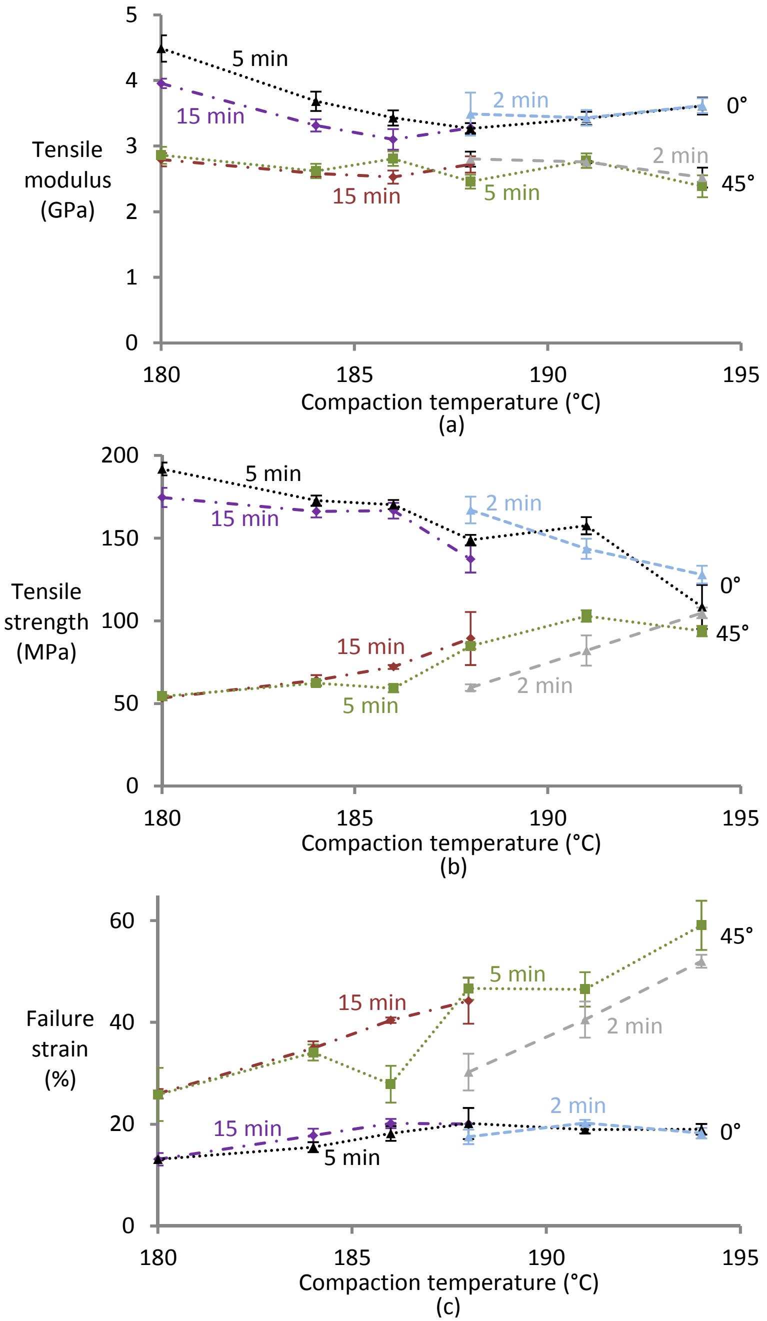

Figure 2-29: Tensile properties of samples compacted at 39 bar with films and tested in 0° and 45° as a function of temperature and dwell time: (a) tensile modulus, (b) tensile strength, and (c) failure strain.

Figure 2-30 summarises the influence of compaction pressure on the 0° and 45° tensile properties for samples without films. The compaction pressure has only a minor influence on the tensile modulus, but a significant influence on tensile strength and failure strain. A reduction of the compaction pressure from 39 to 10 bar decreases the 0° tensile strength, but an increased 45° tensile strength. This effect confirms the expectations from the DSC results. The lower compaction pressure allows more molecular relaxation and melting to occur. These effects reduce the tape properties and hence the 0° tensile strength, but also increase the interlayer bonding. This increase in interlayer bonding improves the 45° tensile strength and failure strain, which are matrix-dominated properties. The increased molecular relaxation also increases the failure strain of the tapes, as evidenced from Figure 2-30c. Lower pressure normally reduces the consolidation quality in conventional thermoplastic composites, but also causes more surface melting of the tapes in SRCs. Interestingly, the lower pressure has a similar influence as a higher temperature. A lower pressure reduces the T_m of the tapes (see Figure 2-22), reducing the gap between processing and melting temperature.

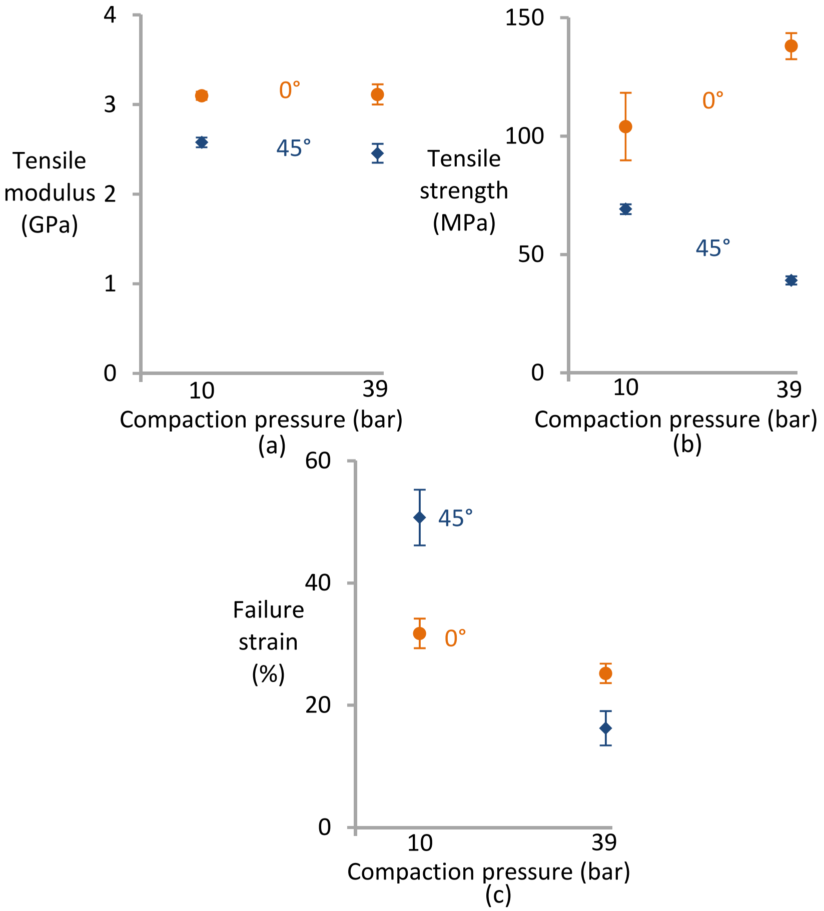

Figure 2-30: Tensile properties in 0° and 45° for samples compacted without films at 188°C for 5 min, compacted at low and high pressure: (a) tensile modulus, (b) tensile strength, and (c) failure strain.

2.3.4 Conclusion

Four production parameters were investigated for hot compacted SRPP: compaction temperature, films, dwell time and compaction pressure.

- An increased compaction temperature improves the interlayer bonding, but also creates more matrix and causes more molecular relaxation. The tensile properties therefore decrease with increasing compaction temperature.
- The addition of films improves interlayer bonding, but does not cause additional molecular relaxation. This results in an improved tensile strength, but the improvements tend to be smaller with increased compaction temperature.
- The increased dwell time was expected to have a similar effect on the tensile properties of hot compacted SRPP as increasing the compaction temperature. The effects of dwell time on tensile properties were, however, too small to detect in most cases.
- The compaction pressure needs to be sufficiently high to limit shrinkage, molecular relaxation and surface melting. Reduced pressure has the same influence on thermal behaviour and tensile properties as increased compaction temperature or addition of films.

These results illustrate that the tensile properties of SRPP can be tailored to specific applications in a range of processing conditions. For general purposes, the optimal processing conditions are 5 min at 188°C and 39 bar. Shorter dwell times may lead to larger variations as the press does not have sufficient time to equilibrate its temperature. Higher temperatures would lead to a reduction in the tensile properties. The pressure of 39 bar is required to limit the shrinkage of SRPP. If films are added, then the temperature can be reduced to 186°C without risking a loss in compaction quality or 45° tensile properties.

For hybrid SRCs, the interlayer bonding is known to be a crucial parameter. The presented results give guidelines for how this bonding can be fine-tuned, and what the consequences are for the tensile properties of the SRPP.

2.4 Impact resistance

Impact resistance is the main advantage of SRPP compared to other SRCs, and is exploited in most of its current applications. Given the influence of processing parameters on the tensile properties, similar influences are expected on the penetration and non-penetration impact resistance. Before moving into the actual influence of process parameters however, some preparatory steps are required. In case of penetration impact resistance, the normalisation by the sample thickness and the proper test geometry should be analysed first. In case of non-penetration impact resistance, the possible testing techniques and the type of damage mechanisms are analysed first.

2.4.1 Penetration impact resistance

This subsection analyses the penetration impact resistance of SRPP. First, the influence of sample thickness on the penetration impact resistance is investigated. Then, the influence of the geometry of the test setup is analysed. These are necessary steps before moving into the influence of process parameters on the penetration impact resistance.

Sample thickness

For a fair comparison between different samples, normalisation of the absolute penetration impact resistance by the sample thickness is common practice. This assumes a linear relationship between impact resistance and sample thickness. This relationship has only rarely been validated in literature. Alcock et al. [60] found that a linear relationship is not valid for SRPP (see Figure 2-31). Instead, the absolute impact resistance seemed to level off for samples thinner than 1.6 mm. Such levelling off cannot continue for thinner samples, as samples with a zero thickness cannot absorb any energy. Their thinnest sample was still 0.9 mm, making it difficult to judge their conclusions. Alcock et al. attributed the non-linearity for thin samples to the larger deflection. This explanation is, however, not convincing.

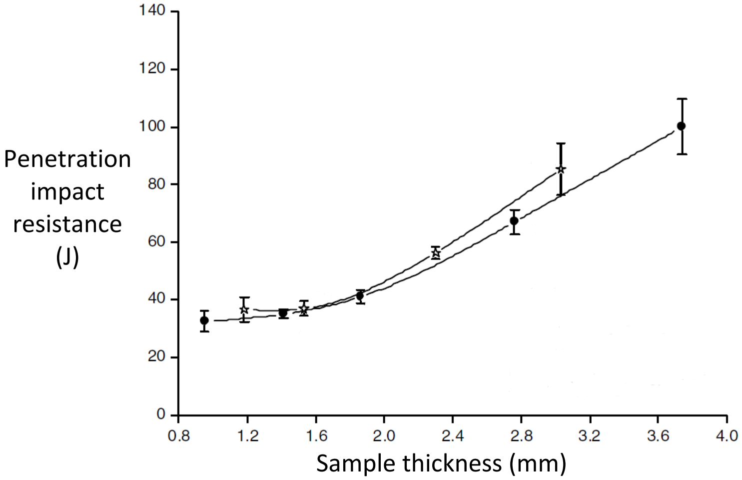

Figure 2-31: Penetration impact resistance for two different SRPP fabrics with bi-component tape technology (adapted from [60], with permission from Elsevier).

To verify the relationship between sample thickness and impact resistance, samples with 1 to 16 layers are hot compacted and tested. Figure 2-32 plots the absolute penetration impact resistance as a function of sample thickness. In contrast with the results of Alcock et al. [60], a linear relationship is found.

A univariate regression analysis yields a specific impact resistance of 26.8 J/mm with $R^2 = 79.7\%$.

The result for the thinnest sample corresponds to a sample consisting of only a single layer. Since delaminations can only occur between two layers, this means that delaminations do not contribute significantly to the energy absorption of SRPP. The main energy absorbing mechanisms are hence tape fracture and tape-matrix debonding. It should be noted that this conclusion is valid at 188°C without films. At lower compaction temperatures, a weaker interlayer bonding is expected, which facilitates delaminations.

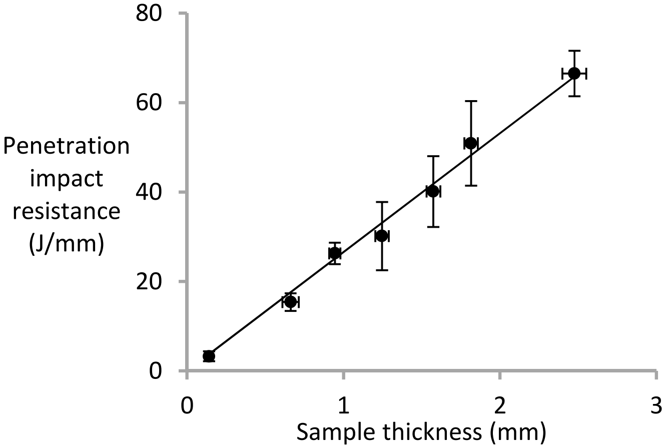

Figure 2-32: Linear relationship between penetration impact resistance and the thickness of SRPP compacted without films for 5 min at 188°C and 39 bar.

Figure 2-32 proves a linear relationship between impact resistance and sample thickness. The question then arises what caused the non-linearity in Alcock et al. [60]. This will be investigated further by looking at the influence of test geometry.

Test geometry

A robust testing technique should be independent of the test setup, or the influence of the testing environment should at least be understood. In literature, falling weight impact tests are performed on SRCs according to ASTM D5628 and ISO 6603-2. These standards were developed for rigid plastics and are widely adopted for polymer composites. Glass and carbon fibre composites are the most commonly investigated composites. Both fibres are brittle, which makes testing according to these standards reasonable. To be able to compare SRCs with conventional brittle fibre composites, the same testing method should be used.

In ductile fibre composites, however, the deformation before penetration can be much larger. This may lead to unwanted sample deformations, which are illustrated in Figure 2-33. Necking is the in-plane deformation of the edges towards the centre of the sample. Wrinkling is an out-of-plane deformation that occurs at the edges of the sample. These damage mechanisms are observed when the samples have dimensions close to the dimensions of the clamp. Large samples have a higher resistance to such deformations. An alternative way to avoid these deformations is to use a rougher clamp and set the clamping pressure to its maximum. Both precautions were taken throughout this study.

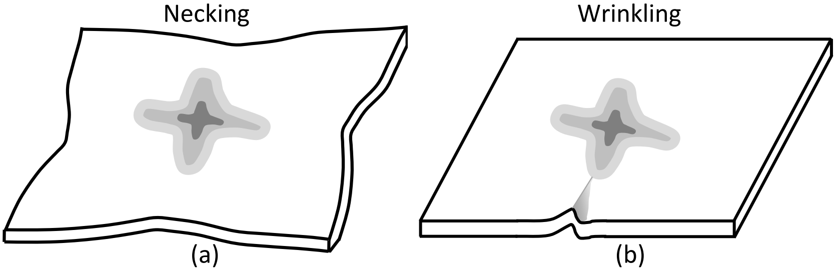

Figure 2-33: Schematic illustration of unwanted sample deformations during penetration impact testing: (a) necking, and (b) wrinkling.

The geometric ratio G_{ratio} is used to characterise whether the sample dimensions are sufficiently large compared to the clamp diameter. This ratio is defined as the edge length L_{edge} of the square sample divided by the outer diameter $\varnothing$ of the clamp (see Figure 2-34). G_{ratio} is a measure of the excess amount of material that sticks outside of the clamp. At a low G_{ratio}, necking and wrinkling are likely to occur.

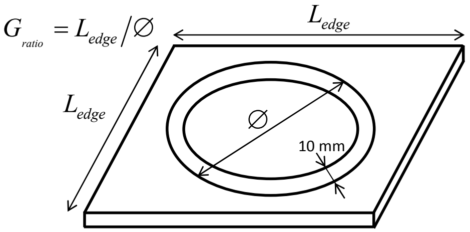

Figure 2-34: Definition of G_{ratio} as the ratio of the sample edge length over the outer diameter of the clamp.

Samples with different sizes were tested to assess the sensitivity of SRPP to wrinkling and necking. Three sample edge lengths were tested on the clamp with 60 mm outer diameter, giving geometric ratios of 1, 1.67 and 2.33. Similarly, four sample edge lengths were tested on the clamp with 100 mm outer diameter, giving geometric ratios of 1, 1.4, 1.67 and 2.33. Analysis of variance (ANOVA) is used to assess the influence of the clamping diameter and the specimen size. This analysis requires grouping together the data for both clamps, as is done in Figure 2-35.

All samples should in principle absorb the same energy, but this is not the case (see Figure 2-35). The impact resistance at higher geometric ratios tends towards a stable value, where the excess amount of material is large enough to prevent any degree of necking and wrinkling. This is proven by the ANOVA analysis. The clamp and specimen size both affected the penetration impact resistance significantly, with a probability of less than 0.1% and 1%

respectively. A value of 0.1% implies that the probability that the size of the clamp does not influence the penetration impact energy is smaller than 0.1%. An interaction between sample size and clamp size was found to be unlikely, with a probability of 11%.

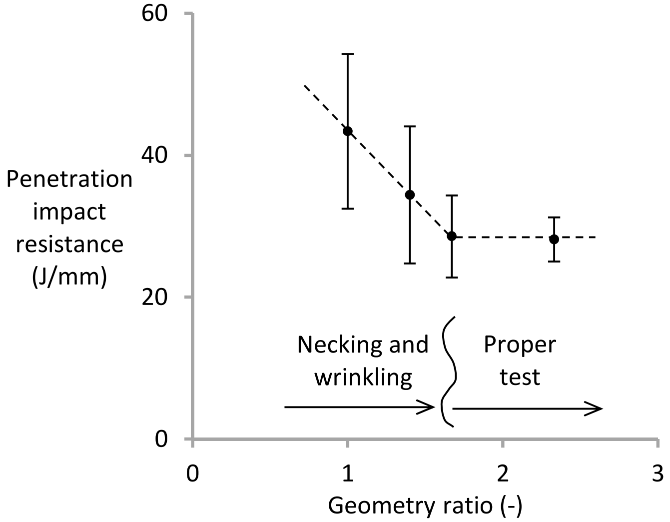

Figure 2-35 Non-linear effect of the test geometry on the impact resistance of SRPP compacted without films for 5 min at 188°C and 39 bar. The trend line is only indicative.

From G_{ratio} of 1.67 onwards, a stable value for the absorbed energy is observed. This is the minimal G_{ratio} for adequate penetration impact testing of these specific samples. For smaller G_{ratio}, necking and wrinkling occurred. The value of 1.67 is valid for samples compacted without films for 5 min at 188°C and 39 bar.

Necking and wrinkling are more likely to occur for lower compaction temperatures, making it difficult to set a strict minimum on G_{ratio}. This was confirmed by testing a second set of samples at a G_{ratio} of 1.4, but this time they were compacted at 184°C. While all samples compacted at 188°C were penetrated, only 1 out of 8 samples compacted at 184°C was penetrated. Figure 2-36 shows an example of an unpenetrated sample next to the only sample that did penetrate. In both cases, severe wrinkling and some necking is observed.

It can be stated that sufficient material outside of the clamp is required to prevent necking and wrinkling. After penetration impact, all samples should be inspected for these unwanted deformations. Samples with these unwanted deformations most likely have a below average interlayer bonding, and hence are likely to absorb more energy than average. Simply leaving out only the samples with these deformations could skew the resulting average value. Instead, larger samples should be made and all the tests should be repeated.

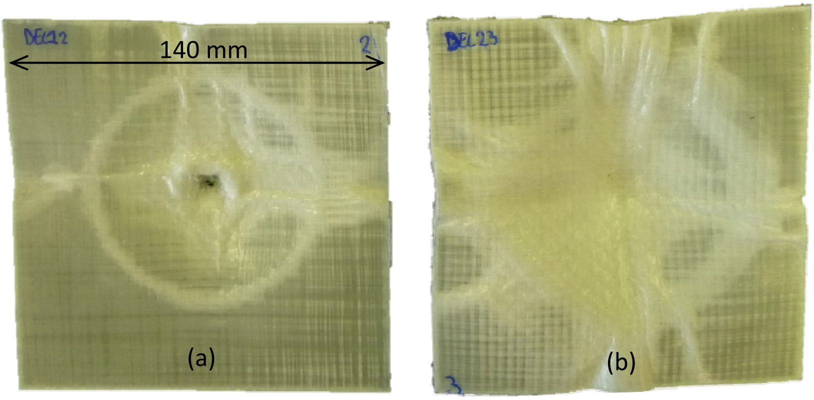

Figure 2-36: Impacted samples compacted without films for 5 min at 184°C and 39 bar: a) the only sample out of 8 that was penetrated, and b) an unpenetrated sample. Both samples show signs of necking and heavy wrinkling.

Influence of process parameters

Figure 2-37 displays the penetration impact resistance as a function of the compaction temperature for samples with a dwell time of 5 min. Figure 2-38 presents the force-displacement diagrams for representative samples, while Figure 2-39 shows the samples after impact. The samples compacted at 180°C without films are not plotted in Figure 2-37 and Figure 2-38a, as these samples could not be penetrated. Instead, the samples completely delaminate during impact, resulting in separated layers folding into the impact ring. An example of such a sample can be seen in Figure 2-39a. Some necking and wrinkling were found in the sample compacted at 180°C with films (see Figure 2-39d), so this data point should be interpreted with care.

Samples with films reach a plateau in penetration impact resistance between 184°C and 191°C, similar to the plateau described by Alcock et al. for SRPP produced with bi-component tape technology [60]. This similarity makes sense, as the outer layer of co-extruded tapes provide matrix similar to the way films do. If enough matrix is present, then a further increase in the matrix fraction will not cause a further increase in interlayer bonding. This explains the observed plateau in penetration impact resistance. Samples without films did not display this plateau, but follow a monotonic decrease of the penetration impact resistance with increasing compaction temperature. This illustrates the difficulty of creating enough matrix material in hot compaction without films.

Above 190°C, significant molecular relaxation occurs, which results in a decreased penetration impact resistance, both for samples with and without films. This is also observed in Figure 2-38, which demonstrated more brittle behaviour for the samples compacted at 194°C. Another crucial feature of these results is that both data sets seem to converge at 191°C. At this compaction temperature or higher, the additional films do not affect the penetration impact resistance.

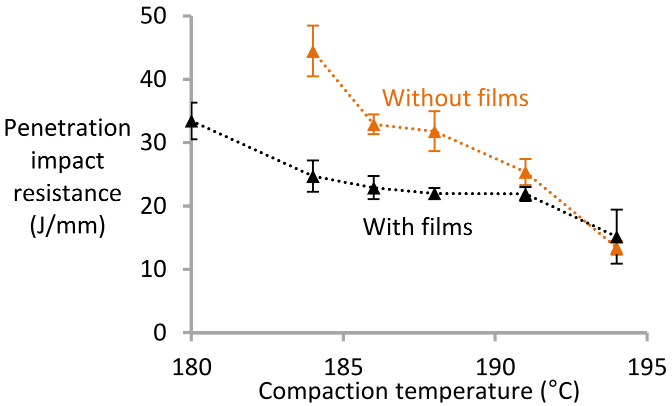

Figure 2-37: The penetration impact resistance as a function of compaction temperature for samples compacted for 5 min at 39 bar without and with films. The samples compacted at 180°C without films are not shown in this figure, as those samples were not penetrated.

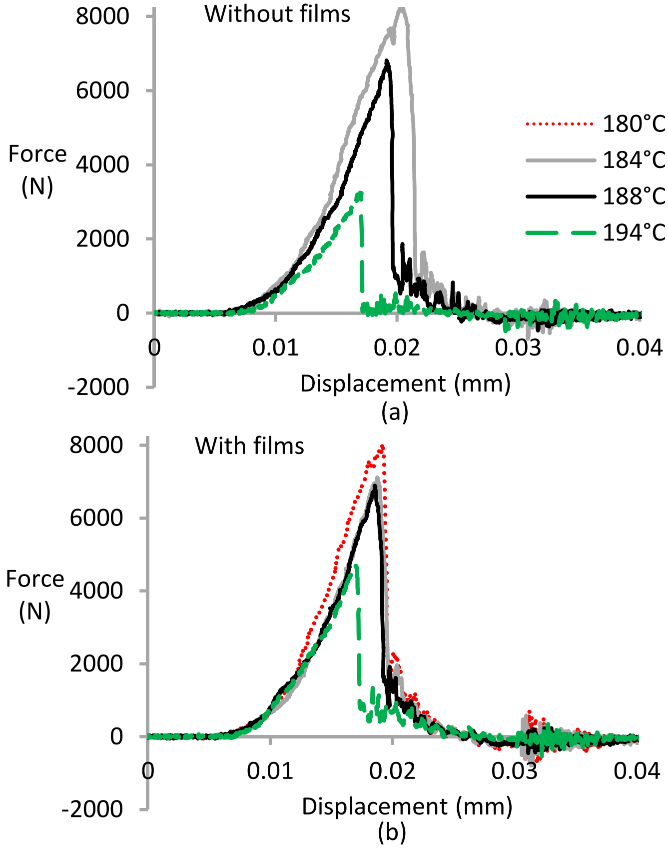

Figure 2-38: Force-displacement diagrams for penetration impact tests on samples compacted for 5 min at 39 bar: (a) without, and (b) with films. The diagrams for 186°C and 191°C are omitted for clarity.

Figure 2-39 presents the photographs of representative samples after penetration. The sample in Figure 2-39a, which was compacted at 180°C without film, demonstrates an insufficient interlayer bonding. The sample heavily deformed by the delamination of the layers and debonding of the tapes. Figure 2-39d illustrates that adding films improves the interlayer bonding and facilitates penetration. At 188°C, the damage is circular, but becomes smaller and more cross-shaped at 194°C. This is caused by the improved interlayer bonding, which changes the dominant damage mechanism from delamination and tape debonding to tape fracture.

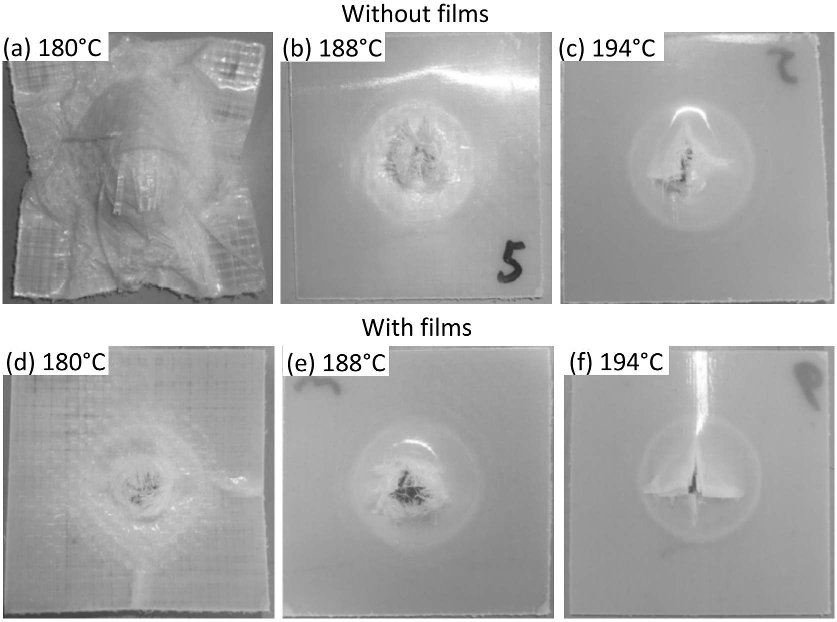

Figure 2-39: Photographs of the tensile side of samples after penetration impact tests: (a) 180° with films, (b) 188°C with films, (c) 194°C with films, (d) 180° without films, (e) 188°C without films, and (f) 194°C without films. All samples were hot compacted for 5 min at 39 bar.

The influence of the dwell time is investigated on samples with films and the results are summarised in Figure 2-40. No clear differences are observed, meaning that dwell time does not significantly affect the penetration impact resistance for samples with films. For samples without films, a higher dwell time is expected to lead to lower penetration impact resistance. Such changes would be attributed to increased matrix fraction and hence improved interlayer bonding. These changes will only become clear at longer dwell times, which were not tested in this study.

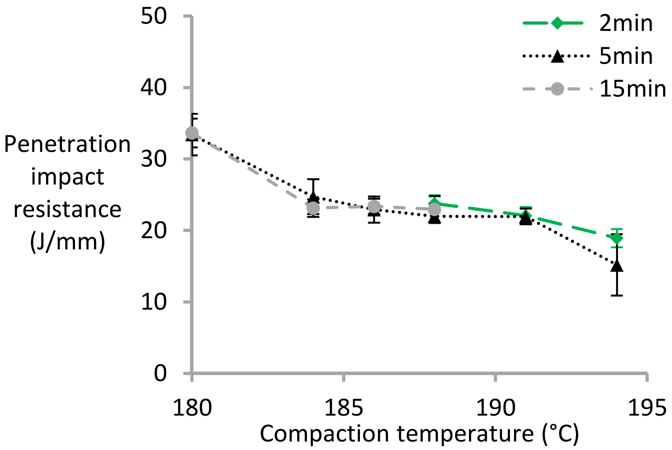

Figure 2-40: The influence of dwell time on the penetration impact resistance of samples compacted at 39 bar with films.

Figure 2-41 summarises the influence of compaction temperature on the penetration impact resistance. The reduced compaction pressure strongly reduces the penetration impact resistance. This is again attributed to more molecular relaxation and surface melting of the tapes. This not only increases the matrix fraction, which is more brittle, but also reduces the energy absorption capability of the tapes. The penetration impact resistance is more sensitive to these changes than tensile properties (see Figure 2-30). It should be emphasised that this finding is of great practical importance, as impact resistance is the main advantage of SRCs.

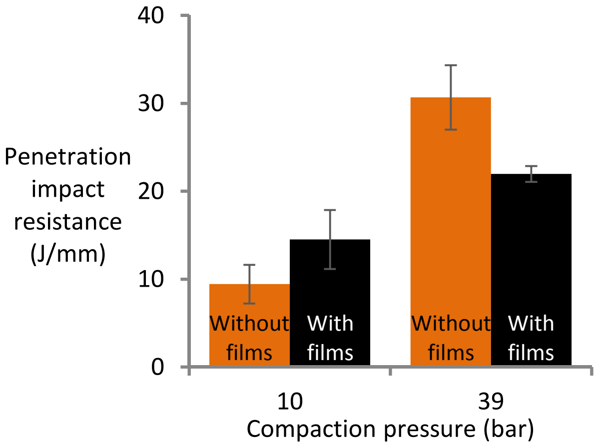

Figure 2-41: The influence of compaction pressure on the penetration impact resistance of samples compacted for 5 min at 188°C.

Conclusion

Several issues in impact testing of SRPP were investigated. For sufficiently large samples, the penetration impact resistance depends linearly on the sample thickness. If the samples are however too small relative to the clamp, then necking and wrinkling can occur. These deformations are unwanted, as they increase the absorbed energy. All impacted samples should be checked for these deformations and, if found, all tests should be repeated on larger samples or the samples should be clamped better. If necking and wrinkling are absent, then a linear relationship between sample thickness and impact resistance is expected.

The importance of the processing parameters was revealed for hot compacted SRPP. The penetration impact resistance decreased with increased compaction temperature. Adding films decreased the impact resistance in general, but also decreased the sensitivity of the impact resistance to the processing temperature. This again indicates that films are an efficient method to widen the processing window. Dwell time had no significant influence, whereas reducing the compaction pressure strongly reduced the impact resistance. This strong reduction was attributed to the increased molecular relaxation and reduced tape fraction. This highlights the practical importance of hot compacting at high pressures.

2.4.2 Non-penetration impact resistance

In composites, penetration impact resistance tends to increase for poorly bonded layers, allowing delaminations to spread easier and hence absorb more energy [115]. Poor bonding also leads to a decrease in other mechanical properties, such as compression strength, compression after impact and shear strength. Poorly bonded composites are thus often unsuitable for structural or semi-structural applications. The non-penetration impact resistance indicates the sensitivity of a material to impact damage. Ultrasonic C-scan is the most common technique to analyse the extent of damage after an impact event. However, several other techniques exist. The strain mapping technique used by Alcock et al. only measures the surface strains, and does not reveal the damage itself (see Figure 2-15) [60]. The indentation depth that remains after an impact event is another measure for the extent of the damage. In some applications, this depth is used to judge whether or not a component should be removed. A new technique, Transmitted Light Imaging, will be introduced to obtain more information than that obtained from C-scans. Finally, the damage mechanisms will be investigated and the influence of process parameters on damaged area will be revealed.

Ultrasonic C-scan

Ultrasonic C-scan is an efficient technique to measure the damaged area and is frequently used for carbon and glass fibre composites. For ductile fibre composites, however, the remaining indentation depth after an impact event can be much larger. This may lead to the introduction of measurement artefacts. Due to the indentation, the ultrasonic waves will not be perpendicular to the sample. For large angles between the incident waves and the local normal to the sample, the wave will not be reflected into the transducer. The equipment would interpret this as damage, while that is not necessarily the case.

The sensitivity of the C-scan equipment to this angle depends on the transducer as well as on the material. Therefore, a set of C-scans is performed by placing the same specimen on two supports, while the transducer height h_{trans} is always 25 mm. The height of one of the two supports is gradually increased to change the angle. This setup is schematically illustrated in Figure 2-42. The height h_1 is kept constant at 15 mm and h_2 is increased from 15 mm to 50 mm with 5 mm increments. The sample is scanned close to the 15 mm high support. The angle θ is calculated by equation 2-4:

$$\theta = \sin^{-1}\left(\frac{h_2 - h_1}{L_{edge}}\right) \cdot 180° \qquad (2\text{-}4)$$

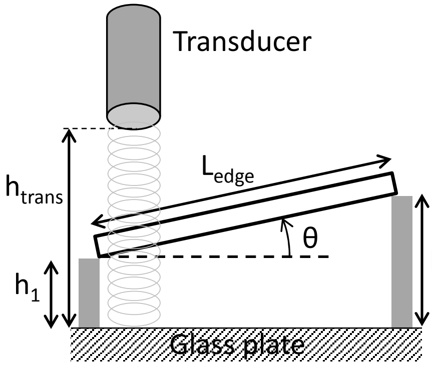

Figure 2-42: Schematic illustration of the calculation of angle in C-scan testing.

Figure 2-43 presents the resulting C-scans and the corresponding histograms. With increased angle θ, the C-scans gradually darken. For a 20.5° angle, the C-scan is almost completely black. The threshold below which everything is considered to be damaged area was 64 in this part of the study. Angles above 14.5º would thus be considered as damaged area even if it contains no damage at all. A rapid change in the greyscale intensity is already seen for angles above 10°. C-scans should hence be treated with caution if samples are indented with an angle θ of more than 10°. It should be noted that the exact value for this angle will depend on the C-scan parameters, such as transducer type and height h_{trans}.

The angle θ was measured on several samples. For samples compacted without films for 5 min at 188°C and 39 bar, the maximum angle is 10° on average after a 15 J impact event. For the same samples impacted with 30 J, however, θ is 14°. This clearly illustrates the limitations of ultrasonic C-scans for measuring damaged areas in ductile fibre composites.

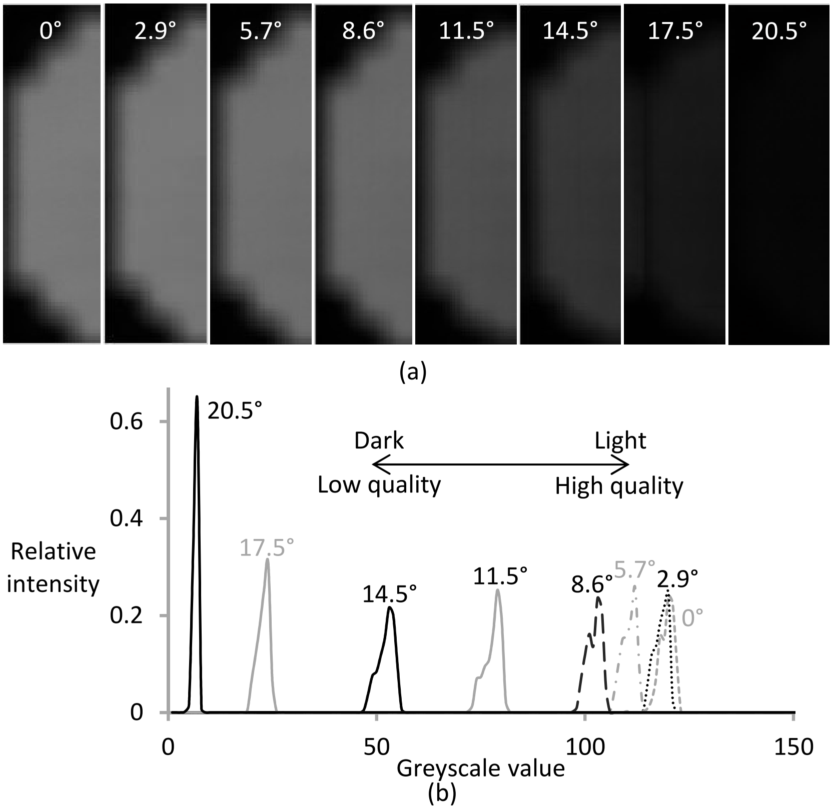

Figure 2-43: Influence of the angle θ on C-scan results for samples compacted for 5 min at 188°C and 39 bar without films: (a) C-scan images, (b) greyscale histogram.

The damaged area is calculated as a function of the impact energy level. Figure 2-44 demonstrates that the damaged area strongly depends on the threshold value. The measured value at 30 J is surprisingly high. This is the last data point before penetration occurred. This can have two reasons. Firstly, some additional damage mechanisms are activated as the impact energy is close to the energy required for penetration. Figure 2-45 reveals that some tape breakage or fibrillation is indeed visible at the indentation tip in the 30 J samples. Such damage is not found in the 25 J samples. Secondly, the maximum angle in these samples reached 14°, which is sufficient for damage detection even without any real damage. The angle θ is larger than 10° in a region with a diameter of about 36 mm. That means that the indentation may have a serious influence on the damaged area calculation.

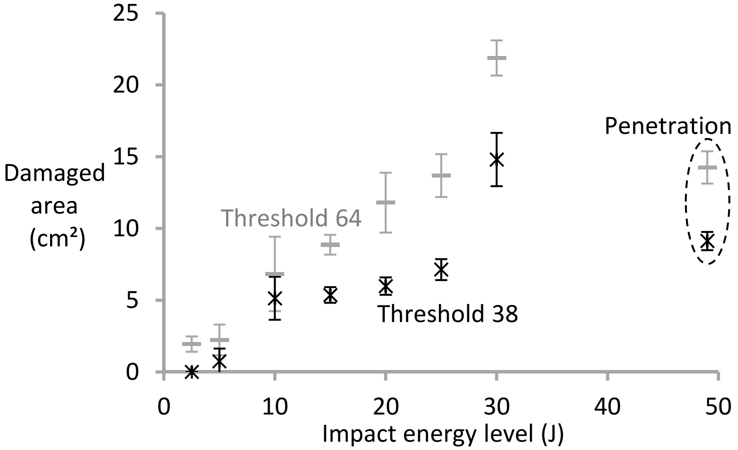

Figure 2-44: Damaged area as a function of the impact energy level for samples compacted for 5 min at 188°C and 39 bar without films.

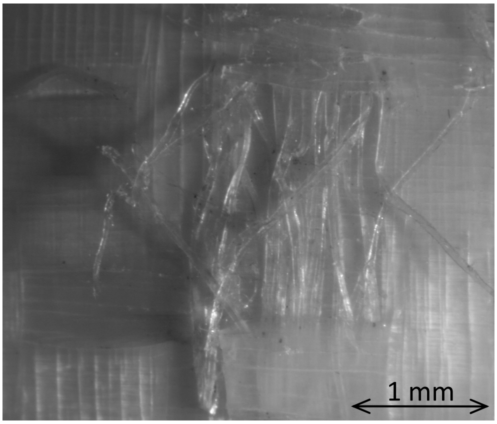

Figure 2-45: Stereomicroscopy image of tape damage at the tensile side near the indentation tip. This sample was compacted for 5 min at 188°C and 39 bar without films and impacted with 30 J.

Indentation depth

Two types of indentation depths are defined in "2.2.4 Falling weight impact tests". The dynamic indentation depth is the depth over which the sample deforms during the test. Some of this indentation will rebound elastically, and only the plastic indentation depth will remain after the test.

Figure 2-46 summarises both measures for the indentation depth for samples without films that were compacted at 188°C. The dynamic indentation depth is always significantly higher than the plastic one. While the dynamic indentation keeps increasing, the plastic indentation seems to level off at about 5 mm indentation or 15 J impact energy. Aurrekoetxea et al. [91] postulated that such levelling off can be caused by a transition from plastic deformation of tapes to tape breakage. Aurrekoetxea et al. found this transition at 6 J/mm, while this study found 15 J or 10 J/mm.

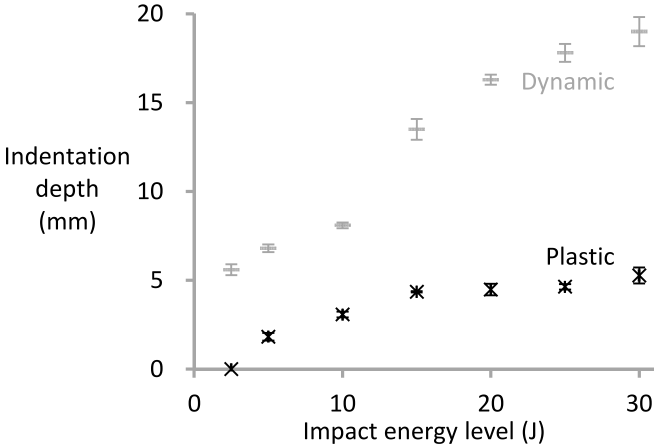

Figure 2-46: Indentation depth as a function of the impact energy level for non-penetrated samples compacted without films for 5 min at 188°C and 39 bar.

Transmitted light imaging

A novel non-destructive technique is developed to gain a deeper understanding of the failure behaviour. Transmitted light imaging exploits the interaction of transmitted light with damage in SRPP.

Figure 2-47 compares the C-scan images at different impact energy levels with the corresponding transmitted light images. In the C-scan, the damaged area can be observed, but the resolution is too low to gain information on the type of damage. Transmitted light images are able to resolve much finer details. Figure 2-48 schematically illustrates the four types of observed damage:

- Damage due to clamping ring
- Transverse tape cracking
- Matrix cracking
- Damage due to striker contact

C-scan is not able to detect the matrix cracking, as this insufficiently scatters the ultrasonic waves. Damage due to striker contact also cannot be detected. This may have been possible to detect by C-scanning at a lower amplification, but that would reduce detection capabilities in other regions.

Transmitted light imaging also yields more information on the type of damage than C-scans. When zooming in on the transmitted light images, horizontal and transversal lines can be observed. These are related to transverse tape cracking. As illustrated in “2.1.1 Oriented polymers”, the high orientation causes weak transverse properties.

Figure 2-44 illustrated a large increase in the damaged area when increasing the impact energy from 25 J to 30 J. This is also visible in the C-scan images in Figure 2-47, but not in the corresponding transmitted light images. This indicates that the angle of the indentation resulted in an overestimation of the damaged area by C-scan.

Finally, perhaps the greatest advantage of transmitted light imaging is that it can detect damages regions in 45° directions. Alcock et al. [60] has previously proven that these directions can be subjected to larger strains than in the 0° and 90° directions (see also Figure 2-15). It is hypothesised that these zones are caused by matrix cracking. The strain in this region is not high enough to cause matrix failure at strain rates typical for tensile tests. In impact tests, however, the strain rates are much higher, which will embrittle the isotropic PP. This embrittlement in falling weight impact tests was reported for isotropic PP of this specific grade in Swolfs et al. [113]. Matrix cracking is therefore a reasonable hypothesis, but microCT is required to confirm it.

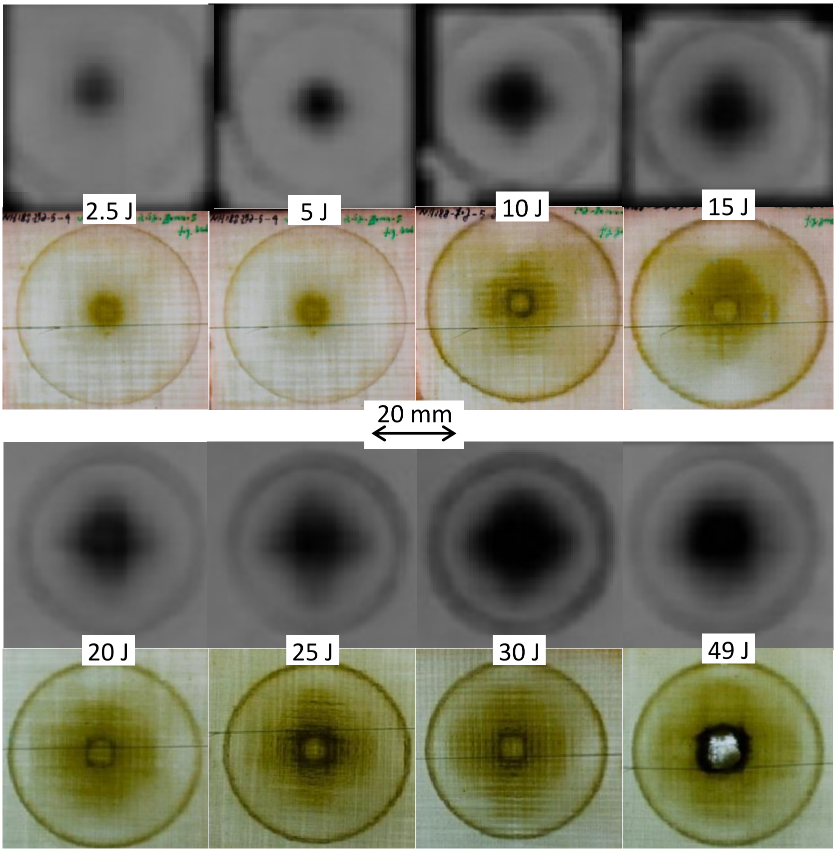

Figure 2-47: C-scan images after different impact energy levels with their corresponding transmitted light image. All samples were compacted without films for 5 min at 188°C and 39 bar.

Based on the information from transmitted light imaging, a schematic overview of damage in SRPP can be set up (see Figure 2-48). It should be noted that not all of these damage mechanisms are always present.

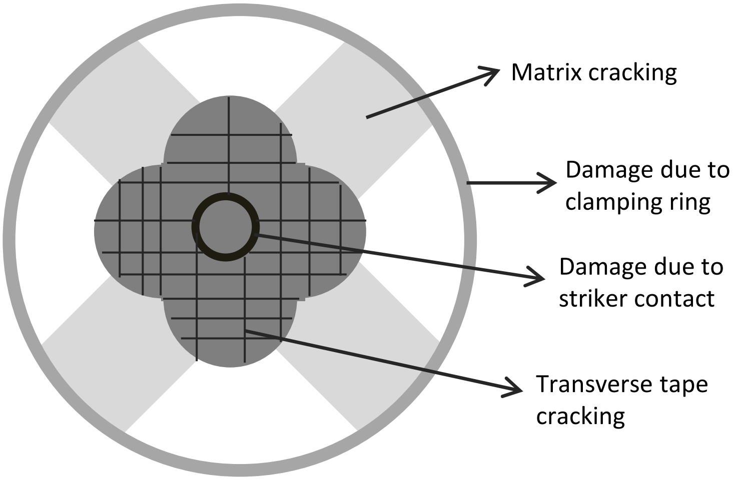

Figure 2-48: Schematic illustration of the types of damage found with transmitted light imaging.

Transmitted light images are better than C-scans at resolving small damage features. Figure 2-49 illustrates this for samples without and with films. While the damaged area from C-scans was only slightly lower for samples with films, the transmitted light images highlight clear differences. The colours are much more intense for samples without films. For the samples with films, the matrix cracking at 45° more or less disappears. This may indicate that matrix cracking initiates at pre-existing defects, as the films would strongly reduce those defects.

Without films

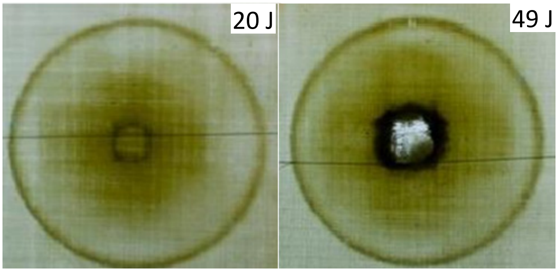

With films

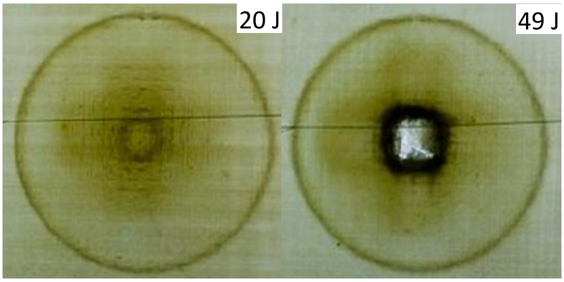

Figure 2-49: Comparison of transmitted light images for samples compacted for 5 min at 188°C and 39 bar without and with films.

Damage mechanisms

To further understand the damage mechanisms in impact tests, microCT is performed on impact samples. Before going into the damage mechanisms in impact samples, a sample prior to impact will be analysed. Figure 2-50 displays a cross-section of a sample prior to impact. The x and y directions correspond to the in-plane directions, while the z-direction is the thickness direction. In the bulk of the material, no damage is detected. At the edge, some delamination or debonding is found, but this is due to the cutting. This damage will not have any influence on the impact results, as the impact samples are penetrated in the middle of the sample.

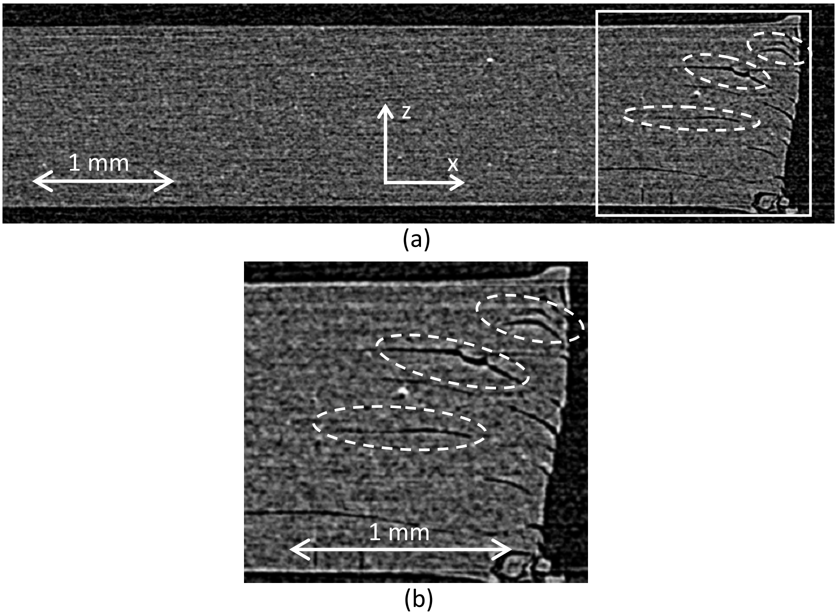

Figure 2-50: MicroCT cross-section of SRPP compacted for 5 min at 188°C and 39 bar without films, prior to impact testing: (a) overview, and (b) zoom in region near the sample edge. Damage due to cutting is observed at the edge (see white circles), but not in the middle of the sample.

Figure 2-51 displays the microCT results of a sample that was impacted with 15 J. Figure 2-51a displays a cross-section near the impact location. Small vertical cracks are observed in the tension side, while the compression side does not reveal any damage. Figure 2-51b is a cross-section perpendicular to the thickness direction and yields more information on the extent of these cracks. A typical crack has a length of 1-2 mm, and seems to follow the weave architecture. As explained in "2.2.1 Materials", the weave architecture is not regular due to the overfeeding. The distance between two interlacing points is 3 mm on average. Careful observation of Figure 2-51b indeed reveals this type of weave architecture.

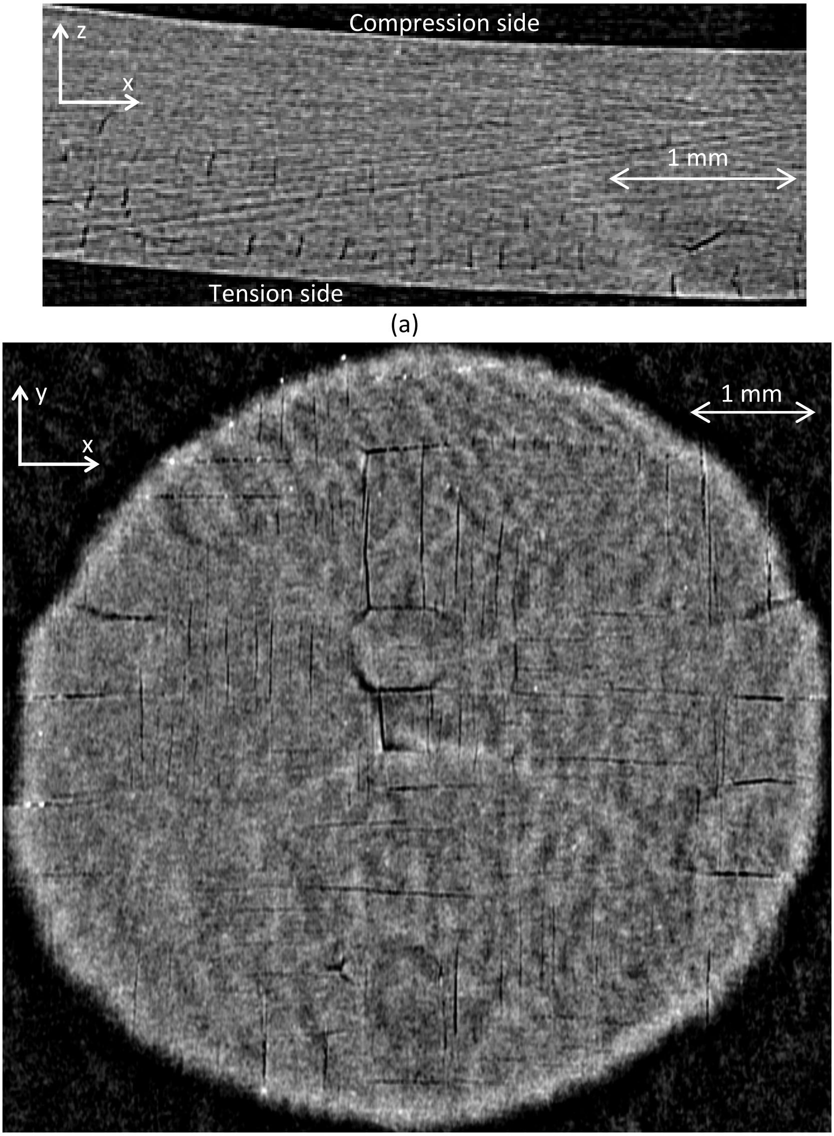

(a)

(b)

Figure 2-51: MicroCT cross-section of SRPP compacted for 5 min at 188°C and 39 bar without films, prior to impact testing, after a 15 J impact event: (a) through-the-thickness cross-section with vertical cracks on the tension side, and (b) cross-section perpendicular to the thickness direction with cracks in both directions.

A further analysis can be performed based on the height of the vertical cracks (see Figure 2-51a). The height of the vertical cracks varies between 60 and 140 µm. This value as well as its scatter are related to the thickness of a tape. A tape is 50 µm thick prior to weaving and hot compaction. During weaving, however, the 150% overfeeding results in an average thickness of 75 µm. After hot compaction, this average thickness is slightly reduced, but no exact value for this reduction is known. In general, the height of the vertical cracks varies between 1 and 2 tape thicknesses. This means the crack propagates from a tape in one layer to a tape in the adjacent layer. Whether this occurs, depends on the nesting of the layers. If two tapes in adjacent layers are oriented in the same direction, then the crack can propagate. If the tapes are perpendicular to each other, then the crack is stopped. This explains the variation in the crack heights in Figure 2-51a.

Combined with the length of the cracks in Figure 2-51b, the cracks can be attributed to transverse cracking and longitudinal splitting of the tapes. Figure 2-52 illustrates that both terminologies refer to the visual appearance, but depend on the loading direction that caused them. Transverse cracking is deemed to be more likely due the microstructure in Figure 2-6, which is weak in the transverse direction. It should be noted that the circumferential clamping leads to a complex biaxial stress state during impact. Transverse stresses can thus occur at any location in the sample. Figure 2-51b confirms that these cracks occur in 0° and 90° directions, irrespective of their relative position to the impact centre.

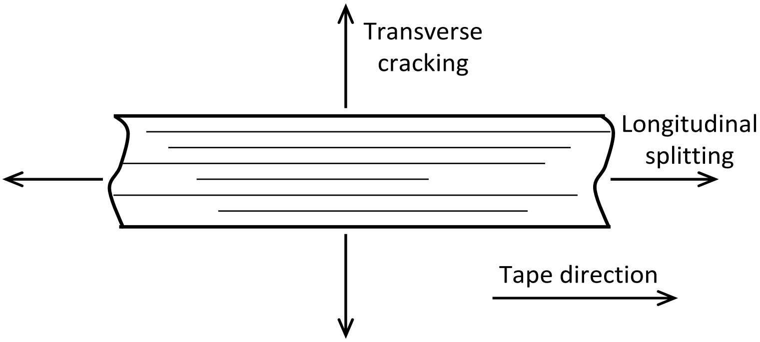

Figure 2-52: Schematic illustration of the difference between transverse cracking and longitudinal splitting. The arrows indicate the loading direction.

Finally, the area near the impact zone is analysed. In the transmitted light images in Figure 2-47, a circular area with a 20 mm diameter is found. Such area could not be found in the microCT images, as the imaged area is only 12 x 18 mm. Figure 2-53 illustrates that some debonding or delaminations are found at the tip of the indentation at the tension side. This type of damage is also found in other parts of the sample. All these locations are within 5 mm distance of the indentation tip.

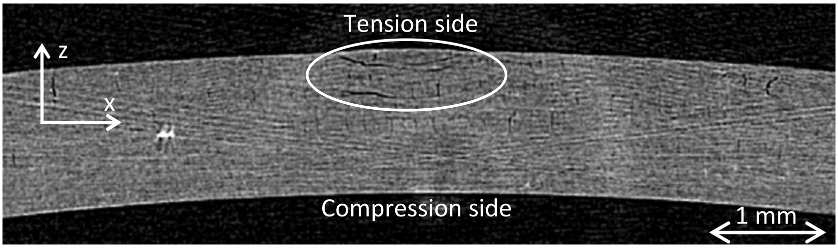

Figure 2-53: Close-up of the through-the-thickness microCT cross-section near the impact zone of SRPP compacted for 5 min at 188°C and 39 bar without films.

Influence of process parameters

Figure 2-54 presents the C-scans for samples with films after a non-penetration impact event. To illustrate the overall quality of the samples, the C-scans of the 5 J samples before impact are displayed in the first column of Figure 2-54. The unimpacted samples without films displayed similar trends, but are not shown here.

At 180°C, the initial sample quality is poor. Dark grey, low quality regions are already visible prior to the impact event. The dark grey regions at the corners and edges should be disregarded, as they are caused by the supports and sinkers. As the compaction temperature is increased, the overall quality also increases. The samples compacted at 184°C or higher all have a high quality, which is indicated by the light grey to white colour over the whole sample. After impact, two features arise in the C-scans: a ring on the outside, and a circular or diamond-shaped zone in the middle. The ring coincides with the clamping region and seems to fade away at higher compaction temperature. The ring is also more pronounced at the higher energy level. This indicates the ring is not purely related to the clamping, but also to damage introduced by the impact event. Clamping of a plate results in high flexural stresses, and even stress concentrations, at the clamp edges. This causes local damage, which is more severe at lower compaction temperatures and higher impact energy.

The central damage changes in size, intensity and shape. The size and intensity are mainly related to the interlaminar bonding and the energy level, while the shape provides an indication of the damage mechanism. A diamond-shaped damage indicates tape debonding and fracture, while delaminations are less direction-dependent and cause circular damage. The circular damage is more obvious at low compaction temperatures, which is consistent with the lower bonding quality. At higher compaction temperatures, the bonding is improved and more diamond shaped pattern is observed. This is difficult to observe at 5 J, but is clear in the 15 J images.

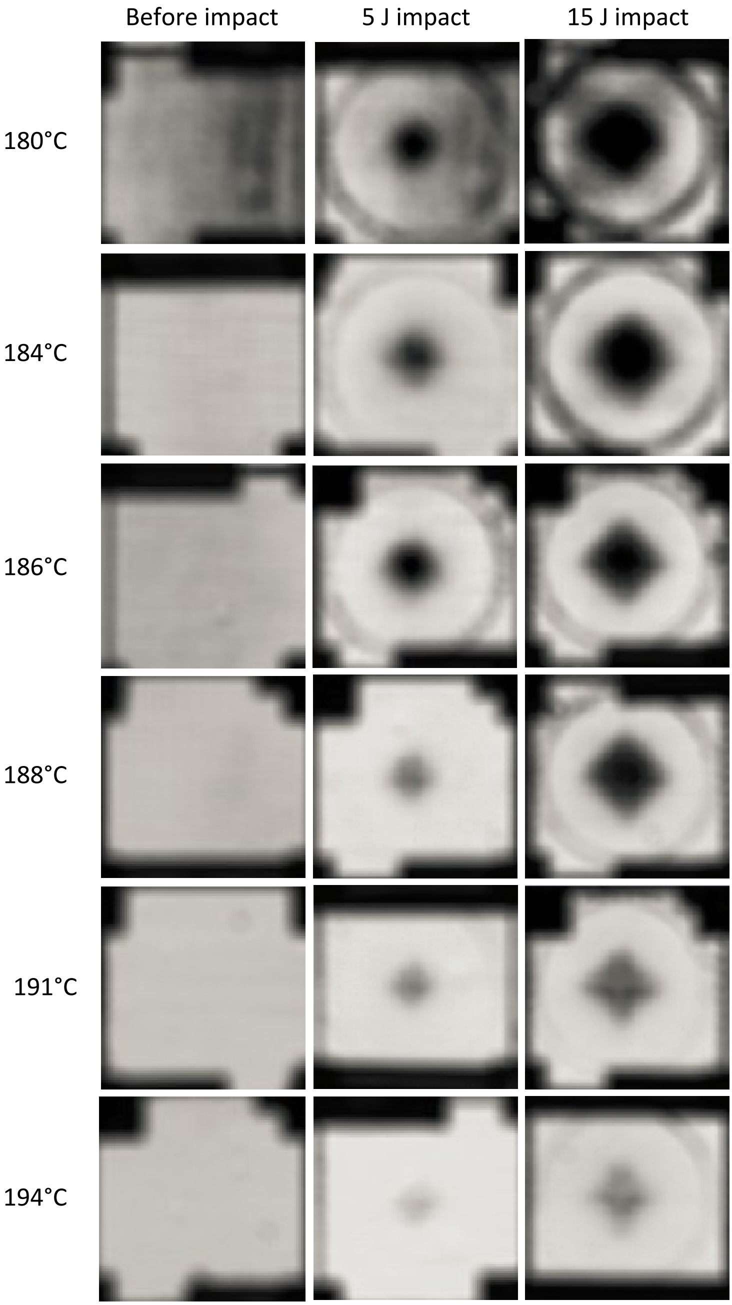

Figure 2-54: C-scan images of samples hot compacted at different temperatures with films. The first column displays the samples before impact, while the second column displays the same samples after a 5 J impact. The third column displays impact samples after a 15 J impact. The black areas at the corners and edges are caused by the sinkers and supports and are not related to material damage.

Based on the C-scan images, the damaged area was calculated. This calculation only takes into account the central damage and neglects the outer ring. The results are summarised in Figure 2-55a and b. Both figures demonstrate a strongly decreasing damaged area with increasing compaction temperature. In general, adding the films seems to slightly reduce the damaged area, although this is not the case for all configurations. Based on the available data, it is difficult to explain the exact mechanisms for these decreasing trends. It is hypothesised that tape debonding and delamination are more difficult due to the increased interlayer bonding. This hypothesis is supported by the fact that both increased temperature and adding films decrease the damaged area.

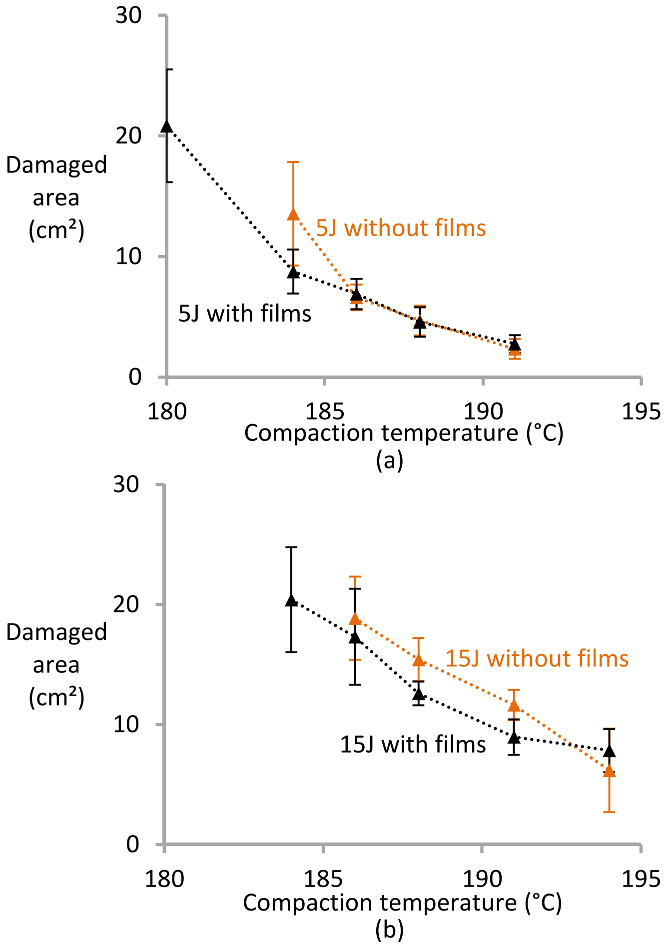

Figure 2-55: Damaged area as a function of compaction temperature for samples compacted for 5 min at 39 bar: (a) after a 5 J impact event, and (b) after a 15 J impact event. Some data points at high and low compaction temperatures are omitted, as the thresholding procedure resulted in the analysed area to be either completely damaged or completely undamaged.

The dwell time has a clear influence on the damaged area, see Figure 2-56. Higher dwell times allow more molecular relaxation and more matrix will be created during hot compaction. The additional matrix improves the bonding, leading to a reduction in the damaged area. The influence of dwell time is not clearly visible in most of the previously described properties, but is clear for the damaged area results. This indicates that the damaged area is more sensitive to the matrix fraction and interlayer bonding than the other properties.

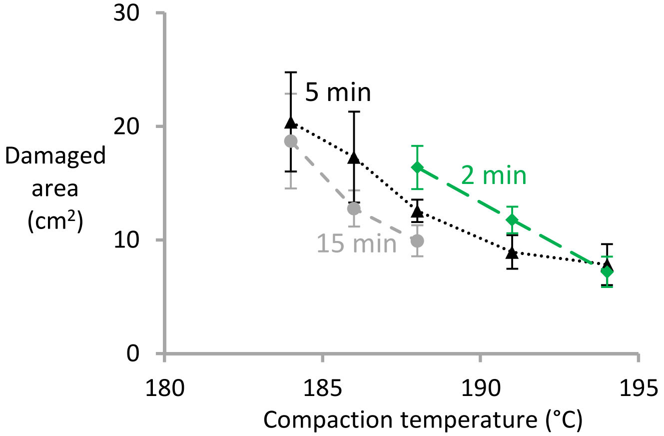

Figure 2-56: The influence of the dwell time on the damaged area for samples compacted with films at 39 bar.

Figure 2-57 summarises the influence of compaction pressure on the damaged area in non-penetration impact tests. At 39 bar, the addition of films reduces the damaged area by improving the interlayer bonding. At 10 bar however, more matrix is created, which already creates a strong interlayer bonding. Adding films to the samples compacted at 10 bar therefore does not yield any additional reduction in damaged area.

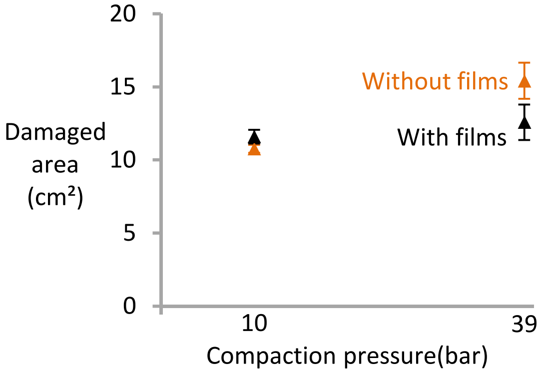

Figure 2-57: The influence of compaction pressure on the damaged area for a 15 J impact event on SRPP compacted for 5 min at 188°C.

Conclusion

Ultrasonic C-scans suffer from the larger deformations that can occur in SRPP. The slope of the indentation can cause detection of damage, while no damage is present. A new technique was developed to avoid these issues. The transmitted light imaging technique is not sensitive to the angle of the indentation and is able to resolve more details of the damage. The limitation of this technique is the requirement for translucent samples. Unfortunately, this technique will not work on hybrid SRCs, as they are either only partially translucent or not translucent at all. The indentation in hybrid SRCs will need to be properly observed to avoid any influence on the C-scans. The dynamic and plastic indentation depth were also identified as alternative techniques to analyse the non-penetration impact resistance.

The damage mechanisms in non-penetration impact were revealed. The main damage mechanism is transverse tape cracking, combined with a limited amount of delamination or debonding. Matrix cracking is not observed, but this damage mechanism is expected to occur further away from the investigated region.

Finally, the influence of process parameters was investigated. Adding films and increasing the compaction temperature reduced the damaged area. The damaged area was also affected by the dwell time. The increased bonding at longer dwell times reduced the damaged area, even though it did not affect any of the other tested mechanical properties. Reducing the compaction pressure had a similar effect: it increased the interlayer bonding and thereby reduced the damaged area.

2.4.3 Conclusion

The impact resistance of SRPP was investigated. The possible testing techniques were analysed and possible pitfalls were identified. The understanding developed in this section is essential for studying the impact resistance of hybrid SRCs in the next chapter.

The impact resistance seems to be more sensitive to the process parameters than the tensile properties (see “2.3.3 Tensile properties”). This is attributed to the fact that tensile properties are dominated by the tape properties, which changes only slightly with the process parameters. Impact resistance on the other hand is strongly influence by the bonding between the layers and tapes, which is known to depend strongly on the process parameters. This conclusion is of great practical importance, as the impact resistance is the main advantage of SRPP over other materials. For a proper comparison among different hybrid SRCs, the processing parameters will need to be the same for all hybrids.

2.5 Influence of weave architecture

The previous section highlighted the sensitivity of hot compaction to the process parameters. As mentioned in “2.1.2 Production of self-reinforced composites”, two other parameters can help to optimise the hot compaction process. The importance of using tapes is well established in the SRC literature, while the weave architecture has hardly been investigated. This influence needs to be understood, as one of the hybridisation strategies will be to co-weave PP tapes with carbon fibre prepregs.

The compaction temperature should be chosen in such a way that sufficient matrix is created to fill all empty spaces. As the volume of empty space depends on the weave architecture, each weave will require a different amount of matrix. The influence of the weave architecture on the mechanical properties will be investigated under the same processing conditions: 5 min at 188°C and 39 bar. The four configurations are described in Table 2-6, together with their sample thickness. Each sample consists of 12 layers of woven cloth, but a 20 μm PP film was added in between each layer for Twill OF-F.

Table 2-6: Overview of the tensile and impact samples for the four configurations.

Label	Tape	Weave pattern	Overfeeding	Films	Thickness (mm)
Twill OF	A	Twill 2/2	Yes	No	1.75 ± 0.3
Plain OF	A	Plain	Yes	No	1.89 ± 0.2
Twill SF	B	Twill 2/2	No	No	1.64 ± 0.1
Twill OF-F	A	Twill 2/2	Yes	Yes	1.96 ± 0.3

The properties of interest are the tensile behaviour, the impact resistance and the peel strength. Before proceeding to the mechanical properties, the production quality will be assessed by DSC and ultrasonic C-scan.

2.5.1 Production quality

To ensure that all samples have experienced the same temperature and pressure cycle, all configurations are verified by DSC. The melting peaks for the four different configurations as well as the PP film are presented in the DSC thermograms in Figure 2-58. The melting peaks of the four configurations are similar, except for the configuration with films (Twill OF-F). No significant differences are found in the melting temperatures (see Table 2-7). Nevertheless, two differences are observed for the configuration with films, which has a lower melting peak and contains a shoulder at about 160°C. The shoulder is caused by the additional matrix created by the films, as can be seen in Figure 2-58. This matrix has a lower crystallinity and less perfect crystals than the tapes. Table 2-7 proves that this results in a slightly lower melting enthalpy for twill OF-F.

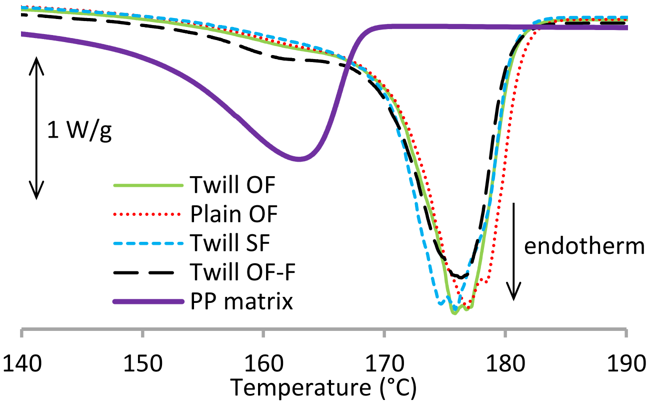

Figure 2-58: DSC thermograms for the different weave architectures. The thermogram for the PP film is added to facilitate comparison.

Table 2-7: Melting temperature and enthalpy for the four configurations.

Label	Melting temperature (°C)	Melting enthalpy (J/g)
Twill OF	176.2 ± 1.2	116.2 ± 3.7
Plain OF	177.5 ± 1.7	119.0 ± 4.3
Twill SF	175.8 ± 0.5	115.0 ± 3.4
Twill OF-F	175.2 ± 1.8	110.7 ± 1.8

The DSC results prove that all configurations were subjected to the same thermal processing and that the results are reproducible. This means that any difference in mechanical properties cannot be directly attributed to a difference in thermal cycle.

A second quality verification tool is C-scan, a technique which is able to assess the compaction quality. The C-scan histograms in Figure 2-59 illustrate the differences in compaction quality. A narrow peak at high intensities is found for the standard fed twill weave. Due to the lack of folded tapes, this weave has a flat surface and does not require much matrix to fill all the voids. For this weave, the hot compaction process created sufficient matrix, resulting in a homogeneous quality.

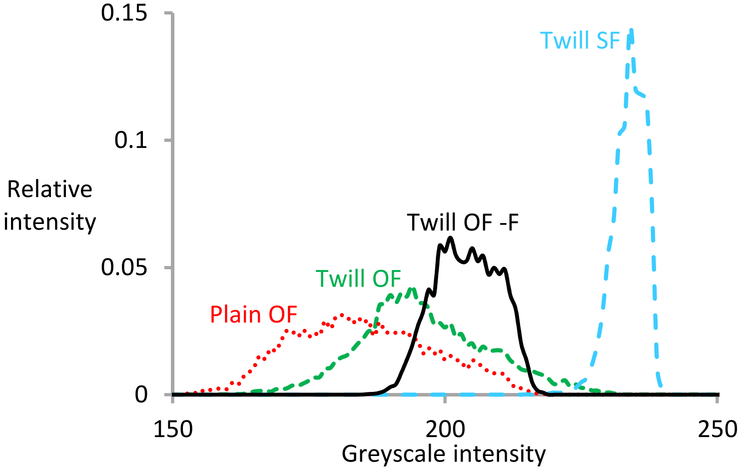

Figure 2-59: C-scan histogram to assess the impregnation quality of the different weave architectures.

The worst compaction quality is found in the plain OF weave. This weave has the highest crimp and requires more matrix to fill up all the voids caused by the overfeeding. The compaction process parameters (188°C, 5 min, 39 bar) were not high enough to fill all the voids, which results in broader histogram at lower greyscale values, see Figure 2-59. The reduced crimp in both overfed twill weaves results in a higher compaction quality. By adding films, the compaction quality can be further increased, as more matrix is created and less voids remain. The additional matrix is still not sufficient to achieve compaction quality as high as in the twill SF. It seems that some of the voids created by the overfeeding can only be filled up if the temperature is further increased. This is undesired, as it will also increase molecular relaxation and decrease the mechanical properties.

In conclusion, these results illustrate that standard feeding and films facilitate achieving sufficient compaction quality, even at lower hot compaction temperatures. Standard feeding results in less voids that need to be filled, while the films provide additional matrix to fill the voids. This decreases the lower temperature limit for hot compaction, which is determined by the compaction quality. The upper temperature limit, which is determined by molecular relaxation and tape melting, can be assumed to be unaffected by the weave architecture or films. This means that, although not directly proven, a wider temperature window for hot compaction is achieved.

2.5.2 Tensile behaviour

Figure 2-60 presents a representative tensile diagram for each of the four configurations. The tensile moduli, calculated between 0.1% and 0.3% strain, are similar for all four configurations, see Figure 2-61a. The only significant difference is found for Twill OF-F compared to Plain OF. Films add more matrix, which reduces the volume fraction of the tapes. The additional films should in theory increase the thickness by 220 µm. This value is close to the 210 µm difference between twill OF and twill OF-F found in Table 2-6. If the stiffness of the film is assumed to be 1.7 GPa, then the linear rule of mixtures predicts a tensile modulus of 3.01 GPa. This prediction lies within the 95% confidence interval of the tensile modulus of twill OF-F, which is 3.06 ± 0.05 GPa.

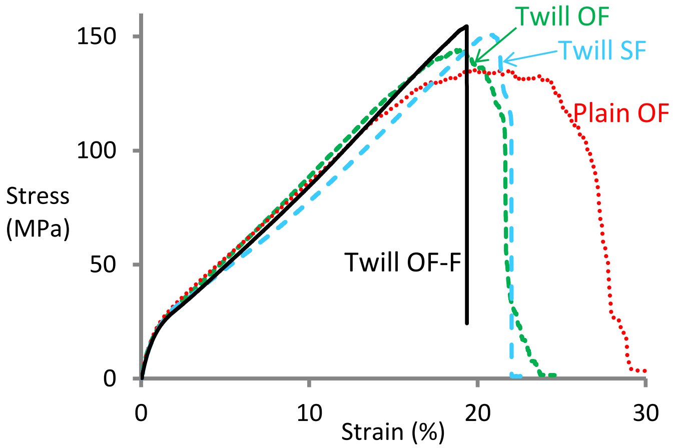

Figure 2-60: Tensile behaviour of SRPP with different weave architectures.

At a stress level of about 20 MPa, all configurations start to yield. This can also be observed in single tape tensile diagrams [32,82], which is an indication that it is not caused by straightening of the tapes. The yielding is caused by the tie molecules which connect the highly oriented crystallites in the drawn tapes. At the yield point, these tie molecules start to flow, which explains the decrease in stiffness. The tie molecules gradually increase their orientation in the tensile direction, and hence the stress further increases. The stiffness reduction in this region is larger for the standard fed twill. The reason for this reduction is unclear.

At 15% strain or higher, deviations from linear behaviour start to appear, which coincides with the appearance of damage in the samples. The damage initiates by debonding of the tapes from the matrix and delaminations in between the layers. Tape fracture is only observed after the stress has reached its maximum. In the plain weave, damage initiates at about 15% strain and the strain interval over which damage is accumulated is more than 15%. In the twill weaves without films, the damage initiation happens a few percent of strain later and over a smaller strain interval. In the samples with films, debonding or delamination is not observed. In samples without films, this can be visually observed by the transition from semi-transparent to white samples. The absence of debonding and delamination leads to a second part of the diagram that remains straight until final failure. This also leads to a higher tensile strength for the twill SF configuration (see Figure 2-61b). The final failure happens suddenly, with hardly any visible damage prior to failure.

Despite the strength differences in Figure 2-61b, Figure 2-61c proves that the strain at which this strength is achieved is the same for all configurations. Finally, Figure 2-61d compares the absorbed energy per volume of loaded material. On one hand, the abrupt failure of the weaves with films results in the smallest energy absorption. On the other hand, the more gradual failure of the plain weave spreads out the damage over a larger strain interval. This results in an increased energy absorption in tension.

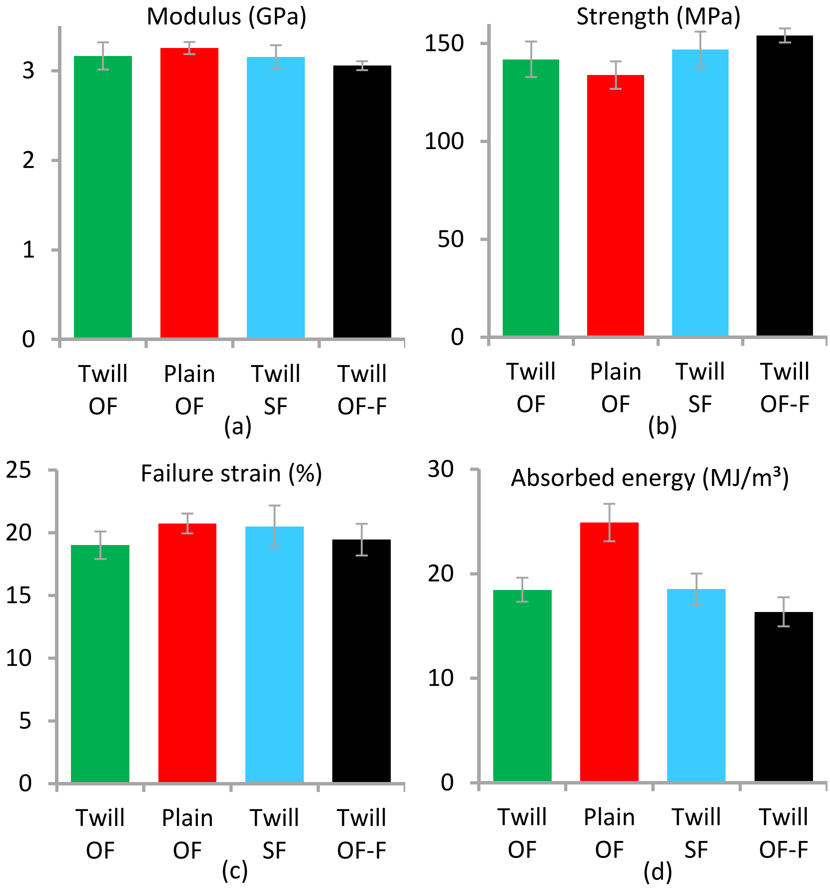

Figure 2-61: Tensile results of different weave architecture: (a) modulus, (b) strength, (c) failure strain, and (d) absorbed energy.

2.5.3 Impact behaviour

On top of the good tensile properties of SRPP, the impact resistance is a vital parameter for many applications. Penetration impact testing has become a standard test procedure to evaluate the impact resistance of SRCs. Figure 2-62 summarises the impact resistance of the different configurations. No significant differences are found in the impact resistance per mm of sample thickness for the weaves without films. As stated by Aurrekoetxea et al. [91] and Alcock et al. [60], the penetration impact resistance of well compacted SRCs is dominated by tape fracture and not by delaminations or debonding.

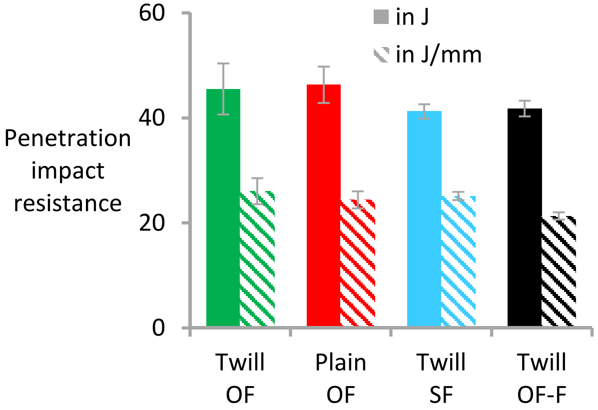

Figure 2-62: Penetration impact resistance per mm of sample thickness and in absolute values.

Twill OF and twill OF-F contain the same number of tapes that can absorb energy. Nevertheless, Figure 2-62 indicates that the twill OF-F has a lower impact resistance per mm thickness. The impact resistance per mm thickness is decreased 18% by the films. This decrease is caused by the two effects. Firstly, Table 2-6 indicates that the additional films increase the sample thickness by 12%. The additional isotropic PP only absorbs a relatively small amount of energy compared to the oriented PP tapes. If the impact resistance is expressed in absolute terms, then the difference reduces to 8%. The p-value of this difference is 8.5% in a two-tailed t-test. Secondly, the films improve the compaction quality by adding more matrix. This increases the strength of the interlayer bonding and reduces the amount of debonding and delamination in impact tests. This decreases the energy absorption during penetration impact. The small difference in absorbed energy confirms that debonding and delaminations only play a small role in the energy absorption during penetration impact tests.

2.5.4 Peel strength

To further understand the tensile behaviour and impact resistance, peel strength tests are performed. This yields information on the force needed to delaminate two layers of the weave. The peel strength relates to mode I type of delamination, in which the force is perpendicular to the crack propagation direction. In impact tests, mode II is dominant, as the delaminations in impact tests are caused by shear stresses. Nevertheless, peel strength is a good measure of the influence of the resistance a material has against delamination. Figure 2-63 illustrates a representative peel load diagram for each configuration, while Figure 2-64 presents the resulting peel strengths.

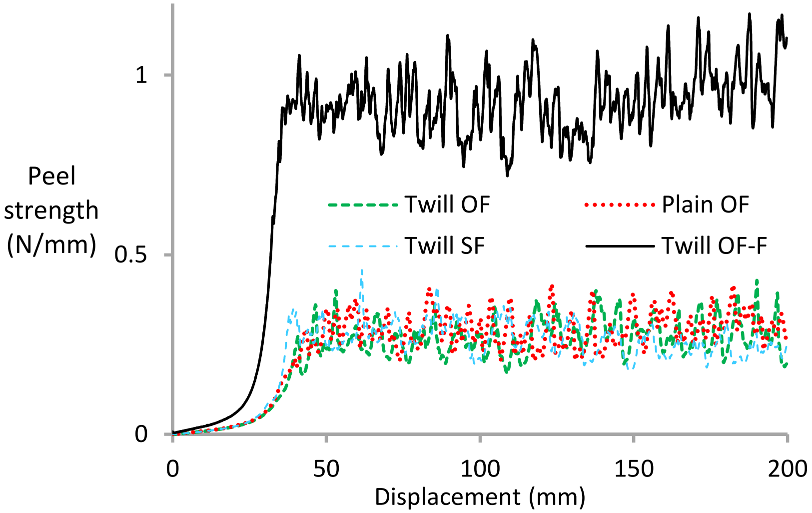

Figure 2-63: Example of a peel load diagram for each configuration, in which peel load is divided by sample width and plotted as a function of displacement.

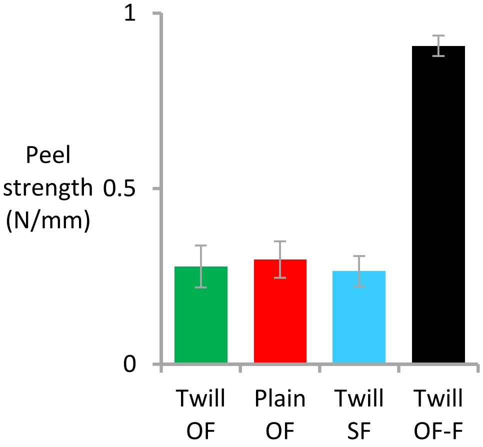

Figure 2-64: Peel strength for each configuration.

No significant differences in peel strength can be discerned for samples without films. On one hand, the twill SF configuration has better compaction quality, which should result in higher peel strength. On the other hand, the twill SF has a flat and smooth surface. Such a surface facilitates delamination and debonding compared to the rough surface of the overfed weaves. These two phenomena seem to balance each other out and result in similar peel strength. This is also confirmed by the stereomicroscopic images of the peel surfaces in Figure 2-65. The white regions reflect the presence of damage created by the debonding and delamination. Most of the damage is concentrated on the transverse tapes, as they are the weakest in the peeling direction.

The configuration with films has significantly higher peel strength, and this is also visible in the peel surface. More white regions are observed in Figure 2-65d and they are also present on the tapes in the peeling direction. This indicates good bonding between the layers and means that films increase the required energy to delaminate SRPP.

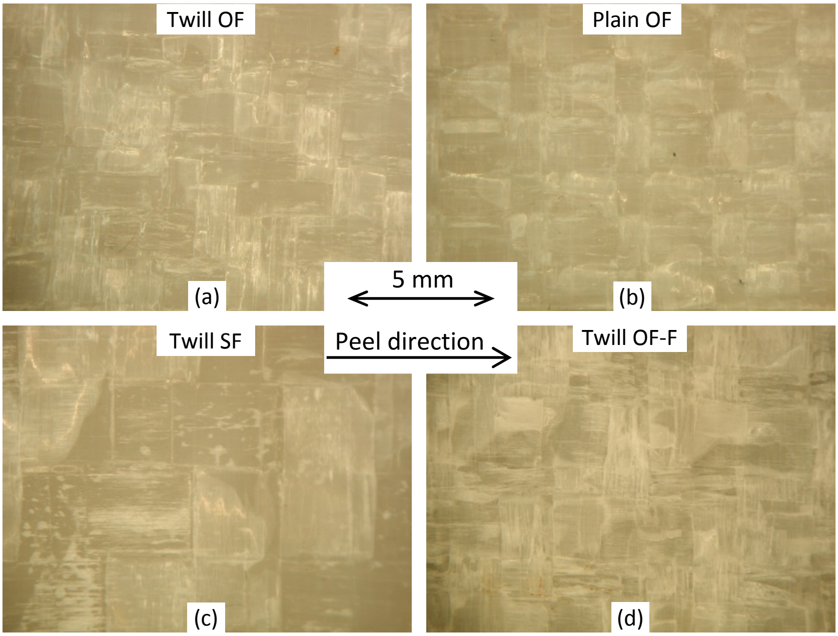

Figure 2-65: Stereomicroscopic images of the peel surfaces of (a) twill OF, (b) plain OF, (c) twill SF, and (d) twill OF-F. The arrow indicates the peeling direction.

2.5.5 Conclusion

The tensile behaviour and impact resistance of hot compacted SRPP was evaluated for three different weave architectures: overfed twill, overfed plain and standard fed twill. The influence of films was also assessed for the overfed twill weave.

- The compaction quality increases with a decrease in the crimp. Lower crimp allows a lower compaction temperature and thereby widens the temperature window for hot compaction. This conclusion is of great practical importance, as it can aid in choosing suitable weaves for hot compaction.
- The tensile behaviour is affected by the compaction quality. Lower compaction quality results in earlier damage initiation, lower strength and more extensive damage. If films are used, the compaction quality is higher and final failure occurs more sudden and at higher stress.
- The penetration impact resistance slightly decreases by adding films, but remains unaffected by the weave architecture.

- The peel strength increases by adding films, but remains unaffected by the weave architecture.

The higher peel strength for the samples with films should reduce the extent of delaminations. Since the films did not significantly affect the impact resistance, it can be concluded that delaminations play only a minor role in the energy absorption during penetration.

For hybrid SRCs, the relative insensitivity of the impact resistance and peel strength to the weave architecture is a vital conclusion. This means that most observed changes can be directly attributed to the carbon fibres, instead of to the altered weave architecture.

2.6 Conclusion

SRPP was investigated with a focus on their tensile behaviour and impact resistance. Both properties are highly sensitive to the processing parameters. While these parameters determine the degree of melting and molecular relaxation, the most important aspect is the change in interlayer bonding. This bonding has a minor influence on the tensile behaviour, but a strong influence on the impact resistance. The interlayer bonding is also known to be crucial for the performance of hybrid composites.

The impact testing procedures for SRCs were critically assessed. In contrast with literature, the penetration impact resistance scaled linearly with sample thickness. The non-linear relationship in literature was attributed to the occurrence of wrinkling and necking as a result of too small samples. These are unwanted energy absorbing mechanisms, indicating that samples should be large enough to avoid these issues. These conclusions facilitate comparisons between samples with a different thickness, which will be unavoidable in hybrid SRCs.

Ultrasonic C-scans may lead to errors in the damage area due to non-penetration impact. If the samples are severely indented, then damage may be wrongfully detected. A novel technique, transmitted light imaging, was developed to study the non-penetration impact resistance of SRCs. Unfortunately, this technique will not work for hybrid SRCs, as translucent samples are required. The final alternative for assessing the non-penetration impact resistance is to measure the indentation depth. This technique should be suitable for hybrid SRCs. MicroCT measurements also revealed the main damage mechanism to be transverse tape cracking. The next chapter will investigate how fibre hybridisation changes the damage mechanisms.

The weave architecture did not have a strong influence on the tensile behaviour and impact resistance. This conclusion is vital for intralayer hybrid SRCs, as the co-weaving process alters the weave architecture. Any observed changes in performance can hence be attributed to the presence of carbon fibres, rather than to changes in the weave architecture.

This chapter was a prerequisite for studying the more complex situation in hybrid SRCs. This chapter developed a fundamental understanding of the mechanical properties of SRPP. This understanding will be crucial in the next chapter to investigate how hybridisation changes these properties.

Chapter 3:

Hybrid self-reinforced composites

Self-reinforced composites will be hybridised with carbon fibres to achieve a better balance between stiffness, strength and toughness. This chapter will illustrate how the mechanical properties of these hybrid self-reinforced composites can be optimised. The initial focus lies on understanding the tensile behaviour of these novel hybrid composites. Later, the flexural behaviour and impact resistance are also investigated. The conclusions from this chapter and chapter 5 will lead to the development of a road map for optimising hybrid self-reinforced composites.

Chapter 2 investigated the processing and mechanical properties of SRPP. In this chapter, carbon fibres are added to SRPP to achieve a better balance between stiffness, strength and toughness. Some work was also performed on hybridising self-reinforced PA with carbon fibre. Most of this work was performed by colleagues from the University of Leeds and will therefore not be reported here. Interested readers can refer to a journal publication on these PA hybrids [116].

The PP tapes and carbon fibre-reinforced polypropylene (CFRPP) prepregs can be combined in several different configurations. The three most important configurations are visualised in Figure 3-1. In the interlayer configuration (see Figure 3-1a), the layers of both fibre types are stacked onto each other. This is the simplest and cheapest method for producing a hybrid composite. In the intralayer configuration on the other hand, the two fibre types are mixed within the layers. This is illustrated in Figure 3-1b, where different yarns are co-woven into a fabric. Other intralayer configurations such as parallel bundles are also possible. The two fibre types can also be mixed or commingled on the fibre level, resulting in an intrayarn hybrid (see Figure 3-1c). More complex configurations can be achieved by combining two of these three configurations. For example, a hybrid yarn can be woven together with a homogeneous yarn.

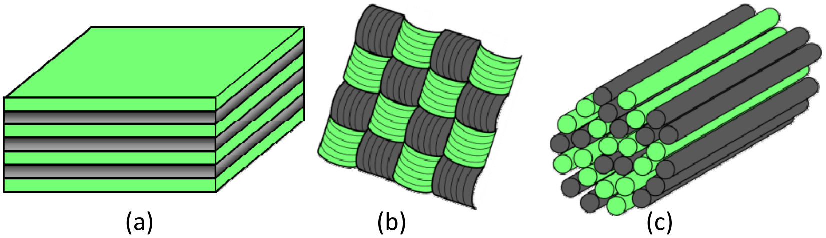

Figure 3-1: The three main hybrid configurations: (a) interlayer or layer-by-layer, (b) intralayer or yarn-by-yarn, and (c) intrayarn or fibre-by-fibre.

All three hybrid configurations in Figure 3-1 were used in this study. The sections of results in this chapter are divided according to these configurations. The subsection "3.2.1 Materials" describes attempts to achieve well mingled carbon fibre/PP intrayarn hybrids. Unfortunately, the state-of-the-art technology does not seem to be capable of producing this. Therefore, the two sections of results focus on interlayer and intralayer hybrids. Figure 3-2 summarises the types of material behaviour that will be investigated in each subsection of results.

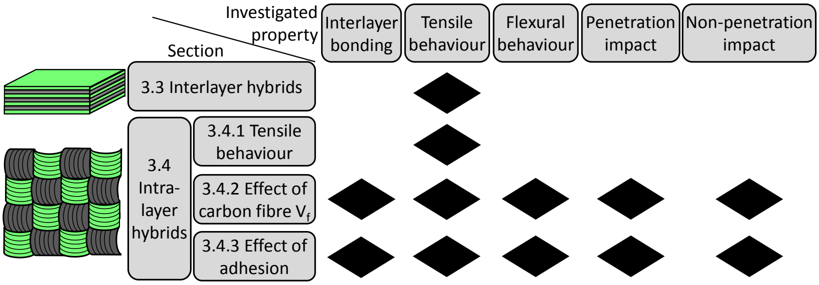

Figure 3-2: Schematic overview of the material behaviour that will be investigated in this chapter.

3.1 State of the art

As mentioned in Chapter 1, the strong need for new lightweight materials with improved toughness revived the research interest in "hybridisation". The term "hybrid composite" is generally used to describe a matrix containing at least two types of reinforcements. This state of the art however is restricted to hybrid composites containing two types of reinforcing fibres. Such composites are also called "fibre hybrids" or "fibre hybrid composites". This review of the state of the art focuses on polymer matrix composites, though some references to hybrid composites with ceramic or metal matrices will be made.

Research on fibre hybrid composites started several decades ago. After the invention of carbon fibres in the sixties [117,118], the high price was their main drawback. Hybridisation became a highly active research area in the seventies and eighties. The objective was mainly to reduce the price, while still exploiting the exceptional properties of carbon fibre. Later, the carbon fibre price dropped significantly [119] and the focus shifted towards improving production technologies and understanding the mechanical behaviour of non-hybrid carbon fibre composites.

The last review paper on the mechanical properties of hybrid composites was written in 1987 by Kretsis [120]. Since then, a much wider range of materials is available and several processing technologies have been invented and improved. This resulted in a renewed interest in hybrid composites as a possible strategy for toughening fibre-reinforced composites.

In general, the purpose of combining two fibre types in a single composite is to maintain the advantages of both fibres and alleviate some disadvantages. For instance, replacing carbon fibres in the middle of a laminate by cheaper glass fibres can significantly reduce the cost, while the flexural properties remain almost unaffected. If a hybrid composite is loaded in the fibre direction in tension, then the more brittle fibres will fail before the more ductile fibres. This fracture behaviour can be used for health monitoring purposes [121] or as a warning sign before final failure [122].

The two fibre types are typically referred to as low elongation (LE) and high elongation (HE) fibres. The first fibre to fail in tension is normally the LE fibre. The HE fibre does not necessarily have a large failure strain, but it is always larger than the one of the LE fibre. This is also the reason why the terminology brittle/ductile fibres instead of LE/HE fibres can lead to confusion.

A crucial aspect in hybrid composites is the dispersion of the two fibre types. This is a measure of how well the two fibre types are mixed and is sometimes defined as the reciprocal of the smallest repeat length [120,123]. Figure 3-3 schematically illustrates the degree of dispersion. Figure 3-3a displays a hybrid with a low degree of dispersion, as the two fibre types are in two distinct layers. This can be improved by decreasing the layer thickness, as illustrated in Figure 3-3b. Another way to increase the dispersion is by hybridising on the fibre bundle level, see Figure 3-3c. The best dispersion is achieved if the two fibre types are distributed completely random, as in Figure 3-3d. It should be noted that the definition for fibre dispersion cannot be applied to a random dispersion as the repeat length cannot be defined.

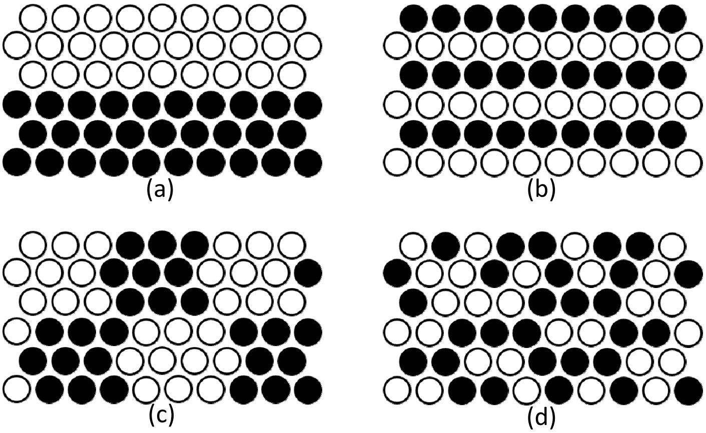

Figure 3-3: Illustration of the various degrees of dispersion: (a) poor layer-by-layer dispersion, (b) fine layer-by-layer dispersion, (c) bundle-by-bundle dispersion, and (d) completely random dispersion.

This review of the state of the art is split up into four subsections. In the first subsection, the synergy between the two fibres, the so-called hybrid effect, will be discussed. The second subsection describes the mechanical properties of composites and how they can be improved by fibre hybridisation. The third subsection provides an overview of the most recent trends in fibre hybridisation. The final subsection gives conclusions as well as recommendations for future work.

3.1.1 The hybrid effect

In 1972, Hayashi [124] reported that the failure strain of the carbon fibre layers in a carbon/glass hybrid composite was 40% higher than in the reference carbon fibre composite. As will be proven in “3.1.2 Tensile properties”, typical values for this remarkable synergistic effect are in the range 10% to 50%.

Various definitions have been coined for this hybrid effect. The most basic definition of the hybrid effect is the apparent failure strain enhancement of the LE fibre in a hybrid composite compared to the failure strain of an LE fibre-reinforced non-hybrid composite. This definition is schematically illustrated in Figure 3-4a and corresponds to Hayashi’s observations [124]. Its calculation requires an accurate determination of the failure strain of the reference carbon fibre composite. This baseline failure strain is often affected by stress concentrations at the grips, while this effect is smaller in hybrid composites. These stress concentrations therefore may cause overestimations of the hybrid effect. It should also be emphasised that calculating the hybrid effect based on the ultimate failure strain of the hybrid composite is not according to the proposed definition. Such improvements in ultimate failure strain may be useful to report, but the terminology “hybrid effect” should be avoided.

Another definition of the hybrid effect, which is able to capture more features, is a deviation from the linear rule of mixtures [125,126]. The advantage of this definition is that it can also be applied to mechanical properties other than failure strain, see Figure 3-4b. Applying this definition however, is not straightforward for three reasons. Firstly, the rule of mixtures is not necessarily linear for all properties. For the tensile strength, the rule of mixtures is bilinear [120,123], while a constant value would be expected for the failure strain of the LE fibre. Secondly, each rule of mixtures needs a certain parameter to define the composition of the hybrid composite. As Phillips [127,128] and Kretsis [120] pointed out, it is vital that the right one is chosen. The relative volume fractions of the LE and HE composites are a good choice, but are not always easy to determine experimentally.

Finally, even though the second definition is more general, it still does not work for all mechanical properties. For example, if the inner layers of a carbon fibre composite are replaced by glass fibre layers, then the flexural modulus would remain almost unaffected. Clearly, linear rules of mixtures would not apply to bending conditions. More advanced theories, such as classical laminate theory, are needed to determine whether a hybrid effect in bending is present or not. This severely complicates the prediction of the hybrid effect, as predictions of the strength and failure strain are difficult in these complex loading conditions.

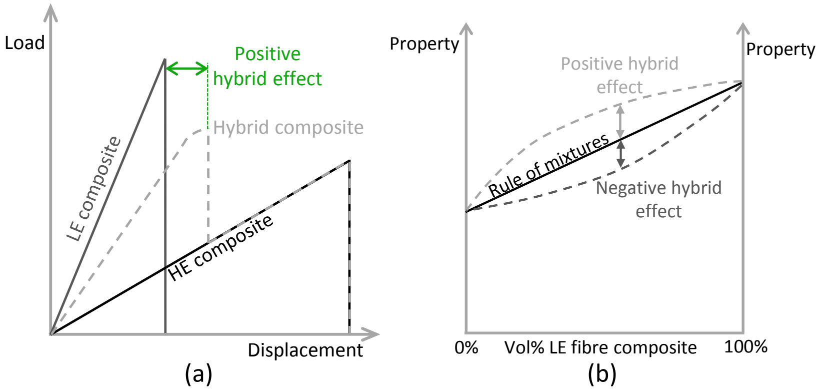

Figure 3-4: Illustration of the definitions of the hybrid effect: (a) the apparent failure strain enhancement of the LE fibres, with the assumption that relative volume fraction is 50/50 and that the hybrid composite is twice as thick as the reference composites, and (b) a deviation from the rule of mixtures.

Controversy and considerable confusion arose in the composites community after Hayashi's report of the hybrid effect for failure strain first appeared [124]. As explained by Phillips [129], some researchers [125,130] did not believe Hayashi's results and thought that the rule of mixtures still applied. The confusion grew by several reports of errors in the way the hybrid effect was determined. Qiu and Schwartz [131] reported that Phillips' baseline for hybrid fatigue resistance [129] was dubious. The failure strain enhancement of 100%, reported by Aveston and Sillwood [132], is quoted by Manders and Bader [123] to be caused by a wrong definition for the failure strain of the hybrid composite. This type of discussions in the seventies and early eighties are well illustrated by Phillips [127,129] and the letter by Marom and Wagner, with corresponding reply by Phillips [128].

The belief in the surprising failure strain enhancement of the LE fibre gradually increased when more experimental data and more convincing theoretical hypotheses became available [133-136]. Three different hypotheses for the hybrid effect have been coined by now: (1) residual stresses, (2) changes in the damage development leading to final failure of the hybrid composite, and (3) dynamic stress concentrations. Most hypotheses have been applied to UD hybrid composites in either the intrayarn or interlayer configuration. These hypotheses can be extended to multidirectional composites, as their failure, although more complex, still coincides with failure of fibres in the loading direction. Therefore, almost all models in literature predict the hybrid effect for UD rather than for multidirectional hybrid composites. The remainder of this subsection discusses the three possible hypotheses for the hybrid effect for failure strain in UD hybrid composites.

Residual stresses

In the first hypothesis, the hybrid effect is attributed to residual shrinkage stresses due to differences in the thermal contraction of the two fibre types. Let us consider the classic combination of carbon fibres and glass fibres in an epoxy matrix. After impregnation of the fibres, the temperature is raised to cure the epoxy. Both fibres will have the tendency to change their length due to their coefficient of thermal expansion (CTE). The CTE of carbon fibre is typically between -1 and $+1.10^{-6}K^{-1}$ [123,137,138], while the CTE of glass fibre is between $+5.10^{-6}$ and $+10.10^{-6}K^{-1}$ [123,139]. This causes the glass fibres to increase their length upon heating, while carbon fibres will more or less maintain their length. This does not yet result in stress build up, as the resin is still liquid.

After the resin is cured and the composite is cooled down, the glass fibres will shrink, while the carbon fibres will more or less maintain their length. This can only occur in a situation without constraints. In reality, the cured resin connects the layers reinforced by different fibre types and prevents them from having a different length. A force equilibrium is established, putting compressive stresses on the carbon fibres and tensile stresses on the glass fibres. These compressive stresses counteract the applied stress and increase the apparent failure strain of the carbon fibres. In contrast, the apparent failure strain of the glass fibres is reduced.

While the thermal effect can contribute to the hybrid effect, it is insufficient to explain the full hybrid effect. This was pointed out by Zweben [133], Manders and Bader [123], and Bunsell and Harris [140]. For example, Zweben hybridised carbon fibres with aramid fibres, which have a lower CTE than that of carbon fibres. This results in residual tensile strains in the carbon fibres. Nevertheless, a positive hybrid effect for the failure strain of the carbon fibres was observed [133]. In all three studies [123,133,140], it is mentioned that the thermal effect can only account for a hybrid effect of 10% according to the definition in Figure 3-4a. This is insufficient to explain reported hybrid effects of up to 50% [120]. Soon, it became clear that other effects are more important.

Failure development

The second hypothesis for the hybrid effect is related to changes in the way failure develops. This can be dealt with in a statistical or a fracture mechanics approach, as explained by Manders and Bader [141]. The fracture mechanics approach deals with a structure that contains a pre-existing crack and determines when it is energetically favourable for that crack to grow. The structural inhomogeneity and anisotropy of fibre-reinforced composites however, make it difficult to use this approach for modelling of the composite strength. Consequently, the statistical approach has received more attention than the fracture mechanics approach.

Consecutive failure of fibres with their stochastically distributed flaws is an intrinsic statistical problem. Fibre strength is indeed not a single, unique value, but is rather a stochastic variable. Often it is assumed that fibre failure is determined by the weakest link, which makes the Weibull distribution an appropriate choice to characterise fibre strength.

The failure development in UD composites is presented in Figure 3-5. An in-depth description will be provided in "Chapter 4: Strength model for UD non-hybrid composites". If all fibres are intact, then the stress is the same in all fibres (see Figure 3-5a). If the strain is further increased, the first fibre will break and locally lose its load carrying capacity. However, this does not lead to composite failure, see Figure 3-5b [142]. After the first fibre break, the surrounding matrix is loaded in shear and transfers stress back onto the broken fibre, which will recover its full load carrying capacity a certain distance from the fracture location. Moreover, the neighbouring fibres will be subjected to stress concentrations and locally take over the additional load caused by the broken fibre [143,144]. These stress concentrations on neighbouring fibres are typically in the range of 5% to 15% [143,145,146] in the plane of the fibre break, but rapidly decrease with increased distance from this fibre break plane.

The stress concentrations lead to an increased failure probability in the neighbouring fibres. When the strain is further increased, this increased probability will lead to the development of clusters of fibre breaks (see Figure 3-5c) [147]. If one of these clusters grows large enough and reaches a certain critical size, then that cluster will grow in an unstable manner and lead to final failure (see Figure 3-5d) [148].

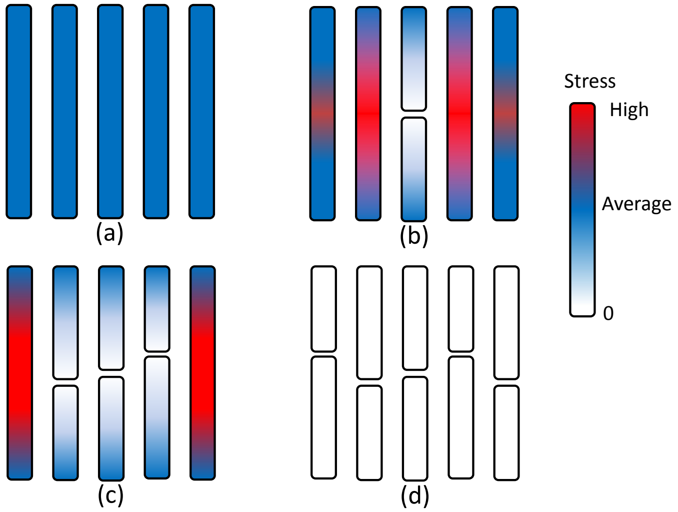

Figure 3-5: Schematic representation of the failure development in UD non-hybrid composites: (a) all fibres intact, (b) one broken fibre, with the surrounding fibres subjected to stress concentrations, (c) development of a broken fibre cluster, and (d) crack propagation and final failure.

Hybrid composites can interfere with this damage development process at several stages. Firstly, the stress concentrations in the intact fibres as well as the stress recovery in the broken fibre can be altered if the LE and HE fibre have a different stiffness or diameter [133]. Secondly, the broken LE fibres can be bridged by the HE fibres [120,149], which does not only hinder the development of the clusters, but can also increase the critical cluster size. The remaining LE fibre fragments will have a higher failure strain, as their weakest link just got eliminated [149]. Thirdly, a size scaling effect can occur. The increasing failure strain of non-hybrid composites with decreasing sample size is now well established [150,151]. This effect can also increase the apparent failure strain of hybrid composites compared to the reference LE composite. More specifically, if an LE/HE fibre hybrid composite is compared with an LE fibre composite of the same volume, then the volume of LE fibres is lower in the hybrid composite, and hence its failure probability is lower.

Dynamic stress concentrations

Some authors have also stressed the importance of dynamic stress concentrations in the failure of UD composites. When a fibre breaks, the load on that fibre is locally relaxed and the fibre springs back. This creates a stress wave travelling along each fibre, causing a temporary increase in the stress concentration. This was first pointed out by Hedgepeth in 1961 [152], and later confirmed by Ji et al. [153]. Hedgepeth used a shear-lag approach to prove that the dynamic stress concentrations are 15% to 27% higher than the static stress concentrations. Hedgepeth mentions the limitations of the shear-lag approach to study these dynamic phenomena. Matrix plasticity and deviations from unidirectionality are mentioned to reduce the dynamic stress concentrations. Ji et al. [153] further extended Hedgepeth’s model to dynamic stress concentrations along the fibres, rather than just at the plane of the fibre break.

Xia and Ruiz [154] predicted the dynamic stress concentration factors to be 20% higher in glass fibre composites than in carbon fibre composites. This indicates that these two fibre types behave differently under dynamic loading. An explanation for this was not provided by Xia and Ruiz, but is most likely caused by the higher longitudinal modulus of carbon fibre. The difference cannot be attributed to the anisotropy of carbon fibres compared to the isotropy of glass fibres, as this was not taken into account in the model.

An extension towards hybrid composites was performed by Xing et al. [155]. These authors considered hybrid composites composed of one row of LE and one row of HE fibres. Their theoretical model demonstrated that two independent stress waves develop and propagate through the hybrid composite when an LE fibre breaks in a hybrid composite. The first wave propagated in the LE layer, while the second one propagated in the HE layer. Both waves were always out-of-phase, which led to lower stress concentrations in LE/HE fibre-reinforced hybrid composites compared to those in LE fibre-reinforced composites. From this point of view, dynamic stress concentrations will always have a positive contribution to the failure strain enhancement of the LE fibre in a hybrid composite.

Unfortunately, this hypothesis for the hybrid effect and dynamic stress concentrations in general remain poorly investigated. This topic has received no attention at all in the past two decades. More refined models are required to advance the understanding in this area.

Conclusion

After the early discussions about 40 years ago, the existence of the hybrid effect for failure strain is now well established, but not thoroughly understood. Three explanations have been coined by various researchers to explain this hybrid effect. The thermal effect is easy to understand and predict, but is limited in magnitude. Dynamic stress concentrations have only rarely been investigated, but may have an important contribution and hence merit more attention. The statistical effect is expected to be the largest effect, but is more complex to predict.

3.1.2 Tensile properties

The previous subsection described the hybrid effect and how it can lead to improved mechanical properties. This subsection describes experimental measurements of the mechanical properties and analyses how they can be maximised.

Tensile modulus

The longitudinal tensile modulus of hybrid composites has been proven to obey a linear rule of mixtures [120,124,125,129,130,140,156]. Values deviating from this behaviour can in most cases be attributed to variations in the fibre volume fraction or fibre orientation. This is for example the case in Ren et al. [157], who reported a higher modulus for intralayer than for interlayer UD carbon fibre/carbon fibre hybrids. The small reported deviations are likely caused by crimp, fibre misorientations or measurement inaccuracies in the fibre volume fraction.

Alternatively, as reported by Phillips [127,128], some deviations can also be explained by an incorrect use of the rule of mixtures. The relative volume fractions of both constituent fibres should be used as composition parameter, but these are often difficult to measure separately in hybrid composites. Estimates based on ply fraction or tow fraction are easier to obtain, but they do not necessarily depend linearly on the fibre volume fraction. This is for example the case if the fibre volume fractions in LE and HE tows are different. In this case, the rule of mixtures would not be linear.

Hybrid effects may not be expected for the longitudinal tensile modulus, but can still occur in the transverse direction, where rule of mixtures are not linear and often less accurate. Taketa [158] demonstrated a positive hybrid effect for the transverse tensile modulus of UD carbon fibre-reinforced polypropylene (PP) hybridised with woven SRPP. This is explained based on the high Poisson's ratio of the SRPP, which means it has a high tendency to shrink in the transverse direction during a tensile test. This transverse direction coincides with the stiff carbon fibres, which counteract the Poisson contraction. As a consequence of the additional constraints, the composite as a whole behaves stiffer than expected from the linear rule of mixtures.

Tensile failure strain

The first definition of the hybrid effect (see Figure 3-4a) was based on the apparent failure strain enhancement of the LE fibre in a hybrid composite compared to the failure strain of an LE fibre-reinforced non-hybrid composite. This hybrid effect has been extensively studied in the past and was also the subject of the first report of a hybrid effect in 1972 [124]. As explained earlier, this hybrid effect was the subject of scientific discussion in the seventies and eighties [127-129]. Currently, the failure strain enhancement is well established in literature. In a review paper, Kretsis [120] analysed literature data prior to 1987 and clearly demonstrated that the hybrid effect increased with decreasing LE fibre content. An overview of the hybrid effect reported in literature can be found in Figure 3-6 [123,124,132,133,140,149,159-165].

A typical range of the hybrid effect for failure strain is 10-50%, though some outliers have been reported. Based on the data reported in Chamis et al. [166], Kretsis [120] calculated negative hybrid effects down to -66%. These results were discarded as unrealistic values, although the exact reason is unknown. Aveston and Sillwood [132] reported a hybrid effect of +116% in carbon/glass interlayer hybrids, but this is mainly due to an unreasonably low failure strain for their carbon fibre reference composite.

A vital caveat for interpreting the literature data that Kretsis [120] gathered is that these data are more than 25 years old. At that time, carbon fibre had a lower failure strain, sometimes even below 1% [124,132] or even below 0.4% [140], and a higher scatter on the fibre strength [119]. As will be proven in the state of the art section of "Chapter 5: Modelling of hybrid composites", both changes in carbon fibre properties are known to increase the hybrid effect. The hybrid effect in hybrid composites with the current carbon fibres are hence expected to be smaller than in the early reports.

Diao et al. [162] recently reported a failure strain decrease of 8% in commingled T700-IM7 carbon fibre/carbon fibre hybrid composite compared to the reference IM7 carbon fibre composite. This decrease was attributed to surface damage introduced by the co-mingling process. The small difference in the failure strains of both fibre types may explain the lack of a positive hybrid effect.

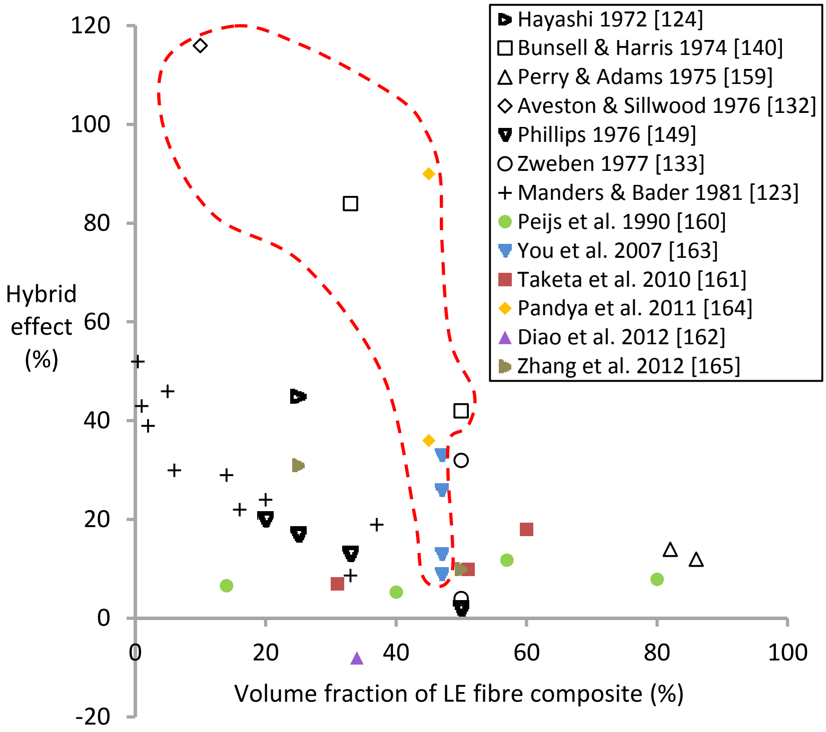

Figure 3-6: The hybrid effect for tensile failure strain as a function of the volume percentage of the LE fibre composite. Data from before Kretsis' review in 1987 are in black, while the others are coloured. Data which has to be interpreted with care can be found within the red dashed region.

Pandya et al. [164] reported a hybrid effect of +36% and +90% for a carbon/glass hybrid composite. Since the relative content of carbon fibre was 47% and the degree of dispersion was low, these results are surprisingly higher than the trends predicted by Kretsis [120]. Moreover, the hybrid effect was increased from +36% to +90% by putting the carbon fibre layers as inner plies rather than outer plies. Their tensile diagrams do not display a vertical drop, which would coincide with failure of the carbon fibre plies. Instead, Pandya et al. [164] achieved a gradual failure, but still used the ultimate failure strain to calculate the hybrid effect. This does not conform to the definition of hybrid effect based on the apparent failure strain enhancement of the LE fibre composite. From their data, it was not possible to deduce the hybrid effect using the proper definition.

You et al. [163] reported a hybrid effect of 9-33% in UD carbon/glass hybrids. The highest hybrid effect was achieved when the fibres were well dispersed. You et al. obtained a failure strain of only 1.25% for UD T700 carbon fibre composites. In our opinion, this surprisingly low failure strain for their reference T700 composites might be partially due to the testing conditions. This would mean that the reported effect may be partially caused by the fact that the hybrid composite is less sensitive to the testing conditions. Their results therefore need to be interpreted with care. Moreover, You et al.

used the ultimate failure strain to calculate the hybrid effect and do not mention whether this coincides with failure of the carbon fibres. Again, it was not possible to deduce the hybrid effect using the proper definition.

Zhang et al. [165] hybridised woven glass and carbon fibre and found improvements in failure strain, ranging between 10 and 31%. The failure of the carbon fibre layers coincided with final failure of the hybrid composite and no further load carrying by the glass fibre layers was observed. This remaining load carrying capacity was observed by several other authors [122,124,140]. It is unclear which parameters are exactly required to maintain this load carrying capacity after the carbon fibre failure, though interlaminar bonding [140] and dispersion [122] have been proven to play a crucial role.

In general, most of the reported values are positive. The values of Bunsell and Harris [140], Aveston and Sillwood [132], Pandya et al. [164], You et al. [163] are found within the red dashed line in Figure 3-6. These values have to be interpreted with care, as they may be affected by improper testing of the reference composites or an improper definition of the hybrid effect. From Figure 3-6, it cannot be concluded that the hybrid effect has decreased compared to before 1987, even though this is expected from theoretical considerations.

Tensile strength

According to many authors, the hybrid effect for tensile strength is based on a bilinear rule of mixtures (see Figure 3-7a) [120,123,167,168]. This prediction is based on a displacement controlled test, in which iso-strain is assumed for both the LE and HE fibres. For simplicity of this explanation, the contribution of the matrix is neglected. It inherently assumes that the failure strain of the LE fibres is a deterministic value, and that its failure does not affect the HE fibres.

Based on their failure strains, the LE fibres fail first, followed by the HE fibres. After the LE fibres have failed, they are assumed to fully delaminate or debond from the HE fibres. The LE fibres hence stop carrying stress, leaving only the HE fibres as load carrying elements. As would be the case in a tensile test, the initial cross-sectional area would still be used to convert load into stress. Two possibilities arise after the LE fibre failure, depending on whether the fraction of HE fibres is high or low. At high fractions of HE fibres, the stress is able to reach levels higher than the stress at the failure strain of the LE fibres, as illustrated in Figure 3-7b. The strength will hence be dominated by the stress contribution of HE fibres at their failure strain, which is represented by the line ACE. At low fractions of HE fibres, these fibres also continue to carry stress, but in this case, the stress at HE failure does not exceed the stress at the failure strain of the LE fibres. This is illustrated in Figure 3-7d. The strength in this region is hence determined by the line BCD, which represents the stress in the hybrid when the LE fibres break. The minimum in this bi-linear rule of mixtures occurs when both peaks in the tensile diagram have the same height, as in Figure 3-7c.

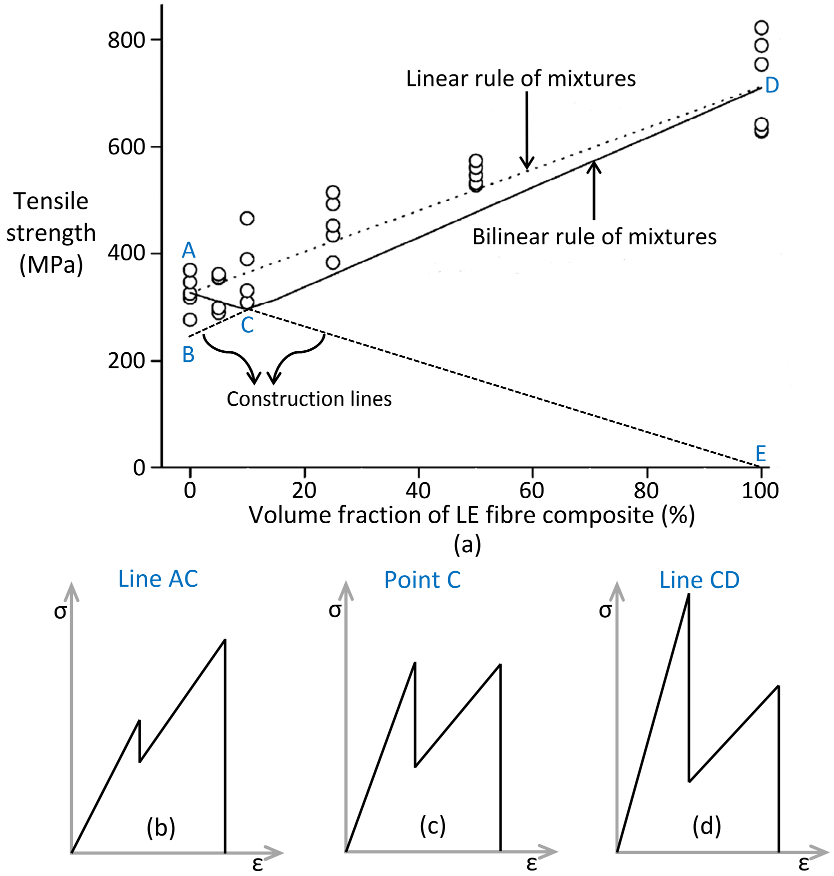

Figure 3-7: (a) Illustration of the bilinear rule of mixtures for the tensile strength of carbon/glass hybrid composites (adapted from Shan and Liao [169], with permission from Elsevier), and corresponding tensile diagrams of hybrid composites for (b) line AC, (c) point C, and (d) line CD.

Figure 3-7 also contains experimental data points for carbon/glass hybrid composites from Shan and Liao [169], indicating that the bilinear rule of mixtures does not yield a satisfactory prediction. A similar positive deviation from the bilinear rule of mixtures was found in Peijs et al. [160].

If both fibres are linearly elastic, then the tensile modulus follows a linear rule of mixtures in the fibre direction. If one observes experimentally that the failure strain is enhanced, then the tensile strength should also be enhanced. This is not as straightforward as it seems. The reason for the failure strain enhancement is often a more gradual failure, meaning that the last part of the tensile diagram is not linear anymore. In some cases, the tensile diagram even has a plateau near the end [122,162].

Zhang et al. [156] found that the ultimate tensile strength of UD glass/flax composites increased by 15% if the dispersion was improved. Ren et al. [157] observed a small but negative hybrid effect by combining two different types of carbon fibres in a single composite. The tensile strength for intralayer hybrids was slightly higher than for interlayer hybrids, demonstrating that increased dispersion leads to better mechanical performance in hybrid composites.

Conclusion

Accurately measuring the hybrid effect requires precise tensile tests on the hybrid composite as well as on the reference carbon fibre composite. Most of the reported hybrid effects were found in unidirectional composites, which are even more difficult to test than multidirectional composites. Therefore, the baseline strength or failure strain of the carbon fibre reference composites is doubtful in several publications. Stress concentrations at the grips may be less detrimental in hybrid composites than in non-hybrid composites. This could lead to an overestimation of the hybrid effect.

Special care should be taken in the sample preparation and the tensile testing setup to ensure a suitable failure away from the grips. Accurate descriptions of the tensile testing procedure and the observed failure mechanisms are highly recommended. This is required to allow a proper interpretation of the reported test data and advance the state of the art.

3.1.3 Flexural properties

Flexural properties of hybrid composites strongly depend on the lay-up, as the stress at the neutral line is zero, but increases away from that line. Hybrid composites yield additional possibilities to optimise the mechanical performance by not only changing the ply angles, but also by changing the material type of each ply.

This also makes the flexural properties of hybrid composites more difficult to interpret than the tensile properties. Just like the tensile modulus, the flexural modulus can be predicted rather well. While simple rules of mixture apply to tensile moduli, the classical laminate theory is commonly used to predict flexural moduli. This part of the state of the art will therefore focus on flexural strength rather than modulus.

Basic effects

The ratio of compressive strength over tensile strength differs for carbon and glass fibre composites. Wonderly et al. [170] for example reported a ratio of 0.73 for glass fibre composites. This ratio was only 0.34 for carbon fibre composites, which may be attributed to their smaller diameter, anisotropic nature and higher stiffness difference with the matrix. These values however may not be generally applicable. They are known to strongly depend on two factors: (1) the carbon fibre type [171] and (2) how well the fibres are supported against buckling. Nevertheless, it may be possible to increase the flexural strength of a composite by replacing carbon fibres in the outer ply on the compressive side by glass fibres. This can potentially lead to large hybrid effects.

Flexural tests do have an advantage over tensile tests: they are not influenced by gripping artefacts. Flexural strength may however be affected by other artefacts, such as stress concentrations at the rollers and difficulties in accurately measuring stresses [172,173]. Size effects are also known to be significant in flexural strength of non-hybrid composites [174,175]. Wisnom et al. [174] pointed out that the strain or stress gradients may be the main contributor to the size effect in flexure. The underlying assumption is that large stress or strain gradients provide larger support of the outer layers by the inner layers. The distribution of stress gradients in hybrid composites can be rather complex in hybrid composites due to the different stiffness of the layers. The literature on hybrid composites has not given any attention to these phenomena. Their importance in determining the hybrid effect is therefore unclear.

Results

Dong et al. [176] obtained experimental flexural strengths for carbon/glass intralayer hybrids, which are 40% and 9% higher than the full carbon and full glass reference composites. The achieved strength for the hybrids was higher than the values predicted by both finite element analysis and classical laminate theory.

Similarly, Giancaspro et al. [177] noticed that glass fibre composites failed on the tension side, while carbon fibre composites failed mainly on the compression side. Adding carbon fibres on the tension side of glass fibre composites increased the flexural strength, while this was not the case when they were added on the compressive side. Adding carbon fibre on the compressive side changed the failure mode from failure in the tension side to crushing on the compression side. Davies et al. [178] demonstrated that replacing 12.5 vol% of carbon fibres on the compression side by silicon carbide fibres increased the flexural strength by 22%. Davies et al. is suggested that silicon carbide fibres have a compressive-to-tensile strength ratio similar to glass fibres and hence, higher than that for carbon fibres.

According to Giancaspro et al. [177] and Dong et al. [179], an optimal level of glass fibre exists to achieve maximum flexural strength. Dong et al. [179] stated that the highest flexural strength in carbon/glass hybrids was achieved at a relative content of 12.5% of glass fibres, all of which are placed on the compressive side. A symmetric lay-up is hence not the optimal design for a hybrid composite that will be subjected to flexural loads [176,179]. A further optimisation revealed that the flexural strength can be further improved if the fibre volume fraction within the glass fibre layers is higher than in the carbon fibre layers [179].

Many authors have investigated the flexural behaviour of hybrid composites with natural fibres. These authors often limited themselves to improving the mechanical and physical properties compared to those of the natural fibres. As expected, hybridisation mostly leads to performance in between the performance of both fibre types, but most research in this area lacks a clear assessment of the hybrid effects and the intrinsic mechanisms controlling it. Some authors reported lower than expected flexural properties due to problems with adhesion and lack of good interface quality [180-182]. Improving the adhesion by surface treatments improved flexural strength in coir/silk hybrid composites [182], in banana/glass fibre hybrid composites [183].

Conclusion

The flexural properties of hybrid composites have received relatively little attention in literature. The stress state of hybrid composites in flexural loading can be complex, which makes interpretation of flexural tests difficult. Further research is needed to identify appropriate testing and analysis methods, and understand how hybrid composites can be optimised for flexural performance.

3.1.4 Impact resistance

Falling weight impact resistance of hybrid composites has been extensively investigated, as toughening is one of the key reasons for fibre hybridisation and impact resistance is strongly related to toughness. The focus lies on falling weight impact resistance, where the composite is impacted in the transverse direction. Charpy and Izod impact tests are less relevant for composite applications. Falling weight impact resistance can be characterised in three ways: energy absorbed during a penetration impact, damaged area after a non-penetration impact event and residual properties after impact. These three properties are governed by different mechanisms and hybridisation will have a different effect on each of them. Hence, it will always be indicated which type of impact was performed on the described hybrids.

In hybrid composites, the lay-up is closely linked with the dispersion and determines the positioning of the layers, both of which are known to be important parameters for impact. In the most common configuration, namely interlayer, the dispersion is completely determined by the lay-up. Therefore, this subsection is split up according to these two parameters: positioning of layers and dispersion.

Positioning

The positioning of the layers in an interlayer hybrid composite is crucial, as this will change the flexural stiffness and strength. These properties are important for transverse impact on a composite plate, and will also influence the type of damage mechanisms. An overview of how various impact properties are affected by the positioning of the layers in symmetric lay-ups is given in Table 3-1. The corresponding information for asymmetric lay-ups is summarised in Table 3-2.

Table 3-1: Overview of how various impact parameters are affected by placing the LE fibre more towards the middle layers in symmetric lay-ups. Empty cells indicate that the property was not characterised.

Ref.	Year	Fibres	Penetration impact resistance	Damaged area	Repeated impact
Kowsika & Mantena [184]	1999	Carbon/glass	improved		
Naik et al. [185]	2001	Carbon/glass		deteriorated	
Sevkat et al. [186]	2009	Carbon/glass	improved	deteriorated	
Sevkat et al. [187]	2010	Carbon/glass			improved
Enfedaque et al. [188]	2010	Carbon/glass	improved		
González et al. [189]	2014	Carbon/glass		improved	

Table 3-2: Overview of how penetration impact resistance is affected by putting the LE fibre closer to the compression side in asymmetric lay-ups.

Ref.	Year	Fibres	Penetration impact resistance
Jang et al. [190]	1989	Carbon/aramid	no effect
Jang et al. [190]	1989	Carbon/PE	deteriorated
Jang et al. [190]	1989	Carbon/PET	deteriorated
Park & Jang [191]	2001	Carbon/glass	improved
Onal & Adanur [192]	2002	Carbon/glass	deteriorated
Sayer et al. [193]	2010	Carbon/glass	improved

Sayer et al. [193] made asymmetric interlayer hybrids of carbon and glass fibres. By this asymmetric lay-up, it becomes possible to test the glass layers and the carbon layers on the tension side, without changing the lay-up. If the carbon layers are on the compression side, then the penetration impact resistance was increased by 30%. Park and Jang [191] did similar tests on asymmetric aramid/carbon hybrids, and found a higher penetration impact resistance if the carbon was on the compression side. This allowed the aramid layers, which are on the tensile side of the sample, to absorb more energy. This improvement largely disappeared when the aramid fibres were surface treated to improve adhesion. Park and Jang mentioned that most energy was absorbed through delamination in the aramid layers, although there is no direct evidence to back up this statement.

Jang et al. [190] investigated asymmetric aramid/carbon fibre hybrids with only two layers and did not find a significant improvement depending on which layer was on the compression side. This was attributed to the similar impact behaviour of both reference composites, which seems surprising for such dissimilar fibre types. Replacing the carbon fibres with polyethylene (PE) fibres did result in an influence. Putting the more ductile PE fibres on the compression side increased the impact resistance by about 50% compared to when they were on the other side. Similar results were achieved for carbon with PET fibres. These results suggest that putting the HE fibres on the compression side is beneficial. This can be attributed to a difference in damage mechanisms. Since the impact face is loaded in compression and the other face is loaded in tension, the damage mechanisms can be different. Surprisingly, the conclusions of Jang et al. [190] seem to contradict with the conclusions of Sayer et al. [193] and Park and Jang [191]. This is most likely caused by differences in the damage mechanisms, which are triggered by differences in the materials and their interfaces. Understanding this relationship is challenging, but crucial for optimising hybrid composites for impact loading. It should also be noted that the samples from Jang et al. showed signs of necking and wrinkling. The subsection “2.4.1 Penetration impact resistance” proved that these unwanted mechanisms may also affect the penetration impact resistance.

Enfedaque et al. [188] and Sevkat et al. [186] found that symmetric carbon/glass hybrids had a better penetration impact resistance if the glass was put on the outside rather than on the inside. Both authors attributed this to the higher failure strain of the glass fibres, which delays the onset of damage. Another confirmation was given by Sevkat et al. [187], who found that damage accumulation after repeated impact tests in carbon fibre-reinforced composites is slowed down by adding glass fibres and especially when they are added as outside layers. Onal and Adanur [192] found similar improvements in the penetration impact resistance of carbon/glass hybrids. Sevkat et al. [186] reported that the damaged area in their carbon/glass fibre hybrids was higher than in both reference composites. This was attributed to a greater susceptibility to delaminations due to the incompatibility of the layers.

De Cuyper [194] hybridised steel fibres with SRPP, both of which have a failure strain of 15-20%, and investigated their penetration impact resistance. It is one of the only studies that combined two fibres with such high ductility. De Cuyper found that putting the steel fibres on the outside improved the penetration impact resistance, as these fibres reach higher stresses for the same failure strain.

Naik et al. [185] reported that the compression-after-impact strength of carbon/glass hybrids was higher than that of both reference composites. Interestingly, the highest values were reported for the hybrids where the carbon was on the outside. This confirms the results of Kowsika and Mantena [184], who concluded that hybrids with carbon on the outside perform better in compression after impact based on the failure index parameter that they defined. Their parameter was defined as the relative ratio of energy required for damage initiation to the total absorbed energy. Their initiation energy is based on the first significant deviation from linearity in the force-displacement diagram. This initiation energy is lower if the carbon fibres are put on the outside, as they have a lower failure strain combined with a higher modulus compared to the glass fibres. This results in a higher failure index, which led the authors to believe that carbon on the outside is bad for the penetration impact resistance of the hybrid composites.

All these data are summarised in Table 3-1 for symmetric lay-ups and Table 3-2 for asymmetric lay-ups. Table 3-1 proves that penetration impact resistance can be improved by placing the LE fibres in the middle of symmetric lay-ups. For the other properties, the conclusions are less clear, as there are either conflicting or insufficient data in literature. As is clear from Table 3-2, no clear conclusion on the influence of positioning of the layers in asymmetric hybrid composites on the penetration impact resistance has been reached in literature.

The importance of the position of the LE and HE layers has also been investigated and confirmed on hybrid composites without carbon fibres. Pavithran et al. [195] hybridised glass fibres with sisal fibres, in which sisal is the LE fibre and glass the HE fibre. Pavithran et al. found that Charpy impact energy increased when moving the LE fibres to the inside, which confirms the trend for penetration impact resistance of carbon/glass hybrids in Table 3-1. De Rosa et al. [196] confirmed that putting the stronger basalt fibres on the outside improved the post-flexural strength in basalt/glass hybrids. Transferring conclusions from one hybrid to the other is however difficult due to the lack of theoretical framework. Despite being the LE fibre, sisal fibres have a lower strength than the glass fibre in the study of Pavithran et al. It is currently unclear how this strength would affect the conclusions.

Dispersion

Sarasini et al. [197] demonstrated that well-dispersed glass/basalt hybrid composites have a smaller damaged area after a non-penetration impact event and a higher post-impact flexural strength than the glass fibre and basalt fibre reference composites. This was attributed to the occurrence of multiple small delaminations in the well-dispersed hybrids compared to extensive fibre breaks or delaminations on the compression side in the less dispersed hybrids. The same authors confirmed these results on aramid/basalt fibre hybrids [198].

De Rosa et al. [196] also demonstrated that a well-dispersed glass/basalt hybrid possessed a higher post-impact flexural strength, which was mainly attributed to the higher flexural strength prior to the impact event. De Rosa et al., however, also found a disadvantage of well-dispersed hybrids: acoustic emission detected a more extensive and complex damage development during post-impact flexural tests.

Park and Jang [199] observed that interlayer aramid/polyethylene (PE) fibre hybrids possessed a higher penetration impact resistance than the corresponding intralayer hybrids. This was attributed to the delaminations which developed easier in the interlayer hybrids than in intralayer hybrids. The intralayer hybrids do have a smaller delaminated area, which should in principle result in better post-impact mechanical properties.

Peijs et al. [200] demonstrated an improvement in penetration impact resistance at higher degrees of dispersion of polyethylene and carbon fibres. In these interlayer hybrid composites, delaminations typically occur at the interfaces between dissimilar layers. Well-dispersed interlayer hybrids have more of these interfaces, which can delaminate and thereby absorb more energy. Other authors have therefore investigated thin plies as a way to increase the number of interfaces in non-hybrid composites [201-203]. Thin plies have only rarely been used in hybrid composites, even though they are potentially interesting materials [122].

Conclusion

A lot of data are available on the impact performance of hybrid composites and how it is affected by the dispersion and the positioning of the layers. Increased dispersion seems to increase non-penetrating impact resistance and residual properties in hybrid composites. Some evidence has been presented that indicates that penetration impact resistance also increases with dispersion. Positioning the fibres with the highest energy-absorption potential on the outside allows the hybrid composite to absorb more energy.

3.1.5 Current trends

In the early days, the focus of research on hybrid composites was on increasing the failure strain of the LE fibres and reducing the material cost by replacing carbon fibres by cheaper fibres. Significant failure strain enhancements are difficult to achieve and, according to the models, are more likely to be achieved with intrayarn hybrids. While cost reduction remains an important driver, the focus has now shifted to achieving either a better balance in different material properties or properties that are not present in the constituents. Hence, these are the trends found in recent literature: pseudo-ductility, ductile fibre hybrids and natural fibre hybrids.

Pseudo-ductility

Traditional fibre-reinforced composites have excellent mechanical properties combined with a low density. Their failure is abrupt and catastrophic, and comes without a warning, see Figure 3-8a. Hidden damage, such as delaminations or matrix cracking, can lead to lower than expected strength of the composite structure. This behaviour leads to large safety factors and sub-optimal use of composites. Hybridisation can be employed to achieve a controlled and more gradual failure in brittle fibre-reinforced composites. This behaviour is termed pseudo-ductility, as it resembles the ductile behaviour typically found in metals. This type of behaviour has already been described in the seventies and eighties by several authors, among which Bunsell and Harris [140] and Manders and Bader [123,141].

The theoretical stress-strain diagram of a hybrid composite is displayed in Figure 3-8b and has a characteristic load drop when the brittle fibres break. By controlling the damage mechanisms, however, it is possible to achieve a more gradual failure and hence pseudo-ductility, as illustrated in Figure 3-8c [122]. Another possibility is that the HE fibres break due to the energy released by the LE fibre failure. This would cause a stress-strain diagram similar to Figure 3-8a.

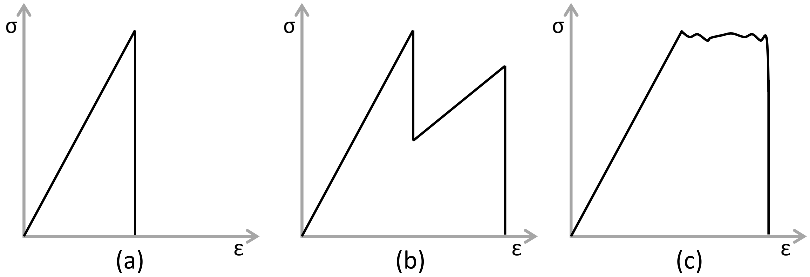

Figure 3-8: Schematic stress-strain diagrams for (a) non-hybrid composites, (b) typical hybrid composites, and (c) pseudo-ductile hybrid composites.

There is a growing interest in pseudo-ductile material systems. This is driven by a strong need to reduce the safety factor in the design of composites and the corresponding need for increased toughness. Pseudo-ductility can also be achieved by controlling the damage mechanisms in non-hybrid composites [204,205], but the focus here is on pseudo-ductility in hybrid composites.

Czél and Wisnom [122] sandwiched a 29 µm thin layer of UD carbon fibre-epoxy in between thicker layers of glass fibre-epoxy on each side. By making the carbon fibre layer thin enough, a change in the material behaviour was observed. The carbon fibre layer is able to break several times along the length of the sample, before the glass fibre layers break. For their specific material combination, an upper limit of 60 µm for the carbon fibre layer thickness was determined both experimentally and theoretically. Further understanding of this phenomenon was performed by Jalalvand et al. [206], who developed a finite element model for these thin ply hybrid composites. This model included the possibility of multiple cracks in the carbon fibre plies, as well as delamination in between the carbon and glass plies. This led to the development of damage mode maps with relative thickness and absolute thickness on x and y-axis (see Figure 3-9), depicting four quadrants, each of which represent a different failure behaviour of the hybrid composite.

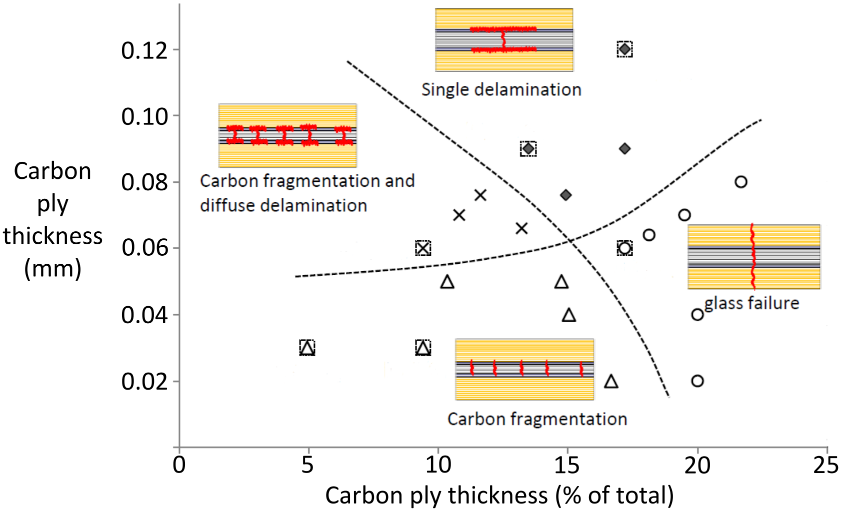

Figure 3-9: Damage mode map for carbon/glass hybrid composites. The experimental data points are marked with an additional square marker (reprinted from [206], with permission from Elsevier).

Jones and Dibenedetto [207] achieved pseudo-ductile behaviour by finely dispersing carbon fibres with glass or aramid fibres. They calculated an upper limit of 92% improvement in the apparent strength of the carbon fibres if all carbon fibres acted independently from each other. This high value could only be achieved at carbon fibre volume fraction below 6%. The importance of fine dispersion for pseudo-ductility is also shown by Bakis et al. [208] on pultruded rods. Pseudo-ductility was only achieved for their most finely dispersed carbon/glass hybrid, while lower dispersion resulted in two distinct peaks as in Figure 3-8b.

Somboonsong et al. [209] achieved pseudo-ductility in hybrid bars, by braiding and pultruding carbon and aramid yarns. The various stress drops were attributed to yarns breaking and transferring their stress to the other yarns. Based on their models, Somboonsong et al. could show that the braiding architecture was important in achieving this pseudo-ductility. A larger braiding angle for the outer yarns reduced the tensile modulus, but increased the pseudo-ductility.

Liang et al. [210] demonstrated that carbon/glass rods break at the failure strain of the carbon fibres when the fibres are well dispersed. Some degree of pseudo-ductility is claimed when all the glass fibres were put on the inside. Their tensile diagrams resemble the one in Figure 3-8b and therefore should not be called pseudo-ductile. Liang et al. also manufactured hybrid composites with the same carbon/glass ratio of 21/79, but with a lower dispersion. Interestingly, the increased dispersion allowed the glass fibres to continue to carry load after the carbon fibre failure. Liang et al. suggest that damage to the glass fibres by the failure of the carbon fibres was limited by the lower dispersion.

Pseudo-ductility has so far only been achieved in composites with a low LE fibre volume fraction. Bunsell and Harris [140] and Manders and Bader [123] did succeed in achieving pseudo-ductility at relatively high carbon fibre fractions, but this was mainly due to the weak carbon fibres in the seventies and eighties. The carbon fibre peak in their hybrids was lower than their glass fibre peak, making it easier to achieve pseudo-ductility. With the strength of the state-of-the-art carbon fibres, the easiest way to reduce the height of the carbon fibre peak in a hybrid is to reduce the carbon fibre volume fraction. Furthermore, it has not yet been proven that improved tensile behaviour also leads to improvements in other mechanical properties, such as fatigue or impact resistance. So far, the research has focused on tensile behaviour.

Ductile fibres

An alternative way of achieving higher failure strains in hybrid composites is to combine brittle fibres with ductile fibres. A large difference in failure strain of the fibres may lead to larger hybrid effects [133] and may lead to increases in energy absorption. In the early literature on hybrid composites, however, carbon fibres were hybridised with either glass or aramid fibres. While these fibres indeed have a larger failure strain than carbon fibres, it is still relatively low. In the past decades, however, ductile fibres for polymer composites have become increasingly popular. Examples include steel [211,212], PP [32], PE [160,213], PA [214], PVA [215], coir [216-218] and silk [182] fibres.

Pegoretti et al. [215] combined glass with PVA fibres. For their interlayer hybrids, better tensile properties were achieved when the glass fibre layers were put in between the PVA layers. The best tensile properties were achieved with intralayer hybrids. The difference in failure strain of both fibres was, however, relatively small, as the failure strain of the PVA fibre composite is, in relative terms, only 10-30% higher than that of the glass fibre composite.

Fibres with a larger difference in failure strains were used by Taketa et al. [161], who combined carbon fibre-reinforced composites with ductile PP fibres. Hybrid effects of up to 18% for failure strain were achieved, but the load carrying capacity of the PP fibres was destroyed by the sudden and explosive carbon fibre failure.

While most literature data deal with hybrid composites with at least one brittle fibre type, the study of De Cuyper [194] investigated the potential of hybrids with two ductile fibre types. De Cuyper hybridised annealed steel fibres with self-reinforced composites in an interlayer fashion. While the tensile strength was according to the expectations, the tensile stress was found to be higher than expected at a given strain. This feature was attributed to the large difference in Poisson contraction of both materials. This difference creates a biaxial stress-strain state in the hybrid, which increases the tensile stress at a given longitudinal strain.

Thysen [212] investigated interlayer hybrid composites of ductile steel fibres and glass fibres. Similar to Czél et al. [122] and Jalalvand et al. [206], Thysen achieved multiple fractures in the LE fibre layers, which are the glass fibres in this case. This only worked when the glass/steel ratio was low. Moreover, a finer dispersion led to smaller delamination lengths, but also to a smaller ultimate failure strain. The same study also investigated the influence of the matrix on the mechanical performance of the hybrid composites. An epoxy matrix led to delaminations, while a similar lay-up with polyamide matrix showed strain localisation around the location of the broken glass fibre layer. These differences in delamination resistance led to higher ductility in the epoxy matrix hybrid than in the polyamide matrix hybrid.

By adding ductile fibres, the ductility of brittle fibre composites can be increased. Larger differences in failure strains seems to lead to more interesting results.

Natural fibre hybrids

The largest boom in hybrid composite publications in the last decade occurred in the field of natural fibre hybrids, mainly driven by environmental concerns. As detailed in the recent review papers by Jawaid and Khalil [219] and Nunna et al. [220], natural fibre hybrid composites are often a combination of a natural fibre with another natural fibre [181,182,221-223] or with a glass fibre [195,217,221,224-230]. Hybridisation with glass fibres is more common, as it allows larger improvements in mechanical properties. If natural fibres are hybridised with glass fibres, the glass fibres will typically improve most mechanical properties, and at the same time reduce property variability, moisture sensitivity, and increase durability and impact resistance. Reports on natural fibre hybrids with carbon fibres are rare [219]. This is most likely due to (1) the large difference in price and stiffness between natural and carbon fibres, and (2) the higher life cycle cost of carbon fibres compared to glass fibres.

When two natural fibres are combined, then the focus lies on getting a better balance in mechanical, chemical and physical properties, rather than on optimising the hybrid effect. Another reason is that research in natural fibre composites often deals with random mats and short fibres, which make hybrid effects more difficult to find.

The lay-up of natural fibre hybrids has been extensively investigated [216,221,231-233]. In most of these reports, the focus lies on improving the properties with respect to the natural fibre reference composite. This does not necessarily imply that hybrid effects are found, as evidenced from the definitions provided in Figure 3-4. The existence of hybrid effects is focused on less in natural fibre hybrid research. Ahmed and Vijayarangan [231] investigated the influence of the stacking sequence on tensile, shear and flexural properties for woven jute/glass interlayer hybrids. The best flexural properties were found when the glass fibre was positioned at the outer layers, as glass fibres have better mechanical properties than the jute fibres. Amico et al. [232] and Khalil et al. [233] reached the same conclusion for interlayer hybrids composed of random mats of sisal/glass and oil palm empty fruit bunch/glass, respectively.

Khalil et al. [233] demonstrated that the impact resistance was higher if the glass fibres were positioned in the middle, although no clear reason for this was given by the authors. Sreekala et al. [229] demonstrated that the Izod impact resistance was higher in hybrid composites than that of the reference glass composites and that of the reference oil palm empty fruit bunch composites.

Ahmed and Vijayarangan [231] found a 10% increase of the tensile strength for woven jute/glass interlayer hybrids by increasing the dispersion. Even though tensile properties are generally not affected by the lay-up, Jawaid et al. [221] noticed a slightly higher tensile strength if the jute layers were positioned on the outside of the oil palm empty fruit bunch layers.

A common problem in natural fibre hybrids is the adhesion. Investigations of the proper fibre treatments for hybrid composites are common in literature [182,230,233-236]. These treatments mainly improve the performance of the natural fibre layers on its own, and do not show synergistic effects.

3.1.6 Conclusion and outlook

The hybrid effect for tensile failure strain is now well established and recognised for traditional hybrid composites such as carbon/glass or carbon/aramid. The three basic mechanisms, namely residual stresses, altered failure development and dynamic effects, have been identified and are qualitatively understood

Tensile properties of hybrid composites are reasonably well understood. The mechanical properties under more complex loading conditions, such as in flexural or impact tests, are not well understood and sometimes even result in apparent contradictions for both the conclusions and mechanisms. More work is needed in this area to clarify the intrinsic mechanisms and to streamline the conclusions.

Despite these issues, hybrid composites are attracting an ever-growing attention from both academia and industry. Fast-growing subfields, such as pseudo-ductility, ductile fibres and natural fibre hybrids, are expected to play an important role in the new developments of hybrid composites. These subfields are pushed forward by an ever-increasing variety in available materials and processes. More research is needed to fully exploit the potential of metallic and polymer fibres. Processes such as tow spreading and comingling have reached a certain maturity for non-hybrid composites, and open new opportunities for hybrid composites. These processes will further widen the applicability of hybrid composites in the future.

3.2 Materials and methods

3.2.1 Materials

PP materials

The description of the PP-based materials can be found “2.2.1 Materials” and will not be repeated here. For subsections “3.4.2 Effect of carbon fibre volume fraction” and “3.4.3 Effect of adhesion”, a black version of the uncoloured PP tape was provided by Propex Fabrics GmbH (Germany). No significant differences in mechanical properties were found between the black and uncoloured tapes.

UD CFRPP prepregs

Three different types of UD CFRPP prepregs were sourced. Table 3-3 summarises the manufacturer, width, thickness, fibre volume fraction and slitting method. The prepregs are labelled according to their thickness: 300 µm, 160 µm or 60 µm prepregs. All prepregs contain T700 carbon fibres, but their exact PP grades are unknown. The 300 µm and 160 µm prepregs contain homopolymer PP, while the 60 µm prepregs contain maleic anhydride polypropylene (MAPP) to improve adhesion [237].

The 300 and 160 µm prepregs were available in a 50 mm and 100 mm width respectively. The 300 µm prepregs were manually slitted by tearing the prepregs along the fibre direction, which was facilitated by the low adhesion between carbon fibre and PP. The 160 µm were automatically slitted by Spoolex (France), but further details are not available. The 60 µm were available in a 5 mm wide version directly from the manufacturer and no further operations were required.

Table 3-3: Summary of the three UD CFRPP prepregs used in this study.

	#1	#2	#3
Manufacturer	Toray Carbon Fibres Europe (France)	Jonam Composites (United Kingdom)	Mitsuya (Japan)
Thickness (µm)	300	160	60
As-received width (mm)	50	100	5
Slitted width (mm)	2.5	3	5
Slitting method	Manual	Automated	Automa
Carbon fibre V_f (%)	45 ± 1	32 ± 1	46 ± 2
Used in (sub)section	3.3 & 3.4.1	3.4.2	3.4.3

Figure 3-10 presents microscopic images of their cross-section. The 300 µm prepregs show a homogeneous distribution of the carbon fibres, but do have some unimpregnated regions (see black regions in Figure 3-10a). The 160 µm prepregs have an excellent impregnation, but have two drawbacks: (1) the carbon fibres are bundled together and (2) matrix-rich regions are found near the surface of the prepregs. The 60 µm prepregs show an excellent impregnation, but do have a large variability in the local V_f and the distribution of the carbon fibres.

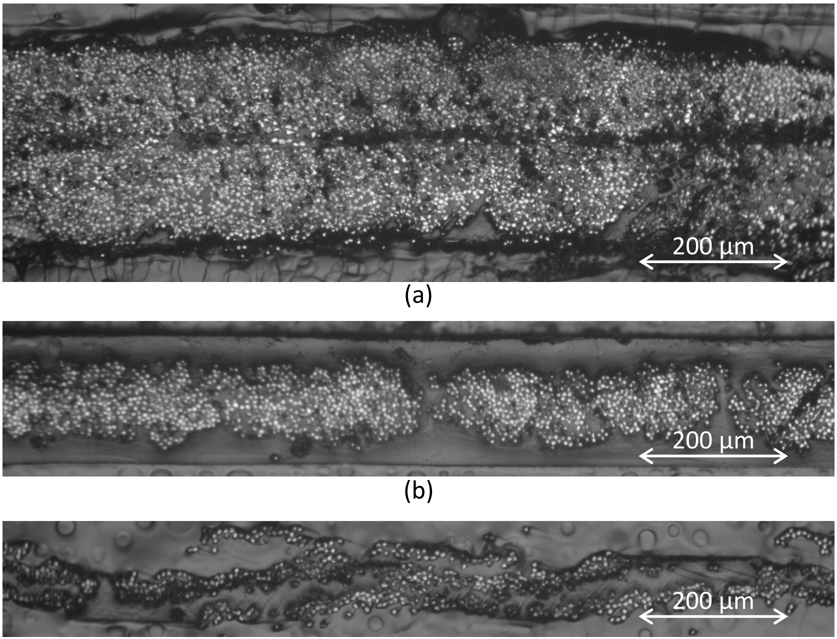

(a)

(b)

(c)

Figure 3-10: Microstructures of the three types of prepregs: (a) 300 µm prepregs, (b) 160 µm prepregs, and (c) 60 µm prepregs. The boundary between prepreg and embedding material is not always clearly visible, especially for the 60 µm prepregs.

Carbon fibre weaves

A balanced plain weave Textreme 80PW was sourced from Oxeon (Sweden). The weave has an areal density of 90 g/m², of which 80 g/m² is UTS50S carbon fibre and the rest is an epoxy binder. This weave hence contains a different type of carbon fibre than the T700 in the UD prepregs. This should not affect the results as the radius, longitudinal stiffness and average failure strain are the same for both fibre types.

Intrayarn hybrids

Finally, attempts were made to achieve well mingled carbon/PP yarns to explore the intrayarn configuration. A collaboration was set up with North Thin Ply Technology (Switzerland) to create mingled plies of PP fibres with carbon fibres. The idea was to spread out both fibres together, hoping that they would mingle during the spreading process. This was unfortunately not the case (see Figure 3-11). Comfil (Denmark) and Carr Reinforcements (United Kingdom) were also contacted as they are both commercial commingling companies. Their attempts to achieve good commingling quality with carbon/PP or carbon/glass were unsuccessful.

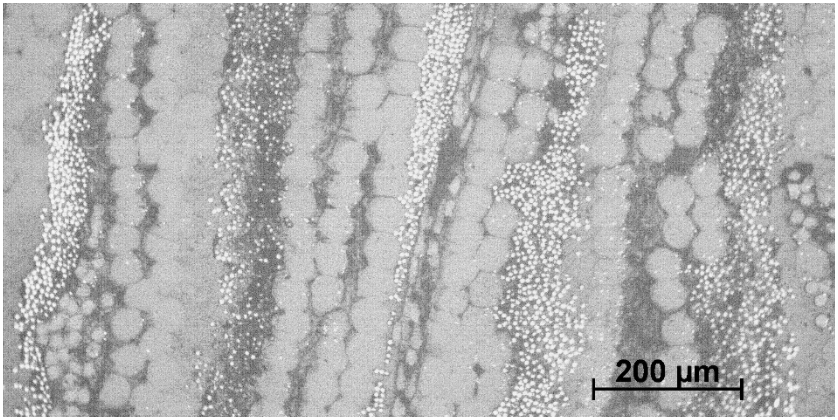

Figure 3-11: Microscopy image of the unsuccessful attempt to achieve mingled hybrids by spreading out thin plies of PP and carbon fibres together. The small, bright fibres are carbon fibres, while the large ones are PP fibres.

3.2.2 Weaving

PP tapes were co-woven with CFRPP prepregs to create intralayer hybrids. Initially, this weaving was performed on a hand loom, but later this was scaled up to an automated pilot loom at Propex Fabrics GmbH.

An important difference between both weaving approaches is the folding of PP tapes and CFRPP prepregs, which is a typical phenomenon in automated tape weaving. The folding effect on the mechanical properties was found to be small for SRPP (see “2.5 Influence of weave architecture”). It therefore seems safe to assume that the SRPP properties in hybrid SRPP are not significantly affected by folding either.

In all cases, the warp direction was composed of only PP tapes, while some of the weft PP tapes are replaced by CFRPP prepreg tapes. Three main iterations were studied:

- Hand weaving with 300 µm thick prepregs
- Pilot-scale weaving with 160 µm thick prepregs
- Pilot-scale weaving with 60 µm thick prepregs

These three woven cloths will be used in this order in the three subsections of section “3.4 Intralayer hybrids”.

300 µm prepreg handwoven weaves

For the hand-weaving trials, 1 out of 4 tapes in the weft direction was a 300 µm thick CFRPP prepreg. This ratio was chosen to yield an overall CFRPP tape volume fraction of around 50% in the final composite sheet, which is equivalent to a carbon fibre volume fraction of 23.5%. Two weave patterns were made to assess the influence of the weave pattern and crimp on the tensile behaviour. To achieve a large difference between both patterns, a plain weave was compared to a satin 8/3 weave (see Figure 3-12a and b). The plain weave pattern has the highest possible crimp of all standard weave patterns. The satin 8/3 pattern has a low number of cross-overs and hence a low crimp. After hot compaction, each layer will have an average thickness of around 130 µm. As reference material, a plain weave without carbon fibre prepregs was also woven on the hand loom (see Figure 3-12c).

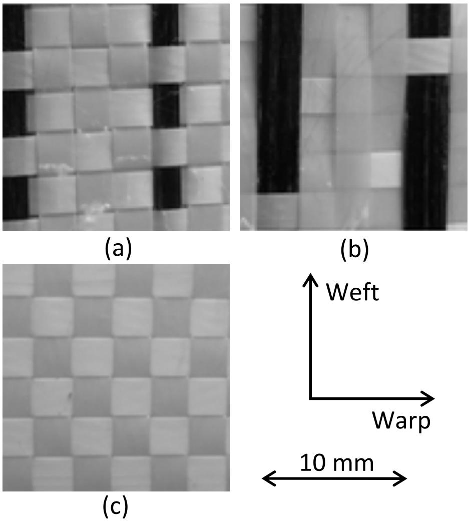

Figure 3-12: The hybrid fabric of PP tapes and CFRPP prepregs (a) plain hybrid weave, (b) satin hybrid weave, and (c) reference PP plain weave.

160 µm prepreg pilot loom weaves

After the first successful hand weaving trials, the co-weaving was scaled up to an automatic pilot loom. The weave pattern was a modified twill 2/2 pattern. The PP tapes were woven into a twill 2/2 pattern, but the 160 µm CFRPP prepregs were only interlaced with this pattern every four tapes (see Figure 3-13). This modified pattern was used for two reasons:

- The CFRPP tapes can be put further away from the neutral line, which should lead to lay-ups with improved flexural properties.
- The fewer interlacing points reduce the crimp in the CFRPP tapes, which should lead to better surface quality.

For the first pilot scale weaving trials, the 160 µm prepregs were used. The idea was to aim for a lower carbon fibre V_f than for the 300 µm prepregs. This was achieved by replacing 1/13, 1/7 and 1/3 of the PP tapes by CFRPP prepreg tapes (see Figure 3-13). This resulted in carbon fibre volume fractions of 3.4% ± 0.1%, 6.9% ± 0.2% and 11.0% ± 0.4%, respectively. Therefore, these hybrid cloths will be referred to as 3%, 7% and 11% cloth.

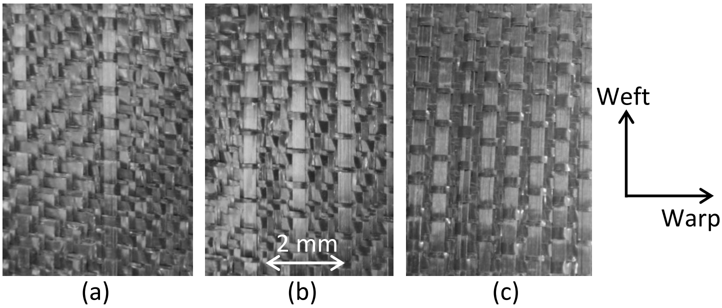

Figure 3-13: Photographs of the intralayer hybrid weaves with 160 µm prepregs: (a) 3% cloth, (b) 7% cloth, and (c) 11% cloth. The carbon fibres are oriented vertically.

60 µm prepreg pilot loom weaves

For the second pilot-scale weaving trials, the 60 µm prepregs were used. The idea of these tapes is that their thickness is close to the thickness of the PP tapes, which should help to avoid out of plane undulations. These tapes however contain MAPP as matrix, as homopolymer PP prepregs were not available in such low thickness.

Two hybrid cloths were produced where 1/8 and 1/3 of the PP tapes were replaced by CFRPP prepreg tapes. This should result in a V_f of 5% and 11% respectively. Based on previous experience, the 5% would yield an optimal value based on previous experience, while the 11% would allow a direct comparison with the 160 µm prepreg hybrids. However, these thin prepregs folded more than expected during weaving, resulting in carbon fibre volume fractions of 7.0% ± 0.2% and 15.7% ± 0.6%, respectively. Therefore, these hybrid cloths are referred to as 7%MA and 16%MA cloths (see Figure 3-14). The “MA” is added to highlight the MAPP in the prepregs and to distinguish with the 160 µm prepreg cloths. The final width of the prepregs in the hot compacted sheets varies between 2.5 and 3.5 mm.

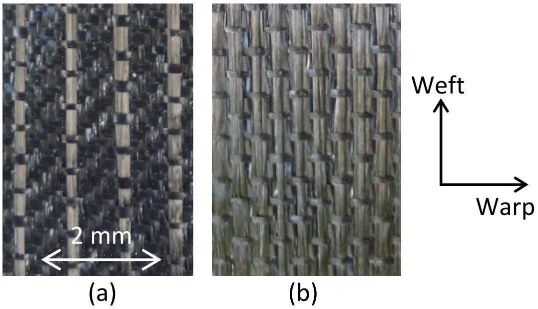

Figure 3-14: Photographs of the intralayer hybrid weaves with 60 µm prepregs: (a) 7%MA cloth, and (b) 16%MA cloth. The carbon fibres are oriented vertically.

3.2.3 Hybrid composite production

The production of hybrid composites follows the same procedure as described in “2.2.2 Hot compaction”. The optimised hot compaction process parameters were used for all hybrid samples: 5 min at 188°C and 39 bar. No films were added, unless otherwise mentioned. This subsection focuses on how the samples were prepared and stacked prior to hot compaction.

Prepregs

The optimal processing conditions for hot compaction are not optimal for impregnating carbon fibre yarns with PP. Therefore, all CFRPP materials were already impregnated prior to hybridisation with SRPP. On one hand, the UD prepregs were sourced in their impregnated form. On the other hand, the carbon fibre weave had to be impregnated in a hot press at 220°C using a 50 μm PP film on one side of the weave. The pressure was alternated between 1 and 10 bar every minute for a total of 10 min to aid impregnation. Despite the high viscosity of PP, this processing cycle resulted in prepregs with an excellent impregnation (see Figure 3-15). This impregnation is facilitated by the final thickness of only 104 μm, which limits the required impregnation length. This thickness corresponds to about 6 fibres through the thickness of each yarn (see Figure 3-15).

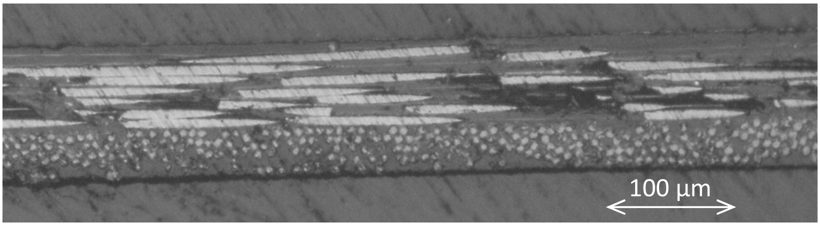

Figure 3-15: Microscopy picture showing the excellent impregnation of the woven CFRPP. Lighter regions correspond to the carbon fibres, which are elliptical for the 90° layer and circular for the 0° layer.

Interlayer hybrids

Different interlayer hybrids of SRPP and CFRPP were produced. The UD CFRPP prepregs used in this case were the 300 μm prepregs in the as-received width of 50 mm. Table 3-4 summarises their lay-up and carbon fibre (CF) volume fraction. “*S*” and “*C*” indicates SRPP and CFRPP layers respectively, while superscripts “w” and “u” indicate woven and unidirectional preforms, respectively. The $S_xC_yS_xC_yS_x$-layups were chosen to yield sufficiently thick samples, while still having a reasonable dispersion. This however prevented very low carbon fibre volume fractions. Therefore, the lowest carbon fibre volume fractions in each configuration were achieved by grouping the carbon fibre layers together in a $S_xC_yS_x$-layup. The values of “x” and “y” in these layups were chosen to yield a similar thickness for the SRPP and CFRPP layers in all combinations of woven and UD layers.

Lay-ups were made by stacking the layers on top of each other. In case of UD SRPP, the tapes were wound onto a 10 mm thick frame (see Figure 3-16) using a winding machine. Each translation of the machine creates one S^u layer on the top and one S^u layer on the bottom of the frame, with an opening of 10 mm in between them. Winding was interrupted at appropriate time intervals to insert the CFRPP prepreg layers.

Figure 3-16: Photograph of the frame used for winding PP tapes.

In contrast with non-hybrid SRPP and intralayer hybrid SRPP, the interlayer hybrids were produced in a copper channel mould (see Figure 3-17). The upright edges were needed to prevent flow of the material at the edges. Spacers were not used in this mould nor were they used anywhere else. Hot compaction was performed at 188°C for 5 min at 45 bar pressure, followed by cooling down to 40°C in 5 min.

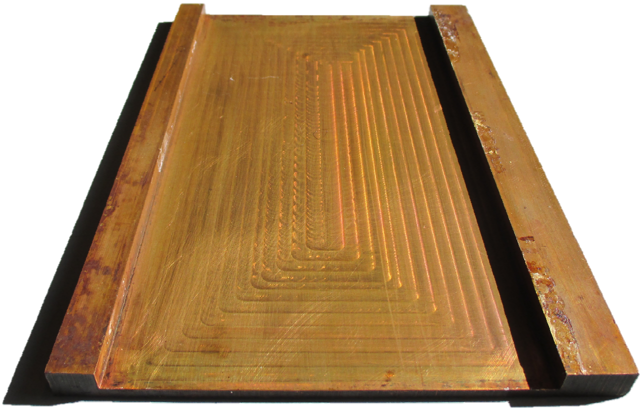

Figure 3-17: Photograph of the channel mould with upright edges on the left- and right-hand side. A top plate is used that just fits between these edges.

The CFRPP reference composites were produced with the same process parameters, but at 5 bar pressure instead of 45 bar. This lower pressure reduces material flow out of the mould and thus limits carbon fibre undulations. The higher pressure for the other lay-ups was required to overcome the intrinsic PP tape shrinkage during hot compaction.

Table 3-4: Identification of the lay-ups, with the measured thickness and overall carbon fibre volume fraction. The carbon fibre volume fraction in the loading direction was obtained by dividing the overall fraction by two in case of woven CFRPP.

CFRPP	SRPP	Lay-up	Thickness (mm)	Carbon fibre volume fraction	
				Overall	in 0° direction
UD	/	C_5^u	1.38 ± 0.02	45% ± 2%	45%
Woven	/	C_{10}^w	1.04 ± 0.02	43% ± 1%	21%
/	UD	S_{20}^u	1.57 ± 0.03	0	0
/	Woven	S_{16}^w	2.35 ± 0.01	0	0
UD	Woven	$S^wC^uS^wC^uS^w$	0.90 ± 0.04	29% ± 1%	29%
		$S_3^wC^uS_3^wC^uS_3^w$	1.79 ± 0.03	13% ± 1%	13%
		$S_6^wC^uS_6^wC^uS_6^w$	3.12 ± 0.02	10% ± 2%	10%
		$S_9^wC^uS_9^w$	2.97 ± 0.04	5.0% ± 2.1%	5.0%
Woven	Woven	$S^wC_2^wS^wC_2^wS^w$	0.85 ± 0.03	20% ± 1%	10%
		$S_3^wC_2^wS_3^wC_2^wS_3^w$	1.71 ± 0.03	11% ± 1%	5.5%
		$S_6^wC_2^wS_6^wC_2^wS_6^w$	3.06 ± 0.06	7.2% ± 0.5%	3.6%
		$S_9^wC_2^wS_9^w$	2.90 ± 0.05	4.7% ± 1.0%	2.3%
Woven	UD	$S_2^uC_2^wS_2^uC_2^wS_2^u$	0.88 ± 0.02	18% ± 2%	8.8%
		$S_4^uC_2^wS_4^uC_2^wS_4^u$	1.35 ± 0.03	12% ± 2%	6.1%
		$S_8^uC_2^wS_8^uC_2^wS_8^u$	2.34 ± 0.06	8.4% ± 0.2%	4.2%
		$S_{12}^uC_2^wS_{12}^u$	2.21 ± 0.05	5.5% ± 0.5%	2.8%

Intralayer hybrids

The produced intralayer hybrids are summarised in Table 3-5. This table is split up according to the three types of prepregs, as each of them will be used in only one subsection of "3.4 Intralayer hybrids".

A total of 8 woven layers were stacked in a 0_8 or $(0/90/0/90)_s$ lay-up. The weft direction, which contains the CFRPP tapes, is labelled as the 0° direction, as this is the stiffest and strongest direction. The lay-ups are abbreviated as 0° and 0°/90° respectively. Note that the lay-up for the reference SRPP fabric is irrelevant, as the 0° and 90° are identical. Unless otherwise mentioned, the 0°/90° lay-up is always used.

All co-woven cloths, apart from the plain weave in Figure 3-12a, have a different front and back face. This implies that the CFRPP prepregs are preferentially on one face of the cloth (see for example Figure 3-12b). This face was always placed towards the outside of the layup to maximise the flexural modulus.

For the 300 µm prepregs, reference samples were made. The 50 mm as-received CFRPP prepregs (see Table 3-3) were positioned parallel to each other, and pressed in a copper channel mould to avoid flow at the edges. This led to a 1.1 mm sample thickness. The processing conditions were the same, apart from the pressure. This was lowered to 5 bar to prevent the material from flowing out of the mould, which would misalign the carbon fibres. This lower pressure is possible, because the shrinkage of the PP tapes does not need to be prevented in this case.

In one lay-up with the 300 µm prepregs, PP films were inserted between each of the eight hybrid layers. Apart from decreasing the carbon fibre volume fraction from 22% to 19%, these films also create more matrix material. Adding films increases the interlayer bonding and also widens the temperature window for hot compaction [81,100]. In these experiments, the same hot compaction parameters were used as for the standard hybrid lay-ups. The thickness increased from 1.09 ± 0.01 mm for plain weave samples without films to 1.22 ± 0.01 mm for plain weave samples with films (see Table 3-5).

Table 3-5: Summary of the lay-ups used for intralayer hybrids.

Prepreg type	Label	Lay-up	Weave pattern	Films	Thickness (mm)	V_f (%)
/	0%	/	Twill	No	1.23 ± 0.02	0
300 µm	/	0°	Plain	No	1.06 ± 0.02	22.4 ± 0.6
	/	0°/90°	Plain	No	1.09 ± 0.01	22.4 ± 0.6
	/	0°/90°	Satin	No	1.22 ± 0.01	23.5 ± 0.7
	/	0°/90°	Plain	Yes	1.22 ± 0.01	18.9 ± 0.3
160 µm	3%	0°/90°	Twill	No	1.32 ± 0.01	3.4 ± 0.1
	7%	0°/90°	Twill	No	1.52 ± 0.01	6.9 ± 0.2
	11%	0°/90°	Twill	No	1.79 ± 0.01	10.9 ± 0.4
60 µm	7%MA	0°/90°	Twill	No	1.40 ± 0.02	7.0 ± 0.5
	7/16%MA	0°/90°	Twill	No	1.66 ± 0.01	11.3 ± 0.8
	16%MA	0°/90°	Twill	No	1.99 ± 0.01	15.7 ± 1.2

For the 160 µm and 60 µm prepreg hybrids, only the $(0/90/0/90)_s$ lay-up was produced using the co-woven cloths. Consistently chosing this layup facilitates comparison between the different types of hybrids. For the 60 µm prepregs, an additional hybrid lay-up was made using the orientations of the layers, but combining 7%MA and 16%MA cloths. This stacking sequence is (16/16/7/7/7/7/16/16), where 16 and 7 represent the 16%MA and 7%MA cloths respectively. The orientations of these layers were $(0/90/0/90)_s$, meaning that the carbon fibres are in both directions. This lay-up is labelled as the 7/16%MA lay-up and should allow a further optimisation of the mechanical properties.

3.2.4 Tensile tests

Tensile tests were performed as described in "2.2.3 Tensile tests". Digital image correlation was again used to measure and average the surface strains. Hybridising with CFRPP however, introduced an additional difficulty. After the CFRPP failure, the sample surface was damaged and the surface strain could not be measured anymore. To solve this problem, the crosshead displacement of the tensile machine was used to calculate the strain after the CFRPP failure. Such indirect measurement was accurate for two reasons. Firstly, the crosshead displacement correction is proportional to the applied load, which varies only slightly after the CFRPP breaks. Secondly, the correction was validated on other samples without damaged surfaces.

The tensile modulus was calculated as the slope between 0.1% and 0.3% strain. The strength was calculated at two different strains: the strain at which CFRPP fails and the strain at which SRPP reaches its maximum stress. Both these strengths and the corresponding failure strains are labelled as I and II (see Figure 3-18). The ultimate failure strain is defined as the strain at which the stress drops to zero or nearly zero. For the reference materials, the same definitions are used, though they are not split up into part I and II.

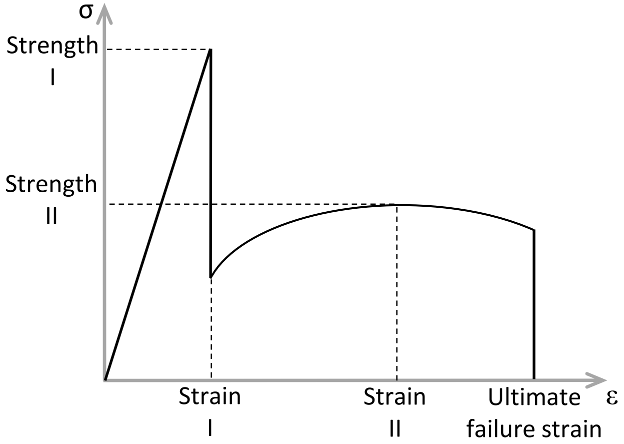

Figure 3-18: A schematic tensile diagram for an intralayer hybrid, with illustration of the relevant tensile properties.

3.2.5 Flexural tests

Three point flexural tests were performed according to the ASTM D790 standard. The span length was chosen to be 60 mm for all samples. This corresponds to an average span-to-thickness ratio of 40 and a minimal ratio of 30. The displacement rate was 4 mm/min, corresponding to a strain rate of 1%/min on average. The nominal sample length was 90 mm, while the nominal sample width was 20 mm instead of the recommended 10 mm. This was required to minimise scatter due to the large unit cell of some intralayer hybrid cloths. A 10 mm width would cause a significant variations in the number of carbon fibre yarns in each sample. At least five samples were tested, all of which had the outer layers in the 0° direction. The flexural modulus was calculated between 0.1 and 0.3% flexural strain.

3.2.6 Peel strength tests

For intralayer hybrids, the peel strength is an indirect measurement of the bonding strength between CFRPP tapes and SRPP. This was measured by peel strength tests. The test conditions were already described in “2.2.7 Peel strength tests”. It should be noted that the addition of CFRPP prepregs increases the stiffness of the peel strength samples. For a proper peel strength test, however, the legs of the sample should be compliant. Therefore, peel samples were prepared that have the CFRPP prepregs perpendicular to the peeling direction. In this case, the stiffness of the legs is nearly the same as for SRPP.

It is important to note that the top and bottom of the co-woven cloths are different. The weave architecture causes the CFRPP prepregs to be preferentially on one side of the cloth (see for example Figure 3-12b). Four co-woven cloths were therefore stacked with the CFRPP side towards the middle. The peel ply and initiation crack was hence in direct contact with the CFRPP prepregs.

3.2.7 Falling weight impact tests

Falling weight impact tests were performed according to the procedures described in “2.2.4 Falling weight impact tests”. Additionally, a second measure for the penetration impact resistance was computed. Chapter 2 only used the “half peak” method, which computes the energy until the force drops to half of its maximum value. This essentially ignores the black area in Figure 3-19, which is relatively small for SRCs. For hybrid composites however, this area often cannot be neglected [215]. By adding this area to the half peak method, the value for the “full” method is obtained.

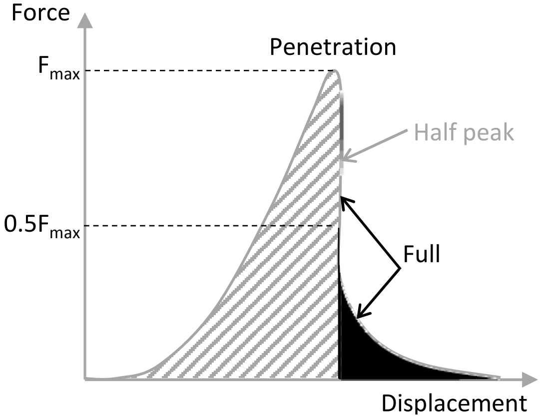

Figure 3-19: A typical force-displacement diagram to illustrate the difference between the half peak method and full method calculating penetration impact resistance.

3.2.8 X-ray microtomography

X-ray microtomography measurements were performed according to the procedures described in “2.2.10 X-ray microtomography”.

3.2.9 Fibre volume fraction determination

The best approach for determining the V_f of carbon fibre composites is to use matrix digestion. In the case of CFRPP, the matrix is chemically inert, making it difficult to completely remove. Instead, matrix burn-off tests were performed according to the ASTM D2584 standard. Samples with a nominal weight of 2 g were prepared and weighed. The samples were heated in a porcelain crucible until the PP matrix ignites. The samples were then inserted into a muffle furnace for 2h to remove the carbonaceous residue. The ASTM standard recommends a furnace temperature of 565°C, but this was found to remove the carbon fibre. Instead, the temperature was set to 450°C, where no further weight loss was found even after 48h.

After cooling down the crucibles, a white residue was found, which was identified as calcium carbonate [238]. This compound is often used as a nucleating agent for PP, and should therefore be taken into account as part of the PP fraction. To remove the residue, the content of the crucible was transferred to a glass filter. A 12% solution of acetic acid was added to dissolve the calcium carbonate. The glass filters were then placed into a drying furnace for 2 h, after which they are cooled down in a desiccator and weighed. The fibre weight fraction was calculated based on the sample weight before burn-off and after drying. These measurements correspond to total sample weight w_{tot} and carbon fibre weight w_{CF} respectively. Equation 3-1 was used to calculate the fibre volume fraction V_f. This calculation assumes a carbon fibre density ρ_{CF} of 1800 kg/m³ and a PP density ρ_{PP} of 920 kg/m³.

$$V_f = \frac{w_{CF}/\rho_{CF}}{w_{CF}/\rho_{CF} + \left(w_{tot} - w_{CF}\right)/\rho_{PP}} \tag{3-1}$$

For intralayer hybrids, a second approach was used to determine the V_f based on the areal densities. Three rectangular specimens of at least 100 cm² were cut and their width and length were measured. Their weight was measured to an accuracy of 0.1 mg. The CFRPP prepregs are then carefully drawn out of the cloth, weighed separately and divided by the dimensions of the hybrid cloth. The ratio of the areal densities of the CFRPP tapes and the hybrid cloth yields the weight fraction of CFRPP. This fraction can be converted into the weight fraction of carbon fibre in the hybrid composite using the weight fraction of carbon fibre in the prepreg. This yields all the necessary information for applying equation 3-1. This approach still requires matrix burn-off to determine the carbon fibre V_f in the prepregs themselves. This value can be measured more accurately due to the higher carbon fibre V_f in the prepregs.

3.2.10 Classical laminate theory

The stiffness of the intralayer hybrid composites is modelled using the classical laminate theory (CLT). The following assumptions were used:

- A co-woven cloth is composed of a woven SRPP and a UD CFRPP layer. The relative fractions are determined by the V_f of CFRPP.
- The CFRPP prepregs are located more towards the outside of the lay-up, but this effect is neglected.
- The crimp of the CFRPP tapes in the weave is neglected. This crimp is small due to the high width-to-thickness ratio of the PP tapes and CFRPP prepregs.

For the CFRPP prepregs, the measured fibre volume fractions were used (see Table 3-3). The volume fraction of tapes in SRPP is difficult to determine experimentally because matrix and tape have similar physical properties. Optical microscopy did not provide sufficient contrast between tape and matrix.

Various DSC-based methods have been employed to quantify tape volume fractions [81,82,110,239]. The first method requires the melting peaks of the matrix and tapes to be sufficiently distinct. If so, the change in melting enthalpy of either of these peaks can be used to calculate their relative fractions [81,82,110]. Unfortunately, these two peaks are not sufficiently distinct for the specific material used here (see Figure 2-23). The second method fits a bimodal Gaussian distribution through both peaks and extracts the area underneath both peaks [239]. This method is more reliable when both peaks slightly overlap. Figure 2-23 indicates that this methodology may also be difficult to apply here, as the matrix peak is very small. The matrix peak was much more pronounced in literature [81,82,110,239]. A final method would be to measure the overall enthalpy of both peaks, and linearly interpolate between the melting enthalpies of tapes and matrix. An attempt was made to utilise this method, but it was found to be unreliable. The annealing that occurs during hot compaction changes the melting enthalpy of the tapes and matrix, making the reference enthalpy of both constituents unreliable. In the absence of a reliable method, a tape volume fraction of 70% is assumed. This implies that 30% of the tapes melted during hot compaction, which is a reasonable value for SRPP [110].

Chamis' formulae were used to calculate the properties of UD SRPP and UD CFRPP [240]. The input parameters for these formulae are summarised in Table 3-6. The carbon fibre properties were estimated from literature [241,242]. The transverse tensile modulus, longitudinal shear modulus and Poisson's ratio of the PP tapes were estimated from [243].

The longitudinal modulus of the PP tapes is 10 GPa prior to hot compaction (see "2.2.1 Materials"). This modulus will however decrease due to molecular relaxation during hot compaction, which implies that the actual modulus of the tapes in SRPP is unknown. The modulus value was hence adapted to yield the correct tensile modulus for a 0/90 lay-up of UD SRPP. This approach neglects the limited crimp in the PP tape weave, but corrects for it by changing the longitudinal tensile modulus of the PP tape. An alternative approach would be to assume 10 GPa for the tape modulus, but reduce the assumed tape volume fraction of 70%. This volume fraction would then be changed until the correct tensile modulus for a 0/90 layup of UD SRPP was obtained. This approach would result in slightly different transverse properties for woven SRPP.

The matrix tensile modulus was measured for the PP grade used in the tapes and published elsewhere [113]. The same properties were assumed for the PP matrix inside the prepregs, although its properties are actually unknown. The matrix Poisson's ratio was taken as a typical value for PP.

Table 3-6: Engineering constants used as input for Chamis' formulae.

	Carbon fibre	PP tape	PP matrix
Longitudinal tensile modulus (GPa)	230	6.9	1.5
Transverse tensile modulus (GPa)	15	1	1.5
Longitudinal shear modulus (GPa)	13.7	0.847	0.536
Longitudinal Poisson's ratio (-)	0.25	0.4	0.4

3.3 Interlayer hybrids

The objective of this section is to understand the parameters governing the failure development in interlayer hybrid composites of carbon fibre and self-reinforced polypropylene. Pseudo-ductility is aimed for by controlling the damage mechanisms through an intelligent design of the hybrid composite.

This section was inspired by work on bendable concrete or engineered cementitious composites [244,245]. Concrete typically fails brittle when the crack from a pre-existing flaw propagates. Ductile or bendable concrete however, fails through excessive cracking over a large volume. This was achieved by adding fibres to control the opening of these cracks. This requires an accurate control over the fibre size, fibre strength and interfacial strength. It allowed a change in the failure development from a single crack to multiple cracks spread over the sample. The extensive microcracks help to redistribute the stresses and strains away from the high stress concentration regions. This microcracking process can significantly toughen concrete. Failure strains of up to 5% were achieved in concrete reinforced with polyvinyl alcohol fibres compared to 0.01% for standard concrete [244,245].

Similar successful examples are found in biological materials. Haversian bone, for example, is capable of undergoing high inelastic strains because of its unique and extensive microcracking process [246]. The cracks are deflected by the lamellar structure of the bone, which significantly increase the energy absorption. Another example is found in nacre, where the inelastic deformation is attributed to progressive sliding and stable pull-out of its platelets [247,248]. In both examples, nature found the optimal balance of microstructural parameters and constituent parameters to activate the suitable mechanisms.

The situation in fibre-reinforced concrete or biological materials is of course significantly different from that in fibre-reinforced polymer composites. Nevertheless, certain concepts can be transferred to the development of ductile carbon fibre composites: (1) a more ductile phase should be added, and (2) multiple cracking should be aimed for. Fibre hybridisation is a promising approach to achieve these goals. Partial replacement of carbon fibres with a more ductile fibre provides more control of the failure mechanisms.

This study is performed on interlayer hybrids instead of intralayer hybrids to facilitate identification of the damage mechanisms. Similar mechanisms are expected to occur in intralayer hybrids, but they will occur on the tape level instead of on the layer level. This would hamper the identification of the damage mechanisms.

3.3.1 Damage mechanisms in hybrid composites

To achieve pseudo-ductility in SRPP/CFRPP hybrid composites, the damage mechanisms after CFRPP failure need to be controlled. These mechanisms depend on a number of parameters, including the stiffness and strength of the SRPP and CFRPP plies, their thicknesses and the interlaminar fracture toughness. Let us consider a situation where all parameters except the interlaminar fracture toughness are the same. Then, this toughness dictates the type of failure of the hybrid composite. For a high fracture toughness, the energy from the CFRPP fracture has no possibility to be released through delamination. Therefore, it has to be taken up by the surrounding SRPP layers, possibly resulting in their immediate failure (see Figure 3-20a). For a low fracture toughness, the sample delaminates quickly over the entire length and no further stress build-up is possible in the CFRPP layers (see Figure 3-20b). The scenario of interest is the one with an intermediate fracture toughness, in which case a small delamination would be allowed (see Figure 3-20c-d). Two possibilities can be distinguished in this case: (1) a single, gradually propagating delamination (see Figure 3-20c) and (2) fragmentation, which implies multiple CFRPP fractures accompanied by delamination (see Figure 3-20d). Fragmentation typically starts off as a single CFRPP failure and delamination, but as stress builds up again, new CFRPP failures appear instead of a growing delamination. In both cases, CFRPP failure may inflict damage to the SRPP layers.

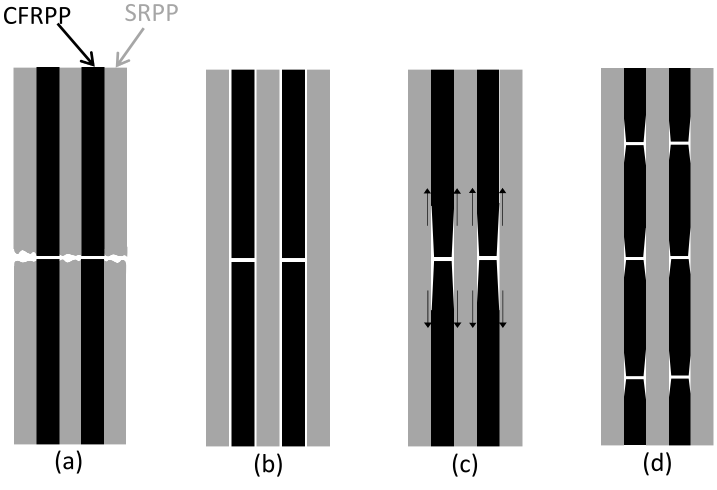

Figure 3-20: Possible damage mechanisms in hybrid composites after failure of the carbon fibre layers: (a) failure of the entire composite, (b) complete delamination, (c) a single, gradually propagating delamination, and (d) fragmentation or multiple CFRPP fractures accompanied by delaminations.

Four parameters will be varied to control the damage mechanisms: carbon fibre volume fraction, CFRPP and SRPP orientation and the relative thickness of the CFRPP layer. The interlaminar fracture toughness is missing from this list, but this value will be varied indirectly by changing the CFRPP and SRPP orientation.

3.3.2 Carbon fibre volume fraction

Figure 3-21 presents the stress-strain diagrams of a UD CFRPP - woven SRPP hybrid with 29%CF.

The tensile behaviour corresponds to the mechanism of a single, gradually growing delamination around each broken CFRPP layer (see Figure 3-20c). This is also confirmed by the sample appearance immediately before and after CFRPP failure (see Figure 3-21b and c). The light grey regions correspond to the delaminations between the CFRPP and SRPP layers. Figure 3-21d indicates that this delamination gradually grows upon further loading. At about 10% strain, the delamination covers the entire sample length. The sample then reverts to the situation of a complete delamination (see Figure 3-20b), where the SRPP layers are loaded independently from the fractured CFRPP layers. It should be noted that some damage is introduced into the SRPP, as the ultimate failure strain is slightly reduced compared to 0%CF.

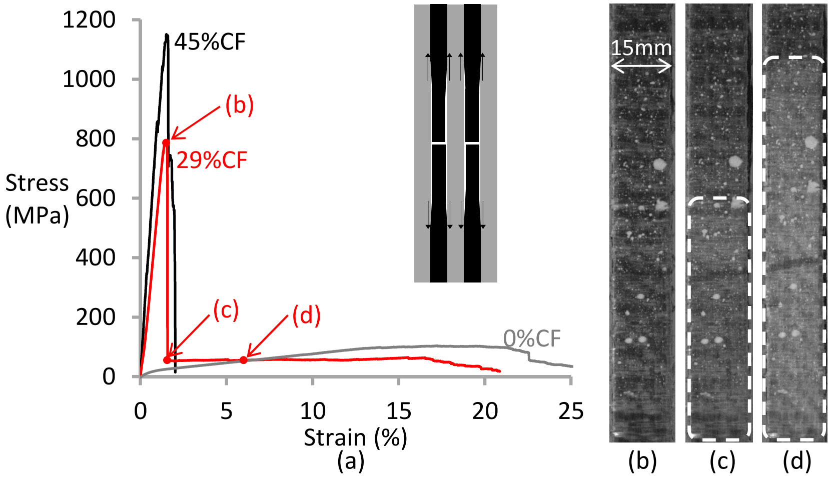

Figure 3-21: A UD CFRPP – woven SRPP hybrid composite with 29%CF: (a) stress-strain diagram along with those of the reference composites, (b) sample right before CFRPP failure, (c) sample immediately after CFRPP failure, and (c) sample after 6% applied strain. The dashed rectangle indicates the delaminated region.

Immediately after CFRPP failure, the delamination length is 70 mm on average, corresponding to nearly half the gauge length. Such large delaminations should be avoided, as they lower the probability of complete stress build up in the CFRPP layers. This stress build up is vital for achieving multiple cracks or fragmentation. The large initial delaminations are facilitated by fibre debonding and splitting due to the low adhesion between carbon fibre and PP.

The available energy for creating delaminations is related to the energy that is stored in the CFRPP and released upon failure. This energy is the same for the 29%CF, 13%CF and 10%CF hybrids, as they all have the same number of carbon fibre plies (see Table 3-4). Their layups also ensure that the number of surfaces that can delaminate is the same. Reducing the V_f from 29% to

13% and 10% therefore did not change the general appearance of the stress-strain diagrams (see Figure 3-22), nor did it change the initial delamination length. The only observed change is the fact that the SRPP ductility is maintained better for the 13%CF and the 10%CF hybrids. This is because these hybrids have more SRPP layers to absorb the released energy.

The 5.0%CF layup only has a single carbon fibre layer compared to two layers for the other layups (see Table 3-4). The lower elastic energy stored in this sample would hence be expected to have an effect on the delamination length. Unfortunately, visual detection of the delaminations was not possible anymore due to the thick SRPP layers blocking the light too much. The damage to the SRPP was limited as the ultimate failure strain only increased slightly with decreasing carbon fibre V_f.

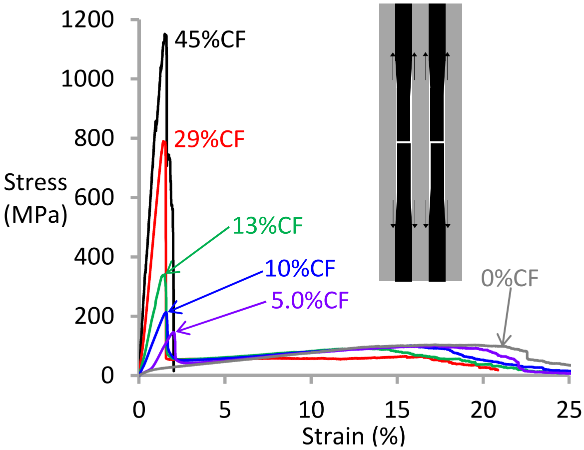

Figure 3-22: Stress-strain diagrams of UD CFRPP – woven SRPP hybrid composites with different carbon fibre volume fractions.

The 5%CF layup led to undulations in the carbon fibres, which cause some degree of nonlinearity in the range of 0-0.8% strain. These undulations are caused by the strong tendency of the PP tapes to shrink [161,249]. This occurs due to the entropic shrinkage of the PP tapes at high temperature, but also during cooling due to the large coefficient of thermal expansion of SRPP. The carbon fibres are straightened before they fail, which is also indicated by the increased failure strain of the CFRPP in Figure 3-22. The undulations thus have only a minor influence on the damage mechanisms and are not studied here. Higher fractions of carbon fibre stabilise the CFRPP for these undulations and reduce the driving force for shrinkage by reducing the SRPP fraction.

3.3.3 Directionality of CFRPP

Reducing the carbon fibre V_f was insufficient to cause a change in the damage mechanism as the released energy and delamination length remained the same. One way to shorten the delamination length, is to increase the interlaminar fracture toughness by adding 90° carbon fibres [250]. This section replaces the UD CFRPP layers with woven CFRPP to investigate its influence on the tensile behaviour.

Figure 3-23 reveals that hybrids with woven CFRPP indeed behave differently. The initial delamination length is reduced to 30 mm (see Figure 3-23c), compared to 70 mm for UD CFRPP (see Figure 3-21c). This proves that 90° fibres help to reduce the extent of fibre debonding and splitting. The delamination grows slightly, but then the SRPP layers start to fail. The SRPP always failed in the region where the CFRPP failed, indicating that CFRPP failure locally introduced damage into the SRPP layers.

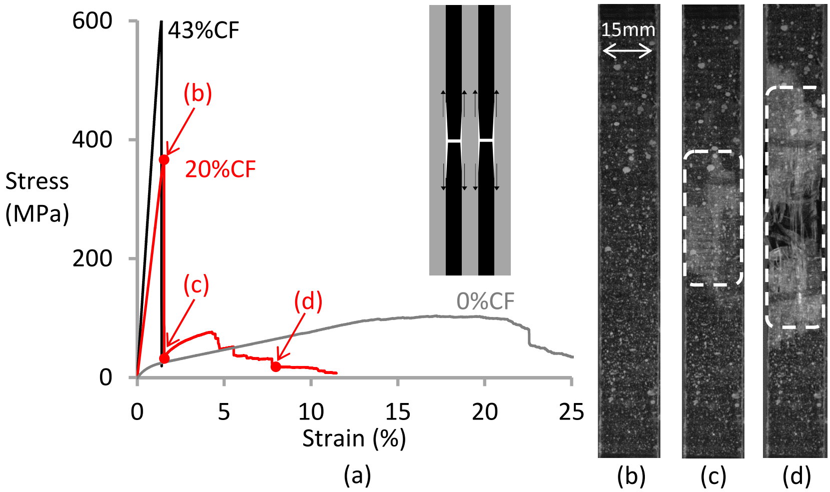

Figure 3-23: A woven CFRPP – woven SRPP hybrid composite with 20%CF: (a) stress-strain diagram along with those of the reference composites, (b) sample right before CFRPP failure, (c) sample immediately after CFRPP failure, and (c) sample after 8% applied strain. The dashed rectangle indicates the delaminated region.

Damage to the SRPP can be avoided by reducing the carbon fibre volume fraction (see Figure 3-24). The energy that is released upon CFRPP failure remains the same for the 20%CF, 11%CF and 7.2%CF hybrids, as they have the same number of CFRPP layers. The 7.2%CF layup however has more SRPP layers, making it more efficient in resisting damage to the SRPP.

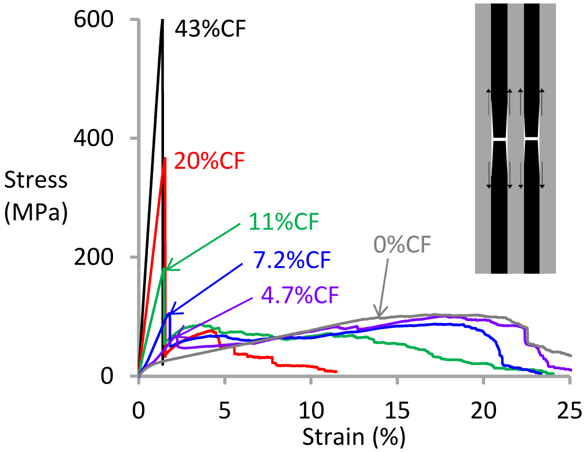

Figure 3-24: Stress-strain diagrams of woven CFRPP – woven SRPP hybrid composites with different carbon fibre volume fractions.

Inspection of the initial delamination lengths revealed that they were consistently around 30 mm for the 20%CF, 11%CF and 7.2%CF hybrids. This is again related to the fact the number of CFRP layers and hence the released energy is the same. The delamination length seems to be even smaller for the 4.7%CF, but the contrast between delaminated and undelaminated regions was too low for accurate measurements.

3.3.4 Directionality of SRPP

The previous subsection highlighted the importance of carbon fibre directionality in hybrids with woven SRPP. The SRPP properties may also have an important effect on the performance and damage mechanisms of the investigated hybrids. This effect was investigated by using UD SRPP instead of woven SRPP, in combination with woven CFRPP. This increases both the stiffness and the strength of the SRPP, making it more suitable to absorb the energy released by the CFRPP failure.

The 18%CF hybrids with UD SRPP (see Figure 3-25) are able to maintain more of the SRPP ductility than the 20%CF hybrids with woven SRPP (see Figure 3-23). Nevertheless, the mechanisms are similar in both hybrids: a single, gradually growing delamination. Again, damage to the SRPP is reduced by lowering the carbon fibre volume fraction. The initial delamination length was 20-25 mm, irrespective of the carbon fibre volume fraction. This is shorter than the 30 mm in the woven CFRPP – woven SRPP hybrids. This is most likely related to the higher stiffness of the UD SRPP, but analysing the influence this has on the delamination is complex. Such analysis would require an energy-based approach, which will not be attempted here. This analysis should also be able to reveal why the delamination length was not lower for the 5.5%CF hybrid, even though this layup has fewer carbon fibre layers (see Table 3-4).

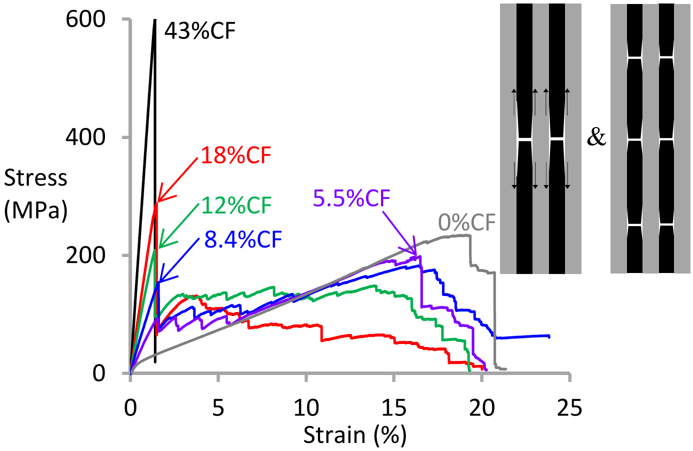

Figure 3-25: Stress-strain diagrams of woven CFRPP – UD SRPP hybrid composites with different carbon fibre volume fractions.

The 18%CF, 12%CF and 8.4%CF hybrids show a single growing delamination, whereas the 5.5%CF lay-ups show fragmentation. Figure 3-26 illustrates this behaviour in more detail. The tensile diagram in Figure 3-26a displays four small peaks, followed by a larger one at about 15% strain. Figure 3-26b shows the sample prior to the test. At this point, the material has a homogeneous colour. The light grey region in Figure 3-26c develops after the first small load drop. This region indicates that the CFRPP has locally failed and is surrounded by a delamination. Further loading of the sample builds up stress, allowing the CFRPP layer to fracture again (see the second light grey region in Figure 3-26d). This fragmentation occurred four times over the sample length, as illustrated in Figure 3-26e. The delamination length was always 20-25 mm, irrespective of whether it was the first delamination or a later one.

The stress increase as a function of strain was synchronised with videos of the sample surface. The onset of the delaminations corresponds to the stress drops in the stress-strain curves. The multiple fractures of the CFRPP layers were confirmed by melting away the PP and observing the CFRPP layers. At about 6% strain, the CFRPP layers are completely delaminated, and SRPP becomes the only load carrying material.

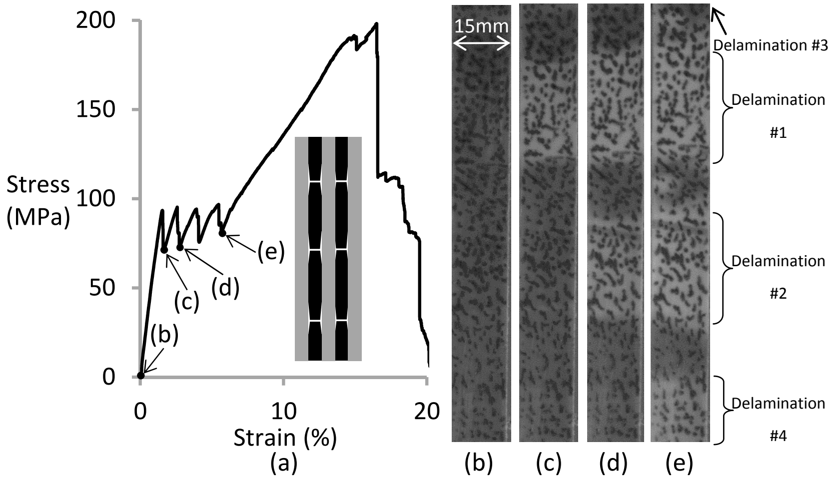

Figure 3-26: Illustration of the fragmentation behaviour in the 5.5%CF hybrids: (a) tensile diagram and sample (b) prior to failure, (c) after first fragmentation, (d) after second fragmentation, and (e) after the fourth and final fragmentation. The third fragmentation occurred outside of the imaged zone. The black speckles are used for digital image correlation.

3.3.5 Relative layer thickness

All 5.5%CF hybrids with woven CFRPP and UD SRPP fragmented, whereas none of the other described lay-ups fragmented. Fragmentation prevents localisation of the strain and allows a higher stress level to be maintained. There is however a maximum relative layer thickness above which fragmentation does not occur anymore [122,206]. To examine the upper limit, hybrid composites with a varying number of SRPP layers and a single woven CFRPP layer in the middle were produced. The carbon fibre volume fractions varied between 2.1% and 10%, see Table 3-7.

The stress-strain diagrams of these hybrid composites are shown in Figure 3-27. The curves of both the fragmented and non-fragmented samples have peaks followed by vertical stress drops. These stress drops are either caused by sudden growth of a delamination or by the fragmentation of the CFRPP layer. To determine whether fragmentation occurred (see Table 3-7), images of the samples during the tensile tests were used to decide whether the samples fragmented.

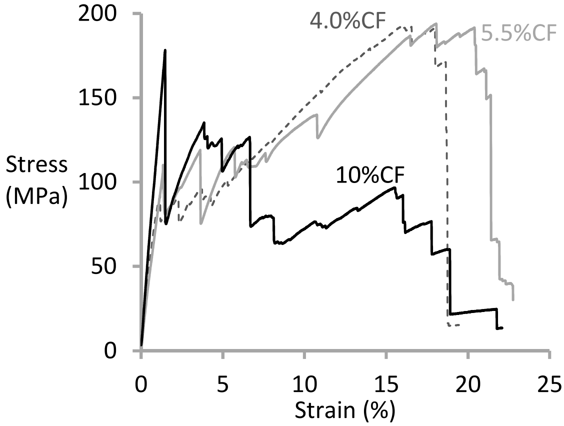

Figure 3-27: Representative stress-strain diagrams of woven CFRPP – UD SRPP hybrid composites with a single carbon fibre layer in the middle. Some lay-ups were omitted to improve clarity.

The number of fragmented samples for each lay-up was counted from the digital image correlation images. All these results are summarised in Table 3-7. The number of fragments in the fragmented samples varied between 2 and 4, but does not seem to depend on the lay-up. While 4/5 samples of the 5.5%CF hybrid still fragment, only 1 out 5 samples of 7.0%CF hybrid did. The critical carbon fibre V_f is hence around 6%CF, above which the samples do not fragment anymore. This value corresponds to a relative layer thickness of 13% or 3%CF in the loading direction.

Table 3-7: The critical layer thickness and number of fragmented samples for various lay-ups of woven CFRPP – UD SRPP composites with a single CFRPP layer.

Lay-up	Overall carbon fibre V_f (%)	Total thickness (mm)	CFRPP thickness (mm)		Critical layer thickness (mm)	Number of fragmented samples
$S^u_{12}C^wS^u_{12}$	2.1 ± 0.1	2.09 ± 0.03	0.104	$<$	0.147	5/5
$S^u_6C^wS^u_6$	4.0 ± 0.1	1.11 ± 0.01	0.104	$<$	0.117	5/5
$S^u_5C^wS^u_5$	4.6 ± 0.6	0.95 ± 0.01	0.104	$<$	0.111	5/5
$S^u_4C^wS^u_4$	5.5 ± 0.4	0.79 ± 0.02	0.104	$\approx$	0.102	4/5
$S^u_3C^wS^u_3$	7.0 ± 1.6	0.62 ± 0.01	0.104	$>$	0.093	1/5
$S^u_2C^wS^u_2$	10 ± 1	0.43 ± 0.01	0.104	$>$	0.080	0/5

Having a single instead of multiple CFRPP layers allows the model proposed in [122] to be applied here. This model establishes an energy criterion for preventing the propagation of a delamination. This criterion is based on changes in the elastic strain energy before and after the CFRPP layer fails. The critical layer thickness t^c_{CFRPP} is found when this energy change is equal to the energy required to cause delamination of the central CFRPP layer. This leads to the equation:

$$G_{II,C} = \frac{\sigma_{CFRPP}^{2} \cdot t_{CFRPP}^{c} \cdot \left(E_{SRPP} \cdot \left(t - t_{CFRPP}^{c}\right) + E_{CFRPP} \cdot t_{CFRPP}^{c}\right)}{4 \cdot E_{SRPP} \cdot E_{CFRPP} \cdot \left(t - t_{CFRPP}^{c}\right)}, \quad (3\text{-}2)$$

where $G_{II,C}$ is the mode II interlaminar fracture toughness for propagation, σ_{CFRPP} is the strength of the central CFRPP layer, E_{SRPP} and E_{CFRPP} are the tensile moduli of the SRPP and CFRPP layers respectively, and t is the total sample thickness. It should be noted that equation 3-2 neglects the energy dissipated by damage to the SRPP layers.

All required input parameters are available from the tensile tests, apart from $G_{II,C}$. This value is challenging to measure due to the low CF/PP adhesion and the low stiffness of hybrid CFRPP/SRPP composites. Since CFRPP is not a common prepreg, the amount of literature on its $G_{II,C}$ is limited. Taketa [158] quoted values of 0.497 ± 0.026, 0.674 ± 0.017 and 0.384 ± 0.010 kJ/m² for fast, medium and slowly cooled UD CFRPP. Since no consistent trend can be observed, the average value of 0.518 kJ/m² was used. This is very close to 0.514 kJ/m² reported by Hu [251]. These values have three important caveats. Firstly, the CFRPP prepregs used by Taketa and Hu are from a different manufacturer. Secondly, they reported $G_{II,C}$ values for UD CFRPP, while the equation 3-2 will be applied to woven CFRPP hybrids. The $G_{II,C}$ is typically somewhat higher for woven than for UD composites [252]. Thirdly, these values were measured for a delamination running between two CFRPP layers, while the delamination in hybrids runs between a CFRPP and SRPP layer.

Equation 3-2 was solved using the appropriate values for CFRPP and SRPP. The resulting critical layer thickness t_{CFRPP}^{c} depends on the lay-up, as the sample thickness t was fixed to the experimental sample thickness. The actual CFRPP thickness should be smaller than the critical layer thickness to prevent delamination propagation. Table 3-7 proves that these calculations correspond well with the experimental data.

As the $G_{II,C}$ value was taken from literature, analysing its significance for the critical layer thickness is a useful exercise. The critical layer thickness indeed seems to be sensitive to the fracture toughness (see Figure 3-28). Using either 0.4 or 0.6 kJ/m² for $G_{II,C}$ would change the critical layer thickness by about 15%. These small variations would change the comparison with the presented experimental data (see Table 3-7).

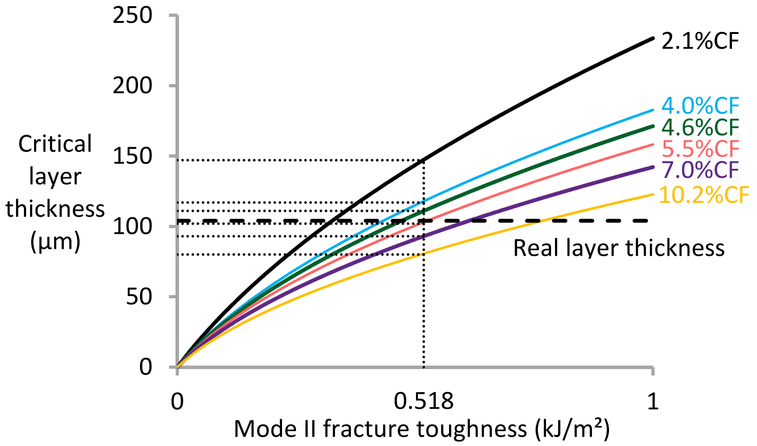

Figure 3-28: Prediction of the critical layer thickness using the model of Czél and Wisnom [122].

3.3.6 Conclusion

The damage mechanisms in CFRPP/SRPP hybrid composites were analysed and the influence of various parameters was demonstrated:

- Carbon fibre volume fraction determines the amount of the damage to the SRPP, but does not necessarily affect the delamination length.
- Woven CFRPP leads to a shorter delamination length than UD CFRPP.
- UD SRPP is stronger and leads to less damage in the SRPP than woven SRPP. Its higher stiffness and strength also facilitates fragmentation.
- Fragmentation was achieved for relative CFRPP layer thicknesses below 14%. The optimal carbon fibre volume fraction is about 6%, of which half is in the loading direction.

The mechanical performance of CFRPP/SRPP interlayer hybrids can be optimised by an intelligent combination of these parameters. These conclusions can also be used to control the damage mechanisms and achieve ductility in other hybrid composites.

3.4 Intralayer hybrids

The previous section described the tensile properties of interlayer hybrids. From the section “3.1 State of the art”, it is known that increased dispersion in hybrid composites leads to improved mechanical performance. Therefore, this section moves from interlayer to intralayer hybrid composites. The first subsection analyses the tensile behaviour and how it is affected by lay-up, weave pattern and films. The understanding developed in the first subsection will be used in the subsections “3.4.2 Effect of carbon fibre volume fraction” and “3.4.3 Effect of adhesion”. These subsections analyse not only tensile behaviour, but also the flexural behaviour and impact resistance. The impact resistance should be kept high, as this is the key advantage of SRPP. The flexural behaviour is studied, as it helps in understanding the impact resistance.

Interlayer bonding was found to be an important parameter in controlling delaminations in interlayer hybrid composites. Similarly, it is expected that the intralayer bonding will be important in controlling debonding of the CFRPP tapes. The inter- and intralayer bonding are similar features, but they occur on a different scale. Interlayer bonding occurs between the layers, while intralayer bonding occurs within a layer. Measuring the intralayer bonding directly is, however, very challenging. Therefore, this chapter will use the peel strength as a measure of the intralayer bonding, even though this actually measures the interlayer bonding. Both properties are intrinsically strongly correlated, as they both depend on the bonding strength between CFRPP and SRPP.

3.4.1 Tensile behaviour

This subsection analyses the tensile behaviour of intralayer hybrid composites with the 300 µm prepregs (see Table 3-5). This is the first step towards optimising the mechanical properties of intralayer hybrid SRPP. The investigated parameters are the lay-up, the weave pattern and films.

Reference material

Figure 3-29 presents the tensile diagrams of the CFRPP and SRPP reference materials, while Table 3-8 summarises the tensile properties of both materials. CFRPP has a high stiffness and strength, but a low failure strain. This is in strong contrast with the low stiffness, low strength and high failure strain of the SRPP, combined with a high failure strain. The remainder of this subsection will examine how these two materials should be hybridised to achieve optimal mechanical properties.

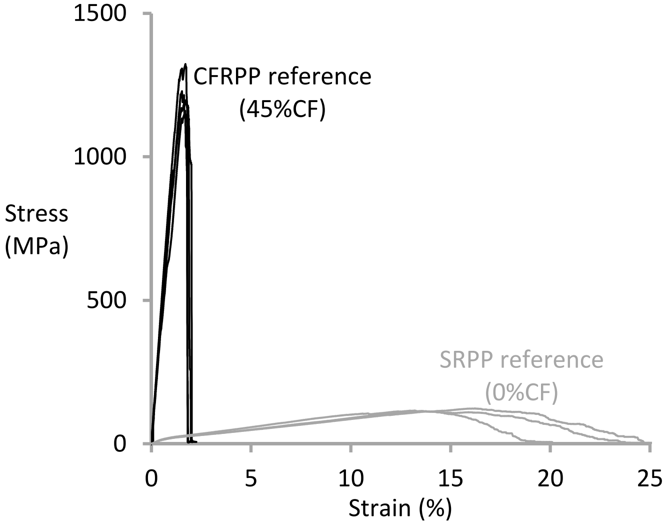

Figure 3-29: Tensile diagrams of the reference materials.

Table 3-8: Tensile properties of the reference materials.

	CFRPP	SRPP
Stiffness (GPa)	91 ± 5	3.0 ± 0.2
Failure strain (%)	1.6 ± 0.1	14.3 ± 1.7
Strength (MPa)	1230 ± 70	117 ± 5

Influence of the lay-up

Since the hybrid weaves only have carbon fibres in the 0° direction, the lay-up is vital for the mechanical properties of the hot compacted sheets. Therefore, 0° and 0°/90° plain weave lay-ups with 22%CF were hot compacted and tested. Their tensile diagrams are presented in Figure 3-30, while Table 3-9 summarises their tensile properties.

Both lay-ups demonstrated a distinct CFRPP peak at about 1.5% strain, followed by an SRPP tail. The lay-up hardly affected the stresses and strains in the second part of the diagram. The SRPP part seems to remain unaffected by the energy released upon CFRPP failure. The high SRPP ductility and the low adhesion between carbon fibre and PP are responsible for this effect.

A crucial difference between the 0° and the 0°/90° lay-ups is the fraction of carbon s in the tensile direction. The 0°/90° lay-up only has half of the carbon fibres in the tensile direction, compared to those in the 0° lay-up. This results in a stiffness difference of a factor of two. According to the classical laminate theory, a stiffness of 53 GPa would be expected for the 0° lay-up, while the measured 33.5 GPa is significantly lower. There are two reasons for the observed difference. Firstly, the modulus of carbon fibre is typically measured between 0.5 and 0.7% strain, while the composite modulus was measured between 0.1 and 0.3% strain. The carbon fibre modulus is known to increase by about 20% for every 1% of applied strain [253,254], which means the expected composite modulus would reduce to 48 GPa. Secondly, the PP tapes have a high tendency to shrink during processing. This can induce local carbon fibre misalignment [161], further reducing the composite tensile modulus. This misalignment was observed in the samples, but was not quantified.

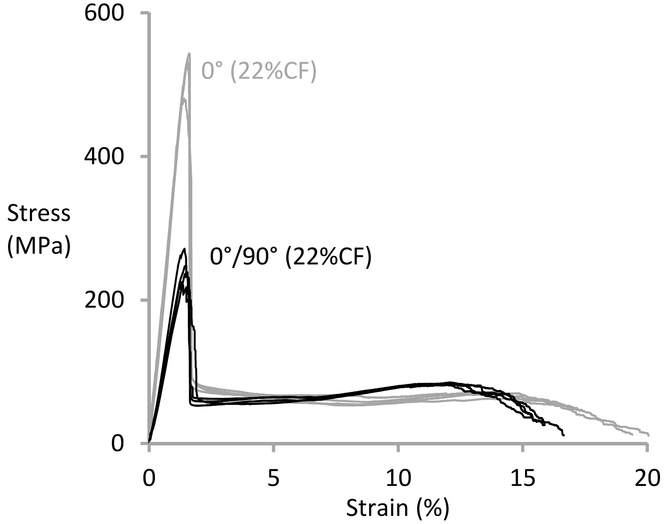

Figure 3-30: Tensile diagrams of the 0° and 0°/90° plain weave intralayer hybrids with 22%CF.

Table 3-9: Tensile properties of the hybrid composites with 300 µm prepregs.

Lay-up	0°	0°/90°	0°/90°	0°/90°
Weave pattern	Plain	Plain	Satin	Plain
Films	No	No	No	Yes
Carbon fibre V_f (%)	22.4 ± 0.6	22.4 ± 0.6	23.5 ± 0.7	18.9 ± 0.3
Stiffness (GPa)	33.5 ± 3.0	16.1 ± 1.7	16.1 ± 2.0	17.8 ± 0.6
Strain I (%)	1.5 ± 0.1	1.4 ± 0.1	1.5 ± 0.2	1.6 ± 0.1
Strength I (MPa)	522 ± 28	245 ± 20	252 ± 11	280 ± 24
Strain II (%)	13.9 ± 0.2	12.1 ± 0.2	10.7 ± 0.6	6.3 ± 3.3
Strength II (MPa)	69 ± 4	84 ± 2	75 ± 2	92 ± 9

It is remarkable that the second part of the tensile diagram is largely lay-up independent, supporting the explanation that the two components are acting mainly independent after the carbon fibre failure.

The measured data can also be compared to the predicted behaviour for the 0° lay-up. The tensile diagram of this lay-up is easier to predict than that of the 0°/90° lay-up, as the 0° lay-up has no carbon fibres in the transverse direction. These predictions use either the rule of mixtures or a linear delamination growth model.

The rule of mixtures prediction is based on the experimental reference material data (see Figure 3-29), weighed by their relative volume fraction. This assumes both components behave in parallel and do not interact with each other. The volume of the CFRPP tapes can be estimated by dividing the carbon fibre volume fraction of the hybrid composite (22%) by the carbon fibre volume fraction of the CFRPP prepregs (45%). This results in a relative ratio of 45% CFRPP and 55% SRPP. These ratios are used as weighing factors for the stress-strain diagrams of the reference materials. It is assumed that the CFRPP stops carrying stress at 1.7% strain.

A further improvement of the simple rule of mixtures model, is achieved by including the effect of the debonding of the CFRPP prepregs. Similar to the interlayer hybrids, this debonding was observed experimentally, but it was more difficult to quantify. The model additionally assumes that the CFRPP is sandwiched between two SRPP layers. The debonding of the CFRPP prepregs therefore becomes equivalent to a delamination. The exact position is irrelevant for the model, although the relative amount of SRPP and CFRPP is vital. An edge view of the model is depicted in Figure 3-31.

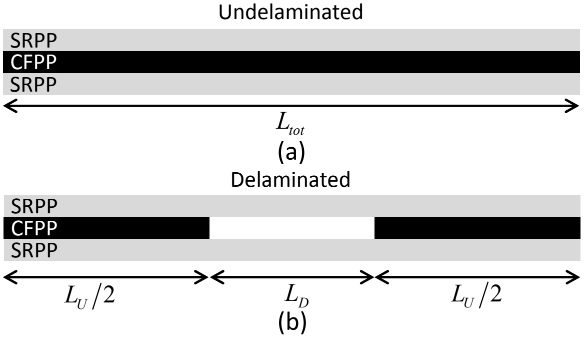

Figure 3-31: Schematic view of the delamination growth model from the edge of the sample: (a) in the undelaminated state, and (b) in the delaminated state. The white zone indicates the location of the delamination.

The model assumes that a delamination starts and grows linearly till a certain length at a certain strain. At each strain, a certain delaminated length is imposed on the model based on a linear growth as a function of the applied strain. A force equilibrium is used to calculate stresses and strains. The force F_D in the delaminated region has to be equal to the force F_U in the undelaminated region, meaning that:

$$F_D = F_U \tag{3-3}$$

This can be rewritten in terms of the stresses σ_D and σ_U in the delaminated and undelaminated region, respectively:

$$\sigma_D \cdot A_D = \sigma_U \cdot A_U \tag{3-4}$$

in which A_D and A_U are the cross-sectional areas of the delaminated and undelaminated region respectively. An alternative expression uses the fraction V_H, which is calculated as the ratio of A_D to A_U:

$$\sigma_D \cdot V_H = \sigma_U \tag{3-5}$$

Based on Figure 3-31, it can be stated that:

$$L_{tot} = L_D + L_U \tag{3-6}$$

Where L_D is the delaminated length, L_U is the undelaminated length and L_{tot} is the total sample length. Moreover, the strains ε_D and ε_U in the delaminated and undelaminated regions are related to the total strain ε, according to equation 3-7.

$$\varepsilon \cdot L_{tot} = \varepsilon_D \cdot L_D + \varepsilon_U \cdot L_U \tag{3-7}$$

Before the CFRPP fails at 1.7% strain, the delaminated length L_D is assumed to be zero. Then, the delaminated length L_D grows linearly from $L_{D,init}$ to $L_{D,full}$, but cannot exceed the sample length. This growth starts at ε^*_{CFRPP} when the CFRPP fails, and stops at ε_{full}. This is captured in equation 3-8:

$$L_D(\varepsilon) = L_{D,init} + \frac{L_{D,full} - L_{D,init}}{\varepsilon_{full} - \varepsilon^*_{CFRPP}} \cdot \left(\varepsilon - \varepsilon^*_{CFRPP}\right) \tag{3-8}$$

When equations 3-5, 3-6 and 3-7 are combined with Hooke's law, assuming linear elastic behaviour of both components, then equation 3-9 can be obtained:

$$\sigma_U = \frac{E_D \cdot L_{tot} \cdot V_H}{L_D + L_U \cdot V_H \cdot E_D / E_U} \cdot \varepsilon \tag{3-9}$$

To extend equation 3-9 to plastic materials, as is the case for SRPP (see Figure 3-29), the moduli are replaced by the secant moduli, which means the moduli depend on the applied strain in the corresponding region. Note that the lengths L_D and L_U depend linearly on the total strain ε. This yields the final equation:

$$\sigma_U(\varepsilon) = \frac{E_D(\varepsilon) \cdot L_{tot} \cdot V_H}{L_D(\varepsilon) + L_U(\varepsilon) \cdot V_H \cdot E_D(\varepsilon) / E_U(\varepsilon)} \cdot \varepsilon \tag{3-10}$$

Equation 3-10 is valid for the entire stress-strain diagram and is solved iteratively.

Figure 3-32 compares the predicted results with the measurements. The linear delamination growth model was fitted to the experimental data, as the delaminations in this material could not be observed visually. This was achieved by changing the initial delamination length $L_{D,init}$ and the strain ε_{full} at which the delamination reaches the total sample length $L_{D,full}$. An initial delamination $L_{D,init}$ of 18 mm was assumed, which grows linearly to the 150 mm sample length $L_{D,full}$ at a total strain ε_{full} of 12%.

Both models overestimate the CFRPP strength. The low adhesion between carbon fibre and PP promotes interfacial debonding during tensile tests on the reference CFRPP. This causes premature damage development and failure near the clamps, and hence an underestimation of the actual strength. Furthermore, the CFs in the hybrids are slightly misaligned by the SRPP shrinkage, which may also cause a strength reduction.

A large difference between both predictions is observed after the CFRPP failure. The rule of mixtures prediction assumes that CFRPP stops carrying load, which means the stress falls back to the level of SRPP at that strain. This results in a vertical stress drop to about 15 MPa. The higher experimental stress is attributed to the partial debonding of the CFRPP prepregs. Around the failure location of the CFRPP, the CFRPP prepregs start to debond. In the debonded region, the local strain in the remaining SRPP is higher than the total strain of the sample. This causes a higher SRPP stress to develop in that region. As the overall strain increases, the debonding also grows in length. The debonded length determines how the strain is distributed over the debonded and intact regions. The overall stress remains nearly constant until the sample fully debonds. By the time that occurs, the strain has already reached 12% and the SRPP starts to fail. These features are captured by the linear delamination growth model. The prediction is fairly accurate, which validates the model assumptions.

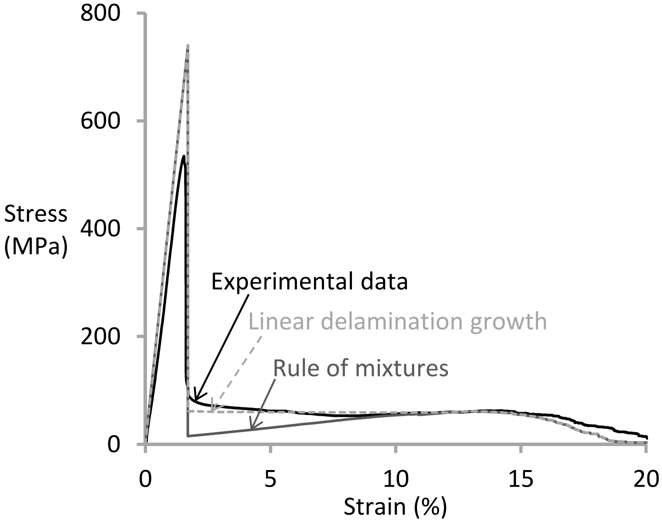

Figure 3-32: Comparison between predictions and measurements of 0° plain weave intralayer hybrids without films.

Debonding of the CFRPP prepregs is crucial for keeping the SRPP ductility after the CFRPP fails and therefore the intralayer bonding has to be optimised. If the intralayer bonding is too strong, then the debonding will not develop and the fracture will localise. If the bonding is too weak, then the debonding spreads rapidly over the entire sample and both components would behave independently. If the intralayer bonding is intermediate, however, the debonded region can grow, preventing localisation as well as immediate complete debonding. The importance of the intralayer bonding can also be gleaned from the $G_{II,C}$ parameter in equation 3-2. This equation from Czél and Wisnom is based on an energy-based approach, and predicts whether a delamination can grow. In contrast, the present model is based on force equilibrium. It does not predict delamination/debonding onset or growth, but predicts the strains and stresses when such a delamination/debonding is present. Both models are therefore different, but complementary.

Influence of the weave pattern

A plain weave is compared to a satin weave to assess the influence of the crimp. The plain weave has more cross-overs, resulting in higher out-of-plane orientation of both the carbon fibres and the PP tapes. Figure 3-33 depicts the tensile diagrams of both weave patterns for 0°/90° lay-ups and Table 3-9 summarises their tensile properties.

No significant differences were found in the stiffness and strength I (see Figure 3-18 for the definition), which means that the crimp is not affecting the behaviour of the carbon fibres. This can be understood from the dimensions of the CFRPP prepregs and PP tapes. Their width over thickness ratio is 8 and 50 respectively, resulting in a low crimp for both weave patterns.

Small differences can be observed in the second part of the tensile diagram. The satin weave has a lower strain II and strength II. This part of the tensile diagram is determined by the damage in SRPP. The cross-overs in the weave pattern hinder the debonding of the CFRPP prepregs. This will tend to limit the extent of the damage that the CFRPP failure introduces into the SRPP. Since the plain weave has more cross-overs, the CFRPP tape failure damages the SRPP over a smaller region. This results in higher strain II and strength II for the plain weave.

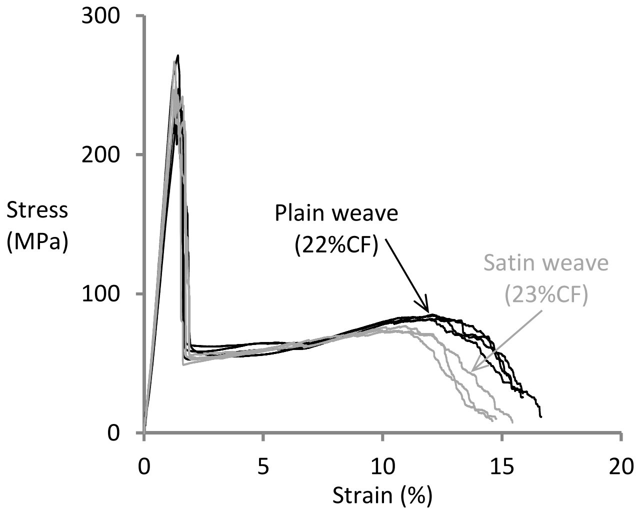

Figure 3-33: Tensile diagrams of 0°/90° intralayer hybrids in plain and satin weave.

In conclusion, a plain weave pattern results in more ductile behaviour, while the stiffness and strength remain unaffected. The observed differences were small due to the small difference in crimp between both weave patterns. Obtaining a highly crimped weave pattern was not possible with the given CFRPP prepregs and PP tapes, as they both have a high aspect ratio.

Influence of films

Films were inserted between the hybrid fabrics to increase the amount of matrix and hence enhance the bonding between SRPP and CFRPP. This increases the resistance to CFRPP debonding, but also facilitates thermoforming. The tensile diagrams are displayed in Figure 3-34 and the tensile properties are summarised in Table 3-9.

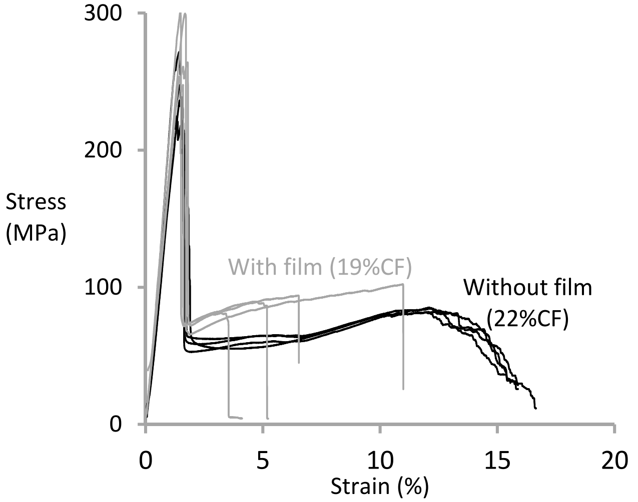

Figure 3-34: Tensile diagrams of 0°/90° plain weave intralayer hybrids with and without films.

The use of films slightly improved the strain I and strength I and resulted in composites with a sharper CFRPP peak. This is assumed to be due to a decrease in the fibre misalignment, as the tensile modulus increased even though the carbon fibre volume fraction decreased. Moreover, the additional matrix improves the compaction quality and hence the bonding between SRPP and CFRPP. The improved bonding can delay the onset of CFRPP failure and increases the sharpness of the CFRPP peak.

The largest difference is observed after carbon fibre failure. Adding films increases the strength II, but strongly decreases the strain II. This can be understood from the difference in bonding between SRPP and CFRPP, which determines the debonding length. In the composite without the films, the bonding is weak, allowing the debonding to spread out over the entire sample. This limits strain localisation and allows the SRPP to be strained independently from the CFRPP, and over a longer length. In composites with films, however, the improved intralayer bonding limits the debonding length. This localises the applied strain over a smaller length, and hence increases the stress carried by the SRPP layers. Locally, the SRPP failure strain is reached, while other parts of the sample are strained less. At the same time, the improved intralayer bonding allows some of the carbon fibres to contribute to the stress even after the first peak. This results in the increased strength II.

To model hybrids with films, the data for SRPP with films were used (see Figure 2-60 in “2.5 Influence of weave architecture”). The films result in a slightly higher strength, and a sharper peak for the SRPP failure.

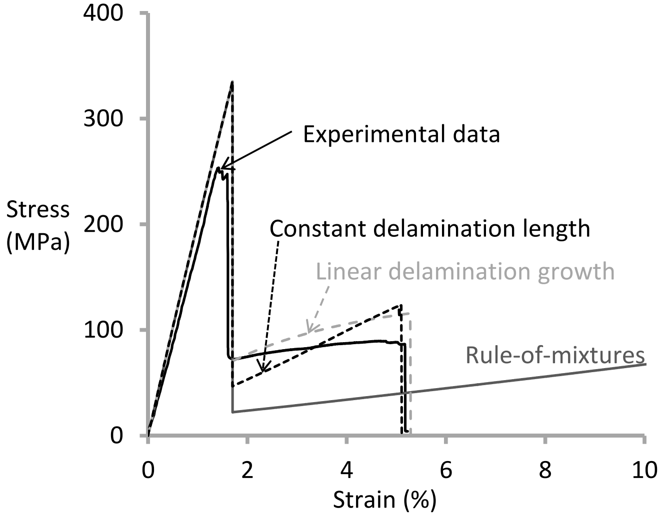

Figure 3-35: Comparison between predictions and measurements of 0°/90 plain weave intralayer hybrids with films. The rule of mixtures prediction is only shown until 10% strain for the sake of clarity.

The developed model used two approaches: a linearly growing delamination length, and a constant delamination length. Since this is a 0°/90° lay-up, only half of the carbon fibres are in the tensile direction. The 90° carbon fibres were assumed to have properties similar to the SRPP and are not taken into account in the model. This is a reasonable assumption, as the transverse CFRPP stiffness is similar to the SRPP stiffness.

Both predictive models were adapted to achieve the best possible fit. In the linear delamination growth prediction, the delamination/debonding grew linearly from 20 mm to 80 mm in the strain interval between 1.7% and 12% global strain. The failure, however, occurred earlier than 12%, as the SRPP locally exceeded its failure strain in the delaminated region at 5% global strain. At that point, the model was interrupted. In the constant delamination length model, the delamination is set to 36 mm and kept constant.

Both predictive models are unable to fully capture the experimental data. Both models overestimate the strength II, indicating that some SRPP damage was introduced when the CFRPP failed.

Conclusion

Intralayer hybrids of SRPP and CFRPP are able to combine the high stiffness and high strength of carbon fibre composites, without losing the ductility of the SRPP. This results in a novel hybrid composites with an interesting stiffness-toughness balance. The main conclusions are:

- The stiffness and strength of the 0° lay-up was twice as high as that for the 0°/90° lay-up, while the lay-up did not significantly affect the ductility.
- The carbon fibres still contribute after their failure, which can be seen from the improvements compared to the linear rule of mixtures. A more refined model, which assumes a linear delamination growth, was set up to further understand the tensile behaviour of these hybrids.
- The satin and plain weave patterns displayed similar mechanical properties. The plain weave pattern had a slightly higher strength in the second part of the tensile diagram, as this pattern was less affected by the carbon fibre failure. The larger number of cross-overs limits the initial debonding length, and thereby also the damage to the SRPP.
- The addition of films, which increased the intralayer bonding, tended to localise the strain after the carbon fibre failure. This increased stress in the second part of the tensile diagram, but reduced the ultimate failure strain. While films may be necessary for thermoformability, they reduce the ultimate failure strain due to the increased intralayer bonding.

3.4.2 Effect of carbon fibre volume fraction

The previous subsection investigated the tensile behaviour of hybrid composites with a carbon fibre V_f of about 22%. This subsection analyses how the mechanical properties depend on the carbon fibre V_f. In contrast with the 300 μm prepregs used in the previous subsection, the hybrid composites in this subsection were produced with 160 µm prepregs (see Table 3-5). The process was also scaled up to pilot scale compared to the cloths woven on lab scale and used in the previous subsection. There were no films added between the woven layers to maximise the ultimate failure strain.

Apart from tensile behaviour, this subsection also analyses the flexural behaviour and impact resistance. But first, the intralayer bonding of these hybrid composites will be discussed, as this was proven to be a crucial parameter in hybrid SRCs (see “3.4.1 Tensile behaviour”).

Previously, the carbon fibre volume fraction was determined using matrix burn-off. This method was, however, found to be inaccurate for low V_f. Therefore, this subsection and the next will use the methodology based on areal densities (see “3.2.9 Fibre volume fraction determination”).

Sample quality

The compacted sheets have a good surface finish immediately after hot compaction. A few hours later however, surface defects start to appear in the 3% and 7% hybrids. These defects are obvious with the naked eye, but difficult to capture in a photograph. Nevertheless, Figure 3-36 attempts to visualise these defects. Similar features were also present in the intralayer hybrids made with the 300 µm prepregs. This surface issue is only discussed now because the previous subsection focused on tensile behaviour, on which the surface defects only have a minor influence.

These surface defects are out-of-plane undulations of the carbon fibre prepregs. When the sheets are cooled down from the hot compaction temperature, the PP tapes have a strong tendency to shrink. The coefficient of thermal expansion of woven SRPP is $70\text{-}80.10^{-6}\ K^{-1}$ [249], whereas that of UD CFRPP is close to $0\ K^{-1}$ in the fibre direction [123,137,138]. This large difference in thermal expansion coefficient causes compressive stresses on the carbon fibres. Since pressure is still applied during the cooling down process, the out-of-plane undulations can only appear after removal from the press. The undulations appear a few hours after removal from the press, as the creep of the PP reduces the resistance against these undulations.

The 11% hybrids only have some small out-of-plane undulations (see Figure 3-36). It should be kept in mind that 11% carbon fibre corresponds to 34% of CFRPP by volume. The increased CFRPP fraction has three consequences:

- The reduced SRPP fraction causes a reduction in the driving force for shrinkage.
- The increased CFRPP fraction makes the hybrid composite stiffer and more resistant against local out-of-plane undulations.
- The increased CFRPP fraction adds additional matrix material, which is expected to increase the bonding of the material.

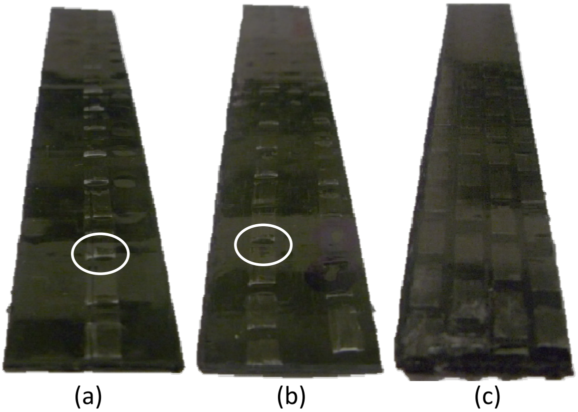
(a) (b) (c)

Figure 3-36: Surface quality of the hybrid SRPP samples: (a) 3% hybrid, (b) 7% hybrid, and (c) 11% hybrid. Some examples of out-of-plane undulations are highlighted using a white circle.

The SRPP shrinkage also caused cracks to appear inside the material, both at the interface between CFRPP and SRPP, and inside the CFRPP tapes (see Figure 3-37). These cracks may function as initiation points for failure.

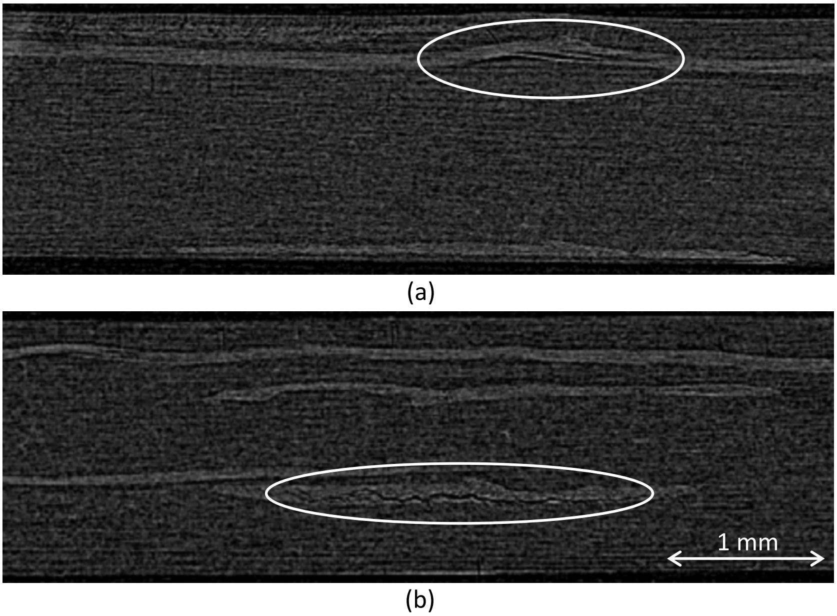

(a)

(b)

Figure 3-37: MicroCT images with cracks encircled in white: (a) between the SRPP (dark grey) and CFRPP (light grey), and (b) inside the CFRPP.

A vital observation is the fact that changing from 300 μm to 160 μm prepregs seemed to reduce the surface defects. The CFRPP prepregs in the hybrid composite are forced to undulate due to the large thickness difference with the 50 μm thick PP tapes. The SRPP shrinkage makes these undulations more pronounced and causes cracks (see Figure 3-37). Two strategies for solving the surface and cracking problem are thus proposed:

- Improving the adhesion between carbon fibre and PP either by applying a sizing or by modifying the PP chemistry.
- Reducing the thickness difference between PP tapes and CFRPP prepregs.

An alternative strategy is to reduce the SRPP shrinkage, but this is not possible without sacrificing other properties. This strategy will thus not be used.

Intralayer bonding

Adding films strongly reduced the tensile failure strain of hybrid SRPP (see "3.4.1 Tensile behaviour"). This was attributed to the increased intralayer bonding. Adding more CFRPP prepregs may cause a similar increase in the intralayer bonding for two reasons:

- The CFRPP prepregs contain excess PP matrix (see Figure 3-10b).
- The reduced SRPP fraction decreases the need for PP matrix, as fewer voids need to be filled.

The peel strength indeed displays a strong increase with increasing carbon fibre volume fraction (see Figure 3-38). The peel strength of the hybrid composite with the highest V_f is nearly the same as for SRPP with films. It should be noted that the observed increase is not caused by the increased stiffness of the layers. This unwanted influence was avoided by performing the peel strength tests on samples with carbon fibres only in the 90° direction (see "3.2.6 Peel strength tests"). The additional carbon fibres will therefore have only a minimal effect on the stiffness of the peel samples.

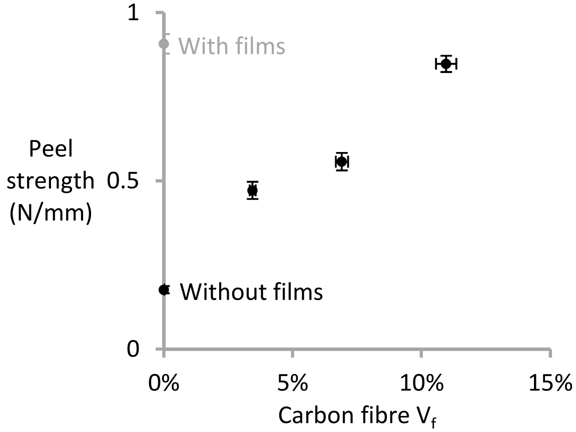

Figure 3-38: Peel strength of hybrid SRPP with 160 µm prepregs as a function of the carbon fibre V_f. The peel strength value for SRPP with films is added to facilitate comparison.

Tensile behaviour

The tensile behaviour of the intralayer hybrid composites is presented in Figure 3-39. Increasing the carbon fibre V_f increases the CFRPP peak, while the SRPP peak is slightly reduced. While the tensile behaviour of the 3% and 7% hybrids is relatively similar, the ultimate failure strain of the 11% hybrid is strongly reduced. This behaviour resembles that of hybrid SRPP with films in “3.4.1 Tensile behaviour”. Immediately after the CFRPP failure, the CFRPP prepregs partially debond, but the strong intralayer bond prevents it from growing over the entire length (see Figure 3-40b). This causes strain localisation and therefore a higher stress level immediately after CFRPP failure. The strain localisation however also causes premature failure of the SRPP. In the 3% and 7%, the debonding of the CFRPP prepregs does spread over the entire sample (see Figure 3-40a), allowing the SRPP to maintain its ductility. This illustrates that there is an upper limit of carbon fibre fraction that still leads to high ultimate failure strains.

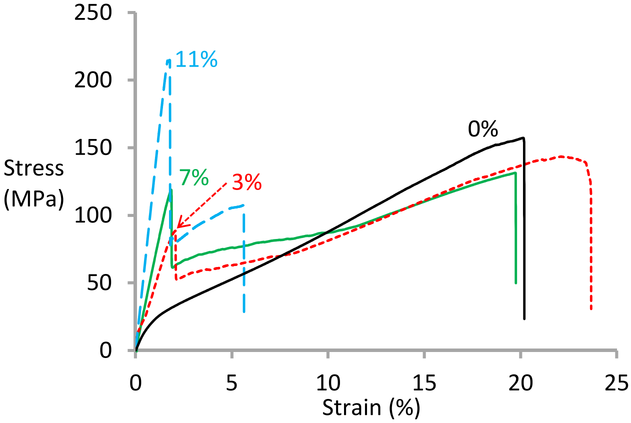

Figure 3-39: Representative tensile diagrams of the hybrid composites with 160 µm prepregs for different carbon fibre V_f.

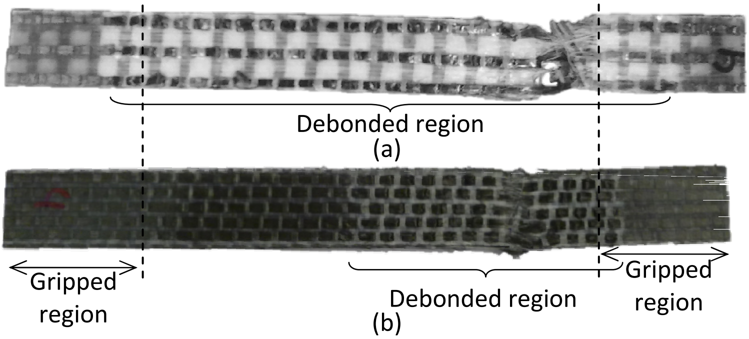

Figure 3-40: Hybrid samples after a tensile test: (a) 7% hybrid, and (b) 11% hybrid. The debonded region extends slightly into the gripped region.

The tensile properties are summarised as a function of the carbon fibre V_f in Figure 3-41. The stiffness increases with increased carbon fibre V_f, but this increase is slower than expected from CLT, see Figure 3-41a. This is attributed to the out-of-plane and in-plane undulations of the CFRPP in the hybrid composite (see Figure 3-36). These undulations are less severe in the

11% hybrid, compared to the 3% and 7% hybrids. The tensile modulus of the 11% hybrid is indeed closer to the CLT predictions in relative terms than that of the other two hybrids.

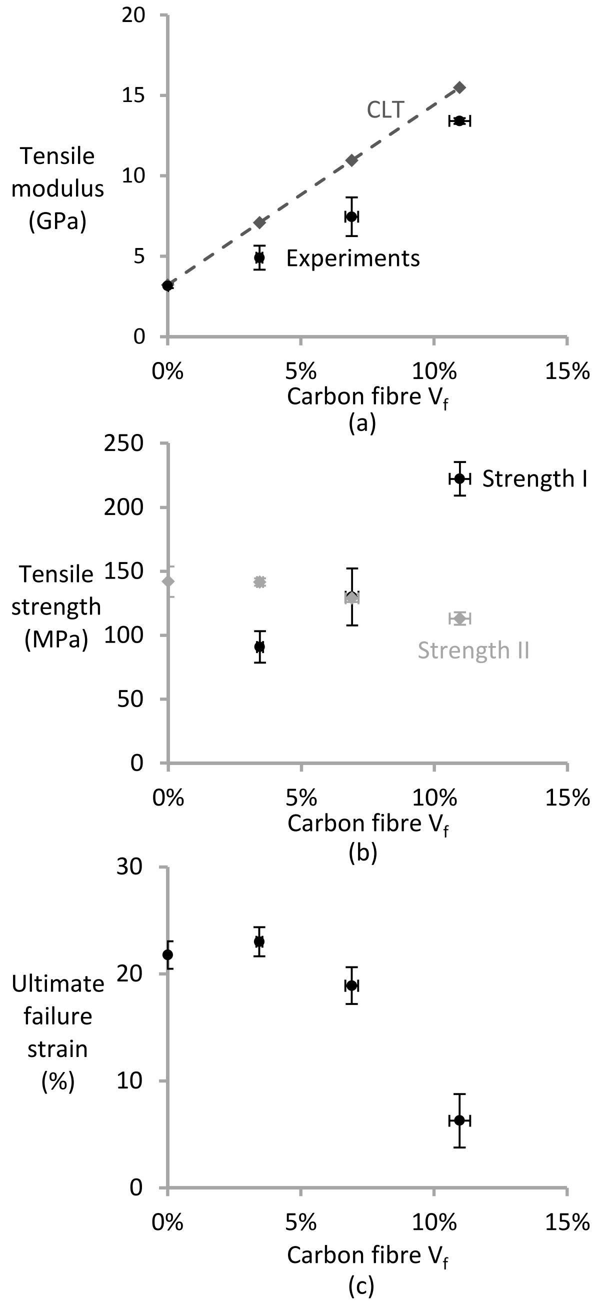

Figure 3-41: Tensile properties of hybrid composites with 160 µm prepregs as a function of the carbon fibre V_f: (a) tensile modulus, (b) tensile strength, and (c) ultimate failure strain.

Figure 3-41b demonstrates that the tensile strength of the CFRPP peak increases with increased carbon fibre volume fraction, while the strength of the SRPP peak decreases. For the 3% cloth, the SRPP peak is higher than the CFRPP peak, meaning that the additional carbon fibre did not influence the overall strength. The CFRPP and SRPP peaks have the same height in the 7% cloth. The tensile strength of the 11% hybrid is nearly twice that of the 7% cloth, but the ultimate failure strain is reduced to 6.3% (see Figure 3-41c). This strong reduction in failure strain is attributed to the strong intralayer bonding (see Figure 3-38), which prevents the debonding from spreading over the entire sample (see Figure 3-40).

The addition of the carbon fibre to SRPP also strongly increased the yield stress. This was increased from about 20 MPa for pure SRPP to 90 MPa (see Figure 3-39) by adding just 3% of carbon fibre. This yield stress is often used as a practical limit above which the material is not used anymore. This widens the applicability of SRPP and can be an additional reason of hybridising SRPP.

Flexural behaviour

While tensile and impact performance are the main focus of this study, it is also worthwhile looking into the flexural behaviour. The focus lies on the flexural modulus, as it was not possible to achieve a fracture on the tensile side of the specimens. Buckling on the compression side always occurred, even at different span lengths and in four point bending instead of three point bending. Although the flexural strength increases with increased carbon fibre V_f, its exact value could not be clearly defined from the diagrams (see Figure 3-42). This subsection therefore focuses on the flexural modulus.

An important difference in flexural behaviour is the smoothness of the flexural diagrams. The 0%, 3% and 7% show smooth curves, whereas the 11% shows some distinct peaks. These peaks correspond to buckling of the carbon fibre yarns on the compressive side. For the 3% and 7% hybrids, the out-of-plane undulations (see Figure 3-36) act as pre-buckled locations, hence causing a smooth stress evolution. These pre-buckled locations are less prominent in the 11% hybrids. When buckling occurs in this hybrid, it occurs suddenly and is accompanied by a stress drop (see Figure 3-42).

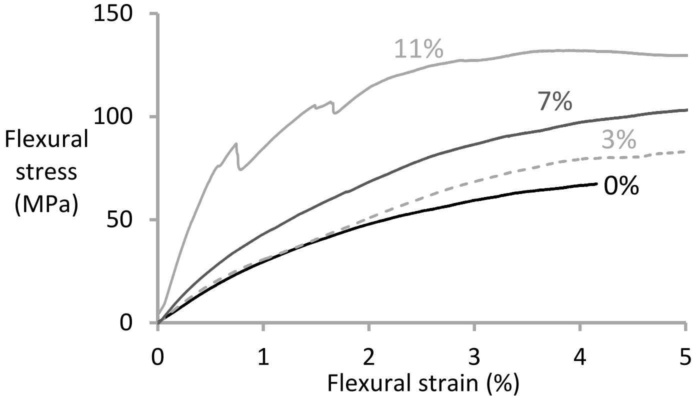

Figure 3-42: Flexural stress-strain diagrams of hybrid composites with 160 µm prepregs for four different carbon fibre V_f.

The flexural modulus increases slowly up until a carbon fibre V_f of 7% (see Figure 3-43). For the 11% hybrid however, the flexural modulus is strongly increased. This is attributed to carbon fibre undulations, which are prominent in the 3% and 7% hybrids, but largely absent in the 11% hybrid (see Figure 3-36). Nevertheless, CLT still overpredicts the flexural modulus of the 11% hybrid. This is attributed to:

- the crimp in the CFRPP prepregs,
- the in-plane undulations of the carbon fibres,
- the out-of-plane undulations of the CFRPP prepregs.

The contribution of the out-of-plane undulations is expected to be small, as the surface contained only a few, small undulations (see Figure 3-43).

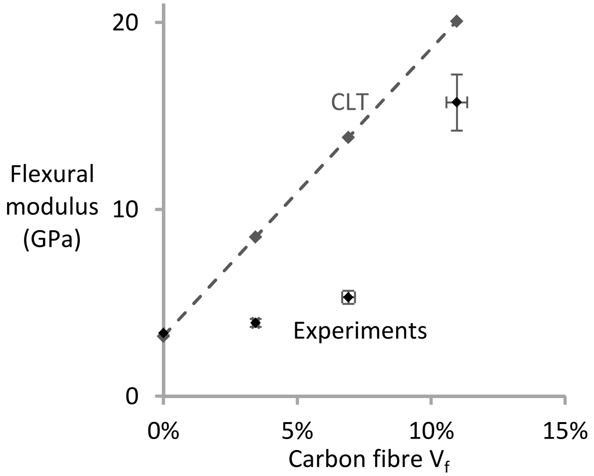

Figure 3-43: Flexural modulus of hybrid composites with 160 µm prepregs as a function of the carbon fibre V_f.

Penetration impact resistance

For penetration impact resistance, it is instructive to compare hybrid CFRPP/SRPP to pure CFRPP composites. Since a weave with only CFRPP prepregs was not available, literature data were used. Unfortunately, the majority of available literature data are for a different fibre/matrix combination or using a different type of impact test. The data that most closely resemble the presented data quotes a value of 9.6 J/mm and 12.9 J/mm for carbon fibre thermoplastic composites [255]. These values were obtained for polyether ether ketone (PEEK) and polyphenylene sulphide (PPS) respectively. Their clamp however had an inner diameter of 50.8 mm, compared to 40 mm in this study. The quoted values would be lower if they were tested on a 40 mm clamp [256]. Therefore, 10 J/mm was chosen as the value for a pure CFRPP composite, which is three times lower than for SRPP.

The penetration impact resistance of the hybrids decreases with increasing carbon fibre V_f (see Figure 3-44). This is expected because a ductile material is partially replaced by a brittle material. Whether this decrease follows the rule of mixtures depends on which data reduction method is used. For hybrid composites, the difference between the full method and half peak method (see Figure 3-19) is significant. This indicates that a significant portion of the energy is absorbed after the initial fracture of the specimen. The experimental data points agree well with the rule of mixtures for the full method. The experimental data points for the half peak method however, are significantly lower than its corresponding rule of mixtures. This would indicate a strong decrease of the penetration impact resistance with increased carbon fibre V_f. The full method however, seems more relevant as it also takes into account the additional energy absorbing mechanisms introduced by hybridisation. The main additional mechanisms are thought to be further fibrillation of the PP tapes and debonding of the CFRPP tapes from the surrounding SRPP.

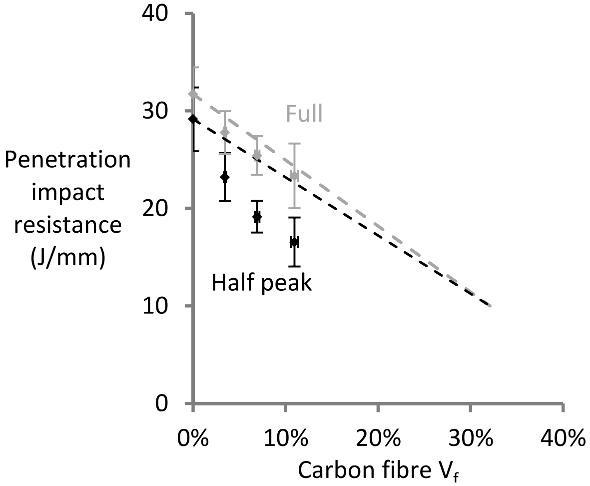

Figure 3-44: Penetration impact resistance of hybrid composites with 160 µm prepregs as a function of the carbon fibre V_f. Dashed lines indicate the linear rule of mixtures, in which 10 J/mm is assumed for the full CFRPP composite. Results for the half peak and full method are compared.

The hybrid samples have a similar appearance after penetration (see Figure 3-45) than the non-hybrid samples compacted at 188°C (see Figure 2-39b and e). This includes fibrillation and debonding of the PP tapes, which is presumably the main energy absorption mechanism. Adding carbon fibres does not prevent these mechanisms from occurring. It may however be that fibrillation and debonding are less prominent in hybrids due to the improved intralayer bonding, but this is difficult to quantify.

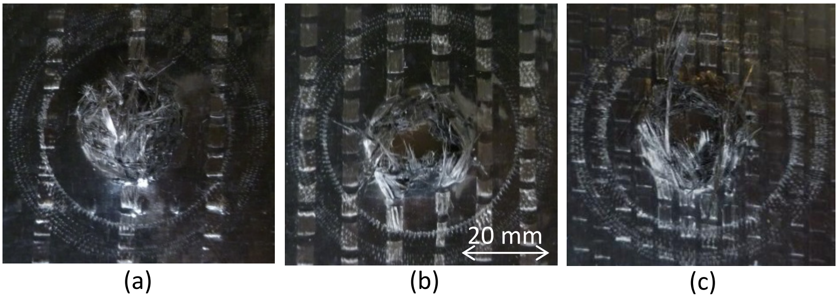

Figure 3-45: Sample appearance after penetration: (a) 3% hybrid, (b) 7% hybrid, and (c) 11% hybrid.

Adding carbon fibres reduces the SRPP fraction, but also increases the intralayer bonding (see Figure 3-38). Which of these two effects causes the decrease in penetration impact resistance in Figure 3-44, is currently unclear. Therefore, 7% hybrid cloths were interleaved with PP films to increase the intralayer bonding. This reduced the penetration impact resistance by about 20% for both data reduction methods (see Figure 3-46), while the thickness increased by only 5%. This proves that the intralayer bonding is at least partially responsible for the decrease observed in Figure 3-44.

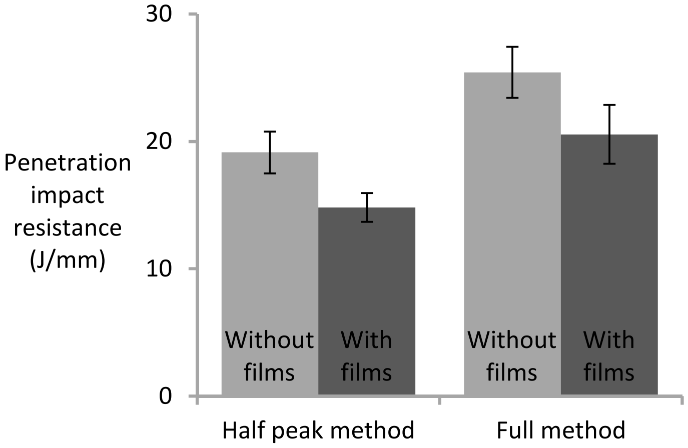

Figure 3-46: Penetration impact resistance of 7% hybrid composites with 160 µm prepregs without and with films. The difference between both data reduction methods is explained in Figure 3-19.

Non-penetration impact resistance

The subsection "2.4.2 Non-penetration impact resistance" used three different methods to assess the non-penetration impact resistance of SRPP: ultrasonic C-scans, backlight imaging and indentation depth. Ultrasonic C-scans were found unsuitable, as the cracks due to the PP tape shrinkage (see Figure 3-37) as well as the SRPP-CFRPP boundaries caused too much reflection. Backlight imaging was ruled out as well, as the CFRPP makes the hybrid SRPP opaque. Therefore, the non-penetration impact resistance was evaluated using the indentation depth after a 15 J impact event.

The 3% and 7% hybrids have nearly the same plastic indentation depth as the SRPP reference sample (see Figure 3-47). For the 11% hybrid however, the plastic indentation depth was significantly lower. This is attributed to

- The increased flexural modulus of this hybrid (see Figure 3-43).
- The delayed start of carbon fibre fracture in terms of overall stress or energy.
- The delayed onset of plastic yielding of SRPP, as the carbon fibres carry the majority of the stress.

There is however one vital caveat: while all samples contained the same number of layers, the thickness of each layer increased with increasing carbon fibre V_f. While the average sample thickness was 1.2 mm for the reference SRPP sample, it increased to 1.8 mm for the 11% hybrids (see Table 3-5). For penetration impact resistance, such thickness differences are often compensated for by dividing the absorbed energy by the sample thickness. For indentation depth, such normalisation would not make sense, as thicker samples are expected to have a smaller indentation. The number of layers could be changed to maintain the same thickness. This was impossible with the available material, given that a balanced and symmetric lay-up is required. More versatility would be possible if the CFRPP prepregs were woven in both directions, but such material was not available.

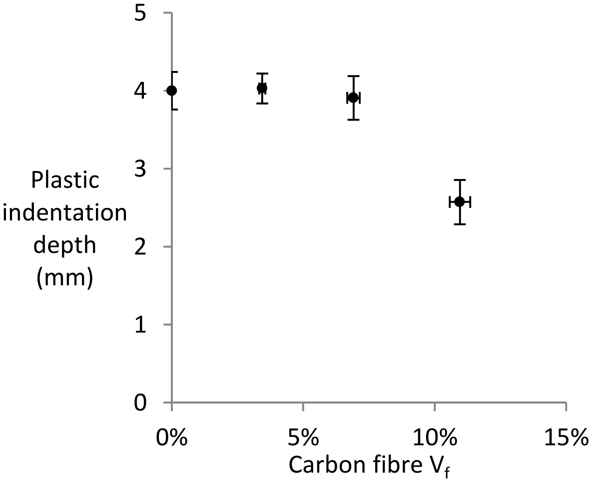

Figure 3-47: Plastic indentation depth of hybrid composites with 160 µm prepregs after a 15 J impact event as a function of the carbon fibre V_f.

The damage mechanisms in intralayer hybrids are different from those in SRPP. The impact energy was not high enough to cause significant carbon fibre failure. Two types of damage mechanisms after a 15 J impact event were observed. The first type is local debonding and buckling of the CFRPP prepregs (see Figure 3-48a), while the second type is debonding of the prepreg along its length (see Figure 3-48b). The two observed damage types are related to the poor bonding between carbon fibre and PP. When the sample deflects during the impact event, some carbon fibres break and debond along their length. This is confirmed by the dry appearances of some of the bundles. When the sample springs back however, the frictional forces prevent the broken carbon fibres from returning to their original position. This causes some small, local buckling of the CFRPP tapes.

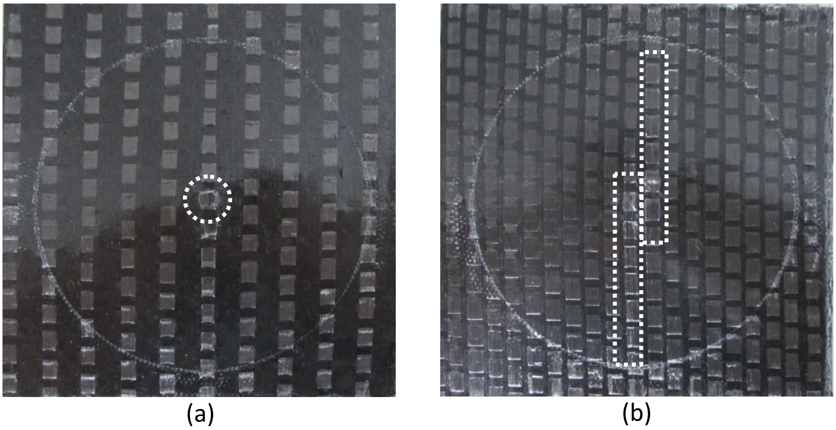

Figure 3-48: Damage types after a 15 J impact event on intralayer hybrids: (a) local debonding and buckling in a 7% hybrid, indicated by the white circle, and (b) debonding along the length of prepreg in a 11% hybrid, indicated by the white rectangles.

Conclusion

The carbon fibre volume fraction had a large effect on the mechanical properties of CFRPP/SRPP intralayer hybrids. The following trends were observed upon increasing the carbon fibre V_f:

- The intralayer bonding strongly increased due to the additional PP matrix present in the CFRPP prepregs.
- The tensile modulus increased, whereas the overall strength of the hybrid composite only increased for carbon fibre volume fractions above 7%.
- The tensile failure strain of SRPP was maintained for 3% and 7% hybrids, but strongly reduced for the 11% hybrids. This indicates that there is an upper limit for the carbon V_f to maintain the SRPP ductility.
- The yield stress of hybrid composites was increased by at least a factor of four compared to pure SRPP, which may be an important benefit in practical applications.
- The flexural modulus and strength increased, but these increases were limited for the 3% and 7% hybrids due to out-of-plane

undulations. The increase was more pronounced for the 11% hybrids, where these undulations were smaller.

- The penetration impact resistance reduced according to a rule of mixtures, but only for the full method. The indentation depth was significantly reduced for the 11% hybrid, but this was mainly due to the increased sample thickness.

3.4.3 Effect of adhesion

The hybrids in subsection “3.4.1 Tensile behaviour” maintained the SRPP ductility in tension, except when films were added. Subsection “3.4.2 Effect of carbon fibre volume fraction” revealed that there is an upper limit for the carbon fibre V_f to maintain this ductility in tension. In both cases however, the CFRPP prepregs contained out-of-plane undulations, which significantly reduced the flexural properties. Reducing the thickness from 300 μm to 160 μm seemed insufficient to avoid this issue. Recently however, a Japanese research project developed new ultrathin CFRPP prepregs. These prepregs have a thickness of only 60 μm, which is close to the 50 μm thickness of the PP tapes. A second crucial difference is that the PP matrix was modified with maleic anhydride (MA) to improve adhesion with carbon fibre. The improved bonding should hamper the development of the cracks observed in Figure 3-37 and reduce out-of-plane undulations. Ultrathin prepregs with regular PP were not available.

For this subsection, two hybrid cloths will be used: 7%MA and 16%MA (see Table 3-5). These cloths were also combined into a 7/16%MA hybrid, where the four outer layers are 16%MA and the four inner layers are 7%MA. The objective of this lay-up is to find a better balance between flexural performance, impact resistance and carbon fibre V_f.

Sample quality

Surface quality was an issue in the hybrids with 160 μm prepregs. This issue was resolved in hybrids with 60 μm prepregs (see Figure 3-49). The samples were however not scanned in microCT. Based on the visual appearance of the samples, it seems reasonable to assume that the sub-surface cracks were not present in the 60 μm prepreg hybrids. This is a significant advantage compared to the 160 μm prepreg hybrids, in which these cracks were present (see Figure 3-37). It is unclear whether these improvements are caused by the improved adhesion of the MAPP or by the reduced thickness of the prepregs.

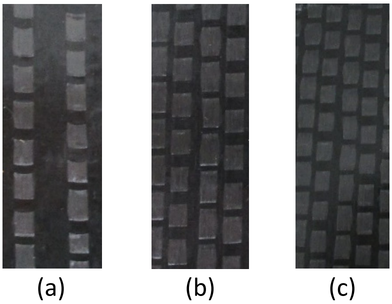

Figure 3-49: Surface quality of the hybrid SRPP samples: (a) 7%MA hybrid, (b) 7/16%MA hybrid, and (c) 16%MA hybrid.

Intralayer bonding

The two previous subsections demonstrated the importance of the intralayer bonding. A side effect of the thinner MAPP prepregs used in this subsection, is the improved bonding between carbon fibres and PP matrix as well as between the layers. The effect on the peel strength is indeed pronounced, as the 7%MA hybrid already has the same peel strength as SRPP with films (see Figure 3-50). The 16%MA hybrid has an even higher peel strength. The increase in peel strength with increased carbon fibre V_f is more pronounced than the increase for the 160 µm prepreg hybrids with regular PP. This stronger intralayer bonding is expected to have a large influence on the tensile properties.

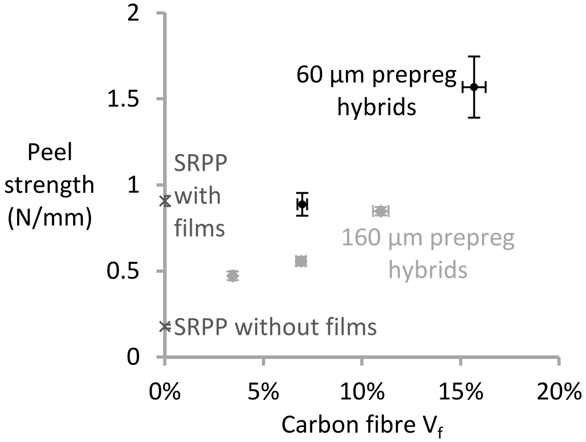

Figure 3-50: Peel strength of hybrid composites with 60 µm prepregs as a function of the carbon fibre volume fraction. The peel strength value for SRPP with films and for the 160 µm prepreg hybrids were added to facilitate comparison.

Tensile behaviour

The tensile behaviour of the hybrid composites strongly depends on the carbon fibre V_f (see Figure 3-51). In the 7%MA hybrids, the strong intralayer bonding already causes a significant loss in the SRPP ductility. This loss is even more pronounced in the 16%MA hybrids. The 7/16%MA hybrids display intermediate behaviour: some have a strong failure strain reduction like the 16%MA hybrids, while others have a failure strain similar to that of the 7%MA hybrids.

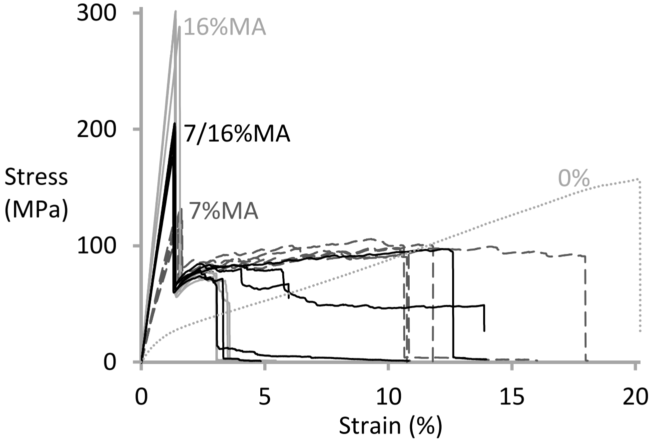

Figure 3-51: Tensile diagrams of the hybrid composites with 60 µm prepregs for different carbon fibre V_f.

The tensile properties of the hybrid composites are summarised in Figure 3-52. The tensile modulus now closely follows the predictions from CLT (see Figure 3-52a). This corresponds with the observation that the out-of-plane undulations were avoided by using the 60 µm prepregs with MAPP.

The tensile strength seems to follow a bilinear rule of mixtures with an initial reduction in strength (see Figure 3-52b). The actual strength of the SRPP fraction is never reached due to the damage introduced by the CFRPP failure. This can also be observed by comparing the 0% curve with the 7%MA curve in Figure 3-51.

The ultimate failure strain strongly reduces with increased carbon fibre V_f. This is a direct consequence of the improved intralayer bonding, which prevents the debonding from growing over the entire length of the sample.

Perhaps the optimal configuration would be a 5%MA hybrid. Based on the results in Figure 3-52, this hybrid would be expected to maintain most of the failure strain of the SRPP and avoid a large load drop at CFRPP failure (see Figure 3-51). Simultaneously, this layup would double the stiffness and increase the yield stress by a factor of five.

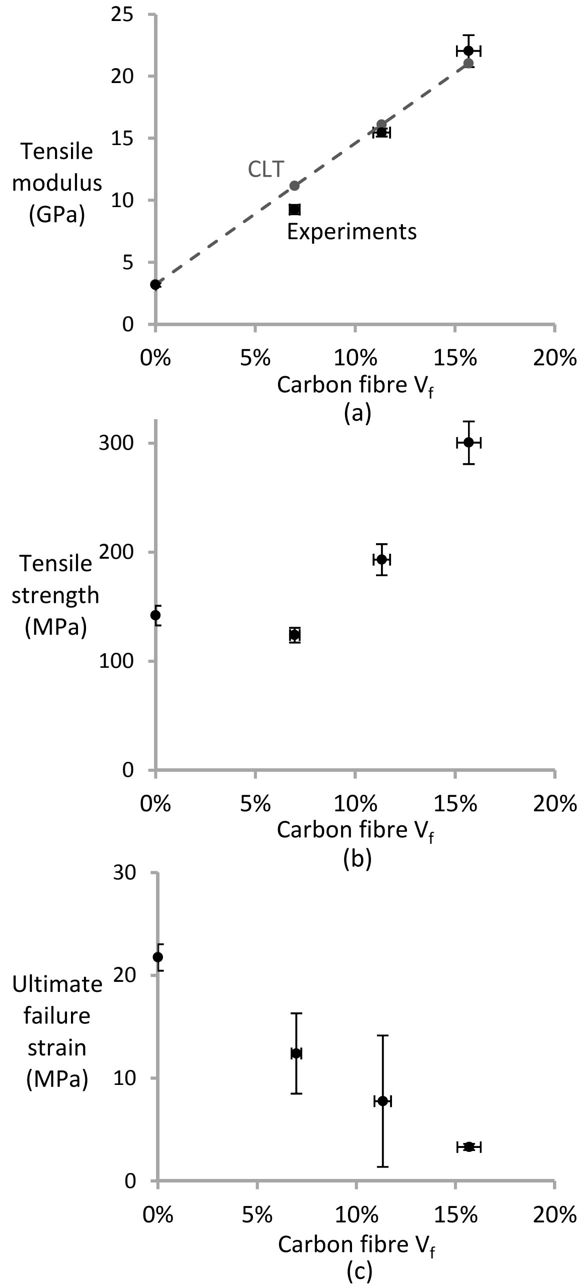

Figure 3-52: Tensile properties of hybrid composites with 60 µm prepregs as a function of the carbon fibre V_f: (a) tensile modulus, (b) tensile strength, and (c) ultimate failure strain.

The 7%MA hybrid can be compared to the 7% hybrid from subsection "3.4.2 Effect of carbon fibre volume fraction". The tensile modulus of the 7%MA hybrid is 9.3 ± 0.3 GPa compared to 7.5 ± 0.8 GPa for the 7% hybrid. This significant difference is attributed to the in-plane and out-of-plane undulations of the carbon fibres in the 7% hybrid (see Figure 3-36). Their tensile strengths are however similar: 124 ± 5 MPa for the 7%MA hybrid and 130 ± 14 MPa for the 7% hybrid. This indicates that the undulations do not affect the tensile strength. The largest difference is found in the ultimate failure strain: 12.4% ± 3.2% for the 7%MA hybrid compared to 18.9% ± 1.1% for the 7% hybrid.

Flexural behaviour

The flexural behaviour of the hybrid composites with 60 µm prepregs (see Figure 3-53) is improved significantly compared to that of the 160 µm prepreg hybrids (see Figure 3-42). The flexural modulus increases directly with carbon fibre V_f (see Figure 3-54), while this was not the case for the 160 µm prepreg hybrids (see Figure 3-43). This is attributed to a large reduction of the out-of-plane undulations.

CLT still slightly overpredicts the flexural modulus in all cases. This overprediction seems surprising, as the tensile modulus predictions agreed well (see Figure 3-52a). Most likely, this is due to the fact that CLT neglects the out-of-plane shear deformations. This shear contribution may be important due to the large difference in stiffness between SRPP and CFRPP.

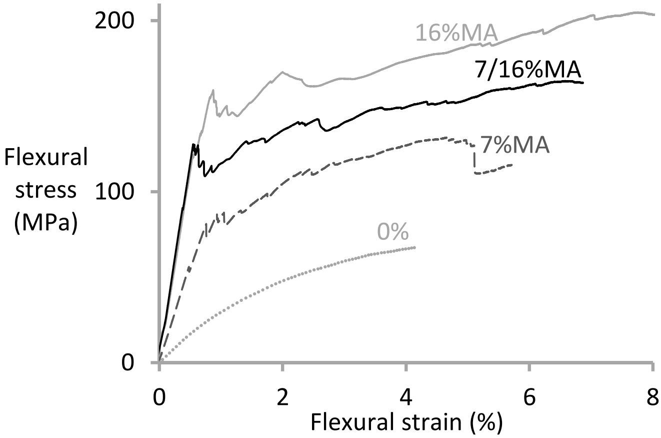

Figure 3-53: Flexural stress-strain diagrams of hybrid composites with 60 µm prepregs for four different carbon fibre V_f.

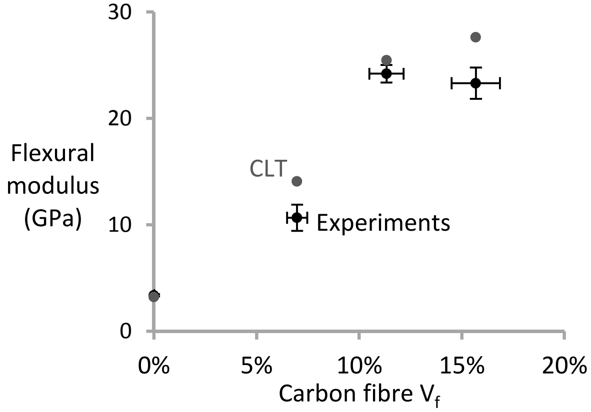

Figure 3-54: Flexural modulus of hybrid composites with 160 µm prepregs as a function of the carbon fibre V_f.

The flexural modulus of the 7%MA hybrid is twice as high as that of the 7% hybrid. This highlights the importance of adhesion for maximising the flexural modulus. Adhesion affects the flexural modulus both directly and indirectly. The direct affect occurs when the intralayer bonding is poor, and the layers can move relative to each other in bending. This effect is expected to occur only after 0.3% of strain, and therefore should not affect the modulus calculation. The indirect effect occurs through the increased undulations for poorly bonded hybrids (see Figure 3-36 compared to Figure 3-49). This effect is thought to be more important than the direct effect.

Penetration impact resistance

The penetration impact resistance of the hybrid composites is strongly reduced (see Figure 3-55) by the addition of the 60 µm prepregs. This increase was much smaller for the 160 µm prepregs (see Figure 3-44). The stronger reduction is attributed to the improved adhesion offered by the MAPP. The penetration impact resistance seems to increase with increased carbon fibre V_f. While this increase is small, it is in contrast with the decrease found for the 160 µm prepreg hybrids (see Figure 3-44). This indicates that carbon fibre breakage is the dominating mechanism, whereas this was debonding and splitting of the PP tapes in the 160 µm hybrids.

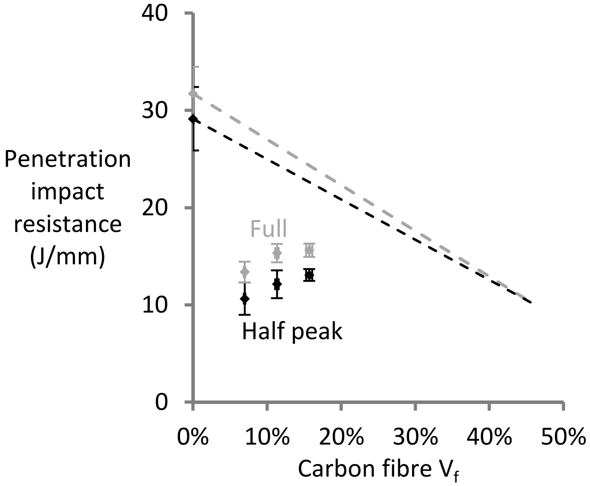

Figure 3-55: Penetration impact resistance for hybrid composites with 60 µm prepregs for four different carbon fibre V_f.

In all three hybrids, failure seems to have initiated by breaking of the carbon fibres in the 0° and 90° direction (see Figure 3-56). This caused a "+"-shaped appearance of the penetrated area. The amount of fibrillation and debonding of the PP tapes is limited. When one carbon fibre bundle breaks, the strong adhesion prevents the energy from spreading over a large area. Instead, the energy is dissipated in a small region around the striker, explaining the large reduction in the penetration impact resistance in Figure 3-55. The sample appearance is significantly different from that of the 160 µm prepreg hybrids in Figure 3-45. In those hybrids, the damage in the impacted region was more severe and circular.

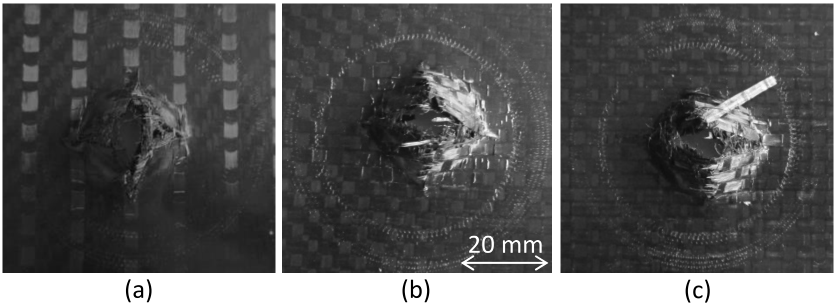

(a) (b) (c)

Figure 3-56: Sample appearance after penetration: (a) 7%MA hybrid, (b) 7/16%MA hybrid, and (c) 16%MA hybrid.

Non-penetration impact resistance

The initial tests were performed at 15 J, which was also used for the other hybrids. This energy level was nearly enough to cause penetration. The energy level was therefore lowered to 10 J.

The plastic indentation depth decreases strongly with increased carbon fibre V_f (see Figure 3-57). The 7/16%MA hybrids behave nearly the same as the

16%MA hybrids due to their similar flexural behaviour (see Figure 3-42). It should however be noted that in all cases, the indentation depth is small. The indentation is mainly caused by damage on the surface, and is not a true indentation in its typical meaning. An example of such damage is displayed in Figure 3-58. Similar to the penetration samples (see Figure 3-56), a "+"-shaped damage region appears. This includes some fibre breaks at the surface.

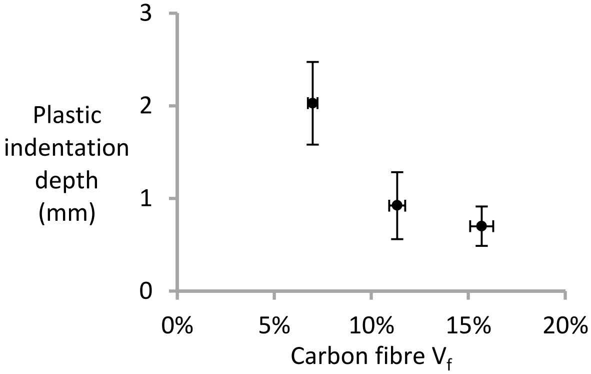

Figure 3-57: Plastic indentation depth of hybrid composites with 60 µm prepregs after a 10 J impact event as a function of the carbon fibre V_f.

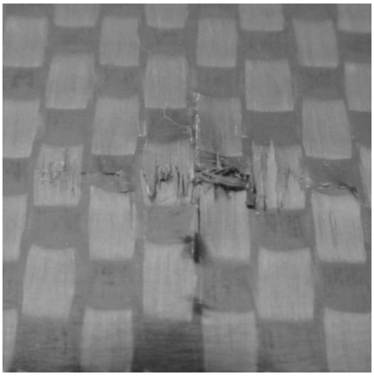

Figure 3-58: Photograph of the damage in a 16%MA hybrid after a 10 J impact event. The carbon fibres in the outer ply are oriented vertically.

Ultrasonic C-scans were found to be unsuitable to measure the damaged area of the 160 µm prepreg hybrids. This was attributed to: (1) cracks in the hybrids (see Figure 3-37), and (2) too much reflection of the ultrasonic waves on the SRPP-CFRPP boundaries. It is believed that these cracks are not present in the 60 µm prepreg hybrids. However, this has not yet been proven. Nevertheless, it still remained impossible to achieve suitable C-scans of these hybrids. This indicates that the reflections on the SRPP-CFRPP boundaries rather than the cracks are the real problem in C-scanning hybrid SRCs.

Conclusion

The increased adhesion of the MAPP prepregs had a large influence on the mechanical performance of hybrid SRCs. While tensile modulus, flexural modulus and flexural strength were improved, most of the other properties deteriorated. The increased adhesion of the MAPP creates a stronger intralayer bonding, which limits the debonding of CFRPP prepregs. This strongly reduces the ultimate failure strain in tension as well as the penetration impact resistance. The advantage of the 60 µm MAPP prepregs is that the surface issues were solved. It is, however, unclear whether this is caused by the increased adhesion or by the reduced thickness of the prepregs.

3.4.4 Conclusion

Intralayer hybrid composites were developed and optimised. The tensile behaviour of these hybrids strongly depends on the intralayer bonding, which is an indirect measurement of the bonding strength between CFRPP and SRPP. A weak bond was found to be crucial for maintaining the high failure strain of the SRPP.

Improving the intralayer bonding leads to improvements in the flexural properties, as buckling on the compressive side is delayed. The intralayer bonding can be strengthened by (1) using MAPP prepregs instead of PP prepregs, (2) increasing the carbon fibre volume fraction or (3) adding films. The first two strategies were found to reduce the out-of-plane undulations of the prepregs. These undulations should be avoided as they have a detrimental effect on the flexural stiffness. It also highlights the importance of selecting the right prepreg.

Increasing the carbon fibre volume fraction has a double negative effect on the penetration impact resistance: (1) it reduces the SRPP fraction, and (2) increases the intralayer bonding. The reduction in penetration impact resistance however does not correlate with the reduction in the ultimate failure strain in tension. To a certain extent, these can be controlled independently.

The low intralayer bonding caused debonding of the CFRPP prepregs during non-penetration impact testing. The increased adhesion of the MAPP prepregs also leads to fibre failure, whereas this was not observed for regular PP prepregs. The indentation depth seems to reduce for increased carbon fibre volume fractions, but this may also have been caused by the increased sample thickness. Improved techniques are required to further investigate the damage introduced by non-penetration impact of hybrid SRCs.

3.5 Conclusion

A novel class of hybrid composites with an interesting balance between stiffness, strength and impact resistance was developed. Inter- and intralayer hybrids were developed and optimised. It was shown how the damage mechanisms can be controlled in interlayer hybrids, and pseudo-ductility was achieved through fragmentation by an intelligent design. This pseudo-ductility through fragmentation was not achieved in intralayer hybrids, presumably because the carbon fibre volume fraction was too high.

Three different iterations of the intralayer hybrids were discussed. In all iterations, the importance of intralayer bonding was highlighted. This the main parameter that should be controlled to achieve an optimal balance in mechanical properties. A strong intralayer bonding reduces the ultimate failure strain in tension and penetration impact resistance, but increases the flexural properties.

Chapter 4:

Strength model for UD non-hybrid composites

This chapter describes the development of a novel strength model for UD non-hybrid composites. A versatile approach is chosen to facilitate the extension towards hybrid composites in Chapter 5. First, the stress redistributions around single fibre breaks are analysed and it is shown how they are affected by the finite element modelling parameters. Then, a strength model is introduced that uses these stress redistributions as input data. The capabilities and limitations of this model are analysed by performing a parametric study. Finally, the model is experimentally validated by comparing it with fibre failure data for synchrotron computed tomography. The understanding developed in this model will be vital for the strength model for hybrid composites.

This chapter describes the development of a strength model for UD fibre-reinforced non-hybrid composites. Chapter 5 will extend this model to UD hybrid composites. To facilitate this extension, versatility was a key requirement in the development stage.

This chapter is divided into five sections (see Figure 4-1). The state of the art section 4.1 describes the key concepts of most strength models for UD composites, and identifies possible issues with existing approaches. The benefits and drawbacks of the available models will be discussed to justify the approach used in this thesis.

Section 4.2 analyses the stress redistribution around fibre breaks. This is a crucial feature in nearly all strength models for UD composites. Parametric studies are performed for four key parameters. This section also sets up the basic procedures for incorporating these stress redistributions in a strength model. The development of this model is extensively described in section 4.3.

Section 4.4 uses the strength model to analyse the influence of the four parameters for which the stress redistribution was analysed. This section also analyses the Weibull distribution, boundary effects and size scaling, as these parameters are vital for interpreting the experimental validation in section 4.5. This section validates the developed strength model by comparing the predictions with experimental data from synchrotron computed tomography.

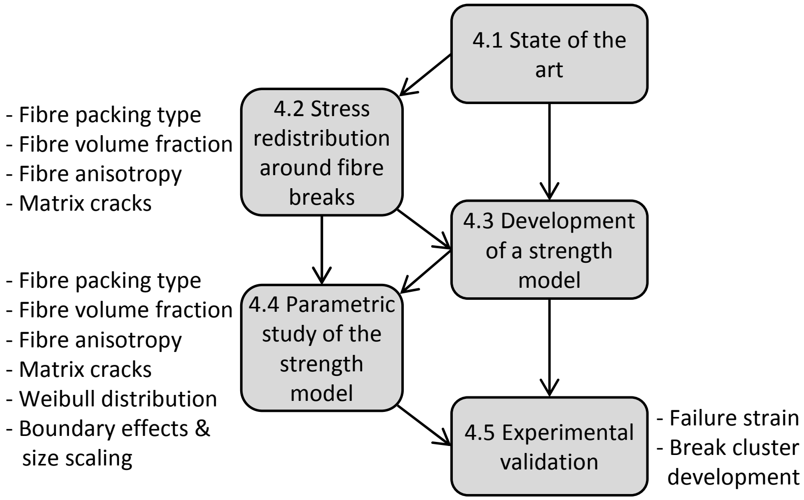

Figure 4-1: Schematic overview of the structure of this chapter.

4.1 State of the art

Predictive models are crucial for designing composite applications in an optimal manner. While some stiffness variability is unavoidable [257], predictions of composite stiffness are often used with confidence. Predictions of strength and damage development, however, remain challenging. The World Wide Failure Exercise I, II and III attempted to predict failure of multidirectional composites under triaxial loading conditions [258-260]. A large spread on the modelling predictions was found, indicating the reason for the lack of confidence. The large spread was attributed to the complex internal structure of fibre-reinforced composites and complex interactions between fibre and matrix.

The tensile failure and damage development of 0° unidirectional (UD) composites under longitudinal loadingis better understood in the composites community. Fibres do not possess a unique strength, but their strength rather follows a Weibull distribution [261]. Upon increasing the applied strain, the weakest fibres fail first. Each broken fibre locally stops carrying load and sheds that load to the nearby fibres. The matrix surrounding the fibre break is loaded in shear and transfers stress back onto the broken fibre. Therefore, the nearby fibres will carry stress concentrations over a certain length [262-264], thereby increasing their failure probability. Eventually, these stress concentrations will lead to the development of clusters of fibre breaks [147,265,266], which further intensify the stress concentrations. One of these clusters will reach a certain critical size, causing unstable propagation and hence final composite failure.

The failure development in UD composites hence has two essential aspects: (1) the Weibull distribution for fibre strength, and (2) the stress redistribution around fibre breaks. An overview of the extensive studies on both aspects will be presented in the next two subsections. Finally, different modelling approaches will be described. At various points in this state of the art review, possible issues or gaps in literature will be highlighted.

4.1.1 Weibull distribution for fibre strength

The strength of a single fibre cannot be captured in one single average value. The most commonly used fibres, such as carbon and glass, are brittle and hence exhibit a weakest-link characteristic. This means they break as soon as the weakest link is overloaded. The probability of failure is thus linked to the presence of weak links. One obvious conclusion is that a shorter fibre will have a lower failure probability and hence a higher strength. The statistical function that describes this weakest-link behaviour is the Weibull distribution.

The standard Weibull probability distribution P for fibre strength is:

$$P\left(\sigma_f\right) = 1 - \exp\left(1 - \left(\frac{L}{L_0}\right)\left(\frac{\sigma_f}{\sigma_0}\right)^m\right), \tag{4-1}$$

with L being the characteristic gauge length, L_0 the reference gauge length, σ_f the fibre strength, σ_0 the scale parameter and m the shape parameter or Weibull modulus [261]. The parameters σ_0 and L are typically calculated from single fibre tests at gauge lengths L_0 between 10 and 50 mm. Most strength models, however, require the Weibull distribution at gauge lengths L in the order of micrometers [267]. Several authors have mentioned that equation 4-1 leads to underestimations of fibre strength at short gauge lengths [267-270]. This was attributed to three causes: (1) fibre diameter variations [270-272], (2) variations of the Weibull distribution from fibre-to-fibre within the same fibre bundle [270,271,273,274], and (3) the presence of different strength-determining flaw populations [268,275]. Explaining how these causes lead to underestimations at short gauge lengths requires an extensive mathematical treatment. Interested readers can refer to the corresponding literature [268,270-275].

Modified Weibull distributions

Several other types of distributions for fibre strength have been proposed in literature. These are often referred to as modified Weibull distributions. The first type adds an exponent α to equation 4-1 to capture the gauge length dependence of the Weibull distribution [269,270,276]:

$$P\left(\sigma_f\right) = 1 - \exp\left(1 - \left(\frac{L}{L_0}\right)^{\alpha}\left(\frac{\sigma_f}{\sigma_0}\right)^m\right). \tag{4-2}$$

Equation 4-2 reduces to equation 4-1 if α equals 1. Values for α of 0.6 [269], 0.7 [276] and 0.9 [270] have been reported. A crucial consequence of this type of distribution is that the strength distribution shifts to lower strengths if L is smaller than L_0. Modelling results will hence depend on the chosen length L.

Curtin [273] proved that equation 4-2 may also arise due to processing and handling of the fibres. Curtin therefore proposed the “Weibull of Weibulls” distribution. This distribution assumes that the strength distribution along a fibre follows the standard Weibull distribution (see eq. 4-1). Based on this Weibull distribution, a characteristic strength at a certain length L can be calculated for each fibre. Curtin then assumes that the characteristic strengths of each fibre are different and follow a Weibull distribution. Such differences can be attributed to processing and handling of the fibres. With these assumptions, the distribution essentially reverts to equation 4-2, but has a more sound physical background.

Many authors have suggested that multiple strength-determining flaw populations may exist [268,275,277-281]. This leads to multimodal Weibull distributions, of which the bimodal is the most popular one:

$$P(\sigma_f)=1-\exp\left(-\left(\frac{L}{L_0}\right)\left(\frac{\sigma_f}{\sigma_{0,1}}\right)^{m_1}-\left(\frac{L}{L_0}\right)\left(\frac{\sigma_f}{\sigma_{0,2}}\right)^{m_2}\right), \tag{4-3}$$

where $\sigma_{0,1}$ and $\sigma_{0,2}$ are the scale parameters and m_1 and m_2 the Weibull moduli for the first and second flaw population, respectively. Thomason indicated that this bimodal distribution may also be caused by an inherent assumption in the Weibull distribution [282]. The Weibull distribution assumes that there is no threshold stress below which the failure probability is zero. This is a common assumption in brittle materials. If however, such a threshold stress does exist, then it can be proven that a bimodal distribution automatically arises in measurements.

Experimental issues

Three issues have been reported in the experimental determination of single fibre strengths. Firstly, Thomason [282] mentions that a minimum strength is needed to extract a fibre from a yarn prior to testing single fibres. This results in a deviation from linearity at low strength in Weibull plots. Such a deviation has been reported by many authors [269,276,283,284] and an example is plotted in Figure 4-2.

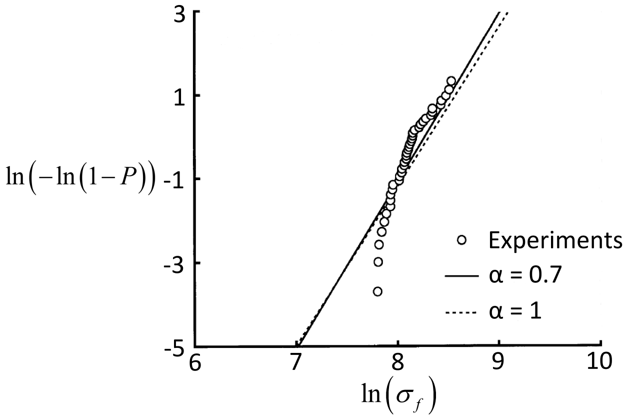

Figure 4-2: Weibull plot for carbon fibre showing the deviation from linearity at low strength. The data points indicate the experimental measurements from single fibre tests, while the trend lines are fitted according to equation 4-2 (adapted from [276], with permission from Elsevier).

Secondly, Thomason also illustrates that a low number of tests may falsely lead to the conclusion of more than one flaw population [282]. The number of tests to extract Weibull parameters typically ranges between 20 and 50 [285,286], while only in a few studies sample sizes of 100 were used [271,275]. Similarly, Berger and Jeulin [272] reported issues with the number of required tests. They proved that 30 tests are insufficient to accurately determine Weibull modulus and scale parameter [272]. Unfortunately, Berger and Jeulin did not determine the magnitude of variations this introduces in strength predictions.

Finally, clamping effects can occur in single fibre testing [281,287]. These effects are particularly pronounced at small gauge lengths for several reasons [287]. Firstly, fibre misalignment and failure in the clamps increase significantly at short gauge lengths. Secondly, the fibre stress needs to be build up through shear stresses between the glue and the fibre surface. The length of this stress build-up region in the glue is independent of the gauge length and hence its relative importance is increased at small gauge lengths. This leads to lower measured fibre strengths as the actual length of loaded material is longer than the gauge length. These effects are more pronounced for low shear strengths of the glue due to the longer stress build-up region. This may be the reason for the gauge length dependence of the Weibull distribution, as described in equation 4-2.

These issues in the experimental determination of the Weibull distribution are also reflected in differences in the Weibull data sets found in literature. For some common carbon fibre types, several Weibull distributions can be found in literature. This is for example the case for T800 [276,288] and AS4 [269,289]. Figure 4-3 plots these Weibull distributions for both fibre types. Some small discrepancies are impossible to avoid due to differences between different batches of carbon fibres. The large observed differences clearly illustrate the difficulties in accurately measuring the Weibull distribution. As the Weibull distribution is a vital parameter in strength models, this also affects the reliability of strength models.

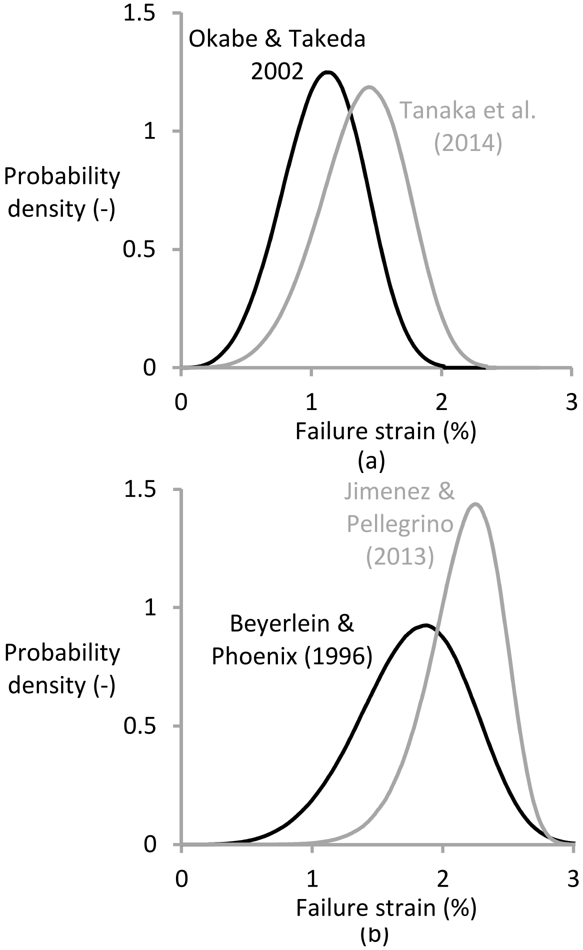

Figure 4-3: Comparison of the Weibull distribution for: (a) T800 carbon fibre at a gauge length of 50 mm [276,288], and (b) AS4 carbon fibre at a gauge length of 10 mm [269,289]. Two of these data sets contain a factor α [269,276], but any influence of this factor was avoided by choosing L equal to L_0.

4.1.2 Stress redistribution around fibre breaks

Once the first weak fibre breaks, the stress in the composite needs to be redistributed. The broken fibre locally loses its load transfer capacity and the nearby fibres are subjected to stress concentrations. This stress redistribution is often characterised by two parameters: the stress concentration factor (SCF) and the ineffective length. The stress concentration factor is defined as the longitudinal stress in an intact fibre due to fibre breaks divided by its nominal value in the absence of fibre breaks. The SCF can be expressed as an absolute value or as the percentage by which it exceeds unity. The ineffective length is a measure of the stress recovery length of the broken fibre.

Typically, this length refers to the length over which the longitudinal fibre stress is below 90% of its nominal value [142].

This stress redistribution is crucial in the failure development of composites. The two possible approaches, shear-lag and finite element (FE) models, will be described.

Shear-lag versus FE models

In 1952, Cox [290] developed the first shear-lag model (SLM) for the stress redistribution after a fibre break. SLM assumes that (1) the fibres carry all the axial loads and (2) the matrix only transmits shear loads. Hedgepeth extended Cox' approach for a single fibre to a 1D packing [152]. A 1D packing is a single-layer arrangement of parallel fibres on a straight line (see Figure 4-4a). Hedgepeth predicted a stress concentration factor (SCF) of 33% for this case [152]. Later, Hedgepeth and Van Dyke [143] extended this SLM to 2D packings, which consist of a planar arrangement of parallel fibres (see Figure 4-4b). The authors calculated an SCF of 14.6% and 10.4% for square and hexagonal 2D packings, respectively.

SLMs are straightforward to incorporate into an analytical strength model, as they give an analytical solution for the stress redistribution after a fibre break. The first SLMs, however, also had several disadvantages:

- they did not include matrix plasticity,
- they did not allow anisotropic properties of fibres,
- they could not predict matrix cracking,
- they assumed perfect fibre-matrix bonding,
- they assumed a regular packing.

Later, many authors published improved SLMs that partially resolved some of these issues [144,291-295]. The SCF has in all cases been estimated to be lower than Hedgepeth's prediction [143,152].

An alternative approach to calculate the stress redistribution is to use 3D FE models. 3D FE models are computationally intensive, which limits the number of fibres that can be included in the model. Therefore, this method on its own is insufficient to predict the full statistical nature of composite failure. Mishnaevsky et al. [296] did use FE models to calculate the strength of UD composites, but only included 20 fibres. Such low a number of fibres is insufficient to yield realistic statistical information.

FE models do yield information on the stress redistribution after a fibre break that can be used as input for strength models [146,297]. Some clear differences between FE and SLMs have been noted by several authors [263,298]. Nedele et al. [263] predicted an SCF of 5.8% for a hexagonal packing of carbon fibres, which is much lower than 10.4% predicted by Hedgepeth et al. [143]. Xia et al. [298] proved that the fibre shear deformation, which is neglected in SLMs, increases the SCFs on the nearest neighbour fibres.

Van den Heuvel et al. [299] experimentally validated the accuracy of the FE approach for calculating SCFs. This validation was performed using micro-Raman spectroscopy in a microcomposite with five fibres. In general, the results agree well with FE predictions, and small discrepancies were found only for small fibre spacings. Similarly, Wagner and Eitan [300] found that their SLM was only accurate for large fibre spacings.

Xia et al. [298] performed an in-depth comparison between shear-lag and FE models. Their results indicate that the SLMs are reasonably accurate for polymer matrix composites if:

- Fibre volume fraction is high,
- Fibre/matrix stiffness ratio is large,
- Matrix yielding occurs before fibre breakage.

Xia et al. concluded that SLMs are applicable in a wide range of properties that are typical for polymer matrix composites. Xia et al. also indicated two drawbacks of SLMs. SLMs neglect the dimensions as well as the shear deformations of the fibres. Even though this was not indicated by the authors themselves, the shear deformation is likely to be important in carbon fibre due to its anisotropic nature.

Fibre packing type

The type of fibre packing is a crucial feature of every model for stress redistribution around fibre breaks. The packing type has two important features: dimensionality and regularity (see Figure 4-4).

In early literature, 1D packings were more common than 2D packings. A 1D packing consists of a single row of fibres and hence greatly simplifies the analysis. 2D packings are, however, a more realistic representation of composites [301]. Several authors have pointed out that the SCFs in 1D packings are significantly higher than in 2D packings [143,294].

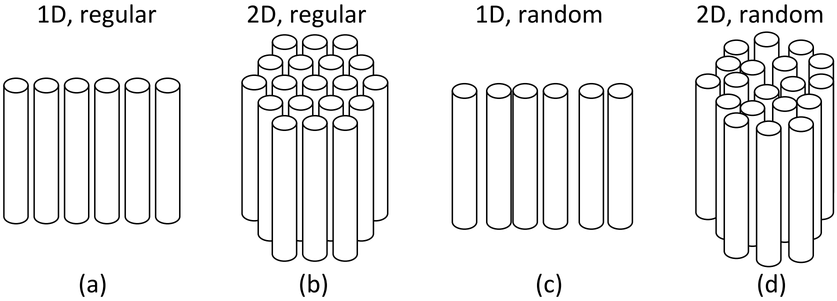

Figure 4-4: Schematic illustration of the dimensionality and regularity of fibre packings: (a) a 1D regular packing, (b) a 2D, regular packing, (c) a 1D, random packing, and (d) a 2D, random packing.

Batdorf and Ghaffarian [302] noticed a significant discrepancy between experimental and modelling results of strength of unidirectional composites. They hypothesised that variations in fibre spacing are the major cause for this discrepancy. Most models use regular packings and hence have deterministic fibre spacings. Incorporation of statistical variations in fibre spacing reduced the discrepancy between experiment and model. The authors themselves realised the limitations of their model and suggested more work was needed to confirm this hypothesis.

Landis et al. [144] introduced some degree of randomness in the square packing used in their SLM. They maintained a square packing for most fibres and either (1) only changed the position of the broken fibre or (2) only moved the nearest neighbour fibres closer to the broken fibre. Such changes affected the SCFs, but their conclusions are difficult to extrapolate to truly random fibre packings.

The number of shear-lag models for random fibre packings is limited. Only two studies have addressed this issue [144,302]. For SLMs, a statistical treatment of SCFs in a truly random 2D fibre packing seems dauntingly complex. For FE models, the lack of 2D random fibre packing models has two main reasons. Firstly, creating 2D random fibre packings is inherently difficult, as they need to be statistically equivalent to fibre packings in real fibre-reinforced composites. Fibre packing generators are often limited to fibre volume fractions of less than 55% [303], which is too low for unidirectional fibre bundles. Some generators are capable of reaching higher a fibre volume fraction, but these were not validated statistically [304,305]. Secondly, random fibre packings may lead to meshing problems due to variations in the fibre spacing.

Matrix and interface properties

The stress recovery in the broken fibre is attributed to shear stress transfer in the matrix. SLMs typically neglect the axial stresses carried by the matrix. Xia et al. [298] proved that this neglect explains part of the discrepancies between SLM and FE approaches, especially for low fibre volume fractions. Micro-Raman spectroscopy measurements proved that the SCF decreased with increasing fibre volume fraction [306-309]. Such decrease could not be explained by SLMs that neglect axial matrix stresses. Consequently, SLMs were developed that do allow the matrix to carry axial stresses [144,292,294,310]. These models revealed that SCFs decrease if the matrix stiffness increases. In fact, the SCF decreases with increased ratio of matrix over fibre modulus and decreased fibre volume fraction.

Another vital assumption concerns the stress singularity around a fibre break. Stress concentrations in the matrix around a fibre break are infinite for elastic, well-bonded materials. The matrix and interface are thus unlikely to be able to cope with this, yet many models assume perfect bonding and an intact matrix [146,263]. Three scenarios or combinations thereof can occur: (1) the matrix yields [143,264,311-315], (2) the fibre-matrix interface debonds [144,313,316], or (3) the matrix cracks in the fibre break plane [317-319]. Matrix yielding is typical in thermoplastic polymer matrix composites, and can also occur in thermosets. Matrix yielding has been shown to reduce the SCFs on intact fibres [292,299], but increase the ineffective length [145,320]. Both Nedele and Wisnom [145] and Van den Heuvel et al. [320]

indicated that the influence on the SCFs in the intact fibres was small. Fibre-matrix debonding typically occurs for weak interfacial bonds, and is common in ceramic matrix composites. This debonding reduces the SCFs on the intact fibres [145,299,321,322], but increases the ineffective length [145,292].

Matrix yielding and fibre-matrix debonding have been extensively investigated [143,144,264,311-316], but studies on matrix cracking remain scarce. Matrix cracks are commonplace in ceramic matrix composites [62], but mainly as a phenomenon occurring prior to fibre failure. In polymer matrix composites however, both phenomena are interlinked. Several authors have observed matrix cracking around fibre breaks during single fibre fragmentation tests [317-319,323,324]. This occurred typically in material systems with a strong fibre/matrix interfacial bond. Including matrix cracking in strength models for polymer matrix composites has lagged behind. Li et al. [325] and Mishnaevsky et al. [296] developed models involving matrix cracks around fibre breaks, but did not investigate the influence of these cracks on stress redistribution and composite strength.

Dynamic effects

A fibre breakage is intrinsically a dynamic phenomenon. The stress that is present in the fibre before the break is released when the fibre breaks. The fibre springs back and hence creates stress waves propagating through the composite. These dynamic effects were already investigated in 1961 by Hedgepeth [152]. Hedgepeth proved that the maximum dynamic SCF was between 15% and 27% higher than the static SCF. This study was performed for a 1D packing using SLM. Hedgepeth's dynamic SLM was improved by Ji et al. [153], but their refined analysis led to similar SCF values.

Apart from the studies from Hedgepeth [152] and Ji et al. [153], only a few other studies of dynamic SCFs are found. Xing et al. [155] extended Hedgepeth's approach towards hybrid composites (see "3.1.1 The hybrid effect"). Sakharova and Ovchinskii [326,327] performed a study similar to that of Hedgepeth [152] and Ji et al. [153], but included matrix yielding and fibre-matrix debonding. Both parameters caused a lower dynamic SCF as well as a faster decay of the stress wave with time. Their study was peformed on boron fibre-reinforced aluminium, making it difficult to extrapolate their conclusions to polymer composites.

Interactions among fibre breaks

Most studies in literature deal with the stress redistribution around non-interacting fibre breaks. Interactions among fibres must be taken into account to accurately predict final composite failure. Influence superposition rules have been developed to predict these stress redistributions around interacting fibre breaks based on solutions for a single break [313,325,328,329]. These rules use Kachanov's approach for interacting cracks in a homogeneous solid [330]. Kachanov used the solution of the stress redistribution around a single crack to deduce the stress profile around multiple cracks. By combining this approach with Hedgepeth's SLM [152], the solution for the stress redistribution around multiple fibre breaks can be predicted. The main advantage of these principles is that they can be easily incorporated in a strength model. While most work has been performed on 1D packings [294], the approach has also been extended to 2D packings [331].

Curtin and colleagues proposed another elegant approach to the problem of interacting fibre breaks by using Green’s function model [332-335]. The Green’s function is essentially a function that determines how the load from a single broken fibre is redistributed on the intact fibres. This function can be set up using either SLM or FE models, and is also suitable to determine the SCFs for multiple fibre breaks.

An alternative approach is the linear superposition principle. This principle assumes that the SCFs caused by different fibre breaks can simply be summed up. This hence neglects any interactions among fibre breaks, but remains an important approach in literature. A downside of linear superposition is that it neglects SCFs that the broken fibres exert on each other. This neglect leads to predictions that do not maintain force equilibrium.

4.1.3 Strength models for unidirectional composites

Strength models for UD composites are widely available in literature. According to Mishnaevsky and Brøndsted [336], the modelling approaches can be divided into four categories:

- Analytical models,
- Fibre bundle models,
- Fracture mechanics models,
- Continuum damage mechanics models.

Fracture and continuum damage mechanics models are helpful in understanding the basic mechanisms, but are often limited to 2D plain strain conditions and axisymmetric models [336]. Extending these models towards hybrid composites with realistic fibre packings is a daunting task and will not be attempted in this thesis. The focus hence lies on analytical models and fibre bundle models.

The load sharing rule is a crucial feature of any strength model. These rules will be reviewed first, before moving into the possible modelling approaches. The results from these strength models are not discussed in this subsection, but in the next one.

Load sharing rules

When a fibre breaks, it locally loses its load transfer capacity. This load is shed onto the nearby fibres. The number of fibres that participate in this load sharing is determined by the load sharing rule. From SLM and FE models, it is known that the nearest neighbour fibres carry the majority of this load. The second and third nearest neighbour fibres carry a small portion of the load. This type of load sharing is called local load sharing. It should be noted that the definition of nearest neighbours depends on the type of packing (see

Figure 4-4). Hexagonal packings have 6 nearest neighbours while square packings have only 4. The nearest neighbours in random fibre packings are not clearly defined, which means this concept should be avoided in random fibre packings.

Some models assume simplified load sharing rules to facilitate the development of strength models. These rules can be divided into two categories. The first rule is called equal or global load sharing [142,337-342]. This load sharing rule assumes that the load is transferred equally to all intact fibres. This rule avoids local stress concentrations and resembles the situation of a dry fibre bundle [336,343]. Some authors make a distinction between equal and global load sharing. Equal load sharing models are often based on Rosen's chain-of-bundle approach [142]. These models were popular among early researchers in the 70s till the 90s. In 1991 however, Curtin developed his global load sharing model [344,345], which was later extended by Neumeister [339,340] and Hui et al. [341]. In contrast with equal load sharing, this model only considers a single fibre. The influence of the other fibres is taken into account through their homogenised response, which leads to analytical solutions for composite strength. The global load sharing model has been particularly useful in ceramic matrix composites.

The second category is the idealised or very local load sharing rule. This rule was introduced by Harlow and Phoenix [346-349], and further developed by other authors [350-352]. This rule assumes the stress concentrations are restricted to only the nearest neighbours. Consequently, such a rule requires a clear definition of the nearest neighbour, and is limited to regular fibre packings. Very local load sharing overestimates the localisation of the stress redistribution [343], but is nevertheless considered a reasonable approximation [351].

The two simplified load sharing rules were popular in early research. Their main advantage is their simplicity, which facilitates analytical solutions. In the past decade however, more authors have shifted towards numerical approaches. The next part will describe the various modelling approaches that have been developed.

Modelling approaches

The majority of strength models for UD composites are statistical in nature. Some approaches lead to analytical solutions [148,295,338-341], while others are numerical [146,296,353-363]. The focus here lies on the modelling approaches themselves, while the results from these models will be discussed in the next subsection.

Peirce [364] and Daniels [365] were the first ones to develop the basic concepts for modelling UD composites. In 1964, Rosen [142] introduced the weakest-link theory for predicting the tensile strength of unidirectional composites. This theory is known as the chain-of-bundles model. A composite is represented as a chain of bundles in series (see Figure 4-5). If one of the bundles breaks, the entire composite fails. This is a reasonable assumption, provided splitting does not occur.

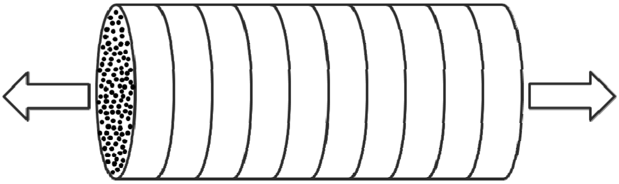

Figure 4-5: Chain-of-bundles model of Rosen [142].

The chain-of-bundles model is a general concept, but the actual failure of the bundle can be implemented in various ways. Rosen [142] for example used equal load sharing. Behzadi et al. [146] on the other hand used FE models to calculate the SCFs in a local load sharing fashion. They modelled the strength of a single bundle with a length equal to the length required for a broken fibre to recover the nominal stress level. The equation of Curtis [366] was then applied to calculate the failure probability of a certain number of bundles. It should be noted that the chain-of-bundles model assumes that each bundle in the composite (see Figure 4-5) acts independent from the bundles. Interactions among the bundles are neglected in this approach, which is expected to lead to overestimations of the strength.

Zhou and Curtin [334] proposed an elegant strength model for UD composites, which is termed the spring element model. This model was later refined by Okabe, Curtin and co-workers [293,357]. The unit cell of this model consists of longitudinal and transverse springs arranged in a hexagonal packing (see Figure 4-6a). The longitudinal springs represent fibres, while the transverse springs are used to incorporate the proper shear stiffness of the composite. An approach similar to the FE method is used to calculate force equilibrium throughout the model. The SCFs and ineffective lengths are therefore intrinsically linked to the transverse spring stiffness. Tuning this stiffness will change the stress redistribution and can be performed using either analytical equations [158] or FE models [357]. All the unit cells together form the RVE (see Figure 4-6b). Displacement is applied in the fibre direction, and the other directions are traction-free. The fibres at the lateral sides of the model have fewer neighbours and hence larger SCFs. This could not only speed up cluster formation, but also localise cluster formation at the sides of the model. Periodic boundary conditions are added to prevent this preferential cluster formation.

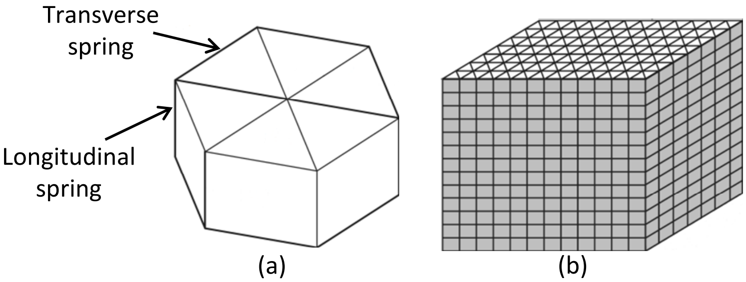

Figure 4-6: Schematic illustration of the spring element model: (a) the hexagonal unit cell, and (b) an RVE consisting of many unit cells (adapted from [357], with permission from Elsevier).

A true multiscale approach was developed by Blassiau et al. [314,355,356,367,368]. Their model links microscale damage to the macroscopic deformations. A unit cell model is developed that contains only 32 fibres in a square packing [314,367]. The inherent assumption is that a single fibre break in those 32 fibres does not affect the fibres outside of the RVE. This assumption is similar to that in the chain-of-bundles approach, which neglected interactions among the bundles. Therefore, also this model is expected to lead to overestimations of the strength. The advantage of this approach however, is that the damage development inside the RVE can include features such as multiple fibre breaks, matrix yielding and fibre-matrix debonding. The statistical information on the damage development and strength of this RVE is then saved and transferred into a macroscopic model, consisting of many RVEs. The macroscopic model determines the local stresses that act on each RVE. These local stresses will determine the stochastic damage inside each RVE [356]. This model can be used for complex part shapes and loading conditions, as is found in pressure vessels [356]. The prerequisite is, however, that the RVE accurately captures the damage in these loading conditions.

Pimenta and Pinho [148] recently developed an analytical model, where the matrix is represented by a perfectly plastic SLM. Combined with the Weibull distribution, this leads to what the authors call “a hierarchical scaling law”. Their model first considers a composite consisting of only two fibres. If one fibre breaks, the model assumes that (1) the stress in the broken fibre recovers linearly, and (2) the stress is shed completely onto the other fibre. Composite failure is hence detected if the intact fibre is not capable of dealing with this additional stress. A recursive analysis is then used to scale up this model to 4, 8, 16, … fibres. This leads to failure predictions in less than a second, even for sample sizes with more than a million fibres.

One noteworthy exception to these statistical models is found in Wisnom and Green [369]. They developed a statistical model to predict the probability of adjacent fibre breaks, but did not include any stress concentrations. They then assumed that a set of adjacent broken fibres starts to debond from the rest of the fibres. The energy balance that they set up contained two contributions. The first contribution came from releasing the stresses in a bundle of fibres. The second contribution was the energy required to propagate the debonding of the bundle. Wisnom and Green then assumed that final composite failure occurs when the first bundle is pulled out. Despite neglecting stress concentrations due to broken fibres, this approach was rather successful in predicting composite failure. The main difficulty however, is to measure the required energy for debonding the fibre bundle.

4.1.4 Key results from strength models

The previous subsection described the state-of-the-art modelling approaches in literature. This subsection describes some of the key results from these strength models.

Matrix and interface properties

The influence of the matrix and fibre-matrix interface on the SCFs were highlighted in "4.1.2 Stress redistribution around fibre breaks". Extensive information is available on how matrix yielding and fibre-matrix debonding influence the stress redistribution around a fibre break. Surprisingly, the amount of data on corresponding results from strength models is much smaller. Some models assume perfect plasticity [148,344,345], while others use an elastic-plastic matrix [146,353,354,358]. Most of them, however, do not compare their results with a linear elastic matrix.

Behzadi, Foreman and co-workers [146,353,354] implemented matrix yielding in their FE model. Those FE results were entered into a strength model, and results with and without matrix yielding were compared. Their predicted failure strain reduced from 1.2% to 1.1% if matrix yielding was introduced [146,354]. It should be noted these authors only incorporated stress concentrations on the nearest neighbour fibres. This may have affected their results, as matrix yielding spreads out the stress concentrations over a larger region. A similar reduction in failure strain was found by increasing the strain rate [353]. Increasing strain rates reduce the elastoplasticity of the matrix due to its viscoelastic nature. This causes a reduction of the ineffective length and an increase of the SCF with increased strain rate.

Unfortunately, their modelling approach contains several flaws. Firstly, their model did not use a Weibull distribution, but an average failure strain with a 20% standard deviation. This causes an overestimation of the strain at which the first fibre fails. Secondly, their SCF predictions were performed for clusters of up to three breaks, but they do not explain what happens for larger clusters. While their conclusion that matrix yielding reduces the predicted failure strain may be valid, these limitations prevent drawing any quantitative conclusion.

Okabe et al. [360] used their spring element model to assess the influence of plastic hardening on the stress-strain diagram of an alumina fibre-reinforced aluminium matrix composite. While some differences in failure strain were observed, the strength predictions were nearly the same for an elastic-perfect plastic and an elastic-plastic hardening matrix (see Figure 4-7).

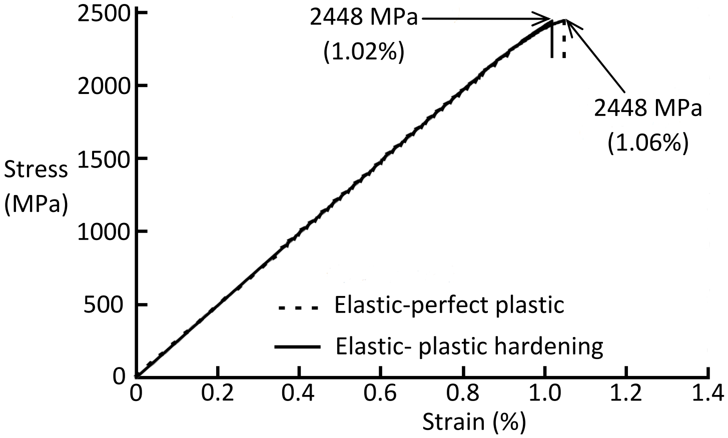

Figure 4-7: Influence of the constitutive behaviour of the matrix on the stress-strain diagram predictions of an alumina fibre-reinforced aluminium matrix composite (adapted from [360], with permission from Elsevier).

De Morais [295] developed an SLM with a linear elastic-perfect plastic matrix behaviour. The modelling predictions were relatively insensitive to the shear modulus of the matrix. The influence of the matrix shear strength was, however, an important factor. Changing this from 40 to 100 MPa increased the tensile strength from 1300 to 1600 MPa for T300 carbon fibre and from 2400 to 3100 MPa for T800 carbon fibre. This is attributed to a faster stress recovery in the broken fibre, which reduces the size of the region with increased SCFs. Pimenta and Pinho also changed the shear strength in their perfectly plastic SLM and found a significant influence on the composite strength [148].

In principle, the full non-linear stress-strain diagram of the matrix should be used to maximise the accuracy of strength models. A crucial issue in all of these comparisons is however which matrix properties to use. From literature, it is known that the strength of epoxy is size-dependent [370,371]. In traditional composites, the average thickness of a resin area is in the order of a few micrometres. Hobbiebrunken et al. [371] for example found that the tensile strength was three times higher in fine epoxy fibres than in the traditional, large dog bone samples. According to the results of de Morais [295] and Pimenta and Pinho [148], this would significantly increase the predicted tensile strengths.

Size scaling effects

Size scaling of composite strength is a topic of particular interest for applications. Size scaling is defined as the change of properties with changed dimensions. The initial work started off with Leonardo da Vinci in the 1500s [372], who found that the strength of iron wires decreases with increased lengths. The elastic modulus is an average property, and hence should not vary with specimen size. In contrast, strength is typically determined by the weakest location or largest defect. Increasing size hence increases the probability of having a large defect and decreases the composite strength.

This is crucial for industrial applications, as most strength predictions are based on small coupon tests.

As evidenced from Zweben [373], significant scientific discussions were ongoing in the nineties. The size scaling effect of composite strength is now well established in the scientific community due to the abundant experimental evidence [151,276,374-377].

Modelling evidence followed soon after the initial experimental evidence, [148,150,337,378,379]. Mahesh et al. [378] proved that the size effect strongly depends on the Weibull modulus of the fibres. In a subsequent paper, equal load sharing was proven to overestimate the size scaling effect [337]. This effect is smaller for local load sharing rules. Curtin later indicated that 1D packings also lead to an overestimation of the size scaling effect.

Pimenta and Pinho [148] have used their hierarchical scaling law to predict size scaling of composites with the number of fibres ranging between 1 and 1 million (see Figure 4-8). Their results are particularly interesting, as they are also compared with experimental data. It should be noted that the matrix shear strength was fitted to achieve a good agreement with the experimental data. The shear strength that gave a good fit was 50% higher than the experimentally reported value. This discrepancy may be attributed to the in situ shear strength of the matrix, which is known to be higher than the macroscopic shear strength [370,371]. Nevertheless, their model captures the size scaling effects well.

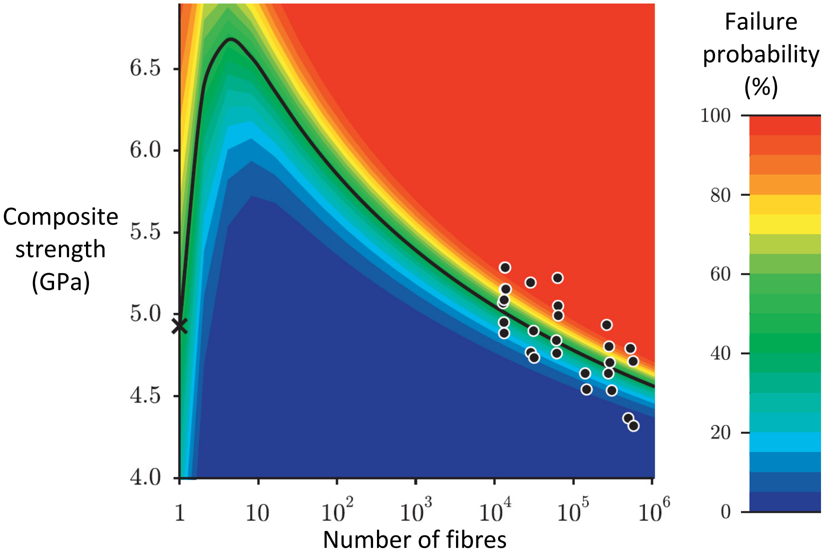

Figure 4-8: Size scaling of composites with a 10 mm length. The contour plot displays the failure probability, while the individual data points are experimental measurements from [276] (adapted from Pimenta and Pinho [148], with permission from Elsevier).

One remarkable effect is that the highest composite strength is found for specimens of about 10 fibres [148]. Such maximum can be understood by considering a composite with only two fibres. If one of the two fibres fails at its weakest location, then the other fibre is subjected to a large SCF. If, however, the other fibre is relatively strong in that location, then final failure would not occur yet. The 2-fibre composite is hence stronger than the 1-fibre composite. Further increases in composite strength occur when more fibres are added, but at some point the probability of having multiple weak fibres together becomes more important. The optimum seems to occur for about 10 fibres.

Critical cluster size

Clusters of fibre breaks are essential for the failure development of UD composites. Near the failure strain, one of those clusters reaches the critical cluster size, which then propagates unstably and causes final failure. Analysing this critical cluster size is thus vital in understanding the failure behaviour of UD composites.

Ibnabdeljalil and Curtin [332] assumed that composites contain regions that are intrinsically weaker than others. They derived equations to predict the probability of such weaker regions, which led to an analytical equation for the critical cluster size n^{crit}. This equation solely depends on the Weibull modulus m:

$$n^{crit} = 403 \cdot m^{-1.28} \tag{4-4}$$

This equation was derived for one specific degree of load sharing. This load sharing determines how localised the stress concentrations are, and can be varied to represent either very local or global load sharing. Unfortunately, the degree of load sharing was not directly related to material properties, making equation 4-4 somewhat arbitrary. Nevertheless, for typical carbon fibre Weibull moduli of 5 to 8 [286,380], the equation predicts critical clusters of 51 to 28 fibres, respectively.

Having a few strong fibres near a group of weak fibres can be sufficient to significantly delay the onset of unstable propagation of the cluster. This distribution of weak and strong fibres is statistical in nature. Ibnabdeljalil and Curtin [332] therefore noted that significant variations in the critical cluster size can be expected from sample to sample.

Landis et al. [331] tried to analyse the critical cluster size using their 3D SLM. The authors note that the critical cluster is often not clearly defined from their simulations. Similarly, several authors have noted that the critical cluster is not constrained within a single plane, but instead spans several layers within the ineffective length [334,381].

Detecting the critical cluster size experimentally is an important validation of strength models for UD composites. Unfortunately, such attempts are bound to fail, as the critical cluster immediately causes final failure. Since the strength of a composite specimen is unknown prior to testing, observing clusters immediately before failure is challenging. Nevertheless, some experimental data are available in literature. Scott et al. [265] used synchrotron computed tomography to find a 14-plet in T700/epoxy composites. This was found at 94% of the final failure strain, meaning that the critical cluster size is probably larger. Similarly, Aroush et al. [382] found critical cluster sizes ranging from 9 to 33. Their study, however, investigated quartz fibre/epoxy composites with only 125 fibres. Aroush et al. did not mention how close to final failure these break-clusters were observed.

Zhao and Takeda proposed an alternative approach to detect the critical cluster size [317,383]. After composite failure, the fracture surface is inspected and the number of fibre breaks that are clustered together are counted. Such an approach does not seem reliable for three reasons. Firstly, the exact location of the critical cluster is unknown and hence cannot be counted. Secondly, whether fibre breaks should be included in a cluster is not properly defined and hence subjective. Finally, when a large cluster is found, there is no proof whether that cluster grew prior to or during unstable propagation.

Despite significant scientific interest, relatively limited experimental data are available on the critical cluster size. Modelling the critical cluster size accurately is also challenging, as it requires an accurate prediction of the SCFs around multiple fibre breaks.

4.1.5 Conclusion

Strength models for UD composites are widely available in literature. Each model has a different balance between computational efficiency and simplicity. When choosing the best approach for this thesis, the final objective should be kept in mind: developing a thorough understanding of the failure in hybrid composites. This objective leads to two vital requirements:

- The model should be able to incorporate different fibre types and diameters.
- The failure development has to be realistic.

The first requirement is a major stumbling block for most models. Many models are restricted to regular packings. Such packings can in principle contain fibres with different diameters, but this would severely restrict the maximum fibre volume fraction. Therefore, a strength model for hybrid composites should allow random fibre packings. Moreover, the models should be able to cope with at least two different fibre types. Such models are currently not available in literature.

The second requirement necessitates the use of 2D fibre packings. Models for random 2D fibre packings are currently not available in literature. A new strength model hence needs to be developed for the purpose of this study.

4.2 Stress redistribution around fibre breaks

The stress redistribution around broken fibres is crucial in nearly all strength models. Together with the Weibull distribution, this redistribution determines the increase in failure probability of the fibres adjacent to a fibre break. The stress redistribution hence also determines the tendency for the development of break-clusters, which is crucial for final composite failure.

This section describes the methodology used for calculating stress redistribution around fibre breaks. After describing the general concepts, the approach will be applied to non-interacting or single fibre breaks. Finally, the stress redistribution around multiple fibre breaks is analysed.

4.2.1 Methodology

Random fibre packing generator

The basic principles of the random fibre packing generator are described in Melro et al. [384]. The algorithm requires three input parameters: the fibre radius, the fibre volume fraction V_f and the size of the representative volume element (RVE).

The first step in the algorithm is a so-called hard-core algorithm. Fibre coordinates within a square RVE are generated at random. They are added to the RVE, only if the fibres do not intersect with each other. Since this step itself is limited to a V_f of about 55%, two more steps are used by the algorithm. The second step tries to move each fibre closer to its nearest, second nearest and third nearest neighbour. The third and final step pushes the fibres on the edges of the RVE inwards. The first step is the only one that adds fibres and hence increases the V_f. The second and third step creates open spaces that can be filled with fibres during the first step. The three steps are repeated until the required V_f is achieved.

A criterion for the minimal fibre distance was added to the original algorithm from Melro et al. [384]. In the original algorithm, the minimal distance between the fibre centres is two times the fibre radius to avoid overlapping fibres. This criterion was adapted to randomly generate the minimal distance in the interval between 2 and 2.1 times the fibre radius. This adaptation increases the similarity of the statistical descriptors between generated and real fibre distributions. This adaptation was the work of Valentin Romanov and has only been co-authored. Interested readers can refer to Romanov et al. [385].

Finite element model description

The finite element model is created using the generated random fibre packings. The square 2D RVE obtained from the generator is reduced to a circle by cutting away the corners (see Figure 4-9a). This circular 2D RVE is then extruded along the third dimension to achieve a cylindrical 3D RVE (see Figure 4-9b).

The mesh is highly refined in the region near the fibre break, which corresponds to the middle of the cylindrical RVE (see Figure 4-9). Such high refinements are required to achieve accurate SCFs within computational limits. The mesh refinement will be verified later in this subsection. Quadratic elements are used, as they are expected to be more efficient in modelling the complex stress state around fibre breaks. The majority of the elements are brick elements, although wedge elements are unavoidable in some regions (see Table 4-1).

The applied boundary conditions are depicted in Figure 4-9b. A displacement is applied to the top surface of the model, corresponding to an applied strain of 0.1%. Symmetry conditions are applied to the entire bottom surface, but not to the middle fibre, representing the broken status of that fibre. Traction-free boundary conditions are applied to the lateral surface of the cylinder. This set of boundary conditions has been used previously to represent a unidirectional composite with a single fibre break [146,264,297].

For some models, matrix cracks around fibre breaks are added. These cracks are simulated in a similar fashion, by replacing the symmetry condition on the corresponding matrix crack area with traction-free conditions. Note that, symmetry conditions are applied to nodes at the boundary between the traction-free and symmetry conditions. Constraining these nodes will have an important influence on the stress redistribution around that broken fibre.

In all cases, linear elasticity and perfect bonding are assumed for matrix and fibres. Table 4-1 summarises some more details of the model.

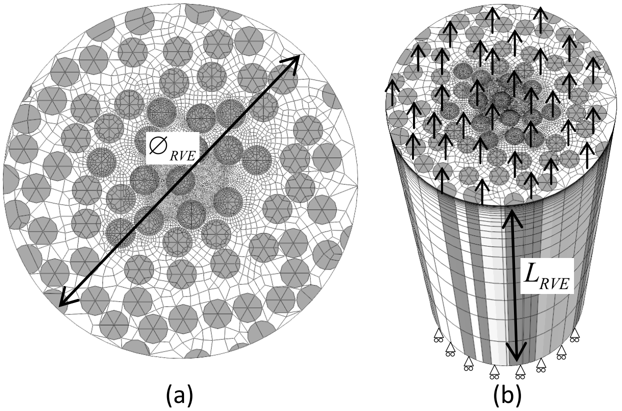

Figure 4-9: Description of the FE model: (a) Cross-sectional view of the mesh, and (b) boundary conditions of the model in 3D view. The black arrows and triangles represent the boundary conditions.

Table 4-1: Parameters of the finite element model.

Parameter	Value
Fibre radius R	3.5 µm
Length L_{RVE}	60R
Diameter $\varnothing_{RVE}$	24R
Number of fibres	42-51 fibres for $V_f = 30\%$ 79-84 fibres for $V_f = 50\%$ 116-122 fibres for $V_f = 70\%$
Number of elements	180.000-300.000 elements
Type of elements	70-90% second-order brick elements 10-30% second-order wedge elements

Input parameters

The stress redistribution around fibre breaks is calculated for a T700 carbon fibre/epoxy composite. The engineering constants for this fibre are summarised in Table 4-2. The set of engineering constants for isotropy is not realistic as carbon fibre is transversely isotropic. SLMs however, often assume isotropic fibres and the errors they introduce can be analysed by comparing the outcome of both symmetry types. The data set for transverse isotropy is taken as the default one.

Table 4-2: Engineering constants of isotropic and transversely isotropic carbon fibres [241,242].

Symmetry	E_{11} (GPa)	E_{22} (GPa)	E_{33} (GPa)	ν_{12}	ν_{13}	ν_{23}	G_{12} (GPa)	G_{13} (GPa)	G_{23} (GPa)
Isotropic	230	230	230	0.25	0.25	0.25	92	92	92
Transversely isotropic	230	15	15	0.25	0.25	0.25	13.7	13.7	6

The matrix is a standard epoxy with 3 GPa stiffness and 0.4 Poisson's ratio. All materials are assumed to be linearly elastic and well bonded.

Data extraction

Finally, the necessary data are extracted from the stress field. The stress field in a cross-section through an intact fibre is not constant if it is near a fibre break (see Figure 4-10). Behzadi et al. [264] solved this by using the stress in the centre of the fibre. The average stress over the cross-section is however more relevant with respect to the objective of developing a strength model.

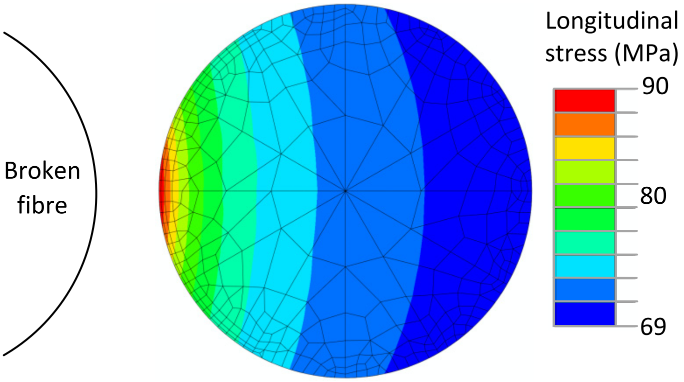

Figure 4-10: The longitudinal stress field of an intact glass fibre near a broken glass fibre in the fibre break plane. The applied strain is 0.1% and V$_f$ and stiffness are 70% and 70 GPa, respectively.

Within each fibre, the average stress is computed within different layers of elements. Each of these layers is parallel to and at distances z^* from the fibre break plane. In each layer, the longitudinal fibre stress is probed in all Gaussian points and averaged out, resulting in the average fibre stress $\sigma_{z,avg}$ at z^*.

Two parameters are derived from the SCF profiles to study the stress redistribution: the ineffective length and the maximum SCF. Firstly, the ineffective length is defined in accordance with Rosen's definition [142]. This length corresponds to twice the fibre length over which 90% of strain recovery in the broken fibre occurs (see Figure 4-11a). Secondly, the stress concentration factor (SCF) at a certain z-coordinate z^* is defined as the relative stress increase in an intact fibre at that point due to the fibre break. An equivalent definition was used: the SCF is calculated as the relative increase in average fibre stress $\sigma_{z,avg}$ at z^* divided by the average fibre stress $\sigma_{z,avg}$ far away from the failure location.

$$SCF(z=z^*)=\frac{\sigma_{z,avg}(z=z^*)-\sigma_{z,avg}(z=L)}{\sigma_{z,avg}(z=L)}.100\% \qquad (4\text{-}5)$$

This definition has also been used by other authors [145,386] and assumes that the fibre stress at $z=L$ is not influenced by the fibre break. This was verified for all models. This definition eliminates the need to calculate the stress field without the fibre break and hence saves calculation time. Figure 4-11b presents an example of the SCF profile in a neighbouring intact fibre as a function of relative the distance along that fibre. The maximum SCF occurs just below the fibre break plane, which corresponds to the findings of Xia et al. [298].

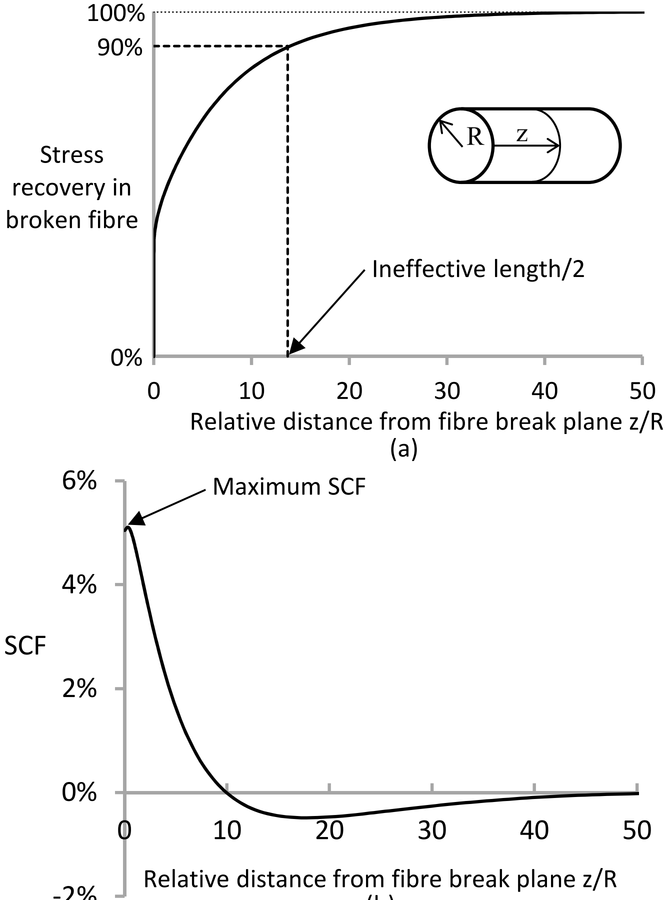

(a)

(b)

Figure 4-11: Illustration of the stress profiles: (a) in a broken fibre, and (b) in an intact fibre.

Mesh verification

Highly refined meshes are needed near the stress concentration sites, but these meshes are computationally expensive. To keep the models tractable, the mesh needs to be optimised. Two of these mesh optimisations will be described here.

The location that requires the highest mesh density is the perimeter of the broken fibre in the fibre break plane. If the mesh density is too low, the stress field in the intact fibres will be influenced. The default mesh is depicted in Figure 4-12a. To verify whether this mesh is refined enough, an FE model with an even finer mesh in the broken fibre was created. This mesh is illustrated in Figure 4-12b. The maximal difference in ineffective length and SCF is only 0.002%. Therefore, the default mesh in Figure 4-12a was used for all models.

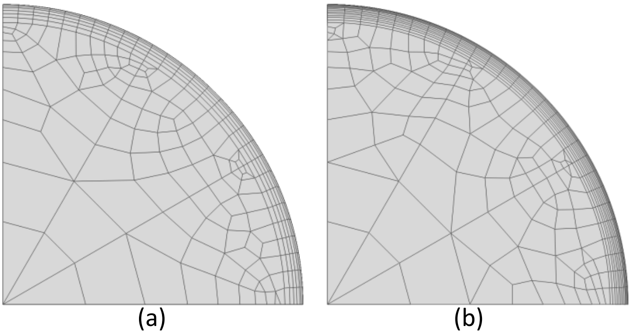

Figure 4-12: Top view of a quarter of the mesh in the broken fibre: (a) default mesh, and (b) refined mesh. Both meshes remain the same in the cross-section, but are gradually elongated along the fibre direction.

The number of fibres that are included in the models can also influence the results. The RVE diameter $\varnothing_{RVE}$ (see Figure 4-9b) and the V_f determine the number of fibres included. Since the model diameter is the most critical for a low V_f, this mesh optimisation was performed for models with a 30% V_f. The diameter $\varnothing_{RVE}$ was increased from 24R to 36R. This changes the ineffective length by less than 3%. The relative change in SCF was 1% at most. Therefore, all the model diameters $\varnothing_{RVE}$ were limited to 24R. Depending on the V_f, this results in a different number of included fibres (see Table 4-1).

4.2.2 Stress redistribution for non-interacting fibre breaks

This subsection analyses the stress redistribution for non-interacting fibre breaks. This can either be a single fibre break in a UD composite, or multiple fibre breaks that are far enough apart to avoid interactions. Four parameters are analysed: matrix cracks, packing type, fibre volume fraction and fibre anisotropy. Unless otherwise mentioned, all models contain matrix cracks in a random fibre packing. Similarly, the default V_f is 50% and the FE models use anisotropic carbon fibres by default. Even though 70% is a more realistic V_f for UD yarns in woven composites [387], 50% was chosen as default fraction. In UD composites however, 70% is only rarely achieved. For continuous UD thermoplastic composites, 40% is a typical value. It hence seems reasonable to use 50% throughout this thesis.

All the FE models in this section assume a linear elastic matrix and perfect fibre-matrix-bonding. FE models were developed with elastic-plastic matrix behaviour, but these results will be published separately.

Matrix cracks

As mentioned in “4.1 State of the art”, a stress singularity occurs around a fibre break in perfectly bonded composite with an elastic matrix. This can be partially remediated by (1) allowing fibre-matrix debonding, (2) including matrix plasticity or (3) adding matrix cracks. While the first two options have received extensive attention in literature, matrix cracking has received relatively little. Nevertheless, this has been reported in single fibre composites by several authors [317-319,323,324].

The primary influence of matrix cracks occurs through a change in the stress redistribution around fibre breaks. This subsection analyses this redistribution in the broken and intact fibres, for the case of a non-interacting or single fibre break. The modelling approach for adding matrix cracks was described in "4.2.1 Methodology".

Five sets of FE models were made. Each set consists of a model without a matrix crack and a model with a matrix crack, both having exactly the same mesh. In the absence of experimental data on the size of the matrix crack, the matrix crack is assumed to be constrained by nearby fibres. Since that defines uniquely neither the size nor the shape of the matrix crack, a sensitivity analysis is performed to assess its influence. Three different matrix crack sizes were implemented in one specific fibre packing (see Figure 4-13). The stress redistribution is not sensitive to the shapes and sizes of the matrix crack. A relative difference of only 12% was found for the maximum SCFs when comparing the smallest and largest crack models. The difference in ineffective length was smaller than 1%. A medium-sized matrix crack will therefore be used in the assessment of SCFs (see Figure 4-13).

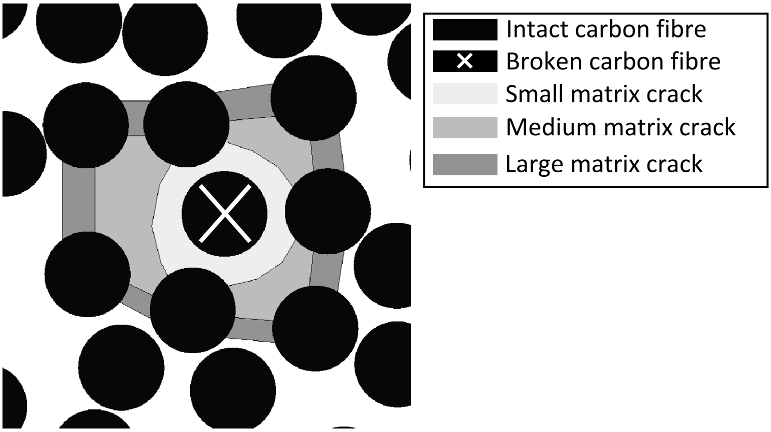

Figure 4-13: Top view of matrix crack sizes in the FE models.

Figure 4-14 depicts stress recovery profiles in the broken fibre. Fibre stress is plotted as a percentage of the nominal level caused by the global axial strain. The fibre stress recovers faster in models without a matrix crack, which confirms the results of Johnson et al. [319]. The matrix crack adds extra compliance to the system, resulting in a slower stress recovery and larger ineffective length. The ineffective length is defined as the length over which the broken fibre recovers 90% of the nominal stress. Its value is 27.3 ± 1.8 and 35.5 ± 1.8 times the fibre radius, without and with matrix cracks, respectively.

A noteworthy feature of Figure 4-14 is the starting point for the stress recovery profiles. The profile for models without a matrix crack seems to start at about 35%, while the one with matrix cracks starts at the origin. Since the entire surface of the fibre break is traction-free, the average longitudinal fibre stress is actually zero in the fibre break plane. In models without a matrix crack, however, the perimeter of the fibre break is constrained. This constraint leads to a rapid stress build-up to 35% within the first layer of elements. This is not visible in Figure 4-14, as this layer has a thickness of only 0.02 times the fibre radius.

The stress recovery profile for models with matrix cracks seems more realistic in comparison with the experimental work by Guild et al. [388]. Guild et al. also mention that the stress singularity at the perimeter of the fibre break in the FE models is not found experimentally. Behzadi et al. [146] tacitly avoided this problem by using the stress in the middle of the broken fibre instead of the average stress. This approach however introduces problems with force equilibrium in the model.

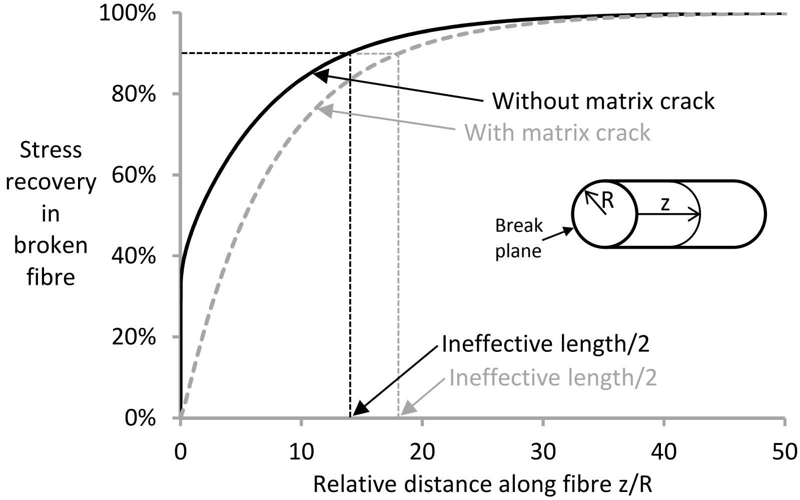

Figure 4-14: Representative stress recovery profiles in fibres with a single break from FE models with and without matrix cracks. The dashed lines indicate half of the ineffective length.

Figure 4-15 depicts the influence of matrix cracks on the maximum SCFs in the intact fibres around the fibre break, defined as the percentage by which it exceeds unity. The addition of matrix cracks doubles the SCF compared to models without matrix cracks.

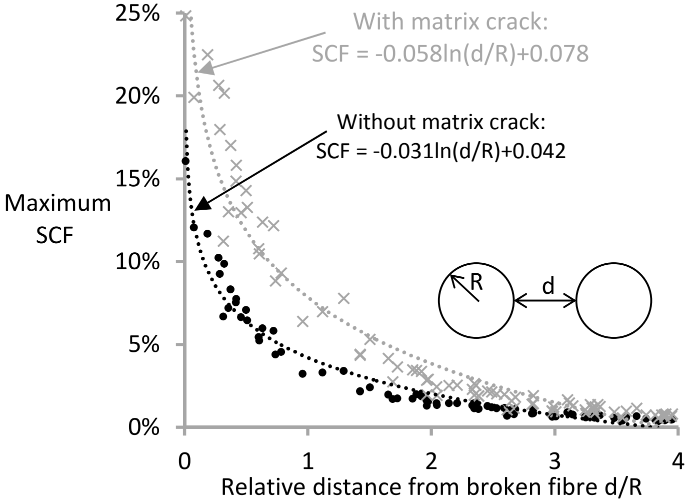

Figure 4-15: The maximum stress concentration factors in intact fibres around a single fibre break as a function of the relative distance from the broken fibre, from five FE models with and without matrix cracks. The stress concentration factor is calculated as the percentage by which it exceeds unity.

Including matrix cracks increases the ineffective length (see Figure 4-14) as well as the maximum SCFs (see Figure 4-15). Since both effects increase the failure probability of adjacent fibres, the predicted failure strain is expected to decrease. This will be further analysed in “4.4.1 Matrix cracks”.

Packing type

This part examines the influence of the fibre packing on the stress redistribution around a single fibre break surrounded by a matrix crack. Two regular fibre packings, namely square and hexagonal, are compared to random fibre packings. The results of five simulations are combined for random packings, while a single simulation is enough for regular packings because of its deterministic nature.

Figure 4-16 presents the ineffective length for the three different packings: single values for the square and hexagonal packings, and an average value with standard deviation for the random packing. The random packing has the lowest ineffective length, while the hexagonal packing has the largest ineffective length. This is attributed to differences in the shear stiffness around the broken fibre. The material immediately surrounding the broken fibre is loaded in shear and transfers the longitudinal stress back on to the broken fibre. In a material with higher shear stiffness, this stress recovery will occur over a smaller length. The shear stresses leading to the stress recovery are mainly located in the material surrounding the broken fibre. Therefore, the shear stiffness of that part of the material will contribute more to the stress recovery. In hexagonal packings, all nearest neighbours of the broken fibre are at the same distance. In random packings, some fibres are almost touching the broken fibre, while others are located further away. If the fibres are closer to each other, then the average shear stiffness around the broken fibre will be higher than if they are far from each other. This leads to a faster stress build up in the broken fibre, and hence to a lower ineffective length for random packings (see Figure 4-16).

The ineffective length of square packings is in between the ineffective lengths for random and hexagonal packings. The nearest neighbours in square packings are closer to the broken fibre than in hexagonal packings, but not as close as in random packings. This explains why the behaviour of square packings typically lies in between that of random and hexagonal packing.

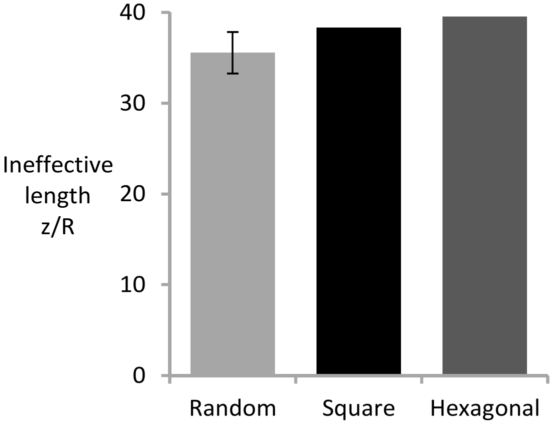

Figure 4-16: The ineffective length for the three fibre packing types.

Figure 4-17 reveals the maximum SCF in the neighbouring fibres for the three fibre packings. The data points for the random fibre packings have SCFs of up to 25%. This is about twice as much as for the regular packings. This is due to the “shielding effect”. The six nearest neighbours in hexagonal packings shield the second nearest neighbours from the stress concentrations. The second nearest neighbours therefore carry a lower SCF, which means that they carry a smaller portion of the load released by broken fibre. Consequently, a larger portion of the load is shed to the nearest neighbours, which hence carry a larger SCF. An alternative point of view is that the closer nearest neighbours increase the local stiffness, which is known to limit the extent of the influence of a defect to a smaller region.

A similar, but much stronger shielding effect is found in random packings. The fibre that is closest to the broken fibre in a random packing is much closer to the broken fibre than the six nearest neighbours in a hexagonal packing. This results in SCFs of up to 25% in random packings (see Figure 4-17). These higher SCFs have already taken over a larger part of the total overload, resulting in a smaller overload on intact fibres that are farther away. When comparing data points at the same relative distance from the broken fibre, however, the SCFs are similar.

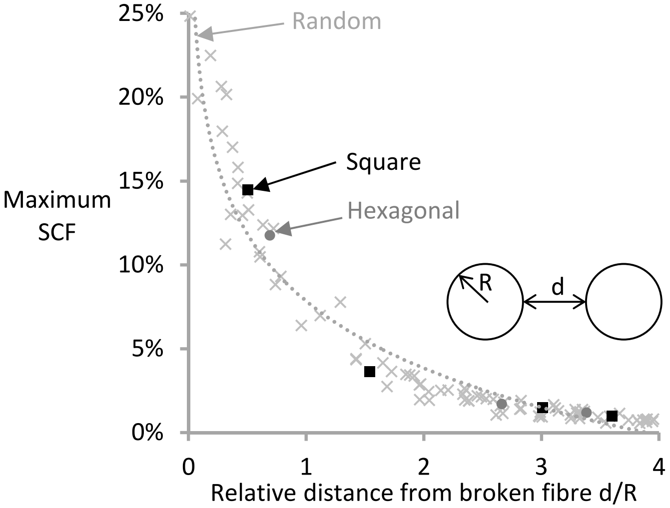

Figure 4-17: The maximum SCF as a function of the relative distance from broken fibre for the three fibre packing types. The results of five FE models are plotted for the random fibre packing.

Fibre volume fraction

All previous models used a 50% V_f. It is now examined how the stress redistribution around a fibre break is influenced by the V_f. The chosen V_f are 30%, 50% and 70%. Five packings were examined with V_f of 50% and 70%. For 30%, this number was increased to 9 to obtain sufficient data points.

Figure 4-18 displays the results for the ineffective length. The ineffective length decreases strongly with increased fibre volume fraction. The $V_f = 70\%$ packings have more fibres at small distances. If the fibres are closer to the broken fibre, then they contribute more to the stress recovery in the broken fibre. This stress recovery is controlled by the average shear stiffness of the material immediately surrounding the broken fibre. A higher fibre volume fraction hence increases the average shear stiffness by the presence of more fibres close to the broken fibre. This explains the observed decrease in ineffective length. A similar effect would be expected in regular fibre packings. The decrease would however be smaller as the fibres in regular packings are further away from the broken fibre.

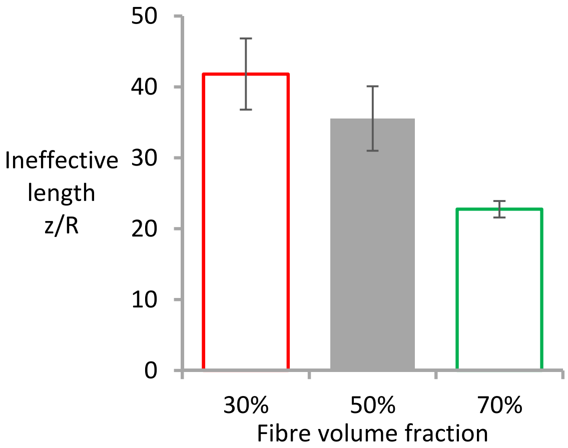

Figure 4-18: The ineffective length for the three fibre volume fractions in a random fibre packing.

A high V_f results in low SCFs for the same distance (see Figure 4-19). The trend line for V_f = 30% is significantly higher than for V_f = 70%. This is again caused by the shielding effect. A high fibre V_f results in a stronger shielding effect because more intact fibres are nearby to contribute in carrying the load.

Interestingly, previous publications [263,298,299] concluded that the SCF increases with V_f. Figure 4-19 may seem to indicate that the opposite is true for random packings. All previous publications with 2D packings however used regular packings, while the presented results are based on random packings. In regular packings, the V_f is directly related to the distance between the considered fibre and the broken fibre. In random packings however, these two parameters are decoupled. A high V_f results in more fibres at small distances and thus more fibres with relatively high SCFs (see Figure 4-19). However, when comparing SCFs at the same distance from the broken fibre (for instance at d/R = 1), the higher V_f results in a lower SCF due to a more pronounced shielding effect. The conclusion from literature was double-checked in our own models with regular packings at different fibre volume fractions. These results confirmed the increasing SCF with increasing V_f, as was the case in [263,298,299].

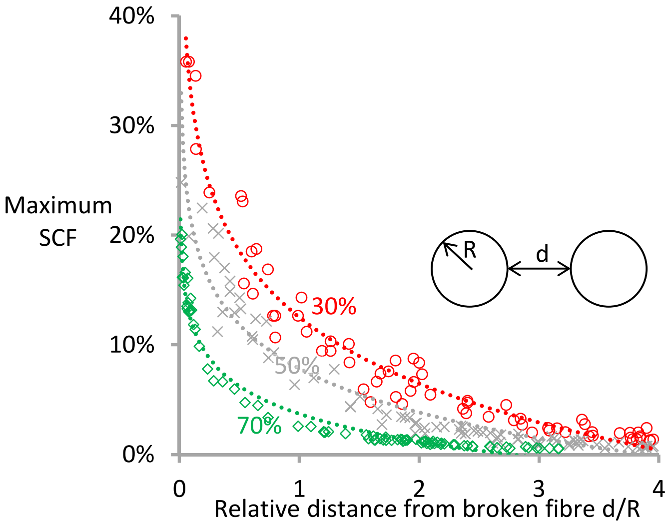

Figure 4-19: The maximum SCF as a function of the relative distance from the broken fibre for the three fibre volume fractions. The results of five FE models are shown for a V_f of 50% and 70%, while this was increased to nine FE models for a V_f of 30%.

While the SCFs reduce with increasing V_f, there are also more intact fibres close to the broken fibre. These intact fibres will be subjected to large SCFs. For low V_f, the SCFs can potentially be higher, but such high SCFs will only be found in a few fibres. The influence of fibre volume fraction on the outcome of strength models is therefore difficult to predict.

Fibre anisotropy

Most SLMs are not capable of incorporating anisotropic elastic properties. In the case of carbon fibres, this results in a major overestimation of the shear modulus. Earlier in this subection, arguments were developed that the shear stress build up in the matrix and surrounding fibres is vital for the stress recovery in the broken fibre. This should hence have an effect on the ineffective length.

Two types of carbon fibres are used here. The first type is assumed to be isotropic, while the second one is transversely isotropic. By comparing results for both fibre types, the importance of including anisotropy can be assessed. The corresponding engineering constants are summarised in Table 4-2.

The anisotropic carbon fibres have a clearly lower shear stiffness (see Table 4-2). This allows the broken fibre to deform more in shear, causing lower shear stress in the matrix and hence a longer ineffective length (see Figure 4-20). This conclusion is valid for models with and without matrix cracks, although the effect is more pronounced in the absence of matrix cracks. Including a matrix crack moves the shear stress transfer away from the broken fibre. The shear deformation of the broken fibre is hence less important, causing a smaller influence of its anisotropy.

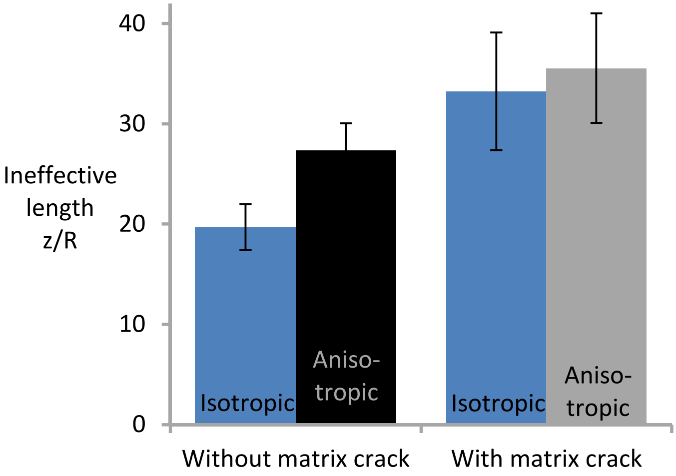

Figure 4-20: Comparison of the ineffective length for anisotropic and isotropic fibres.

Figure 4-21 reveals that anisotropic fibres carry higher SCFs. The anisotropic fibres have a much lower shear stiffness than the isotropic fibres. This lower shear stiffness results in more shear deformation of the broken fibre and more stress transfer onto the intact fibres. Similar to Figure 4-20, this effect is less pronounced in the presence of matrix cracks, as the shear deformation of the broken fibre is reduced.

SLMs assume a zero fibre radius and thus an infinite shear stiffness of the fibres. This simplification is only justified if the ratio of the fibre and matrix shear stiffness is high. This confirms the findings of Xia et al. [298], who also noted an increase in the SCFs when the anisotropy was taken into account.

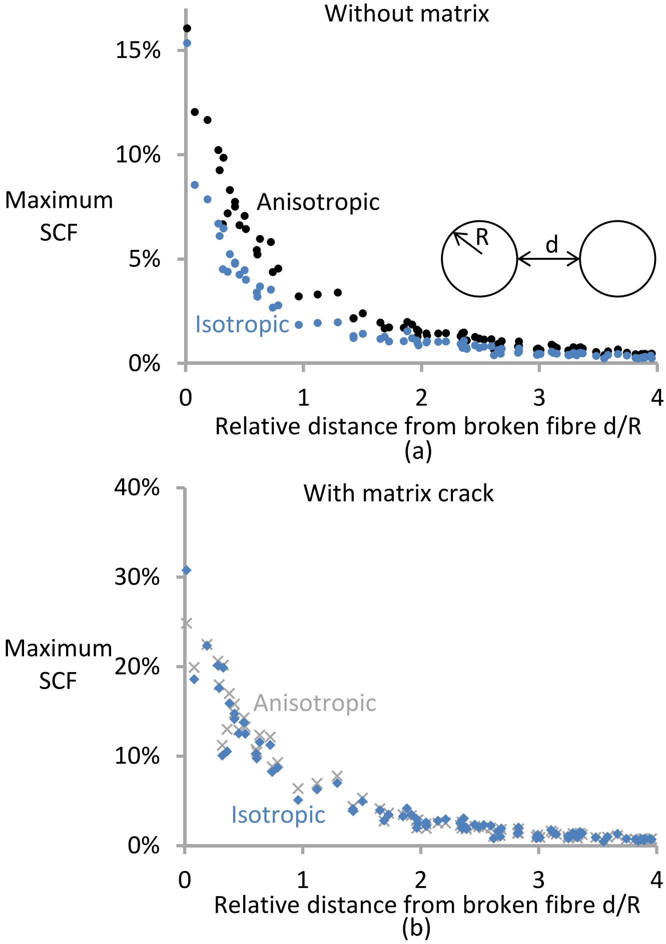

Figure 4-21: Comparison of the maximum SCF as a function of the relative distance from the broken fibre for anisotropic and isotropic fibres: (a) without matrix crack, and (b) with matrix crack. The results of five FE models are plotted for each model type.

Conclusion

The stress redistribution after a single fibre break in various fibre packings was analysed using 3D FE models.

- Matrix cracks were shown to increase the SCF and the ineffective length.
- Random packings had a slightly shorter ineffective length than regular packings. The most crucial difference is the change from deterministic SCFs in regular packings to stochastic SCFs in random packings.
- Fibre volume fraction also had a large influence on the stress redistribution around a fibre break. The ineffective length decreases by increasing the fibre volume fraction. This also reduces the value of the high SCFs, but increases the probability of finding such high SCFs.

- Fibre anisotropy increases the ineffective length and the SCFs compared to isotropic carbon fibres.

All of these four parameters affected the stress redistribution. While it is obvious that larger SCFs will tend to decrease the composite strength, the same is true but less obvious for the ineffective length. The ineffective length is a measure of the length over which the stresses are influenced by the fibre break. If this is larger, then the SCFs in the intact fibres are active over a longer length. This will increase the failure probability of the nearby fibres and hence reduce the composite strength. Therefore, matrix cracks are expected to strongly reduce the strength, as both the SCF and ineffective length were increased. For the other three parameters, counteracting effects were found. Since the relative importance of the SCFs and ineffective length are not known, the outcome of the strength model is difficult to predict. This outcome will be described in “4.4 Parametric study”. But first, the interactions among fibre breaks need to be understood.

4.2.3 Stress redistribution for interacting fibre breaks

The previous subsection only describes the stress redistribution around non-interacting fibre breaks. To accurately predict final failure, however, the interactions among fibre breaks must be taken into account. Fairly advanced rules have been developed to predict these stress redistributions around interacting fibre breaks based on shear-lag solutions for a single break [313,325,328]. While these rules are a powerful approach, they are not easily plugged into a strength model. Instead, an approximate approach was searched for that is more straightforward to apply in the present model. Linear superposition of the single fibre break solutions has been used in literature and would fit into this framework.

The linear superposition principle is illustrated in Figure 4-22a and b for two coplanar fibre breaks in a hexagonal packing. To further simplify the example, very local load sharing is used, which means that all SCFs are concentrated on the 6 nearest neighbours. Figure 4-22a depicts the single fibre break solution, in which all nearest neighbours carry an SCF of 16.7%. For two fibre breaks, the single fibre break solutions are simply summed up (see Figure 4-22b). This results in two fibres with an SCF of 33% each, while the other fibres continue to carry an SCF of 16.7%. These other fibres hence only feel the presence of one of the two fibre breaks. The sum of all the SCFs in the single fibre break case is 100% (see Figure 4-22a). This should be the case to ensure force equilibrium. In the case of two fibre breaks however, the sum is 166.7% (see Figure 4-22b), while it should be 200% to maintain force equilibrium. Linear superposition neglects the SCFs that the fibre breaks exert on each other, which explains the loss of force equilibrium.

Enhanced superposition principle

In view of this, an enhanced superposition principle is developed that does maintain force equilibrium. This principle first applies linear superposition to single break solutions, but then additionally distributes the SCFs that the fibre breaks exert on each other. This redistribution is performed proportionally to the SCFs obtained from linear superposition. This procedure is further clarified in Figure 4-22c. For the linear superposition in Figure 4-22a, an SCF of 33% is missing, which would mean that force equilibrium is not maintained. The enhanced superposition principle solves this problem by redistributing the missing SCF proportional to the SCFs from linear superposition (see Figure 4-22c). This proportional redistribution causes a larger portion of this stress redistribution to end up on the two fibres that previously carried 33%. These fibres receive an additional 6.7%, while this additional SCF is only 3.3% for the other 6 intact fibres (see Figure 4-22c).

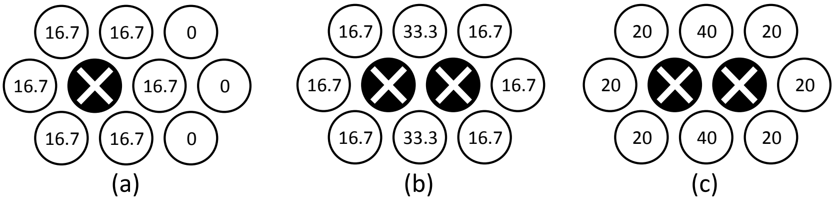

Figure 4-22: Illustration of the superposition principles in the fibre break plane: (a) a single fibre break solution (b) linear superposition of two coplanar fibre breaks, and (c) enhanced superposition of the same two fibre breaks. The white crosses indicate fibre breaks. The numbers inside the fibres indicate the value of the SCF as the percentage by which it exceeds unity. A hexagonal packing is assumed to simplify the situation, and the SCFs are assumed to be concentrated on the nearest neighbours only.

This principle was illustrated for two coplanar fibre breaks, but can easily be extended to multiple non-coplanar fibre breaks. In case of non-coplanar fibre breaks, the stress in the broken fibre is not zero, which causes the SCFs on the intact fibres to be lower. The sum all of SCFs on intact fibres hence has to be equal to the percentage of load that is lost in the broken fibres. The extension towards more than two fibre breaks follows the same procedure.

Validation

A set of four FE models was created to analyse the stress redistribution around three fibre breaks and validate the enhanced superposition principle. Figure 4-23 illustrates these four models, which all have exactly the same random packing realisation and mesh. Three models with single fibre breaks and one with all three fibres broken were created by changing the boundary conditions. Linear and enhanced superposition results are computed based on the individual fibre break solutions. Their relative error in the maximum SCF is computed by comparison of the FE model with three fibre breaks.

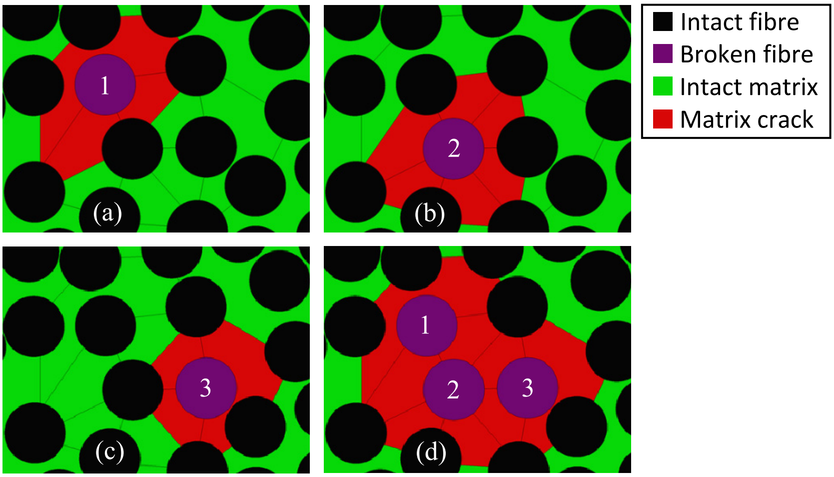

Figure 4-23: Illustration of the four FE models in the fibre break plane: (a) fibre break #1, (b) fibre break #2, (c) fibre break #3, and (d) all three coplanar fibre breaks. For models with matrix cracks, the symmetry condition on the matrix crack region (red) is replaced by traction free conditions.

Figure 4-24 plots the relative errors in the maximum SCFs calculated from both superposition principles compared to the FE solution with all three fibre breaks. For example, assume that the superposition principle and full FE solution predict an SCF of 6% and 5% respectively on one specific fibre. The relative error would then be +20% for that fibre. Figure 4-24a reveals that both superposition principles lead to significant errors if no matrix crack is present. With an average error of +16%, the enhanced superposition principle is slightly less accurate than linear superposition, which has an average error of -12%. These errors are attributed to the complex stress field at the perimeter of the fibre breaks, which is altered by the presence of other fibre breaks. In case of matrix cracks, however, this complex stress field is present in the matrix, where its effect on the SCFs in the fibres is smaller. Figure 4-24b shows that, in the presence of matrix cracks, the enhanced superposition principle is yields smaller errors than linear superposition.

These conclusions were also validated for a cluster of five fibre breaks. The average errors increased from -24% and +0.02% for three fibre breaks to -33% and +2% for five fibre breaks for linear and enhanced superposition, respectively. Matrix cracks shift the stress singularity into the matrix and avoids it in the broken fibre. It is hypothesised that this leads to better SCF predictions in the presence of matrix cracks. The remainder of this study uses the enhanced superposition principle.

The ineffective length increases for larger clusters. This was confirmed by analysing the FE models with multiple fibre breaks and was also found in literature [148]. At present, this is not implemented in the strength model. The interactions among fibre breaks are hence taken into account for intact fibres, but not for the ineffective length of the broken fibres.

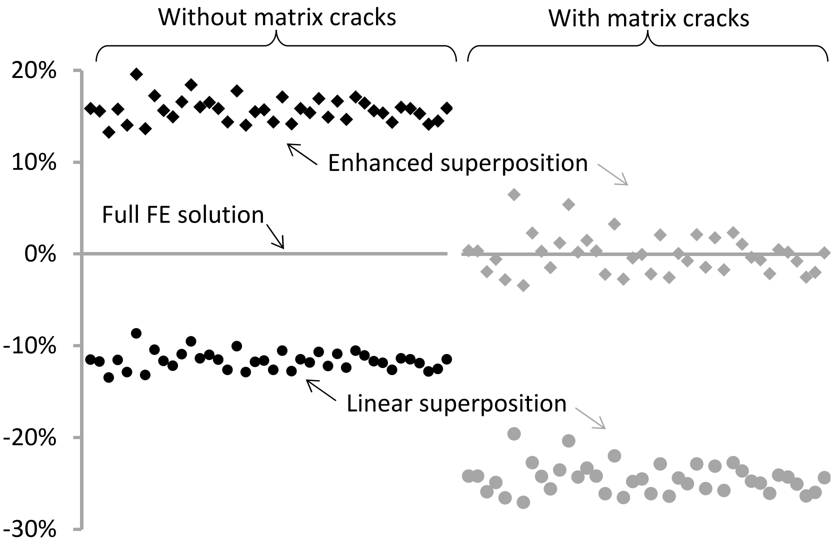

Figure 4-24: The relative error in maximum SCFs from both superposition principles for three coplanar fibre breaks without and with a matrix crack. The horizontal axis is arbitrary to allow depiction of the 40 intact fibres that are close to the three fibre breaks.

Conclusion

A new superposition principle was developed. The SCF predictions for multiple fibre breaks agreed well in the presence of matrix cracks. In the absence of matrix cracks, however, the enhanced superposition principle was slightly worse than linear superposition. The errors do increase with increasing number of fibre breaks, but in the case of matrix cracks, these errors remained small.

4.2.4 Conclusion

A methodology was set up to analyse the stress redistribution around fibre breaks in random fibre packings. The influence of four important parameters was assessed for a single fibre break. While this study generates useful information and provides a deeper understanding of their influence, the outcome on strength predictions remains unknown. These predictions will be analysed in the upcoming sections. Finally, a new superposition principle was developed. This principle remained accurate in the case of matrix cracks and is straightforward to implement.

The next step is to develop a strength model for UD composites and analyse how the outcome is affected by the various parameters.

4.3 Development of a strength model

The primary objective of this chapter is to develop a strength model that can be extended to hybrid composites. Such an extension is either impossible or very challenging with the state-of-the-art models. The model therefore has to be versatile. It should also lead to a realistic failure development to allow a significant advancement in the understanding of failure development in hybrid composites.

The development of a novel strength model for UD non-hybrid composites is described in this section. The next two sections will then demonstrate the capabilities of this model and validate it experimentally.

4.3.1 Basic approach

The first vital choice is how the stress redistribution around fibre breaks will be obtained. FE models are used instead of SLMs, as they (1) yield more accurate solutions for the stress redistribution, and (2) are more versatile towards different fibre types and diameters. The FE methodology explained in the previous section will be used, as this satisfies the requirements of versatility and has the potential to lead to realistic failure development.

The choice for an FE-based load sharing also makes the choice for a numerical model instead of an analytical one straightforward. Out of the numerical models presented in “4.1.3 Strength models for unidirectional composites”, Okabe’s spring element model seems to be the most elegant solution [293,357]. This model was however not used, as its extension towards hybrid composites would encounter serious limitations. Instead, a numerical model based on Rosen’s chain-of-bundles concept was used [142].

It should be emphasised that the present strength model is fundamentally different from Okabe’s spring element model. The spring element model explicitly incorporates the matrix through shear springs, while the present model only incorporates this indirectly. The influence of the matrix is taken into account by the FE model, which calculates the stress redistributions around fibre breaks. This results in stress profiles along the intact and broken fibres, which can be transferred to the strength model. The present strength model hence uses these FE results as input data, but the model itself only considers axial stresses and neglects any shear stresses.

4.3.2 Model description

The first step in the model is to create a representative volume element (RVE), consisting of parallel fibres (see Figure 4-25). These fibres are arranged in a random fibre packing, which is created using the generator of Melro et al. [384]. These packings have a 50% V_f and typically contain 2000 fibres. In some cases, an additional 250 fibres are placed on the perimeter of the RVE. These boundary fibres can carry SCFs, but are not allowed to break. These fibres are also not taken into account in the calculation of the average composite stress. The influence of these boundary fibres will be described in depth in “4.4.3 Boundary effects and size scaling”. Every fibre is split up in 2857 cylindrical elements with a length of 3.5 μm, resulting in a total model length of 10 mm. The total number of elements in the fibre bundle is therefore more than 6 million. A strength consistent with a Weibull distribution is assigned to each of these elements.

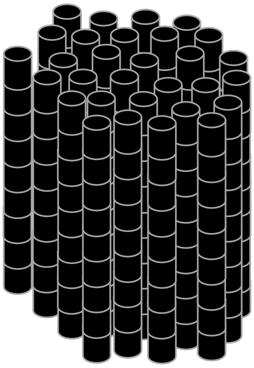

Figure 4-25: Schematic illustration of the RVE used in the strength model. No matrix is present as its effect is taken into account indirectly by using the FE data.

After creating the RVE, the model follows the flow chart in Figure 4-26. The strain is gradually incremented and element stresses are calculated. The stress σ in each element is calculated as: $\sigma = \varepsilon \cdot E \cdot \left(1 + SCF/100\%\right)$, where ε is the global axial strain, E the Young’s modulus of the fibre, and SCF the stress concentration factor as the percentage by which it exceeds unity. The procedure for incorporating these SCFs will be explained in the next subsection.

Failure of each element is checked by comparing the element stress with its strength. If no new elements have failed, then the strain is incremented until this does occur. If new elements have failed, then the model checks for final composite failure. The failure criterion is based on the observation that a critical cluster is typically spread out over several element layers [331,334,381]. Calculations are therefore terminated if at least 10% of the fibres have broken within an axial segment of 35 μm. This criterion always corresponded to a large number of required iterations within the same strain increment. This indicates that the critical cluster is growing in an unstable manner. Further computation of the model becomes slow and meaningless, and is therefore interrupted.

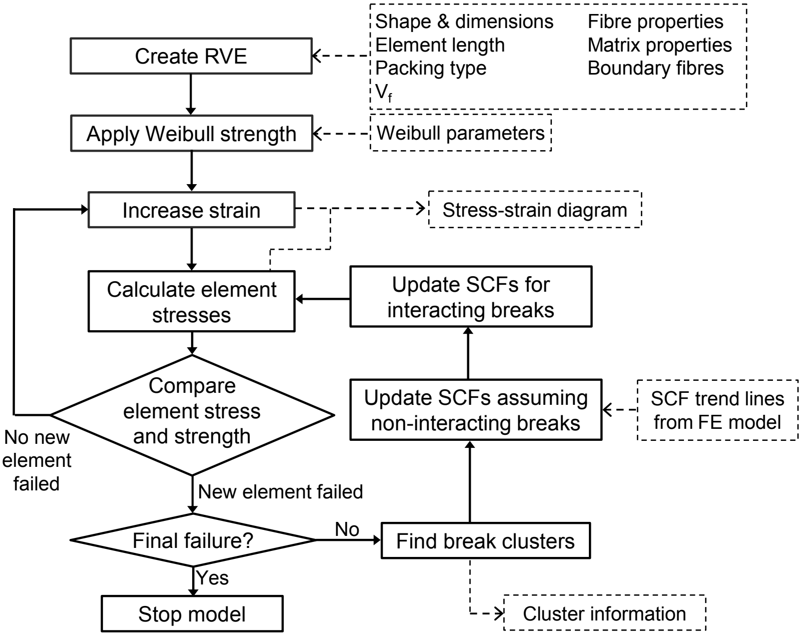

Figure 4-26: Flow chart of the strength model. The dashed rectangles indicate inputs and outputs.

If the composite failure criterion is not satisfied and a new fibre element has failed, then the model updates the break-clusters. Two fibre breaks are considered to be part of the same break-cluster if: (1) the lateral distance between the fibre centres is smaller than 4 fibre radii, and (2) the axial distance between them is less than 10 fibre radii. This definition is illustrated in Figure 4-27. Figure 4-27a displays a cluster of only two fibre breaks, as the other two fibre breaks are too far apart, either in the axial or lateral direction. Figure 4-27b illustrates a cluster of five fibre breaks, where the outer fibre breaks on their own would not satisfy the definition. These breaks are still considered to be part of the same cluster.

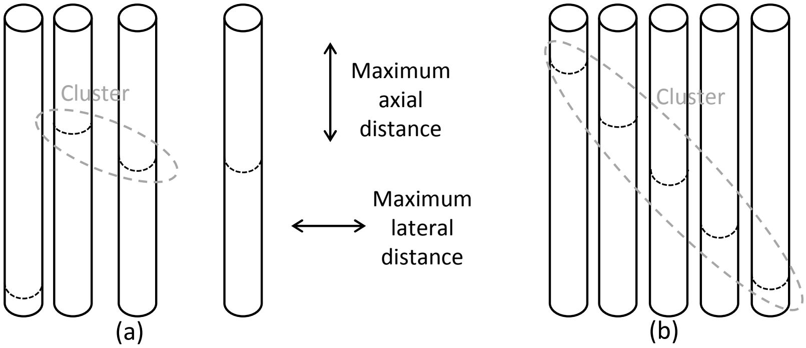

Figure 4-27: Illustration of the definition of a cluster: (a) a cluster of two fibre breaks as the other two fibre breaks are too far away, and (b) a cluster of five fibre breaks even though the fibre breaks on the left and right side on their own are too far apart. This illustration is not made to scale.

The model then updates the SCFs assuming that the breaks do not interact with each other. In the next step, these interactions are taken into account. Since the application of SCFs changes element stresses, these stresses are updated and compared to their strength again. The SCFs and stresses are updated until no new element fails. Then, the strain is further incremented and the procedure is repeated until final composite failure is detected.

The model assumes that all elements are subjected to the same strain. Changes in element length and position due to the applied SCFs are not taken into account. This essentially means that the strain does not localise on planes of elements that have a larger amount of fibre breaks. Such strain localisation would locally increase the compliance and increase the failure probability within those planes. Neglecting this causes the predicted stress-strain diagrams to be completely linear. This is a reasonable approximation for traditional UD composites with many continuous fibres. For a limited number of fibres or for discontinuous fibres, this approximation may not be entirely valid.

The model also does not take into account residual stress due to curing of the matrix. Incorporating this into the model is straightforward, but not relevant for the current purpose.

4.3.3 Incorporation of stress redistributions

The subsection “4.1.2 Stress redistribution around fibre breaks” only presented the maximum SCF values along the fibre and the ineffective length. For an accurate strength model however, the entire SCF profile along the broken and intact fibres is required. These SCF profiles are obtained from the FE solutions with a single fibre break that were described in “4.2 Stress redistribution around fibre breaks”.

For the broken fibre, five reference points are calculated: the first layer and the points where 60%, 75%, 90% and 95% of the stress is recovered (see Figure 4-28). Beyond 95% stress recovery, linear extrapolation is used up until 100% recovery is reached. These points are entered into the strength model, which uses linear interpolation in between the reference points.

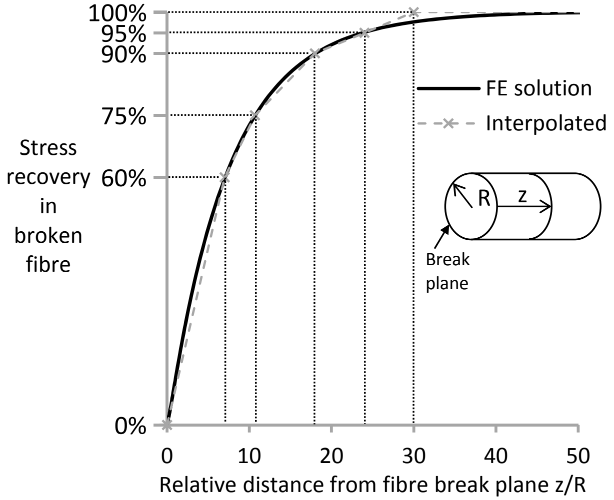

Figure 4-28: Example of the five reference points along the broken fibre that are used to transfer the SCF profiles into the strength model.

For the intact fibres, four reference points are calculated along the SCF profile (see Figure 4-29). For each of these points, the value for each intact fibre is extracted from the FE solutions (see "4.2 Stress redistribution around fibre breaks"). Linear or logarithmic trend line formulae are computed for each of these four points as a function of the relative distance from the fibre break plane. The trend line equations are entered into the strength model, which uses piecewise linear interpolation to compute the value at arbitrary locations. This computation is purely based on the distance from the broken fibre, and does not take into account the exact fibre packing around the broken fibre. The low scatter in Figure 4-15 illustrates that this distance and not the local packing is the dominant parameter controlling the SCF. By using this homogenisation approach, the accuracy of the FE approach is exploited without requiring FE simulations during the strength model.

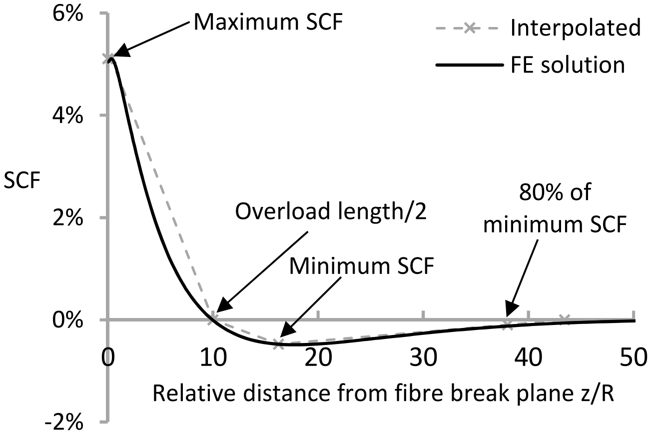

Figure 4-29: Example of the four reference points along an intact fibre that are used to transfer the SCF profiles into the strength model.

Finally, it is known that some part of the load of the broken fibre is shed onto the matrix [298]. The average matrix stress over the entire cross-section was calculated at various distances from the fibre break plane. This average value is then normalised by the nominal fibre stress to obtain an SCF value and facilitate the interpretation of its importance. Figure 4-30 shows that this contribution is up to 15%, but also dies out quickly. In the strength model, the matrix contribution is only relevant two fibre radii away from the fibre break plane. In case of matrix cracks, the stresses in the matrix were negligible. Together with the rapid decrease in Figure 4-30, this indicates that the matrix stress increase is caused by the stress singularity at the perimeter of the broken fibre. In the presence of matrix cracks, this singularity occurs in the matrix where its effect is much smaller. While the contribution of the matrix stresses is small even in the absence of matrix cracks, the strength model does take it into account.

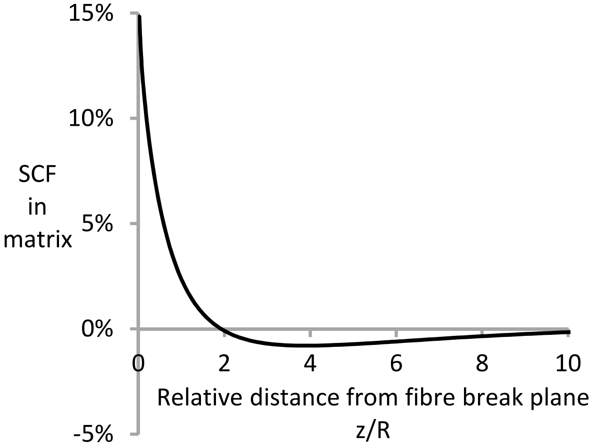

Figure 4-30: Stress concentration factor that is carried by the matrix as a function of the relative distance from the fibre break plane. This is an example for a V_f of 50% without matrix cracks.

When a fibre breaks, the first step of the model considers the break as non-interacting. To keep the model computationally tractable, the SCFs were only applied to fibres with a surface-to-surface distance from the broken fibre of less than four fibre radii. Even though the SCFs on the other fibres were all lower than 1%, their omission still caused a total SCF of 10-15% to be neglected. The sum of all SCFs in the intact fibres should be equal to the SCF that is “lost” in the broken fibre to ensure force equilibrium. To counteract these effects and ensure force equilibrium, the “missing” SCF was redistributed proportionally over the fibres within four fibre radii. This essentially localises the SCFs slightly too much, but this is reasonable as the SCF that is redistributed is only 10-15%.

A fibre element in the strength model has a non-zero length, and thus does not have a constant SCF along its length. The element length was however chosen short enough to ensure that this variation is small. To take this variation into account, the average SCF on the element is used in the strength model. The SCF of an intact element is calculated at both ends of the element using piecewise linear interpolation of the previously described input data (see Figure 4-31a). The average of both values is used in the strength model. The averaging procedure is modified for the broken fibre element, as the model assumes the break occurs in the middle of the element. In that case, the SCF is averaged over both ends and the middle (see Figure 4-31b).

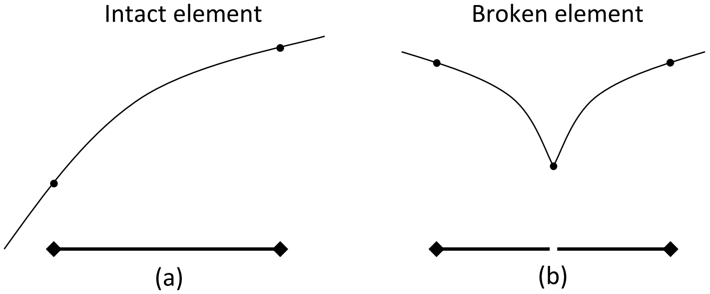

Figure 4-31: Illustration of the procedure for averaging the SCF value over the element length: (a) for an intact element and (b) for a broken element. The black dots indicate the points used to calculate the average.

The procedure described above yields the SCF value at any location near a single fibre break. For the stress redistribution around multiple fibre breaks, the enhanced superposition principle was developed. This principle has been extensively described in "4.2.3 Stress redistribution for interacting fibre breaks".

4.3.4 Model parameters

The material parameters are based on a T700 carbon fibre in an epoxy matrix. For the fibres, the strength model only uses the longitudinal fibre tensile modulus. The FE model for calculating the stress redistribution around fibre breaks however, used the entire set of engineering constants (see Table 4-2). The longitudinal tensile modulus of the carbon fibre is 230 GPa. The epoxy matrix is assumed to be linearly elastic with a tensile modulus of 3 GPa and a Poisson's ratio of 0,4.

A strength consistent with a Weibull distribution is assigned to each fibre element. Various Weibull distributions for T700 carbon fibres have been examined. The data set of Watanabe et al. [275] is found to be the most reliable, as it is based on extensive experiments. This data set is based on a bimodal Weibull distribution in equation 4-3, with the following parameters: $\sigma_{01} = 5200MPa$, $\sigma_{02} = 6100MPa$, $L_0 = 10mm$, $m_1 = 4.8$, and $m_2 = 12$.

The bimodal Weibull distribution is used to assess the influence of matrix cracks on the strength model and for the experimental validation. This is a reliable data set, and is hence suitable for comparisons with experimental value. The other parts of this chapter do not attempt a comparison with experimental values. In those cases, it is better to use the unimodal Weibull distribution in equation 4-1. This distribution is easier to interpret and it is easier to vary its parameters, which will facilitate the parametric study. The Weibull modulus m was set to 6, as this is a reasonable value for carbon fibre [286,380]. The exponent α was deliberately set to 0 to avoid any influence of the chosen element length. The other parameters were chosen to yield a reasonable failure strain prediction: $\sigma_0 = 3500MPa$ and $L_0 = 10mm$.

The strain increments in the model are not constant. The model starts off by calculating the failure strain of the weakest fibre and applies a slightly higher strain in the first increment. In the next strain increments, the global strain is increased by 0.04%. The size of the strain increment is gradually reduced, until near final failure it becomes 0.0025%. Such a scheme allows an optimal balance between computational efficiency and accuracy.

4.3.5 Conclusion

A novel strength model was developed. The model combines the FE approach for stress redistributions around fibre breaks with the chain-of-bundles approach. The versatility of the model is derived from the FE approach, coupled with a versatile method for transferring the FE solutions into the strength models. This allows any fibre or matrix behaviour to be incorporated into the strength model.

4.4 Parametric study of the strength model

This section attempts to gain a deeper understanding of the various parameters involved in modelling of UD composites. In contrast with most studies in literature, this study does not limit itself to analysing the predicted failure strains or strengths. To gain a deeper understanding, this section also analyses the break-cluster development and how it is affected by the various parameters.

The four parameters that were studied in “4.2.2 Stress redistribution for non-interacting fibre breaks” are also analysed here using the strength model. In addition, two other parameters that do not affect the stress redistribution will be studied. Firstly, the number of required tests to measure the Weibull distribution will be analysed. Secondly, boundary effects and their influence on size scaling of composite strength will be studied.

4.4.1 Matrix cracks

Matrix cracks have a large influence on the stress redistribution around fibre breaks, as illustrated in “4.2.2 Stress redistribution for non-interacting fibre breaks”. This subsection analyses how matrix cracks influence the failure strain and development of break-clusters.

Figure 4-14 and Figure 4-15 indicated that matrix cracks lead to larger maximum SCFs in the intact fibres and to a larger ineffective length on the broken fibre. Figure 4-32 confirms that this leads to a reduction in the average predicted failure strain from 2.87% without matrix cracks to 2.46% with them. This significant reduction is remarkable given that most state-of-the-art models do not take into account the effect of matrix cracks. If matrix cracking exists as modelled here, then this may be one explanation for quantitative differences between modelling predictions and experiments. Even though matrix cracks have been found in single fibre composites [317-319,323,324], further experimental work is required to confirm their presence in multiple fibre composites.

Even with matrix cracks, the model still overestimates the failure strain by 0.36% compared to the data sheet value of 2.1% for this carbon fibre/epoxy [389]. This discrepancy is attributed to (1) the small model size, (2) the neglect of the non-linear elastic behaviour of carbon fibre [253,254] and (3) the assumption that splitting does not occur. Splitting is the complete debonding of fibre bundles due to intensive shear stresses around break-clusters [158]. Splitting completely unloads the fibre bundle, causing higher stresses in the remaining fibre bundles. This can lead to premature composite failure.

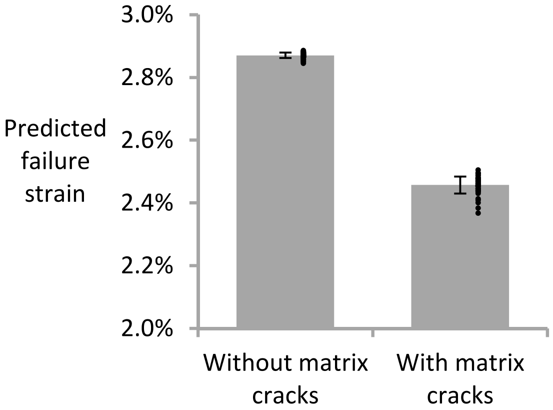

Figure 4-32: Predicted failure strain for 50 realisations of the strength model without and with matrix cracks. The error bars represent the standard deviation, while the dots represent the individual results for each realisation.

The internal damage development is now analysed to further understand the influence of matrix cracks. Figure 4-33 plots the number of fibre breaks in clusters up to 6-plets. An “i-plet” is a cluster where “i” is the number of fibre breaks. The development of 1-plets is almost identical for both models, as this is controlled by the Weibull strength distribution instead of by SCFs. Figure 4-33b demonstrates that 2-plets develop slightly earlier in models with matrix cracks. This difference is more pronounced for large break-clusters. The higher SCFs and larger ineffective lengths associated with the presence of matrix cracks clearly cause a stronger tendency for the onset of break-cluster development.

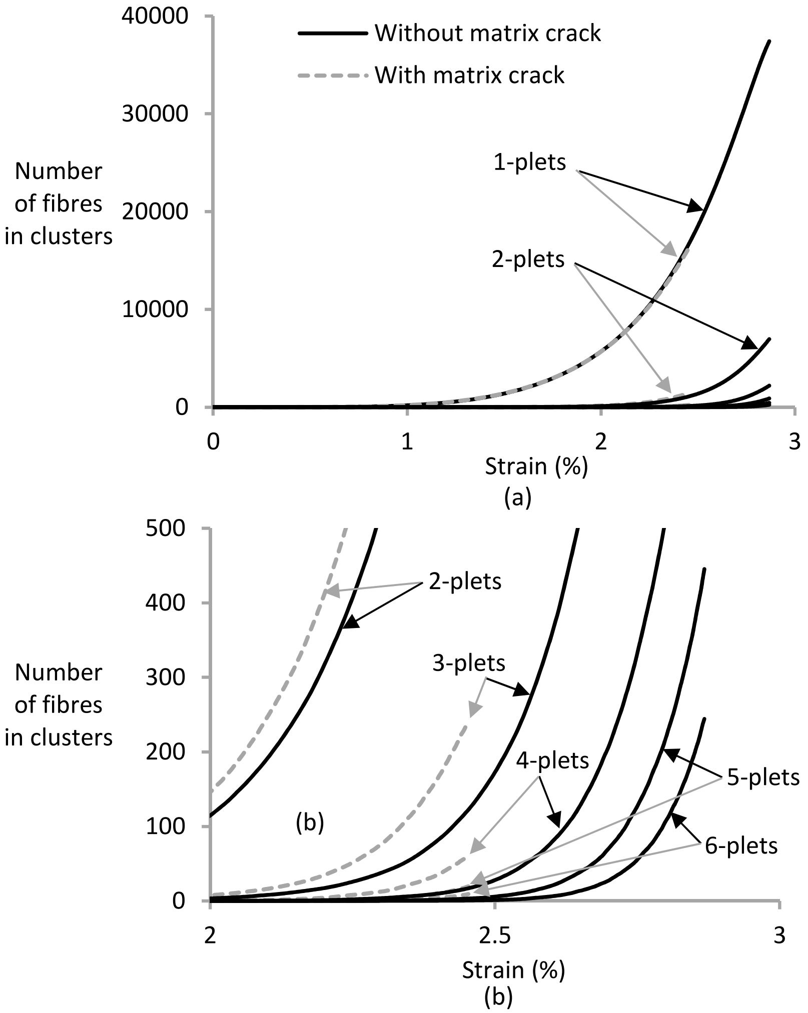

Figure 4-33: Break cluster development for models without and with matrix cracks: (a) overview from zero to 3% strain, and (b) more detailed view at high applied strains.

It should be noted that the number of clusters at final failure is much smaller in models without matrix cracks (see Figure 4-33). This indicates that a cluster is much less critical in models without matrix cracks. To investigate this further, the critical cluster size will be analysed (see Figure 4-34). This size is calculated as the largest cluster in the last strain increment before final failure. The critical cluster size is four times lower for models with matrix cracks. This smaller size is attributed to the higher SCFs in the presence of matrix cracks. The average value of 30 lies closer to the order of magnitude found in experimental data than 115 obtained in the absence of matrix cracks (see “4.1.4 Key results from strength models”).

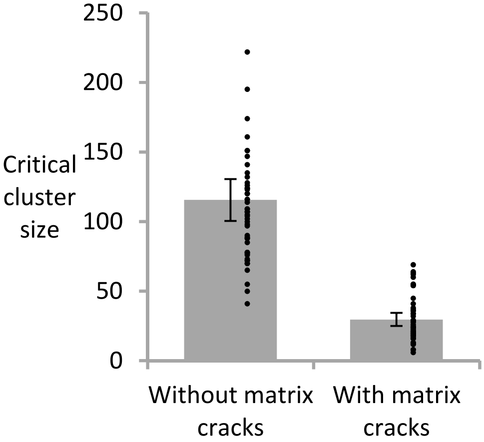

Figure 4-34: The critical cluster size for 50 realisations of the strength model without and with matrix cracks. The individual results are plotted together with the 95% confidence intervals.

Figure 4-35 depicts the largest break-cluster as a function of applied strain. Up to 2.4% strain, the largest clusters in the absence and presence of matrix cracks are similar. At higher strains, the largest cluster rapidly increases in size for models without matrix cracks, leading to final failure. This process is slower for models without matrix cracks, and only speeds up at higher applied strains. This delay is mainly attributed to the lower SCFs in the absence of matrix cracks.

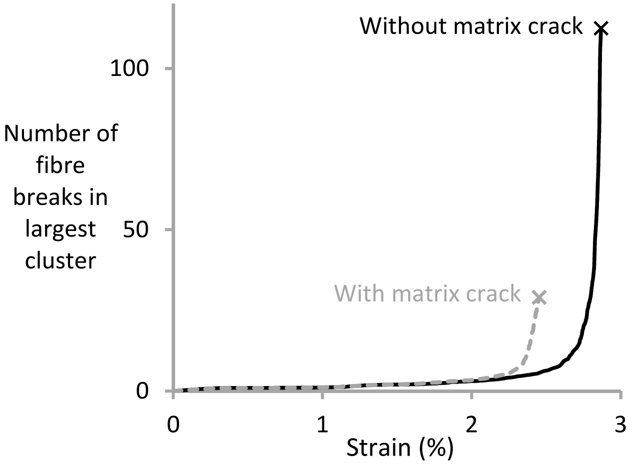

Figure 4-35: Evolution of the largest cluster of fibre breaks as a function of the applied strain, with and without matrix cracks.

Matrix cracks significantly alter the stress redistribution around fibre breaks, and this was reflected in a significant reduction in the predicted failure strain. This reduction brings the predictions closer to the experimental values and was explained based on a more rapid development of break-clusters. This more rapid development is attributed to a combination of higher SCFs and a longer ineffective length. Including matrix cracks in the analysis also led to more realistic predictions of the critical cluster size.

4.4.2 Weibull distribution

Issues with Weibull data sets in literature were highlighted in "4.1.1 Weibull distribution for fibre strength". Even for the same fibre type, strongly different Weibull parameters were found. This subsection hypothesises that this is due to a too small number of tests. To exactly measure the Weibull distribution, an infinite number of single fibre tests is required. Most authors however limit the number of tests to between 25 and 100 due to the cumbersome sample preparation and testing. This small number of tests introduces statistical errors, and may have a large influence on the predicted failure strains.

To analyse this influence, the default data set with $\sigma_0 = 3500MPa$ and $m = 6$ is considered to be the real data set. Single fibre tests are simulated by randomly generating strength values from the real data set at a 10 mm gauge length. This is performed for 10 sets of 25, 100, 400 and 1600 fibres. For each of these 40 data sets, the maximum likelihood approach is used to calculate the Weibull distribution. The resulting Weibull parameters are then used as input parameters in the strength model.

The resulting Weibull parameters are summarised in Figure 4-36. Testing only 25 fibres can lead to large errors in the Weibull parameters. Even for 100 and 400 tested fibres, the estimated Weibull parameters can still significantly deviate from the real parameters. The errors are especially large for the Weibull modulus m. This parameter is difficult to determine accurately, as it is a power law exponent in the Weibull equation (see equation 4-1). For 1600 tested fibres, the estimated Weibull parameters are reasonably accurate.

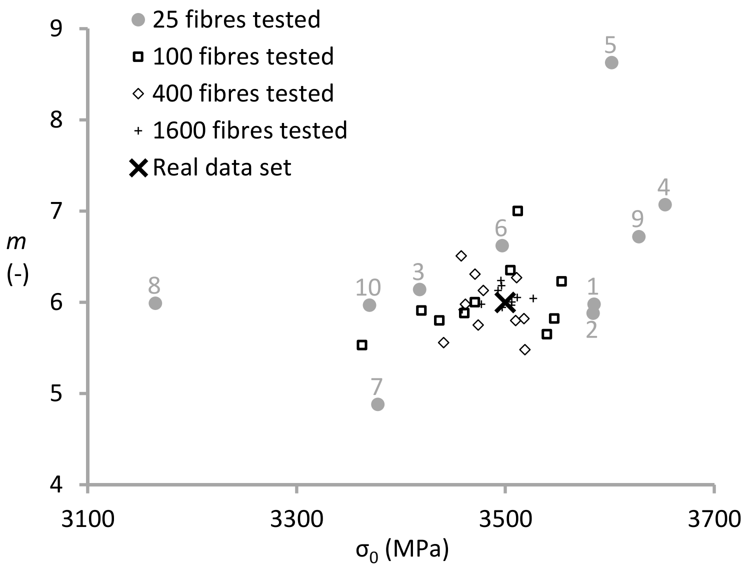

Figure 4-36: Summary of all Weibull parameters for 25, 100, 400 and 1600 fibres tested. The labels for "25 fibres tested" are added to facilitate comparison with Figure 4-37.

These 40 data sets are used as input in the strength model to calculate composite failure strain. Figure 4-37 compares the predicted failure strains for these data sets to the predicted failure strain for the real data set. For 25 fibres tested, the predicted failure strains range between 1.70% and 2.19%. This is a variation of about 25% in failure strain. One way to reduce this scatter is to test more fibres. With 100 tested fibres, the predicted failure strain ranges between 1.83% and 2.09%, or a total variation of 13%. This total variation reduces to 12% for 400 tested fibres and 3% for 1600 tested fibres.

These results limit the predictive capabilities of strength models for three reasons. Firstly, most authors limit themselves to testing only 25-100 fibres, while Figure 4-37 illustrates that this leads to significant errors in the failure strain predictions. Secondly, the approach used here only takes into account statistical errors. This assumes fibre strength can be measured accurately. Experimental difficulties in single fibre tests introduce even larger errors in the Weibull distribution and hence in the predicted failure strains. Thirdly, experimental errors may be skewed towards one side. Clamping effects in single fibre testing are known to be more severe for strong fibres [281], while weak fibres may break during sample preparation [282].

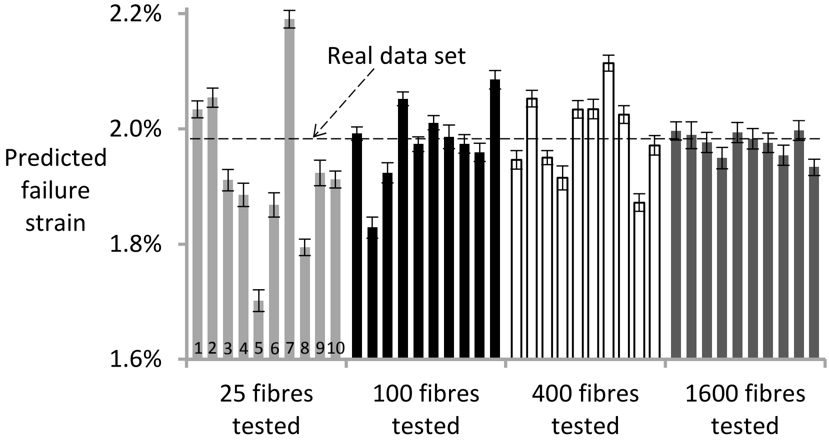

Figure 4-37: Predicted failure strains for 25, 100, 400 and 1600 fibres tested. The dashed line indicates the predicted failure strain for the real data set.

The results illustrate the importance of testing a sufficient number of fibres to determine the Weibull distribution. Results will converge to the real value, but this may require a number of tests that are unfeasible from a practical point of view. The development of improved testing methodologies is highly recommended to allow more data collection in a shorter time period. Measuring the Weibull distribution at gauge lengths below 10 mm may be even more difficult due to additional experimental errors (see “4.1.1 Weibull distribution for fibre strength”). Unfortunately, it is exactly these gauge lengths that are relevant for most strength models. Extrapolation down to small gauge lengths causes an even larger uncertainty if the Weibull modulus is not known accurately. Unfortunately, it is especially the determination of the Weibull modulus that is troublesome (see Figure 4-36)

4.4.3 Boundary effects and size scaling

The number of fibres in strength models is typically in the order of 1000 fibres. Typical tensile samples do not only contain more than a million fibres, but they are also longer than typical lengths used in strength models. Due to the stochastic variability of fibre strength, composite strength depends on the size of the tested samples [148,390]. Modelling results hence need to be interpreted with care. Apart from these size scaling effects, boundary effects can also be vital in small RVEs. If a fibre breaks near the model perimeter, then that fibre will have fewer neighbouring fibres. Those neighbouring fibres will carry a larger SCF than if the break would occur in the centre of the model. This larger SCF increases the probability for cluster formation near the perimeter.

Three approaches exist to deal with this problem. The first approach uses periodic boundary conditions at the edge of a model, typically applied to square RVEs [332,357]. A fibre break on one edge of the model hence causes stress concentrations in fibres on the opposite edge. Implementing these boundary conditions in the presented model is challenging due to the random fibre packings. The second approach is more straightforward to implement in random fibre packings and was hence used in this study. In this approach, boundary fibres are added so that they can carry SCFs but are not allowed to break. Another approach is to neglect this issue altogether. While this may seem crude at first, this preferential cluster formation at the perimeter also occurs in real tests. In real tests however, the number of fibres is much larger than in models, thereby reducing the importance of fibres at the perimeter.

The role of boundary effects can be analysed by comparing models with and without unbreakable boundary fibres for different numbers of breakable fibres. For models with boundary fibres, a ring of boundary fibres is added that is about two fibres thick. The number of breakable fibres is the same as in the models without boundary fibres. This is necessary to avoid size scaling effects when comparing models with and without boundary fibres. Models with 250 breakable fibres contain 90 boundary fibres, while this number increases to 540 boundary fibres for models with 10000 breakable fibres. The relative number of boundary fibres hence decreases with increased model size.

Figure 4-38 presents the predicted composite failure strains with and without boundary fibres. The failure strain of models with boundary fibres decreases with increased number of breakable fibres. This size scaling effect has been extensively described in literature [148,151,390]. Interestingly, such an effect is not observed in models without boundary fibres. In that case, cluster formation occurs preferentially near the perimeter and this become less likely for larger composites. This reduced probability will tend to increase the failure strain, and hence cancels out the size scaling effect. Both model types converge with increased number of breakable fibres. This convergence is expected, as the importance of the perimeter decreases with increased number of breakable fibres.

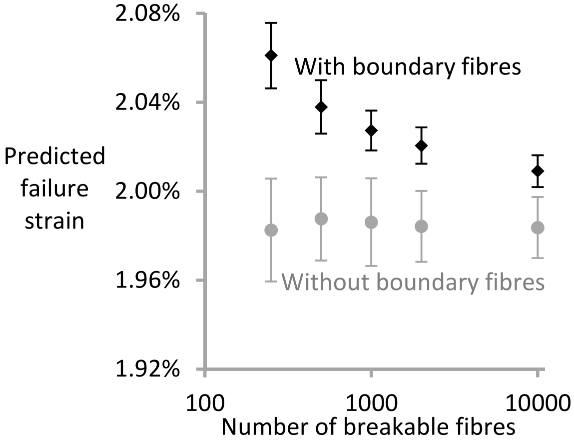

Figure 4-38: Predicted failure strain with and without the unbreakable boundary fibres as a function of the number of breakable fibres. All models are 10 mm long.

To further understand the origin of the difference in failure strain, the cluster development is analysed. The development of 1, 2 and 3-plets was not affected by the boundary fibres, except near final failure (see Figure 4-39). The same conclusion was confirmed for larger clusters and models with a different number of breakable fibres.

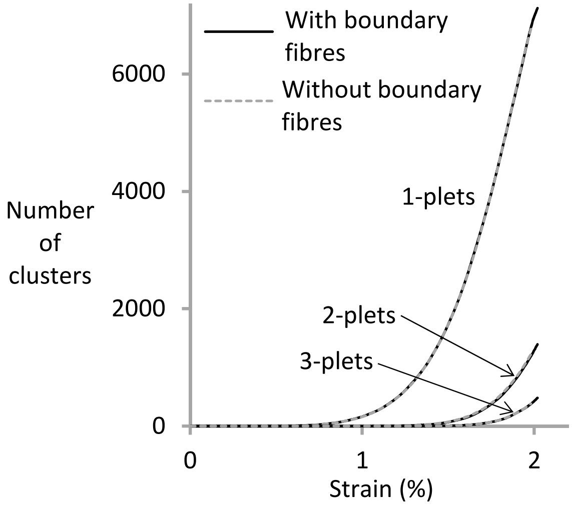

Figure 4-39: The development of 1-plets, 2-plets and 3-plets for models with and without boundary fibres. The number of breakable fibres is 2000 in both cases.

The presence of boundary fibres does create larger critical cluster sizes (see Figure 4-40). Careful analysis of the locations of these critical clusters leads to a crucial difference between models with and without boundary fibres. Figure 4-41 illustrates this difference by plotting a 2D view of all fibre breaks in the last strain increment before final failure. The colour of each fibre indicates the largest cluster along its length, thus providing a projection of all fibre breaks in a 2D view. In models without boundary fibres, the critical cluster occurs near the model perimeter. In models with boundary fibres however, the critical cluster occurs at random locations in the model. It is hypothesised that a smaller cluster is sufficient to cause unstable propagation in the absence of boundary fibres. This is attributed to the fact that these clusters can develop near the perimeter, where they have fewer neighbours and hence higher SCFs. These higher SCFs will more rapidly lead to unstable propagation.

Figure 4-40 also reveals an increase in the critical cluster size with increased number of breakable fibres in the model. This increase is obvious for models without boundary fibres, but is less pronounced for models with boundary fibres. This agrees with the analytical equation for critical cluster size derived by Ibnabdeljalil and Curtin [332] (see equation 4-4). This equation was derived using periodic conditions at the perimeter, which is similar to models with boundary fibres. Their equation only depends on the Weibull modulus, and not on the number of fibres.

The critical cluster size for both model types should converge for a large number of fibres. Figure 4-40 indicates a slow convergence, which is not yet reached for 10000 fibres.

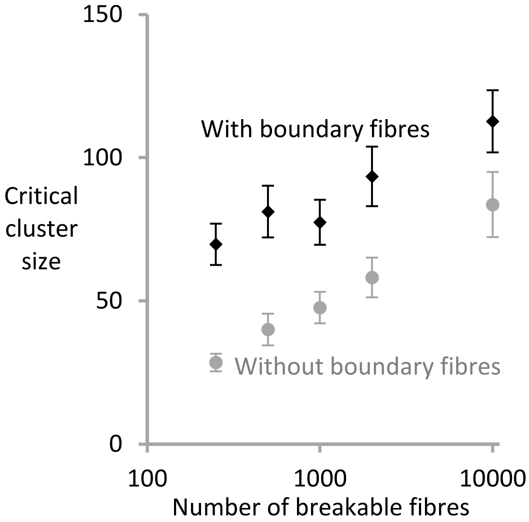

Figure 4-40: The critical cluster size as a function of the number of breakable fibres.

It is difficult to decide whether boundary fibres should be included in strength models. The answer depends on the aim of the model. Without boundary fibres, the model corresponds to the experimental situation if the number of fibres is similar. If it is not computationally feasible to model the large experimental number of fibres, then boundary fibres make the model more representative of larger sample sizes.

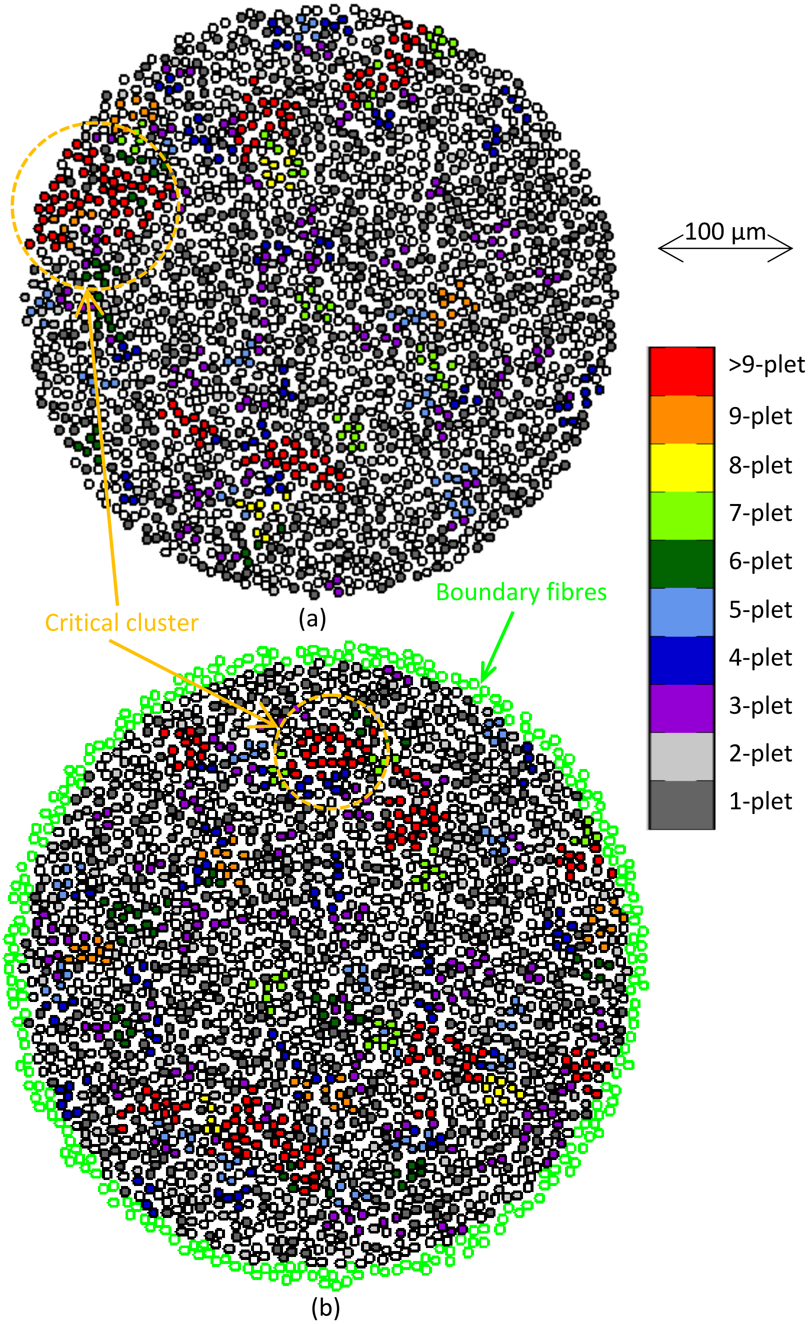

Figure 4-41: 2D view of the cluster development in models with 2000 breakable fibres: (a) without boundary fibres, and (b) with boundary fibres. Hollow black circles indicate that there are no fibre breaks along the length of the fibre, while hollow green circles represent the boundary fibres. The size of the largest cluster along the fibre is indicated by filling the circle with the corresponding colour. The critical cluster is indicated by the large orange circle.

4.4.4 Fibre packing type

Figure 4-42 summarises the influence of the packing type on the predicted failure strain. All observed differences are small but statistically significant. The largest strain difference is only 0.06%, which is smaller than the scatter caused by errors in the Weibull distribution.

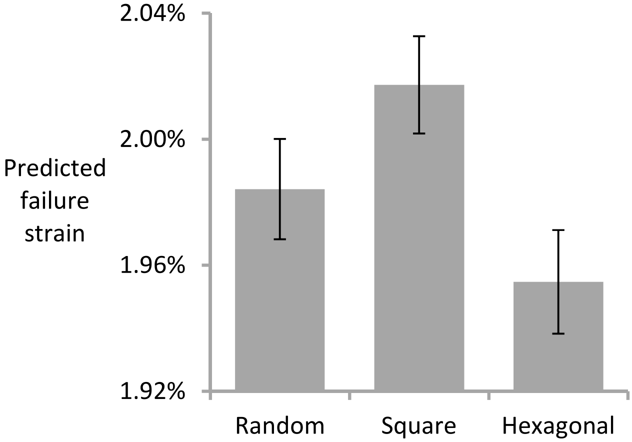

Figure 4-42: Predicted composite failure strains for models with the three packing types.

Figure 4-43 proves that all packings have a similar cluster development up to a certain strain. Near final failure however, the largest cluster is significantly larger for square packings. The results hence indicate that the packing type has a minor influence on the failure development and failure strain. The fundamental reason can be found in Figure 4-17. The highest SCFs in random fibre packings are more than twice as high as in hexagonal packings. This does not mean that the SCFs in general are twice as high. Consider the 6 nearest neighbour fibres, which are all at the same distance for hexagonal packings, but at varying distances for random packings. In a specific random fibre packing, three fibres on average will be closer to the broken fibre than in hexagonal packings. This can be observed from the results of the five different packings, which are indicated with different markers in Figure 4-17. These three fibres carry a larger SCF than in hexagonal packings. The other fibres, however, carry a smaller SCF than in hexagonal packings. These two aspects roughly cancel each other out, leading to a similar failure development and failure strain for the three packing types.

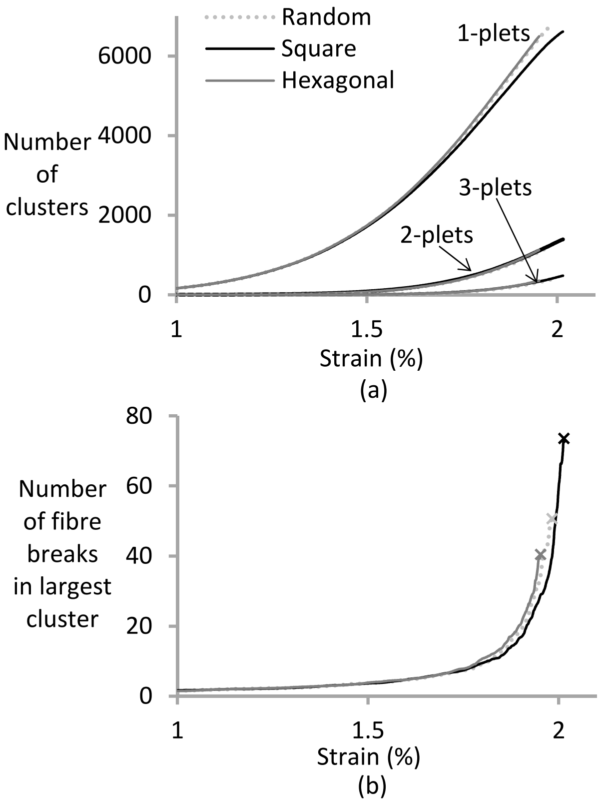

Figure 4-43: Cluster development for the three fibre packings: (a) 1-plet, 2-plet and 3-plet evolution, and (b) largest cluster development. These results are averaged over 50 simulations for each packing.

This is the first confirmation that square and hexagonal packings are accurate assumptions for modelling the 0° tensile strength of UD composites. This conclusion is valid within the modelling assumptions presented earlier, but needs to be verified when other effects are taken into account. Including matrix plasticity or fibre-matrix debonding might lead to differences between predictions for different fibre packings.

Random fibre packings can still be required in two cases: (1) for off-axis loading cases, and (2) in hybrid composites. The importance of random packings in off-axis loading has already been proven in literature [391]. In hybrid composites, the two fibre types often have different radii. Firstly, this difference would limit the maximum V_f in regular, hybrid packings. Secondly, the dispersion of both fibre types would not be completely random, as their fibre centres would have fixed locations. This degree of dispersion is crucial in hybrid composites.

4.4.5 Fibre volume fraction

As discussed briefly in “4.2.2 Stress redistribution for non-interacting fibre breaks”, it can be argued which V_f should be used in strength models. In case of a direct comparison with experimental data, the correct V_f should of course be used. The influence of V_f needs to be understood to be able to conduct a parametric study in a correct manner.

Figure 4-44 summarises the predicted failure strains for the three different V_f. The predictions are similar for a V_f of 50% and 70%, but significantly lower for that of 30%.

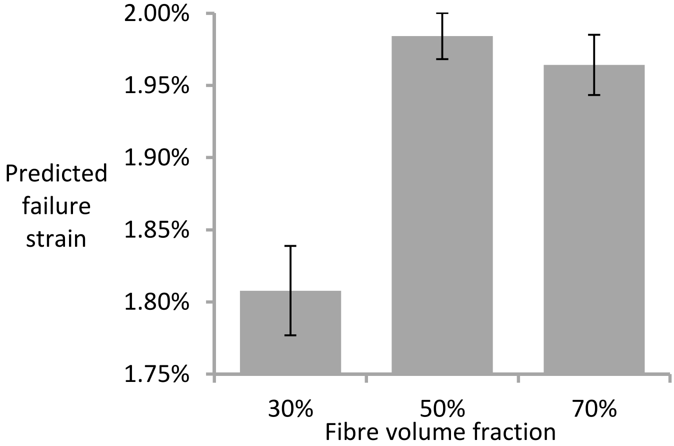

Figure 4-44: Predicted composite failure strains for models with three different fibre volume fractions.

The cluster development was analysed to understand the reasons for the differences in predicted failure strains. Figure 4-45a shows that the development of 1, 2 and 3-plets is relatively similar for the three volume fractions up until about 1.7% strain. The reason for the difference in failure strains can be seen from Figure 4-45b. The largest cluster again develops relatively similar for all V_f. There is however a large difference in the critical cluster size, which can be observed as the largest cluster prior to final failure in Figure 4-45b. The critical cluster size is 51 and 63 for $V_f = 50\%$ and 70%, while it decreases to 14 for $V_f = 30\%$.

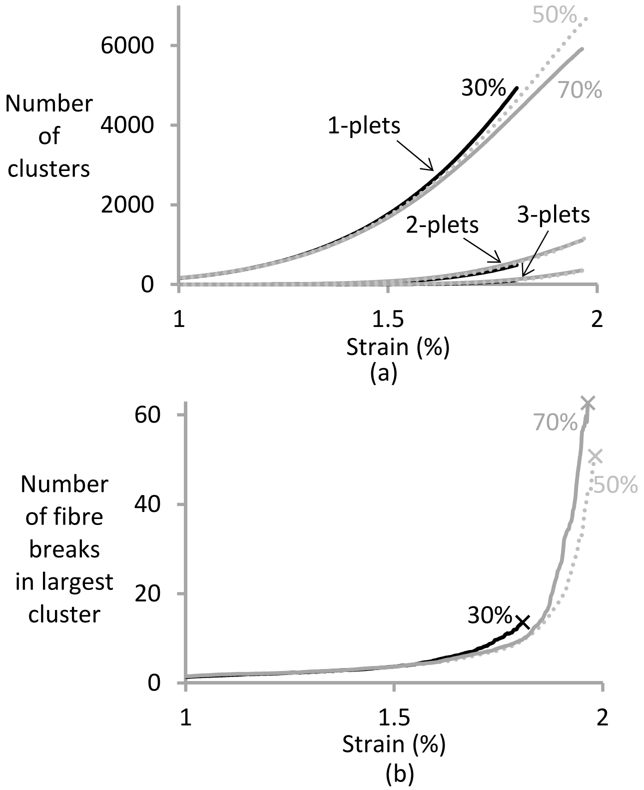

Figure 4-45: Cluster development for models with three different fibre volume fractions: (a) 1-plet, 2-plet and 3-plet evolution, and (b) largest cluster development. These results are averaged over 50 simulations for each fibre volume fraction.

Explaining the small critical cluster size for the V_f = 30% models is not straightforward. The higher maximum SCF (see Figure 4-19) is one important aspect. It is however hypothesised that a model artefact also contributes to the small critical cluster size. Fibre packings at such low V_f contain significant variations in the local V_f (see Figure 4-46). The model neglects such local variations as it applies SCFs based merely on the distance from the broken fibre. The applied SCFs can therefore be much too high for the local V_f. Attempts were made to confirm this hypothesis by visualising the growth of the largest cluster just before final failure, similar to Figure 4-41. Unfortunately, this analysis was inconclusive due to difficulties in analysing what triggers the critical cluster. The best way to analyse this artefact would be to take into account the local V_f in the strength model. Such an adaptation would also require an extensive FE study, and was not attempted.

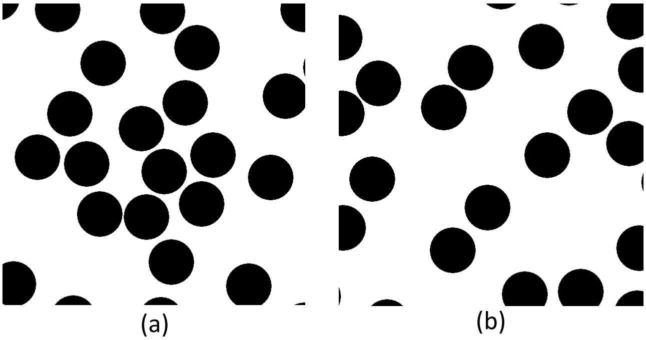

Figure 4-46: Local variations in a packing with 30% fibre volume fraction: (a) a region with high fibre volume fraction, and (b) a region with low fibre volume fraction.

4.4.6 Fibre anisotropy

Fibre anisotropy is typically neglected in SLMs. The subsection "4.2.2 Stress redistribution for non-interacting fibre breaks" proved that anisotropy increases the SCFs and the ineffective length. This increase was small in the presence of matrix cracks, but larger in its absence.

The isotropic fibres result in higher predicted composite failure strains for models without matrix cracks (see Figure 4-47). For models with matrix cracks, the difference is much smaller, but still statistically significant. These trends originate from the differences in the stress redistributions. The larger SCFs for anisotropic fibres increase the failure probability of the nearby fibres. The larger ineffective length for anisotropic fibres has a similar effect, albeit indirectly. It is a measure of the length over which the SCFs are active. A larger ineffective length therefore also reduces the composite strength.

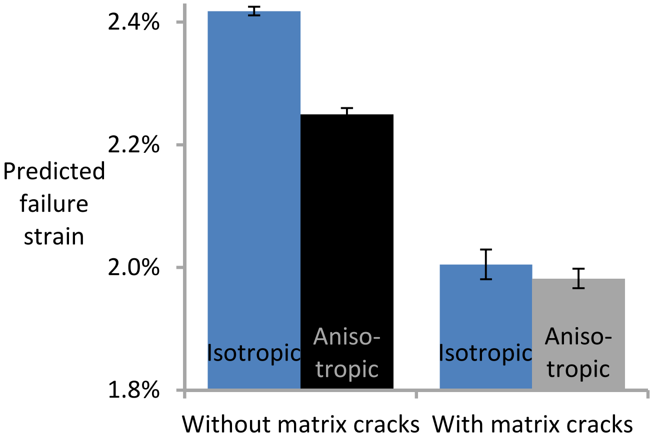

Figure 4-47: Predicted composite failure strains for models with isotropic and anisotropic carbon fibres.

The cluster development of models without matrix cracks is now analysed to further understand the differences in composite failure strain. The analysis for models with matrix cracks is not presented here, as the differences between the two fibre types are small.

Figure 4-48a proves that the cluster development is relatively similar for isotropic and anisotropic fibres. Interestingly, the largest difference is observed in the 1-plet development. Even though the creation of 1-plets is determined by the Weibull distribution, the anisotropic fibre models contain less 1-plets than the isotropic fibre models. This means that 1-plets evolve into higher order clusters more easily in the anisotropic fibre models. While this is not obvious for 2-plets and 3-plets, it becomes clear from the evolution of the largest cluster (see Figure 4-48b). The higher SCFs and longer ineffective length cause larger clusters to develop, which will eventually lead to earlier final failure. The average critical cluster size is almost the same for both fibre types.

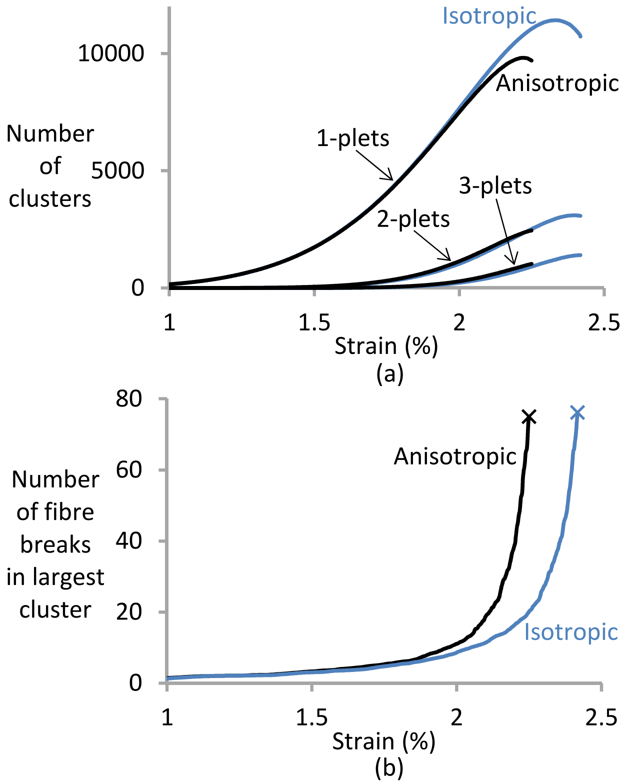

Figure 4-48: Cluster development for models with isotropic and anisotropic fibres, and without matrix cracks: (a) 1-plet, 2-plet and 3-plet evolution, and (b) largest cluster development. These results are averaged over 50 simulations for each fibre type.

These results shed new light on the fact that SLMs neglect fibre anisotropy. Such neglect should be avoided if the model does not contain matrix cracks. In the presence of matrix cracks however, neglecting fibre anisotropy is a reasonable assumption. It should be noted that matrix yielding of fibre-matrix debonding may have a similar effect as including matrix cracks.

4.4.7 Conclusion

The newly developed strength model was used to perform a parametric study with the following conclusions:

- The presence of matrix cracks has a large influence on the failure development. Since matrix cracks also have the advantage of avoiding the FE stress singularity in the broken fibre, they will be used throughout this thesis.
- The Weibull distribution is difficult to measure accurately enough to avoid any influence on the predicted failure strain. Improved experimental methods should be developed.
- The influence of boundary effects was analysed and guidelines are provided when boundary fibres should be used.
- The fibre packing type only had a minor influence on the failure strain and break-cluster development. This validates the use of regular packings for modelling non-hybrid composites.
- The predicted failure strain of models with 30% fibre volume fraction was lower than for 50% and 70% models due to a smaller critical cluster size. This may be attributed to neglecting the local variations in fibre volume fraction.
- The anisotropy of carbon fibres had a significant influence only in the absence of matrix cracks.

The analysis of the cluster development proved useful in understanding how the various parameters affected the predicted failure strain. The largest cluster and critical cluster analysis was particularly helpful in explaining the observed differences.

4.5 Experimental validation

Experimental validations of strength models are often limited to comparing failure strains. Such validations are useful, but nevertheless fail to yield much feedback for future modelling developments. More in-depth experimental validations are needed to advance the state of the art in strength modelling of UD composites.

A fruitful collaboration was set up with Hannah Morton, Anna Scott and Mark Spearing from the University of Southampton. They used synchrotron radiation computed tomography to visualise fibre breaks, yielding data-rich information. They also set up procedures to extract the number of fibre breaks as well as the number of clusters. Their experimental data on T700 carbon fibre in M21 epoxy are used in this section to experimentally validate the developed strength model.

A comparison with the same data set has already been attempted in Scott et al. [265] by using the model of Blassiau et al. [314,355,356,367,368]. Their model predictions were reasonable at low applied strains, but seemed to diverge at higher strains. The model was also less accurate at predicting clustering parameters, especially for larger clusters. This may have been caused by the inherent assumptions in their model. Firstly, Weibull data for a T600S carbon fibre were applied to model a T700S carbon fibre composite. The T600S data sheet quotes a failure strain of 1.8% [392], which is significantly lower than the 2.1% quoted for T700S [389]. Secondly, the model neglects matrix cracks around fibre breaks found in the experiments. As demonstrated earlier, this has a large influence on the stress redistribution and failure strain prediction. Finally, their model is only capable of predicting cluster sizes with a number of fibres equal to a power of two. This hampers an accurate comparison between model and experiments, especially near final failure.

4.5.1 Materials

$[90/0]_s$ Hexcel HexPly T700/M21 aerospace-grade carbon fibre/epoxy prepreg were provided by Airbus. They were used to manufacture composites with a V_f of 55%. The 4 mm wide double-notched coupons were prepared for tensile testing as described in Wright et al. [393]. Coupons were cut by abrasive water jet, which previous research has shown induces no significant damage in similar specimens [393]. Notched samples were used as they enable the damage mechanisms close to final failure to be observed by constraining failure in a limited volume accessible by computed tomography. The 90° plies delaminate from the 0° plies at 70% of the failure load and do not influence the failure development in the 0° plies. Nevertheless, they were added as they limit damage during water jet cutting and help to prevent splitting along the 0° plies during testing.

The section width between the notch roots was 0.8 mm, with an overall composite thickness of 1 mm. This leads to a total of about 5500 0° fibres in the cross-section. Aluminium tabs were bonded to the specimen ends to aid loading, and to reduce stress concentrations at the loading ends. Ten specimens were tensile tested to failure in the 0° direction in a screw-driven load rig to determine the nominal failure load. A description of the rig and the testing methodology is provided in further detail in Wright et al. [393].

4.5.2 Synchrotron radiation computed tomography

Tomographic X-ray scans were undertaken on the ID19 beamline at the European Synchrotron Radiation Facility, Grenoble France. A voxel resolution of 1.4 µm was used, which allowed the identification of individual fibres. A propagation distance of 37 mm allowed a degree of near-field Fresnel edge enhancement, which made it easier to identify individual fibre breaks. A tensile specimen was taken to seven different percentages of nominal failure load (40%, 63%, 70%, 79%, 84%, 89%, 94%) and scanned at each load step. The region of the notch, with a total length of 2.3 mm was monitored. All breaks occurred within a length of 1.54 mm, which corresponds to a volume of 0.61 mm^3 for the 0° fibre plies. This length and volume were used in the strength model and in the normalisation of the break densities.

Data reconstruction was undertaken using in-house software at the European Synchrotron Radiation Facility. The break analysis was performed using VG-Studio™ and FIJI™. An example of the analysed volume is displayed in Figure 4-49a, in which delaminations, matrix cracks due to 0° splitting and fibre breaks can all clearly be seen. Figure 4-49b and c show a fibre break in two orthogonal views, where the break is a distinct black zone. The black zone seems to extend into the matrix, indicating the presence of a matrix crack around the fibre break. Breaks were quantified through visual inspection of the data files in at least two orthogonal planes to ensure accuracy, and extracted from the bulk composite.

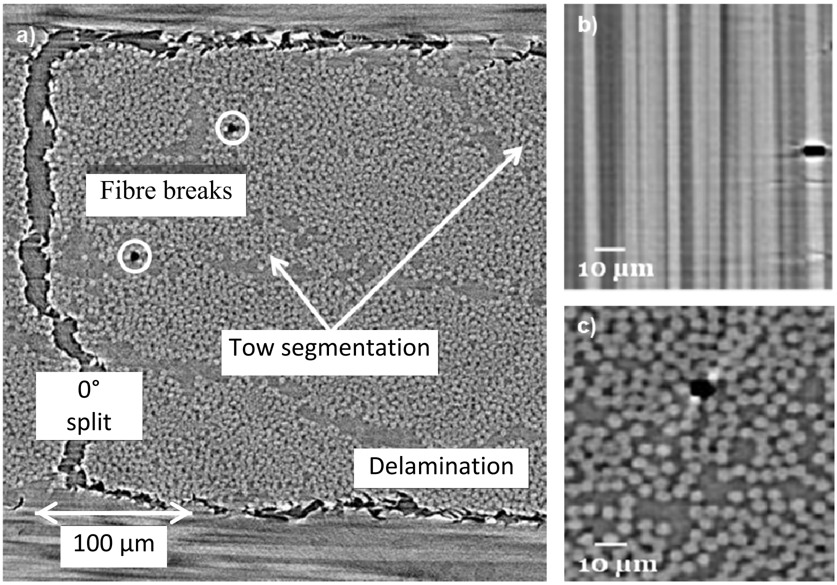

Figure 4-49: Synchrotron radiation computed tomography images near the root of the notch: (a) transverse cross-section at 94% of final failure, showing fibre breaks in the 0° ply, a delamination, a 0° split and tow segmentation, (b) cross-section showing a fibre break with the loading direction being vertical, and (c) the same fibre break in a cross-section perpendicular to (b).

4.5.3 Model parameters

The general procedure has already been extensively described in “4.3 Development of a strength model”. This subsection merely describes the model parameters that were used in the experimental validation.

The bimodal distribution for T700 carbon fibres was used (see equation 4-3 and “4.3.4 Model parameters”). Fibre packings with a 55% V_f were generated and used in both the FE and strength models. The FE models contained T700 carbon fibres with the transversely isotropic engineering constants in Table 4-2. For the M21 epoxy matrix, a tensile modulus of 1.26 GPa was provided by the manufacturer, with an assumed Poisson’s ratio of 0.4. Only the longitudinal tensile modulus of fibre and matrix are used in the strength simulations. Matrix cracks around fibre breaks were implemented in the FE models, as they were also observed in the experiments (see Figure 4-49b and c).

The residual stresses that are induced by curing of the laminate are neglected. These stresses are expected to be small and should not influence the interpretation of the results.

The RVE of the strength model was changed from cylindrical to rectangular cuboid to more accurately represent the tested specimens. The cross-section had rectangular dimensions of 0.8 x 1 mm and contained 5500 fibres. Each fibre was 1.54 mm long and divided into 440 elements of 3.5 µm length.

4.5.4 Tensile response

Achieving scans just before final failure is difficult, as the sample strength is unknown a priori. The highest strain, for which a computed tomography image was obtained, was 1.94%, close to the ultimate failure strain of this particular sample of 2.06%. The stress-strain response predicted by the model and measured in the experiments is compared in Figure 4-50. The specimen response was nearly linear until failure. The ultimate failure strain predicted by the model was 2.42% ± 0.04% which is higher than the experimentally measured failure strain of 2.06% ± 0.10%. The reason for this difference is presumably that the model underestimates the cluster development at strains approaching failure. This will be explored in detail in the next subsections.

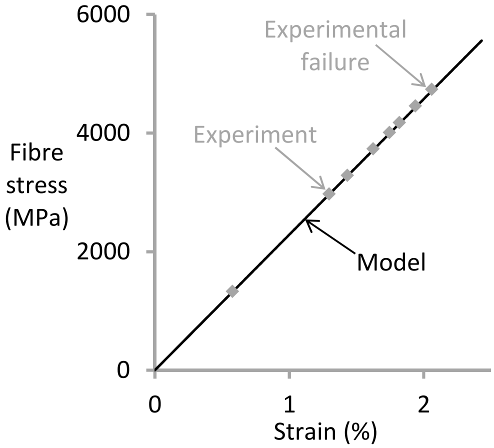

Figure 4-50: Stress-strain diagram of the model and the experimental data points.

4.5.5 Fibre break density

The fibre break density as a function of strain is shown in Figure 4-51. Experimentally, few fibres within the composite break before final failure; in a specimen with 5500 fibres, there were fewer than 500 broken fibres/mm^3, meaning that less than 10% of the fibres were broken. Significant numbers of fibre breaks only accumulated at strains above 1.7% at an increasing rate with applied strain.

At these low fibre break densities, it is useful to compare the in situ fibre breaks with the Weibull prediction. This prediction neglects any stress concentration or stress transfer around breaks. This estimate of fibre break accumulation, together with that due to the model is shown in Figure 4-51. Both the model and the direct application of the Weibull data over-predict the break density, particularly at lower strains. In reality, broken fibres cause SCFs and increase failure probabilities, and hence the model exhibits a larger over-prediction than the Weibull prediction. The fact that the Weibull data over-predict the experimental data suggests that (1) the Weibull distribution is inaccurate or (2) the presence of the composite matrix reduces the in situ defect sensitivity of the fibres.

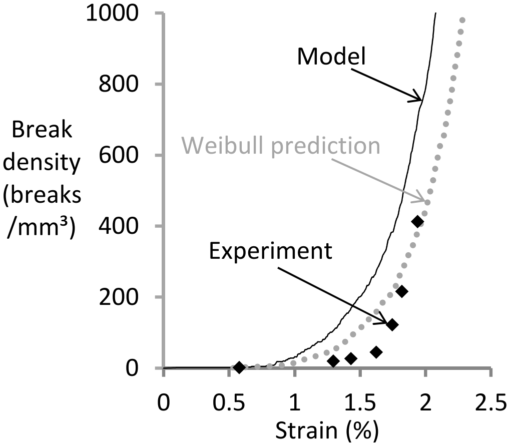

Figure 4-51: Accumulation of fibre break density as a function of applied strain. The prediction based on the Weibull data set is also added.

The model prediction and the experimental break density measurements converge at strains above 2.0% (i.e. near failure). This may simply be a result of the in situ Weibull strength distribution being narrower than that measured from virgin and extracted fibres, due to some as yet unexplained influence of the matrix.

4.5.6 Cluster development

The occurrence of groups of interacting fibre breaks, termed a cluster, indicates the important role of local load sharing in the accumulation of damage. In the experimental work, a cluster was defined as two or more breaks in neighbouring fibres, separated by less than 70 μm in the axial direction. This length was identified previously in [147]. Correspondingly, in the model two fibre breaks were considered as a cluster if (1) the surface-to-surface distance between the fibres was smaller than twice the fibre radius, and (2) the axial distance between fibre break planes was less than 10 times the fibre radius. The second criterion corresponds approximately to 90% stress recovery in the broken fibre. Whilst these definitions are not exactly the same, they are sufficiently similar to allow a useful comparison between the model predictions and experimental results. Changing this definition had little effect on the number of clusters, both for the modelling and experimental procedure. Three different cluster parameters are analysed: cluster pattern, accumulation, and growth.

Cluster patterns

Experimental work identified two different cluster patterns: diffuse clusters (see Figure 4-52a) and coplanar clusters (see Figure 4-52b). The coplanar clusters were defined as clusters of breaks with an axial separation of less than a fibre radius, whilst diffuse clusters were those with an axial offset greater than this value. Approximately 70% of the clusters found experimentally were coplanar, while the model predicted only 15-30% coplanar clusters. This low percentage predicted by the model can be explained based on the stress profiles in the fibres near fibre breaks. While the stresses reach their maximum in the fibre break plane, the stresses remain high over several fibre radii from the fibre berak plane. This smeared out stress increase results in a finite failure probability of the fibre over this distance, and hence allowing diffuse clusters.

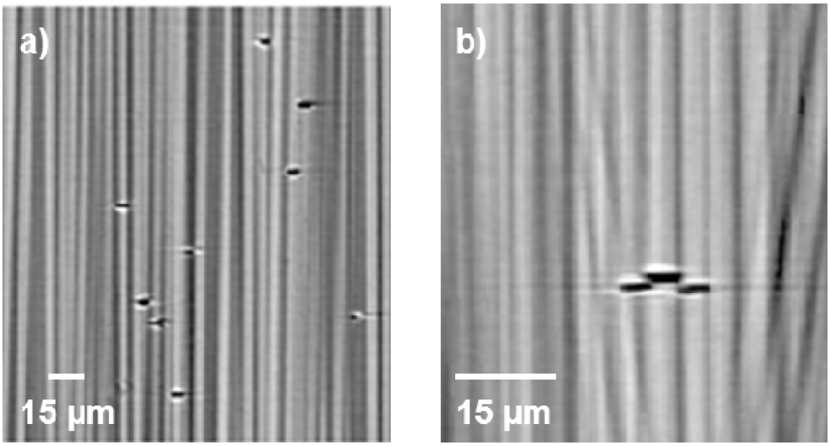

Figure 4-52: Computed tomography image of: (a) diffuse, and (b) coplanar clusters.

The higher percentage of coplanar clusters in the experiment is assumed to be caused by two effects. Both effects are challenging to model and are currently not taken into account in any state-of-the-art model. Firstly, the dynamic SCFs, which occur when the fibre breaks and springs back [153,155,326,327], were not incorporated into the model. Secondly, high stress gradients may occur across the fibres. In the specific case of an intact fibre nearly touching a broken fibre, the FE model predicted local SCFs of up to 260%. This is much higher than the 23% found for SCF averaged over the cross-section. According to the Weibull distribution, small volumes are expected to have a high strength. It is questionable whether the Weibull distribution is still valid in such small volumes and with high stress gradients. The local microstructure of the fibres will also play a key role. Incorporating matrix plasticity into the FE model will tend to reduce these high local SCFs, but they will undoubtedly remain higher than the calculated average SCF value.

Cluster accumulation

In situ loading allows for the damage progression and the accumulation of clusters to be quantified. In calculating the number of breaks in clusters, each break in a cluster was counted instead of only counting the number of clusters. For example, a 3-plet contributed three breaks to the overall break count.

The largest cluster found experimentally was a 14-plet at a strain of 1.94%. At the same strain, the largest cluster size in the model was predicted to be between 2 and 4, depending on the individual Monte Carlo simulation. It may be more relevant to compare the 14-plet with the largest predicted cluster in the last strain increment before final failure. The average size of the largest predicted cluster in the last strain increment was 24. This size corresponds well with the experimentally found 14-plet, given the fact that the 14-plet was found at 1.94%, which is 0.12% strain before final failure.

The accumulation of clusters as a function of strain is displayed in Figure 4-53. As expected from Figure 4-51, the number of 1-plets is overestimated by the model. The number of clusters, however, is consistently underestimated and predicted to start only at higher strains. As noted earlier, this suggests that in the experiments the effective stress concentrations are higher than in the model.

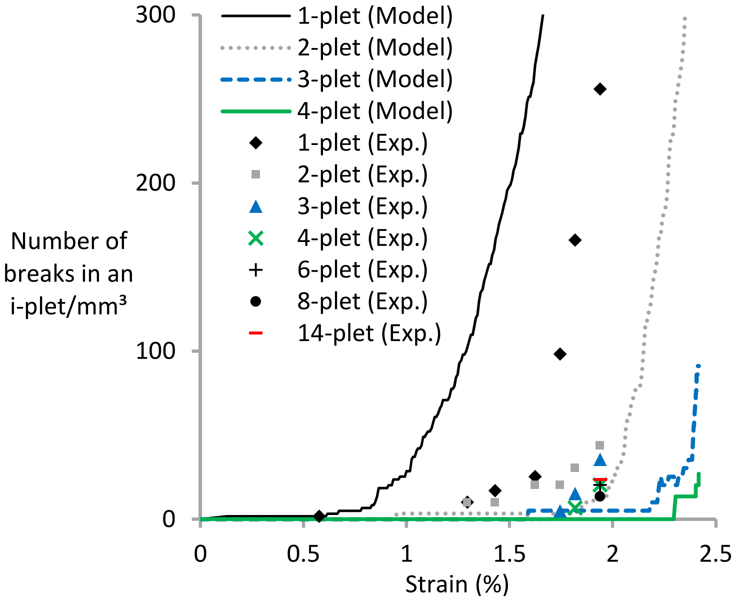

Figure 4-53: i-plet accumulation as a function of applied strain. Values are normalised to the experimental sample volume.

In the experiments, up to 50% of the total breaks occurred in clusters. However, there was no correlation between this cluster percentage and the applied strain. Higher strains did not always result in higher cluster percentages. In the model, the cluster percentage gradually increases with strain, but never reaches more than 30%. This difference may again be explained by the two effects suggested earlier: dynamic and local SCFs.

Cluster growth

The experimental results showed that as larger clusters formed, there was no reduction in the number of smaller clusters. This may imply that clustering is a dynamic process and that once formed, clusters do not grow further in size. To verify this hypothesis, all clusters in the experiment were tracked through the different strain increments. It was found that clusters formed at one strain increment and stayed at a constant size as the strain increased. This suggests that the dynamic stress concentrations that occur when a cluster develops must have been of significant magnitude. The model only includes static stress concentrations and found that clusters grew gradually with increasing strain increments. This again suggests that incorporation of the dynamic nature of stress concentrations is crucial for an accurate prediction of the cluster growth. Unfortunately, little effort has been made in this area (see "4.1.2 Stress redistribution around fibre breaks"). Such a study was also outside the scope of this thesis.

4.5.7 Conclusion

The failure strain and cluster development predicted by the strength model has been compared to experimental data. The model predicted the final failure strain and strength of the UD composite reasonably well, with only a small overestimation. The accumulation of break density with applied strain was significantly overestimated by the model. This was attributed to errors in the Weibull strength distribution.

The model also predicted that diffuse clusters would dominate, whilst coplanar clusters were dominant in the experiments. The largest experimentally observed cluster was a 14-plet, while the model predicted that 24-plets would occur on average before final failure. The model predicted the development of large clusters to occur at higher strains, which is consistent with an underestimation of the stress concentrations.

Another crucial difference between the model and the experimental observations was the static versus dynamic formation of clusters. In the experiments, clusters formed within a single load step and did not increase in size upon further loading. This is in contrast with the modelling predictions, where clusters gradually grew in size as strain was incremented. This difference was attributed to the effect of dynamic stress concentrations and local stress concentrations at the matrix crack tip. These aspects are currently not incorporated in the model nor are they incorporated in any state-of-the-art models. These aspects merit further modelling attention.

4.6 Conclusion

A versatile FE methodology was set up to analyse the stress redistribution around non-interacting fibre breaks. An enhanced superposition principle was set up to calculate the stress redistribution around interacting fibre breaks based on single fibre break solutions. These results have been incorporated into a numerical strength model based on the chain-of-bundles approach.

A parametric study was performed to develop a deeper understanding of the behaviour of the strength model. This study also highlighted the versatility of the strength model, which will be crucial for the extension to hybrid composites.

Finally, the model was validated by comparing it to experimental data. Although some discrepancies in the cluster development were found, the results agreed reasonably well. The discrepancies were mainly attributed to: (1) errors in the Weibull distribution, (2) neglecting the dynamic stress concentrations and (3) averaging of the high local SCFs over the entire cross-section of the fibre. While the first cause is related to obtaining the right input parameters, the other two causes are currently not taken into account by any state-of-the-art model.

The next step is to extend the strength model to hybrid composites. This extension will be described in the next chapter.

Chapter 5:

Strength model for UD hybrid composites

This chapter will analyse the synergistic failure strain enhancement that occurs when carbon fibre composites are hybridised. This hybrid effect is investigated for carbon/glass hybrids to facilitate comparisons with literature data. First, the stress redistribution around fibre breaks is analysed. Then, the strength model for UD non-hybrid composites is extended to UD hybrid composites. This model will be used to do a parametric study and to establish which parameters influence the hybrid effect. Finally, a new methodology for measuring the hybrid effect is proposed and the model is validated against experimental results. The conclusions in this chapter are also extended to hybrid self-reinforced composites and will feed into the road map for the optimisation of hybrid self-reinforced composites.

This chapter develops a strength model for UD hybrid composites. The objective is to study the hybrid effect for failure strain and understand how it can be maximised. The model focuses on the failure of carbon fibres, and does not attempt to model what happens after this occurs.

There are three important differences between this chapter and “Chapter 3: Hybrid self-reinforced composites”. Firstly, this chapter focuses on unidirectional hybrid composites, whereas chapter 3 investigated multidirectional ones. The state of the art in hybrid composites (see “3.1 State of the art”) has paid nearly no attention to modelling of multidirectional hybrid composites. This thesis attempts to develop a detailed understanding of the failure development in unidirectional hybrid composites, which should facilitate the development of models for multidirectional hybrid composites in the future. Secondly, this chapter focuses on carbon/glass hybrids, whereas chapter 3 focused on carbon/PP hybrids. This was a deliberate choice to facilitate comparison with literature data. Nevertheless, the findings on carbon/glass hybrids will be used to derive the implications for carbon/PP hybrids. Finally, this chapter deals with intrayarn hybrids, whereas the previous chapter dealt with interlayer and intralayer hybrids. All state-of-the-art models focus on intrayarn hybrids, but these are unfortunately highly challenging to obtain experimentally. Nevertheless, the model will also be applied to layered or bundled configurations, provided they are reasonably well dispersed.

This chapter follows the same structure as “Chapter 4: Strength model for UD non-hybrid composites” and is also divided into five sections (see Figure 5-1). The state of the art section 5.1 describes existing strength models for UD hybrid composites. This section also provides an overview of all the parameters that can influence the hybrid effect. The parameters that are found to be relevant will be analysed in the other sections.

Section 5.2 studies the stress redistribution around fibre breaks. The influence of the hybrid volume fraction and fibre dispersion on the stress redistribution will be analysed.

Section 5.3 describes how the strength model for non-hybrid composites was extended to hybrid composites. This section also proposes a modified version of the strength model, which is more suitable to model the influence of fibre dispersion on the hybrid effect.

Section 5.4 reports the results of a parametric study of the hybrid effect in carbon/glass hybrid composites. The information from the state of the art will be used to select the most relevant parameters to study. The conclusions from this section are also extended to carbon/PP hybrid composites by studying the influence of the stiffness and failure strain of the high elongation fibre on the hybrid effect.

Section 5.5 proposes a new methodology for measuring the baseline failure strain that is required to calculate the hybrid effect. Next, this methodology is used to experimentally validate the strength model for carbon/glass hybrid composites.

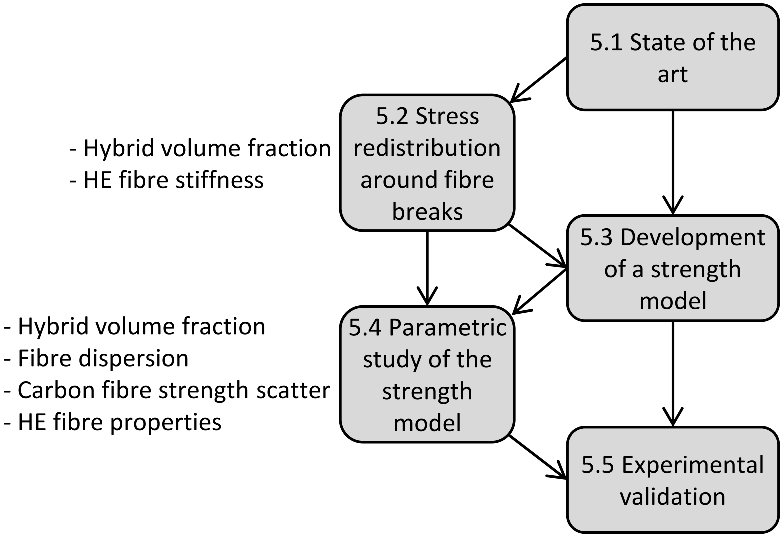

Figure 5-1: Schematic overview of the structure of this chapter.

5.1 State of the art

The previous chapters already provided reviews on the state of the art in hybrid composites (see “3.1 State of the art”) and models for UD non-hybrid composites (see “4.1 State of the art”). This state of the art section will therefore be shorter than previous ones.

Modelling the strength of UD hybrid composites adds another layer of complexity compared to non-hybrid composites. The fibre types may be arranged in various configurations such as intrayarn or interlayer. Both the stress concentrations and ineffective length are expected to depend on the type of the nearby fibres. This additional geometrical complexity makes modelling hybrid composites a challenging task.

Zweben [133] developed the first statistical model to predict the hybrid effect. Despite being published more than 35 years ago, this work remains a seminal model for hybrid composites. The first subsection describes Zweben’s model and its conclusions in detail. The second subsection describes later improvements to this model as well as other approaches. The final subsection provides an overview of all the parameters that influence the hybrid effect for failure strain. This overview will distinguish the crucial parameters from the less important parameters. This will help in deciding which parameters to study using the newly developed model.

5.1.1 Zweben's model

In 1977, Zweben [133] was the first author to extend shear-lag models for unidirectional composites to hybrid composites and model the hybrid effect for failure strain. His model is based on local load sharing instead of very local or global load sharing (see "4.1.3 Strength models for unidirectional composites"). Zweben modelled 1D fibre packings, consisting of a single row of LE fibres (see Figure 5-2a). This was modelled and compared to a similar packing with alternating LE and HE fibres, as illustrated in Figure 5-2b. This type of packing is common in models for hybrid composites [135,394-396], as it is the most straightforward way to simplify the geometrical complexity of hybrid composites.

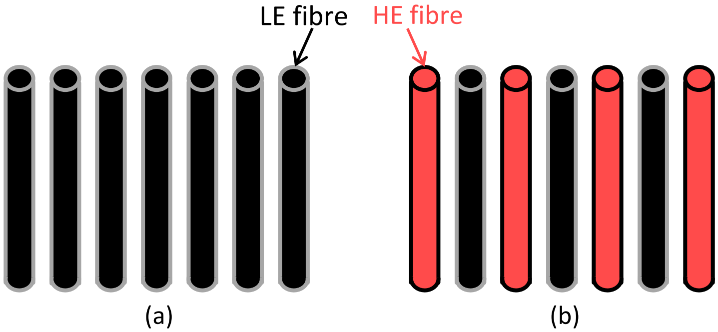

Figure 5-2: Schematical representation of 1D fibre packings used in Zweben's model: (a) a non-hybrid composite with only LE fibres, and (b) a hybrid composite with alternating LE and HE fibres.

Zweben derived analytical expressions for the strain concentrations and ineffective length in both packings. The strain concentration factor k was defined as the ratio of the strain in a fibre next to a single broken fibre over the applied strain. Since all fractures were assumed to occur in a single plane, this parameter was only defined in the plane of fibre break. The strain concentration factor for hybrid composites k_h only depends on R_{EA}, which is the ratio of normalised stiffnesses of both fibre types:

$$R_{EA} = \frac{E_{LE} \cdot A_{LE}}{E_{HE} \cdot A_{HE}} , \tag{5-1}$$

in which E_{LE} and E_{HE} are the Young's moduli of the LE and HE fibres, respectively, and A_{LE} and A_{HE} are the cross-sectional areas of the LE and HE fibres, respectively. For the exact relationship between k_h and R_{EA}, the reader is referred to Zweben [133]. The factor k_h monotonically increases with R_{EA} and is larger than k for R_{EA}-values above 1.

The ineffective length δ_h for the hybrid composite can be calculated as:

$$\delta_h = N_{EA} \cdot \sqrt{\frac{E_{LE} \cdot A_{LE} \cdot w_m}{G \cdot t_m}}, \tag{5-2}$$

in which w_m and t_m are the width and thickness of the matrix region between the fibres, G is the matrix shear modulus, and N_{EA} is a factor which solely depends on ρ_{EA}. The strain concentration factor k_{LE} and ineffective length δ_{LE} for an LE fibre composite are achieved by setting R_{EA} equal to 1.

Zweben assumed that composite failure occurs when the first HE fibre breaks, resulting in a lower bound for composite strength. This led to the derivation of an expression for the hybrid effect R^{hybrid}. This is a dimensionless parameter, which is defined as the ratio of the failure strain of the hybrid composite $\overline{\varepsilon}_{h,\mathrm{c}}$ over the failure strain of the LE fibre-reinforced composite $\overline{\varepsilon}_{LE,\mathrm{c}}$. Please note that this definition does not seem to correspond to the first definition given in Figure 3-4. Zweben defined failure to coincide with the first failure of an HE fibre next to a broken LE fibre, whereas our definition is based on unstable failure of the LE fibres. Zweben however assumes that this first HE failure will trigger unstable failure of all the other LE fibres. With these assumptions, Zweben's definition does conform to the definition described in Figure 3-4. Combining equations 5-1 and 5-2 with the Weibull distributions for fibre strength yields equation 5-3 for the hybrid effect R^{hybrid}:

$$R^{hybrid} = \frac{\overline{\varepsilon}_{h,c}}{\overline{\varepsilon}_{\mathrm{LE},c}} = \sqrt{\frac{\overline{\varepsilon}_{\mathrm{HE,f}}}{\overline{\varepsilon}_{\mathrm{LE,f}}}} \cdot \left[\frac{\delta_h \cdot \left(k_h^m - 1\right)}{2 \cdot \delta_{LE} \cdot \left(k_{LE}^m - 1\right)}\right]^{-1/2 \cdot m}, \tag{5-3}$$

in which $\overline{\varepsilon}_{LE,f}$ and $\overline{\varepsilon}_{HE,f}$ are the mean failure strains of the LE and HE fibres at the tested gauge length, respectively, and m is the Weibull modulus of both fibres. Note that Zweben assumed both fibres to have the same Weibull modulus to simplify the equations.

Zweben also compared his model predictions to experimental data. Zweben's model predicted a hybrid effect of 22% for unidirectional carbon/aramid hybrids. This is significantly higher than the 4% found in their experiments. Zweben also compared this prediction with a multidirectional carbon/aramid composite, which showed a hybrid effect of 31%. This is closer to the predicted value of 22%, but questions arise whether this model can be applied to the more complex situation of multidirectional hybrids.

If Zweben's equations are further analysed and interpreted, then several important conclusions can be drawn:

- The strain concentration factor depends only on the normalised ratio R_{EA} of the extensional stiffness of the two fibre types. In the rare occasion of a hybrid composite with two fibre types with the same extensional stiffnes $E \cdot A$, the strain concentrations are the same in the hybrid and non-hybrid composite.
- The most influential parameter in Zweben's model is the ratio of the failure strains. If this ratio is larger, then the hybrid effect will be larger. Therefore, hybridisation with very high elongation fibres should be effective.
- The exponent $-1/(2 \cdot m)$ is negative and typically small, as most carbon fibre Weibull moduli are between 5 and 8 [286,380]. This means that the ineffective length and stress concentration factor only have a small influence on the magnitude of the hybrid effect.
- Although this was not mentioned by Zweben, fibres with small Weibull moduli should yield a larger hybrid effect. This means that a large spread on the fibre strength is beneficial for the hybrid effect. This was later confirmed by Fukunaga et al. [397].

5.1.2 Later improvements

Zweben's model is powerful, as it is simple and allows for an easy interpretation. The simplified 1D fibre packing however leads to three limitations. Firstly, the fibre packing is a one-dimensional row of fibres, which leads to overestimations of the stress concentrations compared to the more realistic 2D packings [143]. Secondly, the LE and HE fibres are arranged in an alternating manner, leading to the highest possible dispersion for the fixed 50/50 ratio of LE/HE fibres. A broken LE fibre is always shielded from the next LE fibre by the HE fibre in between. Zweben's model is not capable of investigating the influence of fibre dispersion. Finally, the packing leads to a fixed ratio of LE over HE fibres, which means Zweben's model cannot investigate the influence of the LE fibre volume fraction. This fraction was proven to be a key parameter for maximising the hybrid effect [120].

Fukuda [394] pointed out three other intrinsic shortcomings of Zweben's model [133], which he improved in his own model. Firstly, Zweben used the first failure of an HE fibre near a broken LE fibre as failure criterion, which may not be a realistic criterion for hybrid composites and does not conform to the definition given in Figure 3-4. Secondly, Zweben [133] assumes that failure occurs when an HE fibre fails next to a broken LE fibre. This means Zweben calculated a lower bound for the failure strain of hybrid composites. In hybrid composites, however, a broken LE fibre typically leads to failure of the adjacent LE fibres instead of the adjacent HE fibre. This surrounds an HE fibre by two broken LE fibres and leads to larger stress concentrations than predicted by Zweben. Finally, Zweben's approximate method [133,398] predicts stress concentration factors smaller than Hedgepeth's solution. Fukuda [394] mentions that this may lead to an overestimation of the composite strength. The last argument of Fukuda may not be a valid one, as other authors [145,343] later demonstrated that Hedgepeth's approach [143,152] actually overestimates the stress concentrations.

After addressing these three shortcomings, Fukuda [394] obtained equation 5-4 for the enhancement of the LE composite failure strain.

$$R = \left[\frac{\delta_h \cdot \left(k_h^m - 1\right)}{2 \cdot \delta \cdot \left(k^m - 1\right)} \right]^{-1/2 \cdot m} \tag{5-4}$$

This equation is similar to equation 5-3, but with two vital differences. Firstly, the ratio of failure strains of both fibres is not included in this model anymore. This would mean that the failure strain of the HE fibres does not affect the hybrid effect. Secondly, the stress concentrations and ineffective lengths were calculated more accurately. Fukuda's equation results in a better correlation with the experimental results of Zweben [133] and Bunsell and Harris [140].

Fukuda and Chou [134] extended Hedgepeth's approach [152] to calculate the stress concentrations adjacent to a group of broken fibres. Their results indicate that hybrid composites with high and low modulus fibres display lower stress concentrations on the high modulus fibre than composites with only high modulus fibres. This effect leads to an increased failure strain of the high modulus fibres and hence, a positive hybrid effect. Their terminology may be confusing, as in their work high and low modulus fibres are the LE and HE fibres, respectively. Zeng [322] confirmed the conclusion that the stress concentrations on LE fibres decrease by adding HE fibres with a lower modulus. Fukunaga et al. [399] later showed that the stress concentrations could also be higher in hybrid composites if the number of adjacent LE fibres increases. Their model was, however, based on a single row of only four fibres.

All these models applied shear-lag theory to 1D fibre packings [133-135,322,394-397,399,400]. Recently, Pimenta and Robinson developed the first shear-lag model for hybrid composites in a square 2D packing [401]. Their model builds on the hierarchical scaling law [148] described in "4.1.3 Strength models for unidirectional composites". They were able to predict the influence of the carbon/glass ratio and showed an increased hybrid effect with increased dispersion. Unfortunately, the nature of their model does not allow an in-depth understanding of the damage development of hybrid composites. While their model can investigate various dispersions, it is limited to a few, simple configurations. Furthermore, their stress concentrations are unrealistic, which makes the failure development unrealistic.

The previous paragraphs focused on the hybrid effect for failure strain. The damage development, however, can also be altered by hybridisation. Using a Monte Carlo approach, Fukuda and Chou [400] demonstrated that the initial fibre failures occurred at the same strain in hybrid and non-hybrid composites, but that hybrid composites failed more gradually, leading to a higher ultimate failure strain. This feature was attributed to the crack-arresting of the LE fibre breaks by the HE fibres. Zeng's model for hybrid composites reached a similar conclusion after observing a change in the failure mode of the LE fibres [322]. Zeng demonstrated that the stress concentrations around a broken LE fibre are more localised in hybrid composites and therefore have a tendency to break at multiple, independent locations along their gauge length.

A more advanced model was developed by Mishnaevsky and Dai [361,362]. They created a numerical fibre bundle model with about 250 fibres in a random 2D packing. They showed that the tensile strength of a carbon/glass hybrid composite may be lower than the tensile strength of its constituent composites. This conclusion is indeed expected from the bilinear rule of mixtures for tensile strength (see Figure 3-7). Unfortunately, the overall fibre volume fraction in their model was only 25% and they did not analyse the hybrid effect. Furthermore, they defined tensile strength as the stress at which the stiffness was reduced by 50%. This indicates their model did not actually predict a catastrophic failure, as is the case in experiments.

Several authors indicated that HE fibres act as crack arresters in hybrid composites [135,400]. Since HE fibres have a higher failure strain, they can bridge the cracks formed by the broken LE fibres. This understanding is vital, as it also helps to explain why the hybrid effect is more pronounced at lower LE fibre content and higher degrees of dispersion. In both cases, the crack arresting effect is more pronounced. The low LE fibre content argument was confirmed by Kretsis' overview of experimental results of other authors [120]. The higher hybrid effect with better dispersion has also been confirmed by the models of Fukunaga et al. [397,399], Pan and Postle [402], Fariborz et al. [395,403] and Harlow [404].

Fukunaga et al. [399] proved that a hybrid effect only exists if the LE fibres have a spread on their strength. This was also indicated by Manders [405], who stated that: "*the hybrid effect arises from a failure to realise the full potential strength of the fibres in all-carbon fibre composites, rather than from an enhancement of their strength in the hybrids*". If all LE fibres have the same strength, then they will already realise their full potential in non-hybrid composites and no hybrid effect can exist. This is in line with Zweben's model, where an increased scatter in fibre strength also leads to an increased hybrid effect.

With the exception of Mishnaevsky and Dai [361,362], all models for hybrid composites are shear-lag based. This is the reason for their inherent limitations with respect to fibre dispersion and packing types. More refined models are needed to advance the state of the art of hybrid composites.

5.1.3 Influencing parameters

The previous subsections described various aspects of understanding the failure of hybrid composites. This subsection aims to give an overview of the different parameters that influence the hybrid effect, and to assess which parameters are the most important ones. The focus is put on the hybrid effect for failure strain, as most available data are concerned with this specific hybrid effect.

Relative amount of fibres

The relative amount of both fibres is a crucial parameter for the hybrid effect. As illustrated by Kretsis [120], a larger hybrid effect for failure strain of the LE fibre composite is found in experiments if the relative volume of LE fibres over the volume of all fibres is lower. The corresponding modelling evidence is unfortunately limited. This is attributed to alternating 1D packings (see Figure 5-2b), which limits most models to 50/50 hybrids. Some authors were not limited by this type of packing and did prove the importance of the relative amount of both fibres. First, Fukunaga et al. [399] determined that the hybrid effect is maximised at low LE fibre content. Later, this was confirmed by the model of Jones and Dibenedetto [207], who showed an increase in the apparent breaking strength of carbon fibre by 92% if the carbon fibres were isolated from each other by the addition of many glass fibres. Pimenta and Robinson [401] also reported an increase in the failure strain by increasing the dispersion. They also noted that for poorly dispersed hybrids, it may be necessary to include splitting of the LE bundles.

Elastic properties of the fibres

The elastic properties of the two fibres are important, as they affect (1) the static stress concentrations [133,134,394,406], (2) the ineffective length [133] (3) the dynamic stress concentrations [155]. It should be noted that Zweben's model predicted only a small influence of the first two parameters, but his conclusions need to be verified with more refined models. If the coefficients of thermal expansion remain the same, but the stiffness changes, then the thermal effect will also be influenced. Therefore, all three hypotheses for the hybrid effect are affected by the elastic properties of the fibres.

Failure strain ratio

Zweben's model [133] indicated that the ratio of the average failure strains of both fibre types plays a crucial role in the hybrid effect. His definition of the hybrid effect was based on fracture of an HE fibre near a broken LE fibre. In contrast, Fukuda [394] defined the hybrid effect based on fracture of an LE fibre near a broken LE fibre. In that case, the ratio of the failure strains has no effect on the hybrid effect. Both Zweben's and Fukuda's model are simplified and require several assumptions, which probably means the reality lies somewhere in the middle. If the HE fibre failure strain is close to the LE fibre failure strain, then some HE fibres will break prior to full failure of the LE fibres. This should reduce the hybrid effect. By contrast, if the HE fibre failure strain is much larger than LE fibre failure strain, then the two fibres act independently and a larger hybrid effect can be expected. This was also pointed out by Fariborz et al. [395]. More work is needed to establish how important the ratio of average fibre failure strains is in determining the hybrid effect for composite failure strain.

Fibre strength distribution

The fibre strength distribution plays a crucial role. Fukunaga et al. [399] revealed that the hybrid effect is zero when there is no scatter on the LE fibre strength. If the strength of the LE fibres has a large scatter and hence a small Weibull modulus, then the hybrid effect is expected to be larger. This can also be derived from the models of Zweben [133] and Fukuda [394].

Degree of dispersion

The degree of dispersion is yet another important parameter. Some of the early models were not able to model this, as they used the simplified 1D packing with alternating LE and HE fibres [133,134,394,402]. Some authors have claimed to find an increase in the hybrid effect for failure strain with increased dispersion, but they simultaneously changed the relative volume fractions of both fibre types. This was for example the case in Harlow [404]. Fukunaga et al. [399] were the first ones to prove that the hybrid effect increases when the dispersion was increased, while keeping the relative volume fractions constant. Fukunaga et al. did not mention how large the increase was, but from their figures an increase in the strength by about 10% can be estimated. A recent study by Mishnaevsky and Dai [361] reported that a finer dispersion leads to slower development of internal damage. This was only true for displacement-controlled models, while a faster damage development was found for load-controlled models. Mishnaevsky and Dai however, do not describe how the load is distributed over the two fibre types in their load-controlled models. This makes it impossible to judge whether this loading condition is relevant.

Due to the overwhelming amount of experimental data confirming the importance of dispersion [123,157,208,210,407,408], there is no doubt that this is one of the most critical parameters. In these experiments, additional improvements of about 20% in failure strain by increasing the dispersion have been reported by several authors [210,407,408].

Matrix properties

Finally, the matrix properties also affect the hybrid effect, indirectly through their influence on the stress concentrations and ineffective length. The influence of the matrix on the ineffective length is determined by its shear modulus G, as can be seen in equation 5-2. Zweben's equations [133] for the stress concentration are only affected by the fibre moduli and cross-sectional areas. This is due to the assumptions of the shear-lag theory, which assumes the matrix does not carry axial loads. As Pan and Postle [402] showed in their models, an increased matrix shear yield strength can also increase the hybrid effect, but only at a high LE V_f. The matrix properties are hence expected to have only a secondary effect.

Other parameters

There are several other parameters, such as fibre-matrix interface strength and interlaminar and interfacial fracture toughness, which may also influence the hybrid effect. These properties will for example influence the debonding of LE fibre bundles. So far, none of the models take into account these properties and it is therefore difficult to judge their importance. More advanced models are required to establish the importance of these parameters.

5.1.4 Conclusion

In the seventies and eighties, several models for hybrid composites were developed. In the past two decades, however, hybrid models ground to a halt, while the state-of-the-art models for non-hybrid composites have advanced significantly. Currently, the models for hybrid composites are lagging behind on those for non-hybrid composites.

While the initial fibre failures occur at the same strain, the failure development in hybrid composites is more gradual than in non-hybrid composites. Predicting this failure development remains a challenging task, due to the complex interplay of many parameters. The additional geometric complexity compared to non-hybrid composites makes the currently available models limited to qualitative statements. This gap between experiments and models was also confirmed by Jawaid et al. [219]. To increase the use of hybrid composites, there is a strong need for quantitative predictions of the mechanical properties of hybrid composites. These predictions should not only focus on the initial failure of the LE fibres, but also on the failure development and on the final failure of hybrid composites. None of the state-of-the-art models are currently capable of making such predictions.

5.2 Stress redistribution around fibre breaks

The FE methodology for calculating the stress redistributions around fibre breaks has been set up in “4.2.1 Methodology”. This section describes how this methodology was extended to hybrid composites. Next, the stress concentrations around single fibre breaks in hybrid composites are analysed. The hybrid volume fraction and HE fibre stiffness is varied and its effect on the stress redistribution is analysed. The enhanced superposition principle is assumed to remain valid for hybrid composites and will not be analysed again here.

5.2.1 Extension to hybrid composites

Carbon and glass fibres do not have the same radius. Assuming that they have the same fibre radius leads to large errors in the stress redistribution around fibre breaks. These results are not presented here, but have been published elsewhere [406]. Models should thus use the correct fibre radii.

Incorporating different fibre radii does not create any issues in the FE methodology. Two adaptations were required. Firstly, the generator needs to be able create random fibre packings with arbitrary fibre radii. Basically, the criterion for overlapping fibres needs to be adapted. Overlapping is normally detected if the distance between the fibre centres is smaller than two times the fibre radius. Chapter 4 already adapted this criterion to randomly generate a value between 2 and 2.1 times the fibre radius. For creating hybrid packings, the criterion is changed to a value between 1 and 1.05 times the sum of the radii of both fibre types. For composites where all fibres have the same radius, this criterion reduces back to the previous criterion.

Secondly, the generator needs to be extended with a criterion to decide which fibre type will be placed next. The fibre packing will depend on the order in which the fibre locations for the two fibre types are generated. If all the large glass fibres are generated first, then the smaller carbon fibres will mainly end up in the holes between the glass fibres. A better approach is to generate both fibre types simultaneously. The generator therefore calculates the current carbon/glass fraction before a new fibre location is generated. If this fraction is higher than the required fraction, then the next fibre will be a glass fibre and vice versa. In this way, the average fraction is close to the required fraction at each step in the generating process.

Similar to the case of non-hybrid composites, all SCFs will be plotted as a function of the relative distance between the broken and intact fibre. For hybrid composites, this distance is defined as the surface-to-surface distance d between the broken fibre and the intact fibre, divided by the radius R_{CF} of the carbon fibre (see Figure 5-3).

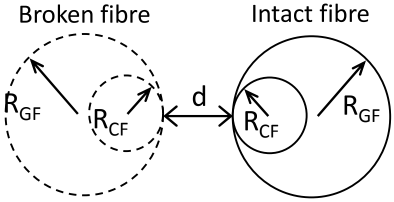

Figure 5-3: Schematic drawing of the relative surface-to-surface distance d/R.

The same modelling parameters as in "4.2.1 Methodology" are used. All models have an overall V_f of 50%. Additionally, the glass fibres are assumed to be linear elastic and isotropic with a Young's modulus of 70 GPa and a Poisson's ratio of 0.22. The glass fibre radius was assumed to be 6 µm, which is significantly larger than the 3.5 µm carbon fibre radius.

Matrix cracks were not included in the models for this section nor in the rest of this chapter. Including them in the model would increase the SCFs and ineffective length (see “4.2.2 Stress redistribution for non-interacting fibre breaks”). The distribution of the SCFs between carbon and glass fibres however, would not be affected.

5.2.2 Hybrid volume fraction

The hybrid volume fraction, which is defined as the volume of glass fibres over the total volume of fibres, is an essential parameter for hybrid composites. Literature commonly states that higher hybrid fibre volume fractions, which is equivalent to low carbon fibre content, result in a higher hybrid effect.

To further understand this effect, carbon fibres will be hybridised with glass fibres in 7 different hybrid volume fractions: 0%, 10%, 25%, 50%, 75%, 90% and 100%. Five FE realisations of the microstructure are generated for each hybrid volume fraction at an overall V_f of 50%. Some examples of these realisations for a broken carbon fibre are depicted in Figure 5-4.

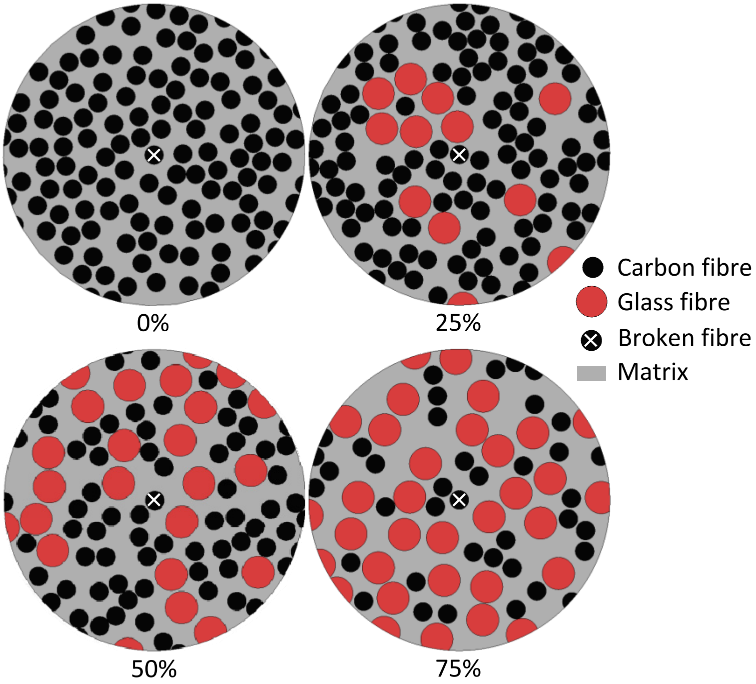

Figure 5-4: Example of one of the five realisations for each hybrid volume fraction with a broken carbon fibre in the middle. The overall V_f is 50%.

For the sake of clarity, the FE results are split up into maximum SCFs around a broken carbon fibre (see Figure 5-5) and a broken glass fibre (see Figure 5-6). In both figures, the results are split up into maximum SCFs on intact glass fibres and on intact carbon fibres. Results are plotted for all five realisations of each of the hybrid volume fractions. Results for 10% and 90% are omitted to improve clarity. The hybrid volume fraction does not have a significant influence on the maximum SCFs. This conclusion is valid for all cases shown here. The intact carbon and glass fibre carry nearly the same SCFs, but this is merely a coincidence for this specific combination of carbon/glass. For carbon/aramid hybrids, this was not the case. The interested reader can refer to Swolfs et al. [406] for more details.

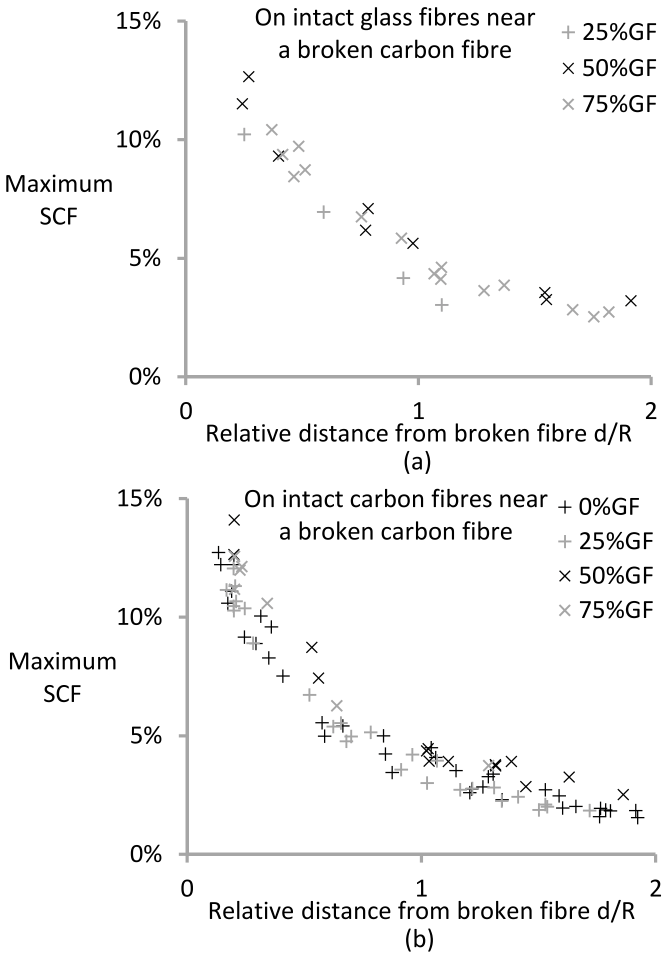

Figure 5-5: Maximum stress concentration factors as a function of the relative distance from the broken carbon fibre: (a) on the intact glass fibres, and (b) on the intact carbon fibres. The results of five FE models are plotted for each hybrid volume fraction at an overall V_f of 50%.

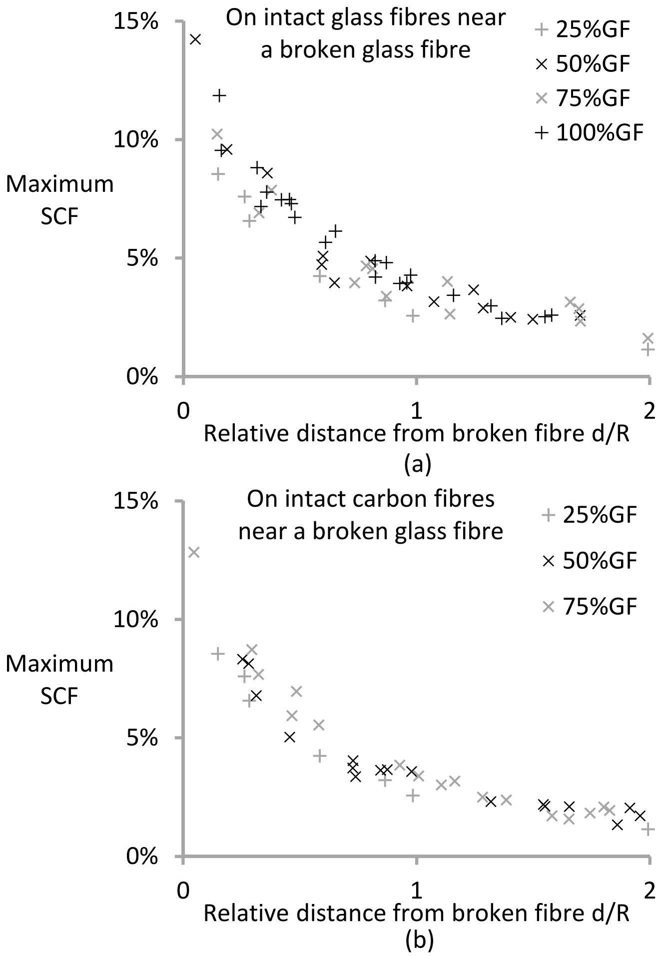

Figure 5-6: Maximum stress concentration factors as a function of the relative distance from the broken glass fibre: (a) on the intact glass fibres and (b) on the intact carbon fibres. The results of five FE models are plotted for each hybrid volume fraction at an overall V_f of 50%.

The hybrid volume fraction also does not have a significant influence on the ineffective length of the broken fibre (see Figure 5-7). Two effects are counteracting each other in this case. The first effect is the higher shear modulus of the glass fibre, resulting in a higher composite shear stiffness for high hybrid volume fractions. This results in faster stress recovery at higher hybrid volume fractions and hence a smaller ineffective length. This trend is not observed, as the second effect appears to counteract this. For high hybrid volume fractions, the broken fibre is mainly surrounded by large glass fibres. These fibres can be packed less efficiently around the broken fibre, as the carbon fibres are not small enough to fit in between the glass fibres (see Figure 5-4). Hence, models with high hybrid volume fractions have less fibrous material in the vicinity of the broken fibre. Since the stress recovery is dominated by the material nearby the broken fibre, high hybrid volume fractions locally have a lower shear stiffness, which results in slower stress recovery and larger ineffective length. Both effects seem to cancel each other out.

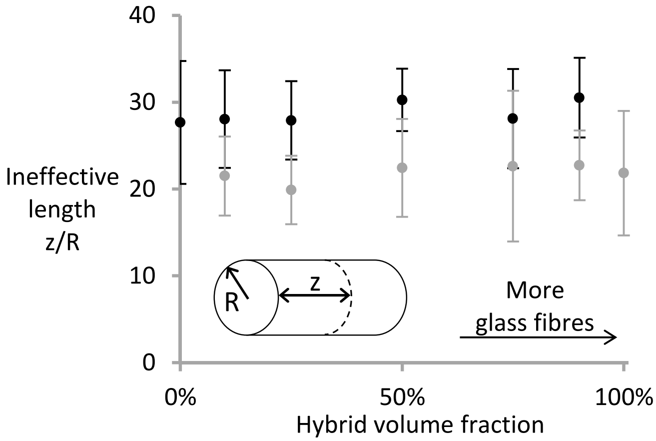

Figure 5-7: The ineffective length of carbon-glass hybrids for different hybrid volume fractions at an overall V_f of 50%. The error bars indicate the 95% confidence interval based on five realisations.

5.2.3 HE fibre stiffness

The influence of the longitudinal fibre stiffness on the stress redistribution was analysed by changing the glass fibre stiffness to 40 GPa and 10 GPa in the FE models. These stiffnesses are not realistic values for glass fibres. Therefore, the terminology high elongation (HE) fibres will be used here. The Poisson's ratio of the HE fibre was kept constant at 0.22, which implies that the shear stiffness reduces together with the longitudinal HE fibre stiffness. The hybrid volume fraction was 50%.

The SCFs on the intact HE fibres are increased strongly (see Figure 5-8a). It should be kept in mind that the SCF is defined as a relative stress increase compared to the nominal stress level. Since the lower HE stiffness reduces this nominal stress level, a small stress increase actually causes a large SCF. In general however, reducing the HE stiffness reduces its load carrying capacity. This causes a slight increase in the SCFs on the intact carbon fibres with decreasing HE fibre stiffness (see Figure 5-8b).

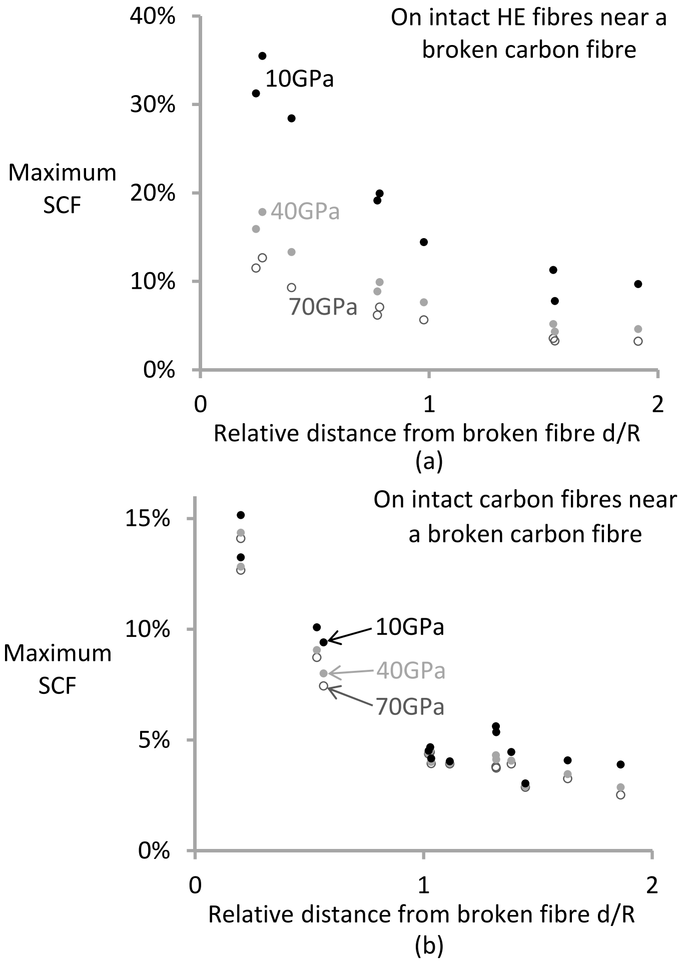

Figure 5-8: The maximum stress concentration factors around a broken carbon fibre for HE fibres with a stiffness of 10, 40 and 70 GPa: (a) for intact HE fibres, and (b) for intact carbon fibres. The results of five FE models are plotted for each HE fibre stiffness. The hybrid and overall volume fraction was 50% in all cases.

The situation around a broken HE fibre (see Figure 5-9) is the opposite from the situation around a broken carbon fibre (see Figure 5-8). The lower HE stiffness causes the relative stiffness of the carbon fibre to be higher. The carbon fibres therefore carry a larger portion of the load released by the broken fibre, which decreases the SCF on the HE fibres (see Figure 5-9a). This however does not result in a larger SCF on the intact carbon fibres (see Figure 5-9b), as the amount of load that is released also decreases with decreased HE stiffness.

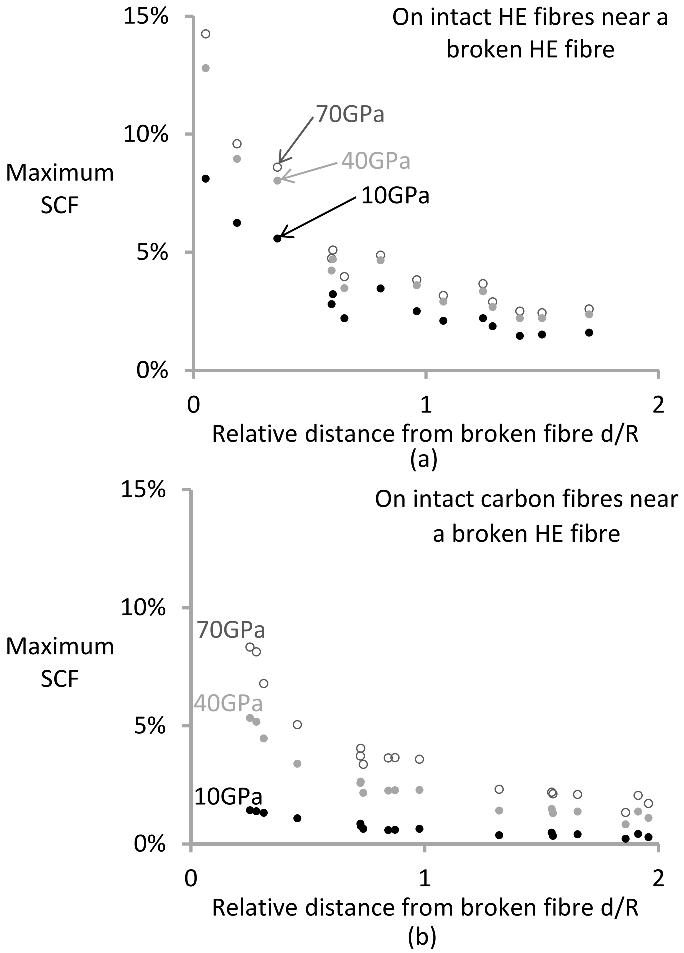

Figure 5-9: The maximum stress concentration factors around a broken HE fibre for HE fibres with a stiffness of 10, 40 and 70 GPa: (a) for intact HE fibres, and (b) for intact carbon fibres. The results of five FE models are plotted for each HE fibre stiffness. The hybrid and overall volume fraction was 50% in all cases.

The ineffective length of a broken carbon fibre seems to slightly increase with decreased HE fibre stiffness (see Figure 5-10). This increase is however not statistically significant. Such a small increase can be expected for theoretical reasons. As shown in “4.2.2 Stress redistribution for non-interacting fibre breaks”, the shear stiffness of the intact fibres contributes to the stress recovery of the broken fibre. By reducing the HE fibre stiffness, its shear stiffness is also reduced. This should lead to a slower stress recovery in the broken fibre and hence a longer ineffective length.

In contrast, the ineffective length of a broken HE fibre strongly reduces with decreasing HE fibre stiffness. A low HE fibre stiffness requires less stress build up to reach the nominal value again. The stress recovery hence occurs faster, resulting in a shorter ineffective length for a low HE fibre stiffness.

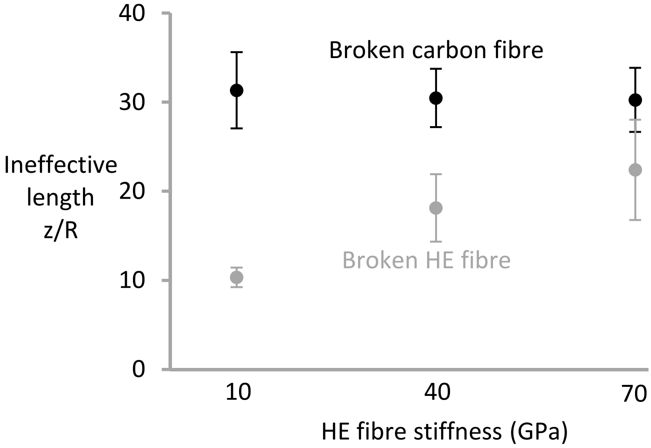

Figure 5-10: The ineffective length for broken carbon and HE fibres as a function of the HE fibre stiffness. The overall V_f was 50%.

5.2.4 Conclusion

Some minor modifications to the FE methodology were necessary to analyse the stress redistributions in hybrid composites. The stress redistribution around a broken carbon fibre was hardly affected by the hybrid volume fraction. These are the first results ever to prove this important aspect of the failure behaviour of hybrid composites.

The HE fibre stiffness did have a significant influence on stress redistribution around broken fibres. Around a broken carbon fibre, the SCFs on the intact fibres increased with decreasing HE fibre stiffness. Around a broken HE fibre however, the SCFs on the intact fibres decreased with decreasing HE fibre stiffness. These trends were explained based on the lower load carrying capacity of the HE fibres, in combination with a lower load released by a broken HE fibre. The ineffective length of a broken carbon fibre did not depend on the HE fibre stiffness. The decreased HE fibre stiffness did result in a smaller ineffective length for a broken HE fibre, as less stress needs to be build up in such a fibre.

These results will be used as input data for the strength model for hybrid composites. This model can then predict whether the hybrid volume fraction and HE fibre stiffness influence the failure development and hybrid effect in hybrid composites.

5.3 Development of a strength model

The model for UD non-hybrid composites has been extensively described and validated in Chapter 4. This model was developed in a versatile manner to facilitate the extension towards hybrid composites. The first subsection will briefly describe this extension, whereas the second subsection describes a slight modification of the strength model. This modification was developed specifically to facilitate the study of dispersion in hybrid composites. The final subsection describes the model parameters.

5.3.1 Extension to hybrid composites

Only two adaptations are required to extend the developed local load sharing model to hybrid composites. The first adaptation is the extension of the fibre packing generator to work with different fibre radii. This has already been described in the section “5.2 Stress redistribution around fibre breaks”.

The second adaptation deals with the way SCFs are distributed after a fibre breaks. The contribution of the matrix will be ignored in this explanation to facilitate the argument. In non-hybrid composites, the SCF that is lost in the broken fibre is redistributed over the nearby fibres. The first step of the procedure uses the SCFs obtained from the FE results. This step however, does not ensure force equilibrium as the FE results are derived from a different realisation of the same fibre packing type. Therefore, the second step of the model calculates the average SCFs for each plane of elements. The SCFs are then slightly adapted to ensure that the average SCF on each plane is 1. This ensures that all planes carry the same force. In hybrid composites however, this redistribution approach has to be adapted to account for the stiffness and cross-sectional area of both fibres. The redistribution for hybrid composites is hence directly based on the force carried by each fibre, instead of indirectly through the SCFs. For non-hybrid composites, these two approaches yield exactly the same results.

The models for hybrid composites described in this chapter do not include matrix cracks. The subsection “4.4.1 Matrix cracks” showed that these matrix cracks reduce the predicted failure strain in non-hybrid composites. A similar reduction is expected for hybrid composites. For hybrid composites however, the parameter of interest is the hybrid effect, which is calculated as a relative failure strain enhancement. The hybrid effect should hence be relatively independent of the presence of matrix cracks.

It should be noted that the strength model tracks both the carbon and glass fibre breaks at every point in the model. Clusters can in principle include both carbon and glass fibres, although the majority of the clusters will only contain carbon fibres.

5.3.2 Very local load sharing model

The dispersion of both fibre types is a vital parameter in hybrid composites. The local load sharing model uses random fibre packings with two different fibre radii. Analysing the influence of dispersion in such a packing is possible, but not very instructive or educational. Simplified dispersion configurations are easier to develop in the framework of a regular packing. To remediate this drawback, a simplified version of the strength model was developed. The modified model uses hexagonal packings with both fibres having the same fibre radius. Very local load sharing was assumed, which means that all the load of the broken fibre is shed onto the nearest neighbours only. This simplified model will be referred to as the very local load sharing model compared to the local load sharing model developed in the previous chapter.

To further simplify the model, linear stress recovery is assumed in the broken fibres (see Figure 5-11), just as in the Kelly-Tyson model [409]. The ineffective length for these profiles was obtained from FE calculations without matrix cracks and an overall V_f of 50%. Matrix cracks were not included, as they were also not included in the local load sharing model (see “5.3.1 Extension to hybrid composites”). The ineffective length yields one point on the stress recovery profile, while the other point on each plot is the origin (see Figure 5-11). The ineffective length in the finite element simulations was found to be 52 µm and 26 µm for carbon and glass fibre, respectively. The subsection “5.2.2 Hybrid volume fraction” proved that hybridisation has little influence on the ineffective length for each fibre type. The above estimates can thus be used with confidence for hybrid composites.

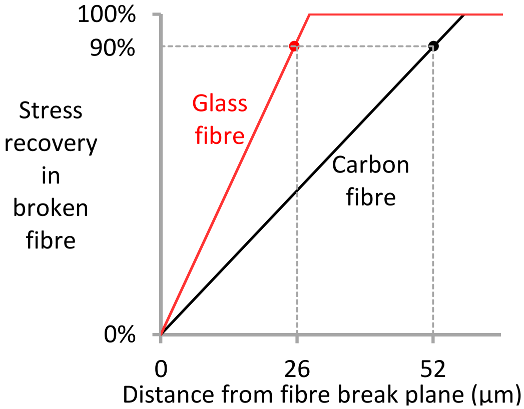

Figure 5-11: Stress recovery in a single broken fibre as a function of the distance from the fibre break plane. The red and black dots indicate the two data points coming from the FE calculations for glass and carbon fibre respectively.

To determine how the SCFs in hybrid composites are distributed on the carbon and glass fibres, the information from FE models for hybrid composites is used. Since the very local load sharing model assumes both fibres to have the same radius, the stress redistribution around such fibres should be analysed using FE analysis. Such analysis was not performed here, but has been published elsewhere [406]. Glass fibres around a single broken carbon fibre carried a higher SCF than the carbon fibres around that broken fibre. This is in contrast with the results in Figure 5-5 and Figure 5-6, where both fibres carried nearly the same SCF. This difference is caused by the fact that Figure 5-5 and Figure 5-6 were calculated using a 3.5 µm and 6 µm radius for carbon and glass fibre respectively. The lower stiffness of the glass fibres is therefore compensated by the fact that its SCF is averaged over a larger cross-section. Such compensation is absent if both fibre types have the same radius. In this case, the ratio of the SCF shed to glass fibres over that shed to carbon fibres was found to be approximately equal to the inverse ratio of their stiffness, 230 GPa/70 GPa [406]. A single broken carbon fibre is assumed to have nearest neighbour carbon fibres with an SCF equal to 7/6. The nearest neighbour glass fibres then carry an SCF equal to 1 + 1/6x230/70 = 1.548. This stress redistribution is illustrated in Figure 5-12a. The second and third nearest neighbours are not influenced by the fibre break.

Similarly, a single broken glass fibre is assumed to have nearest neighbour glass fibres with an SCF equal to 7/6. The nearest neighbour carbon fibres then carry an SCF equal to 1 + 1/6*70/230 = 1.051. Examples of the resulting SCFs for a single fibre break are displayed in Figure 5-12b. The SCFs on these 7 fibres, with the broken one having an SCF = 0, do not add up to 7 as one might expect. This is not required, as the fibre stiffnesses are different. Instead, the total load on the fibres should be kept constant before and after the fibre break. The proposed scheme achieves this force equilibrium.

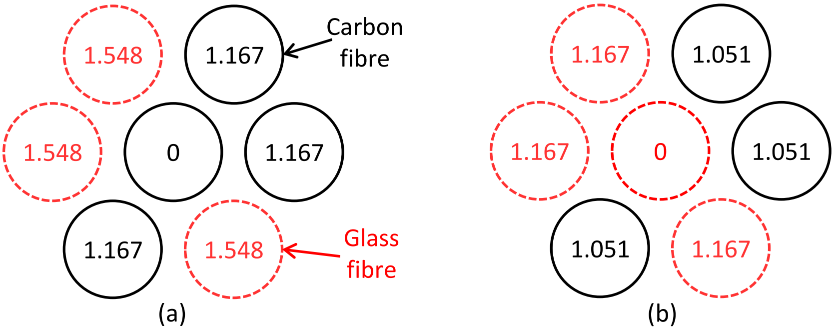

Figure 5-12: Illustration of the stress concentration factors (SCFs) in the fibre break plane according to very local load sharing around (a) a broken carbon fibre, and (b) a broken glass fibre.

Stress concentrations in the matrix are not taken into account in this model, as all the SCFs are assumed to be carried by the fibres. The very local load sharing model uses the same enhanced superposition principle to calculate the stress redistribution around multiple, interacting fibre breaks (see "4.2.3 Stress redistribution for interacting fibre breaks").

5.3.3 Model parameters

The same Weibull data set for carbon and glass fibres are used in both model types. The Weibull data set from Beyerlein et al. [269] is used for AS4 carbon fibre, with $\sigma_0 = 4493MPa$, $L_0 = 10mm$, $m = 4.8$ and $\alpha = 0.6$. For glass fibres, most available data sets are consistent with the standard Weibull equation with $\alpha = 1$. The data set for E-glass is taken from Okabe et al. [293], with $\sigma_0 = 1550MPa$, $L_0 = 24mm$, $m = 6.34$ and $\alpha = 1$. The glass fibre stiffness is assumed to be 70 GPa, corresponding to the value used in the FE models for the stress redistribution around a fibre break.

The fibre types will be assigned through various schemes. Unless otherwise mentioned, the fibre types are assigned at random. Boundary fibres were added in all cases to prevent preferential cluster formation at the edge. For more details on the effect on these boundary fibres, the reader can refer to subsection “4.4.3 Boundary effects and size scaling”.

Similar to models in Chapter 4, all models contain 2000 breakable fibres plus about 250 boundary fibres. Each fibre is divided into 2857 elements with a length of 3.5 µm, corresponding to a total model length of 10 mm.

5.4 Parametric study of the strength model

This section performs a parametric study on the hybrid effect for failure strain. The focus lies on carbon/glass hybrid composites, as this facilitates comparison with literature data. The investigated parameters are: (1) the hybrid volume fraction, (2) fibre dispersion, (3) carbon fibre strength scatter and (4) HE fibre properties. The majority of this section uses the local load sharing model, while the very local load sharing model will be mainly used for analysing the fibre dispersion. A comparison between both will be made for various hybrid volume fractions. Analysing the HE fibre properties will allow an extension of the conclusions towards the hybrid effect in carbon/PP hybrid composites.

The hybrid effect is defined as the relative failure strain increase of the carbon fibres in the hybrid composite compared to the failure strain of an all-carbon fibre composite. These failure strains are defined as the strain at which a critical cluster develops in the carbon fibres. This does not necessarily correspond to the ultimate failure strain of the composite. The current model does not predict what would happen to the glass fibres after carbon fibre failure. Such an extension is possible, but not required to model the hybrid effect. The failure strains predicted by the model are hence not ultimate failure strains of the hybrid composites, but rather the failure strains of the carbon fibres inside the hybrid composite.

5.4.1 Hybrid volume fraction

The hybrid volume fraction is defined as the volume fraction of glass fibres divided by the total fibre volume fraction. It is arguably the most important parameter in the design of hybrid composites. The section "3.1 State of the art" convincingly showed that higher hybrid volume fractions yield larger hybrid effects. Since many models are limited to 50/50 hybrids, relatively little modelling evidence has been published on this parameter. An in-depth understanding of the mechanisms controlling the hybrid effect is therefore lacking. This analysis will be performed using the local load sharing model.

Hybrid volume fractions of 0%, 10%, 25%, 50%, 75%, 90% and 100% are modelled using a random fibre dispersion with a 50% overall V_f (see Figure 5-4). Figure 5-13 depicts their stress-strain diagrams. By adding more glass fibres, the stiffness and strength are reduced, but the failure strain is increased compared to the reference all-carbon fibre composite. This relative increase of the failure strain of the carbon fibre composite is a synergistic effect caused by hybridisation and is called the hybrid effect.

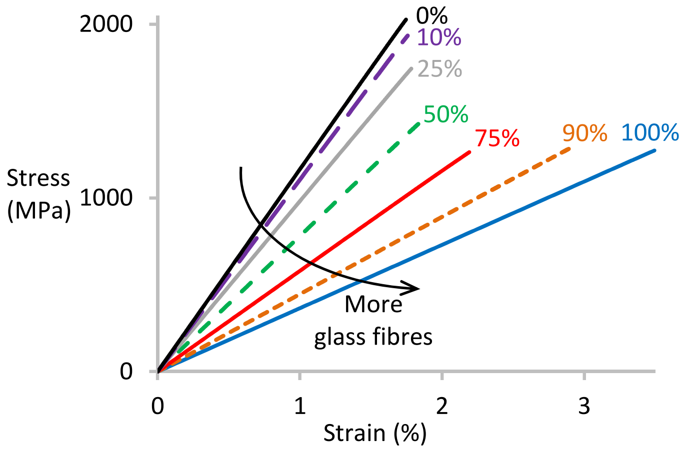

Figure 5-13: Stress-strain diagrams of carbon/glass hybrid composites with various hybrid volume fractions at an overall V_f of 50%.

Figure 5-14 plots the hybrid effect as a function of the hybrid volume fraction to analyse it in more detail. The value for a hybrid volume fraction of 100% is omitted, as this composite does not contain any carbon fibres. The hybrid effect strongly depends on the hybrid volume fraction. For 25%, the hybrid effect is only 2%, but then rapidly increases up to 65% for a hybrid volume fraction of 90%. This large hybrid effect of 65% may raise questions whether this can still be considered a hybrid effect. The failure of this hybrid composite has to be associated with a critical cluster of carbon fibres that propagates unstably within the same strain increment. If this is not the case, then it cannot be considered a hybrid effect. This was indeed confirmed by a thorough analysis of the model. Furthermore, the number of carbon fibre breaks at final failure is about 7 times higher than the number of glass fibre breaks. This confirms that this 65% is indeed a hybrid effect, as the critical cluster is dominated by carbon fibre breaks.

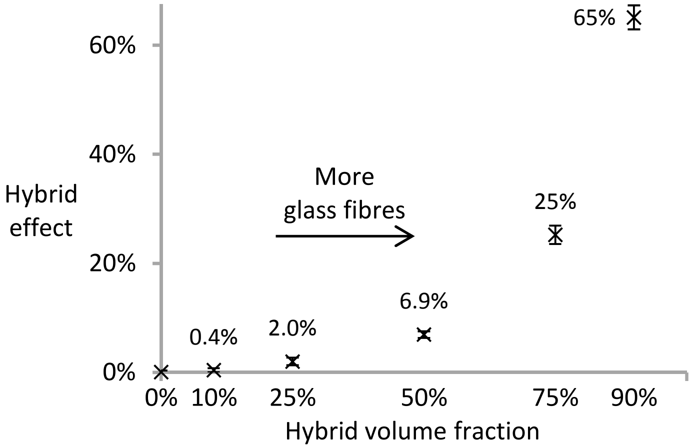

Figure 5-14: The hybrid effect as a function of the hybrid volume fraction at an overall V_f of 50%.

To understand the origin of the hybrid effect, the cluster development is analysed. The development of 3-plets is chosen as a marker for cluster development. These 3-plets can contain both carbon and glass fibre breaks, although the majority will only contain carbon fibre breaks. Figure 5-15 plots the average number of 3-plets as a function of the applied strain for the various hybrid volume fractions. The addition of glass fibres strongly delays the development of break-clusters. This delay is achieved by reducing the number of possible paths for cluster growth.

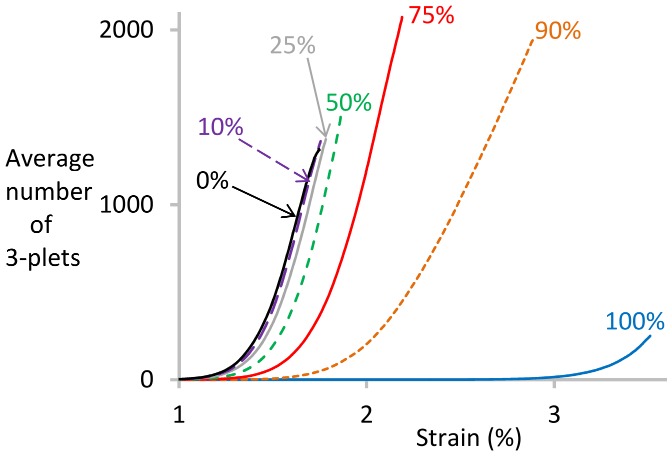

Figure 5-15: Development of average number of 3-plets as a function of the applied strain for various hybrid volume fractions at an overall V_f of 50%. The number of 3-plets is averaged over 50 simulations.

The critical cluster size of the carbon fibres is larger as it has a Weibull modulus of 4.8 compared to 6.34 for the glass fibres (see Figure 5-16). The critical cluster size of the hybrid composites follows the linear rule of mixtures well. This means that the critical cluster decreases by the addition of glass fibres, which will tend to counteract the increase in failure strain by a delay in the cluster development (see Figure 5-15). On the other hand, this decrease is expected as the higher strains facilitate the development of a cluster into a critical cluster.

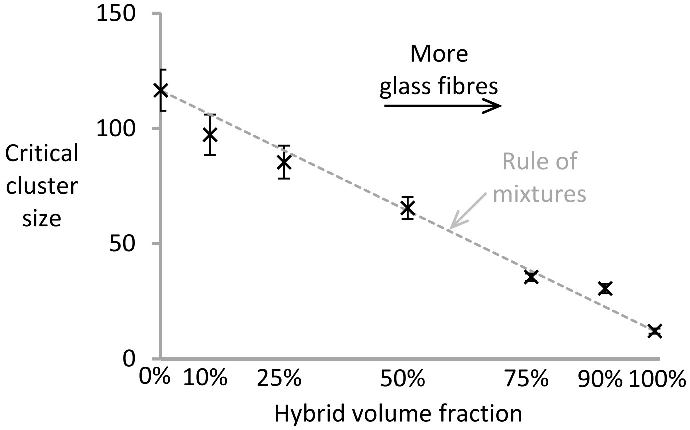

Figure 5-16: The critical cluster size for various hybrid volume fractions at an overall V_f of 50%.

The next subsection will analyse the fibre dispersion using the very local instead of the local load sharing model used in this subsection. Before proceeding however, both models are compared. The predicted failure strains for the all-carbon fibre composite are 1.50% ± 0.03% and 1.75% ± 0.01% for very local and local load sharing respectively. This difference is mainly attributed to the overestimation of the SCFs in the very local load sharing model.

Figure 5-17 plots the effect of the load sharing rule on the hybrid effect. In general, the predictions agree well. The discrepancies at high hybrid volume fraction are attributed to the high SCFs in the very local load sharing model. This will trigger cluster development more rapidly, which makes the addition of glass fibres less efficient in delaying that cluster development.

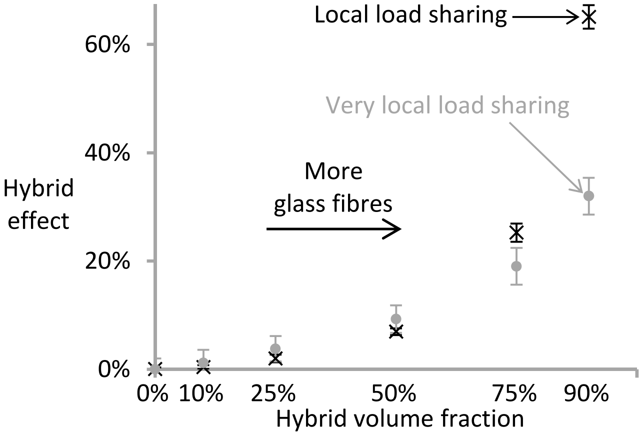

Figure 5-17: Comparison of the hybrid effects predicted by very local and local load sharing at an overall V_f of 50%.

5.4.2 Fibre dispersion

As mentioned in “5.3.2 Very local load sharing model”, the local load sharing model uses random fibre packings with two different fibre radii, which makes varying the degree of dispersion less instructive. Therefore, this subsection uses the very local load sharing model instead. As proven in Figure 5-17, the predictions of both models are similar for hybrid volume fractions of 50% or less. Therefore, this subsection mainly focuses on hybrid volume fractions of 50%.

Fibre dispersion is a measure of how well two fibre types in a hybrid composite are mingled. In this subsection, the influence of the fibre dispersion on the hybrid effect and failure development is analysed. The first dispersion type is bundle-by-bundle (see Figure 5-18). The fibre dispersion is labelled by the number of bundles intersected by a horizontal line in the middle of the circular cross-sections. The number of carbon fibres in each bundle ranges from 500 for the “2 bundles”-model down to about 10 for the “16 bundles”-model. Labelling fibre dispersion according to the number of fibre bundles in each model would have perhaps been more intuitive. Unfortunately, the circular cross-section of the model leads to incomplete -- fibre bundles.

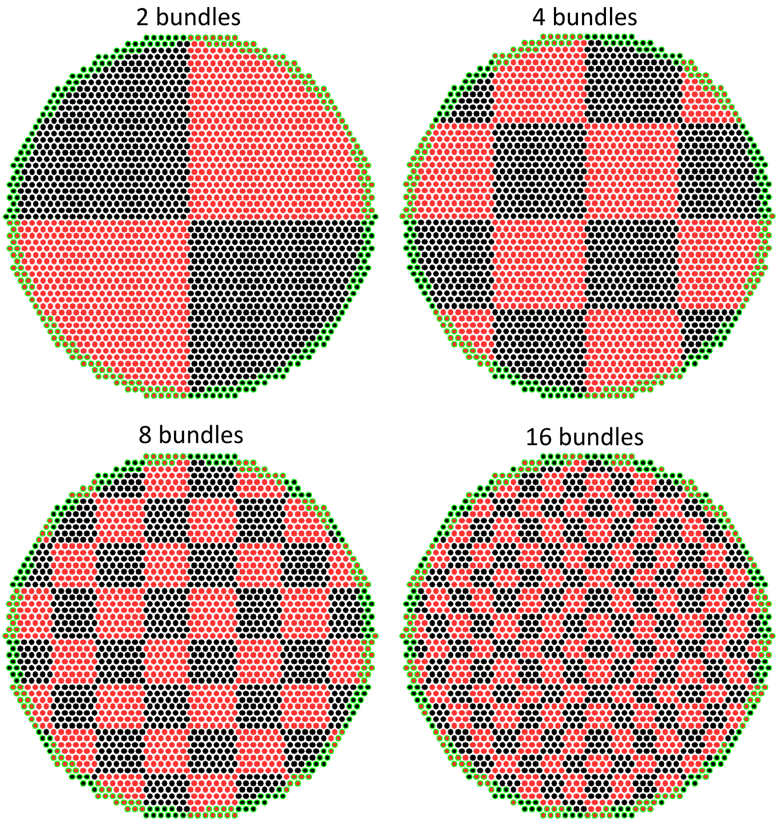

Figure 5-18: Illustration of bundle-by-bundle dispersion, where black circles are carbon fibres and red denotes glass fibres. Boundary fibres have a green outline.

For the 2 bundles model, the hybrid effect is only 1.4%, while it increases to 7% for 16 bundles, as can be seen in Figure 5-19. This effect approaches the 9% hybrid effect observed for random dispersion at 50% hybrid volume fraction.

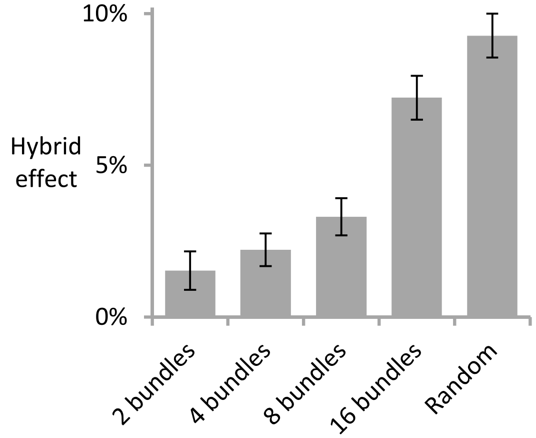

Figure 5-19: The hybrid effect for bundle-by-bundle fibre dispersion at an overall V_f of 50%. The result for random dispersion was added to facilitate comparisons. The error bars represent the 95% confidence intervals.

Figure 5-20 proves that increased dispersion leads to a delay in break-cluster development. Other cluster sizes revealed similar delays in the cluster development, but are not shown here.

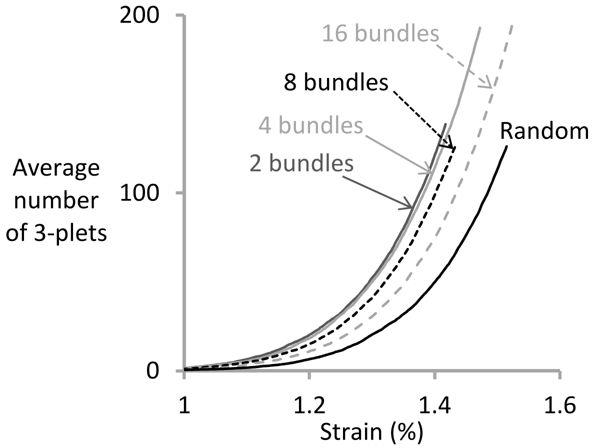

Figure 5-20: The evolution of 3-plets (clusters of three fibre breaks) as a function of strain. The result for random dispersion was added to facilitate comparisons. The overall V_f was 50%.

The second dispersion type is layer-by-layer (see Figure 5-21). This fibre dispersion is labelled according to the number of fibres across the thickness of each layer.

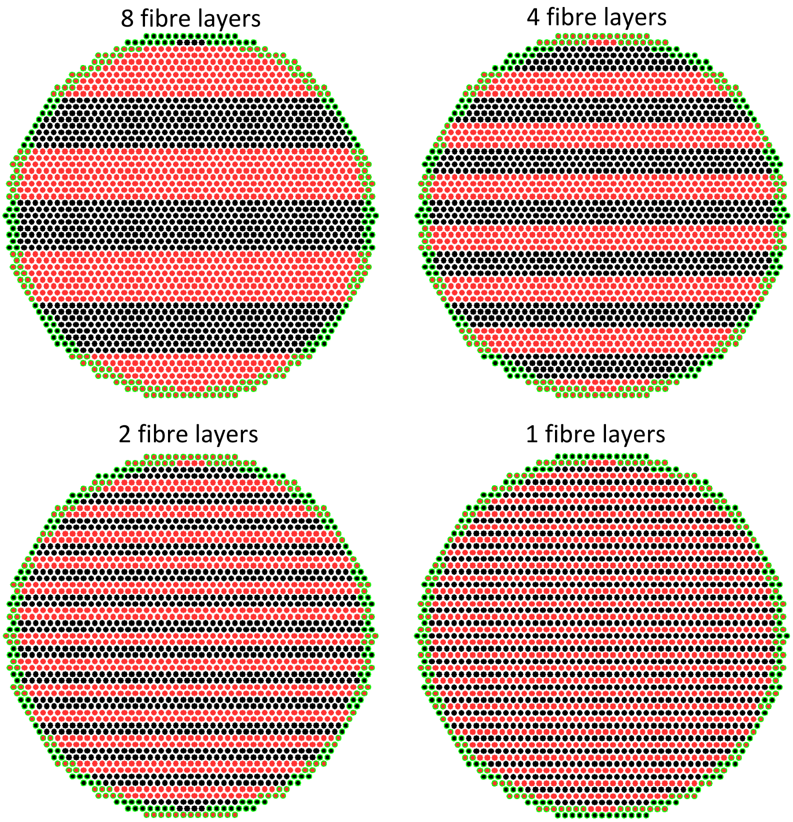

Figure 5-21: Illustration of layer-by-layer dispersion, where black circles are carbon fibres and red denotes glass fibres. Boundary fibres have a green outline.

The corresponding hybrid effects and sequences of triplet evolution are displayed in Figure 5-22. Even though these layer-by-layer hybrids seem less dispersed than randomly dispersed hybrids, they are able to reach a higher hybrid effect. For the 1 fibre layers case, the hybrid effect is 16%, which is significantly higher than the 9% found for random dispersion.

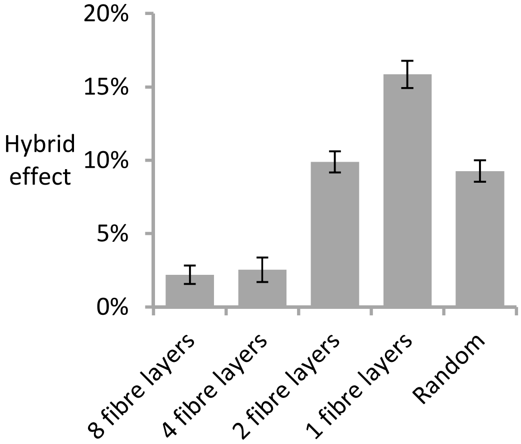

Figure 5-22: The hybrid effect for layer-by-layer fibre dispersion at an overall V_f of 50%. The result for random dispersion is added to facilitate comparisons. The error bars represent the 95% confidence intervals.

This remarkable effect can be explained based on the sequence of break-cluster development. The development of triplets or break-clusters in general is delayed (see Figure 5-23), because forming break-clusters is more difficult in a single layer of carbon fibres. If two neighbouring carbon fibres break, then the nearest neighbours of that 2-plet are two carbon fibres and four glass fibres (see Figure 5-24a). The applied strain, combined with the SCFs, is not yet high enough to break glass fibres. Therefore, the break-cluster can only grow in the direction of the layer. If one of the two neighbouring carbon fibres happens to be relatively strong, then there is only one pathway for the break-cluster to grow. In a random packing, on the other hand, the number of pathways for the break-cluster to grow is larger. For a random dispersion with 50% hybrid volume fraction, the average number of neighbouring carbon fibres is three (see Figure 5-24b). A strong neighbouring fibre is less likely to stop break-cluster development, as there are other pathways for the cluster to grow.

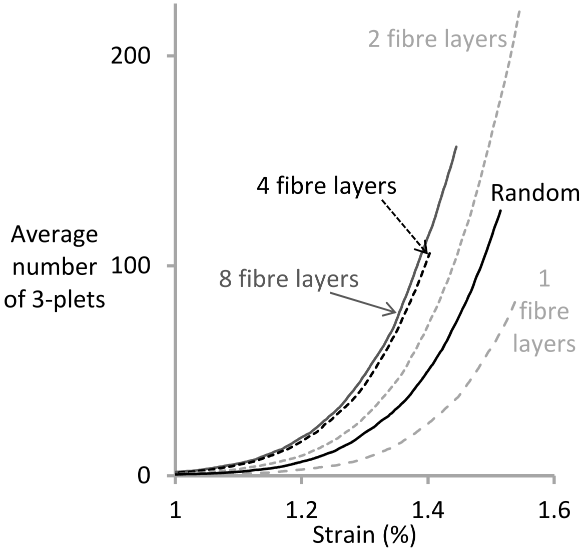

Figure 5-23: The evolution of 3-plets (break-clusters of three fibres) as a function of strain for layer-by-layer dispersion at an overall V_f of 50%. The result for random dispersion is added to facilitate comparisons.

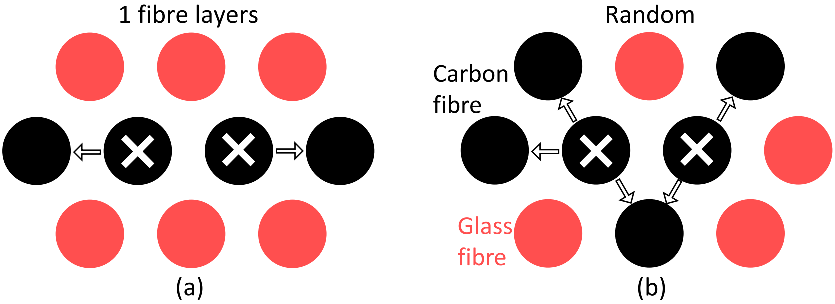

Figure 5-24: Schematic illustration of how the number of possible cluster growth paths is smaller for (a) 1 fibre layers than for (b) random dispersion. The arrows indicate possible growth paths for the 2-plet to develop into a 3-plet.

The critical cluster sizes for the various fibre dispersions are summarised in Figure 5-25. The dispersion does not seem to have a significant effect on the critical cluster size. A small, but statistically significant decrease with increased dispersion can be observed for bundle-by-bundle dispersion. This effect does not seem to be present for layer-by-layer dispersion.

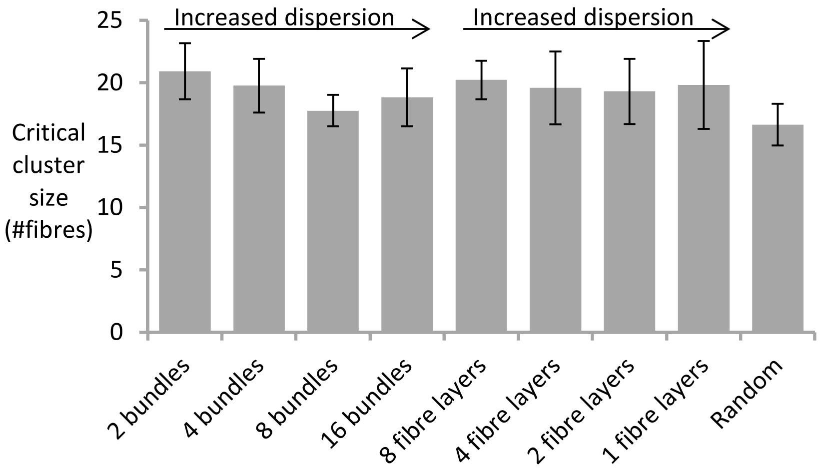

Figure 5-25: The critical cluster size for various fibre dispersions studied for 10 mm long fibres. The error bars represent the 95% confidence intervals.

Interestingly, the decrease of the critical cluster size with increased dispersion was larger for models that were only 1 mm long instead of 10 mm (see Figure 5-26). This decrease makes sense from the viewpoint of failure development. By the time a large cluster develops in well-dispersed hybrids, the stresses are already very high. These high stresses allow a smaller cluster to rapidly develop into a critical cluster. It is currently unclear why this decrease is more obvious for smaller models. Further analysis is required to investigate the importance of model size in hybrid composites.

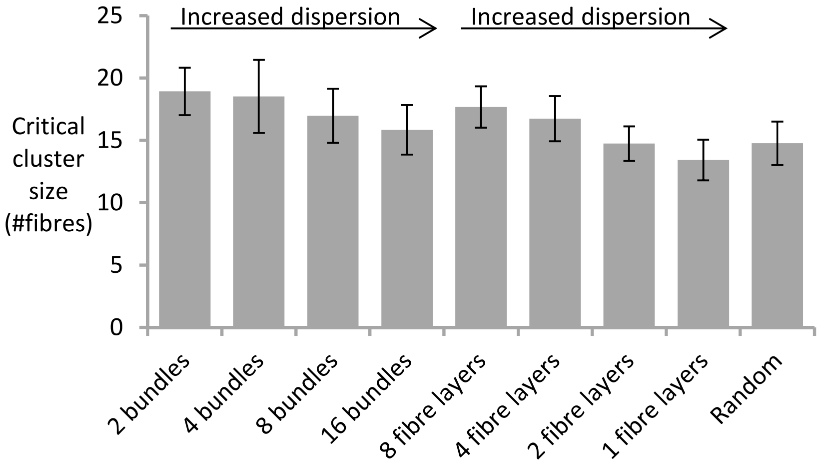

Figure 5-26: The critical cluster size for various fibre dispersions studied for 1 mm long fibres. The error bars represent the 95% confidence intervals.

The decrease in the critical cluster size (see Figure 5-26 as well as Figure 5-16) will tend to decrease the hybrid effect, while the delay in cluster development will tend to increase it. Since the hybrid effect is positive, it is the delay in break-cluster development that is the key parameter determining the hybrid effect.

In general, these results demonstrate that the dispersion is a vital parameter for the hybrid effect. This was the first study to optimise the hybrid effect by improving dispersion in 2D packings. In contrast with what could have been expected from literature, random dispersion was not the optimal dispersion for maximising the hybrid effect. Layer-by-layer hybrids seem to be more efficient in delaying the failure development, which increases the hybrid effect. From a practical point of view, this would mean that hybrid composites made with thin plies have more potential than commingled hybrids.

These conclusions are however limited to hybrids with a 50% hybrid volume fraction. For other hybrid volume fractions, layer-by-layer hybrids are not necessarily the optimal choice. This was analysed by modelling layer-by-layer hybrid composites where the carbon fibre layers are only a single fibre thick. The glass fibre content was changed by increasing the layer thickness from a single fibre to 8 fibres. Increasing this glass fibre layer thickness increases the hybrid effect, but the effect levels off for glass fibre layers thicker than two fibres (see Figure 5-27). This is attributed to the fact that only the nearest neighbours of broken fibres are subjected to SCFs in the very local load sharing model. In a glass fibre layer that is three fibres thick, the middle glass fibre layer is unlikely to be subjected to stress concentrations. That would require glass fibres to break, but their failure probability is low.

The levelling off is not valid anymore for the composite with 8 fibre thick glass layers. In this case, the size scaling starts to have an influence. The fraction of carbon fibre in this hybrid is so low that the probability of having a few weak fibres next to each other is reduced. This further increases the hybrid effect compared to the composite with two fibre thick glass layers.

For a 90% hybrid volume fraction, the random dispersion shows a higher hybrid effect. This makes sense as the pathways for cluster growth are more effectively limited by random dispersion at those high hybrid volume fractions. The optimal configuration is to completely isolate the carbon fibres from each other (see Figure 5-28). This corresponds to the configuration mentioned by Jones and Dibenedetto [207], but is only possible at very high hybrid volume fractions.

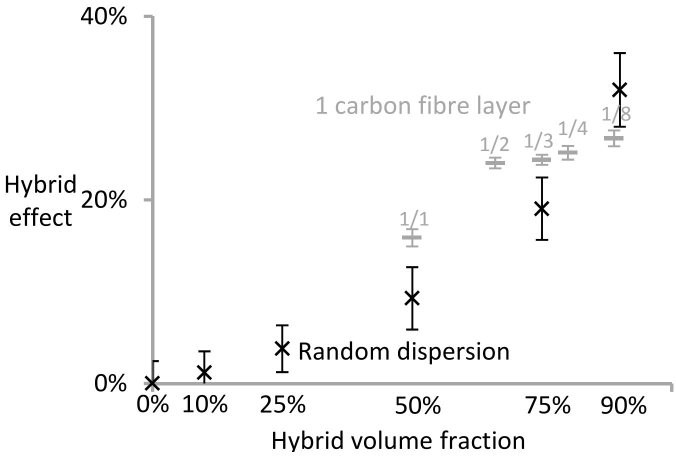

Figure 5-27: The hybrid effect for hybrid composites either with random dispersion or layer-by-layer dispersion at an overall V_f of 50%. The label “1/y” indicates that the carbon fibre layers are 1 fibre thick, while the glass fibre layers are “y” fibres thick.

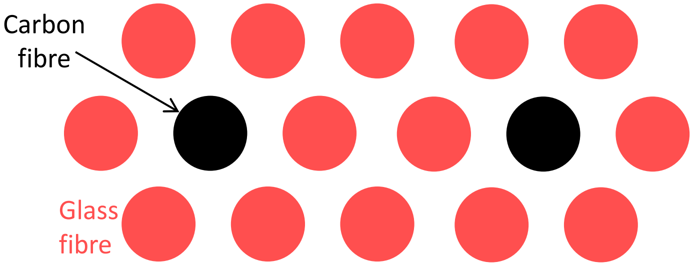

Figure 5-28: Optimal fibre dispersion of carbon/glass hybrid for very high hybrid volume fractions.

5.4.3 Carbon fibre strength scatter

Zweben [133] developed the first model for hybrid composites. Zweben’s seminal work pointed towards the Weibull modulus of carbon fibre as one of the key parameters. Assessing the importance of this parameter is, however, not straightforward. By changing just the Weibull modulus of carbon fibre, the failure strain of the all-carbon fibre composite also changes. To maintain a constant reference for calculating the hybrid effect, this failure strain should remain the same. This can be achieved by simultaneously changing the Weibull scale parameter σ_0 and Weibull modulus. The Weibull moduli are chosen to be 3, 4, 4.8, 6 and 10. The corresponding Weibull scale parameters 4280 MPa, 4411 MPa, 4493 MPa, 4580 MPa and 4710 MPa, respectively, all yield an average failure strain of 1.75% for the all-carbon fibre composite. This subsection uses the local load sharing model again, with an overall V_f of 50%.

The hybrid effects for 50/50 carbon/glass hybrids with varying carbon fibre Weibull moduli are summarised in Figure 5-29. This clearly illustrates the importance of the Weibull modulus of carbon fibre for the hybrid effect. A hybrid effect of 7% is expected for the actual Weibull modulus. By changing this from 4.8 down to 3, the hybrid effect is almost doubled. For a Weibull modulus of 10, which indicates a small strength scatter, the hybrid effect decreases to just 1%.

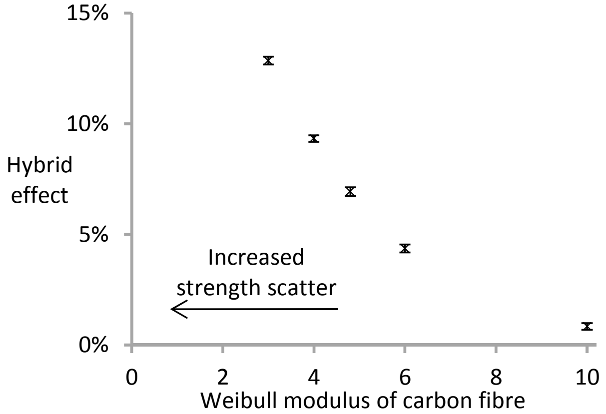

Figure 5-29: The hybrid effect as a function of the Weibull modulus at an overall and hybrid V_f of 50%. The five all-carbon fibre composites all had a failure strain of 1.75%.

Figure 5-30 plots the evolution of 3-plets in the reference composites and the corresponding hybrid composites. The full lines indicate the reference composites, which all have the same failure strain, while the dashed lines indicate the corresponding hybrid composites. All hybrid composites have a delayed cluster development compared to their reference composites. This delay becomes smaller for higher Weibull moduli, as the development of 3-plets occurs over a much smaller strain interval. Fibre-hybridisation is an efficient way to delay cluster development, but the delay is less pronounced for high Weibull moduli.

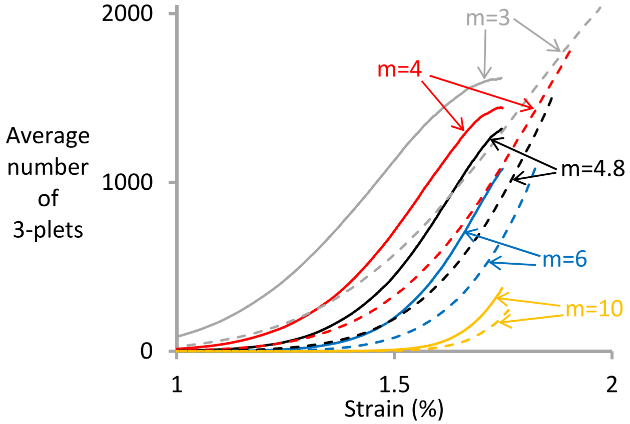

Figure 5-30: The evolution of 3-plets as a function of the applied strain. The overall and hybrid V_f were both 50%. Full lines indicate the reference all-carbon fibre composites, while dashed lines indicate the corresponding 50/50 carbon/glass hybrid composites.

As stated already in 1979 [405], the hybrid effect actually arises from carbon fibre composites failing to exploit the potential strength of carbon fibres. Fibre-hybridisation allows the fibres to get closer to this potential strength. Carbon fibre composites with lower Weibull moduli are further away from exploiting the potential strength of its carbon fibres. Therefore, achieving large hybrid effects should be easier, which is confirmed by Figure 5-29. This also illustrates that large hybrid effects were easier to achieve in the seventies, when carbon fibres still had a relatively low quality [119]. This also indicates that exploiting the hybrid effect is more beneficial in some types of carbon fibre than in others. Firstly, a lower quality carbon fibre such as T300 instead of T700 carbon fibre may have a larger potential for hybrid effects. Secondly, pitch-based carbon fibres are known to have a lower Weibull modulus [286] and hence have more potential for large hybrid effects.

5.4.4 HE fibre properties

The previous subsections highlighted that adding glass fibres to a carbon fibre composite is an efficient way to increase the failure strain of carbon fibres. It is, however, unclear from literature how important the failure strain of the glass fibres is in determining the hybrid effect. This can be analysed in terms of the failure strain ratio, which is the ratio of the failure strains of the glass fibre composite over that of the carbon fibre composite. The importance of the failure strain ratio of both fibre types for the hybrid effect has been debated in literature. Zweben's model indicated a strong dependence [133], while Fukuda later did not find any dependence [394]. While both models were crucial for the initial understanding of hybrid composites, they are based on simple 1D fibre packings. This can introduce significant artefacts and strongly limit the accuracy of both models. Moreover, their predictions of the hybrid effect strongly depend on the definition of failure, which is not clearly defined in their models.

The influence of the failure strain ratio on the hybrid effect can be analysed by changing the Weibull scale parameter σ_0 and leaving all other parameters constant. This approach maintains the fibre stiffness, but increases the failure strain. Such situation is not realistic, as stiffness and failure strain are always linked together. Therefore, the influence of the HE fibre stiffness will also be investigated.

Failure strain ratio

The failure strain of the HE fibre composite is varied by increasing its Weibull scale parameter σ_0 while keeping other parameters constant. The failure strain ratio is defined as the ratio of the failure strain of the HE fibre composite over that of the all-carbon fibre composite. In the previous results, this was 3.51% and 1.75% respectively, leading to a failure strain ratio of two.

Figure 5-31 plots the hybrid effect for 50/50 carbon/HE hybrids with various failure strain ratios. A strong increase is seen up to a failure strain ratio of about 2, after which the hybrid effect levels off. This leads to two vital conclusions. Firstly, to maximise the hybrid effect, the failure strains of both fibre types should be sufficiently far apart. Secondly, adding very ductile fibres to carbon fibre composites does not lead to a higher hybrid effect. This means that the importance of the failure strain ratio was overestimated by Zweben [133], but underestimated by Fukuda [394].

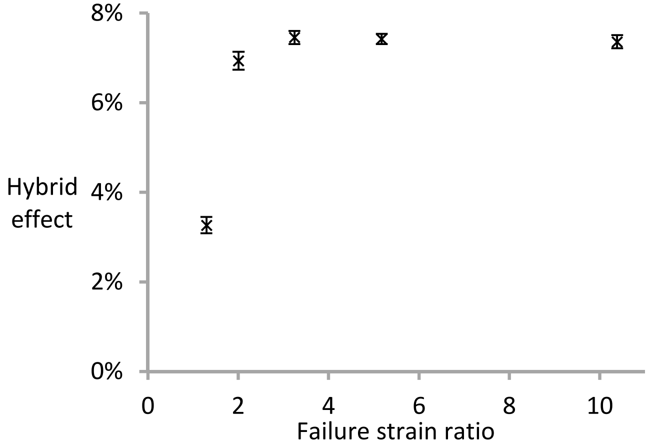

Figure 5-31: The hybrid effect for 50/50 carbon/HE hybrid composites at various failure strain ratios. The overall V_f was 50%.

The question arises why a failure strain ratio above two does not lead to an increased hybrid effect. A first hint can be found in Fukuda's work on 1D packings [394]. Fukuda assumes that a hybrid composite fails when the second nearest neighbour to a broken carbon fibre breaks. This inherently assumes that the nearest neighbour, which is an HE fibre in Fukuda's 1D packing, does not fail. In that case, the failure strain ratio can be expected to have no influence on the hybrid effect. This reasoning can be extended to the current model. The failure probability of the HE fibres is not zero as in Fukuda's model, but is relatively low compared to that of carbon fibre.

To confirm this hypothesis, Figure 5-32 plots the average number of HE fibre breaks in the carbon/HE hybrid as a function of applied strain. The number of HE fibre breaks is indeed small compared to the 20.000-40.000 carbon fibre breaks near final failure. The result for a failure strain ratio of 10 is not plotted because its maximum was lower than 0.1 on average. Higher failure strain ratios delay the onset of HE fibre breaks and strongly reduce the number of HE fibre breaks near final failure. Nevertheless, the model still predicts the hybrid composite to fail at the same failure strain. HE fibre breaks are hence not needed for unstable propagation of a critical cluster. This explains why the hybrid effect levels off for failure strain ratios above two.

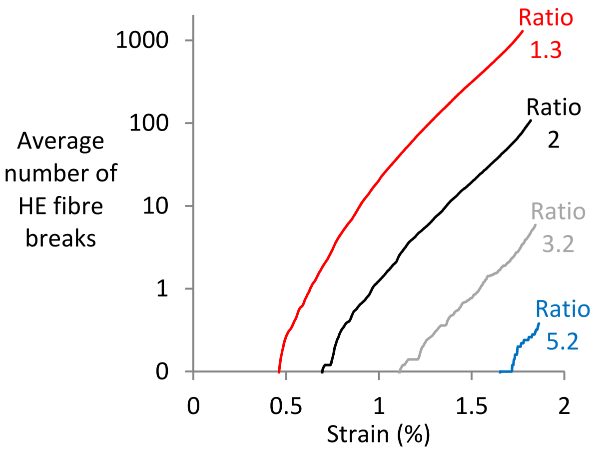

Figure 5-32: Average number of HE fibre breaks for hybrid composites with different failure strain ratios. The overall and hybrid V_f were both 50%.

These conclusions have three limitations. Firstly, the model assumes final failure when the critical cluster develops in the LE carbon fibres. At that point, most HE fibres are still intact. Especially at high failure strain ratios, the HE fibres should be able to continue carrying load. The model is currently not able to predict this residual load carrying capacity. This would only change the ultimate failure strain of the hybrid composite. The hybrid effect itself would not change, however, as its definition is based on the delay of carbon fibre failure. From a practical point of view however, the residual load carrying capacity may be important. It can for example help to achieve pseudo-ductility. This depends on the objective of the hybridisation, which can either be to increase the carbon fibre failure strain or the area underneath the stress-strain diagram.

Secondly, the previous results assume that the failure strain increases 10-fold, while the fibre maintains the same tensile modulus. In practice, however, an increased failure strain is often associated with more compliant fibres. More compliant fibres can be expected to have a lower hybrid effect, as they are less efficient load carriers. Therefore, an optimum combination of failure strain and fibre tensile modulus should exist. This optimum cannot be determined from the current results, but glass fibre is expected to be close as its failure strain ratio is two. The influence of the HE fibre stiffness is investigated in the next part of this subsection.

Finally, the model highlighted a failure strain ratio of two as the threshold value. This threshold is expected to depend on the Weibull modulus of both fibre types, as that determines the overlap in the failure strains of both fibres.

HE fibre stiffness

The influence of the HE fibre stiffness on the stress redistribution around carbon fibre breaks was already investigated in “5.2 Stress redistribution around fibre breaks”. These input data were entered into the strength model, and the hybrid effect for 50/50 hybrid carbon/HE composites was predicted.

All the other parameters were kept constant. By keeping σ_0 constant, a decreasing HE fibre stiffness will increase the failure strain. As shown previously, this failure strain ratio has a negligible influence on the hybrid effect.

A decreased HE fibre stiffness slightly decreases the hybrid effect (see Figure 5-33). This decrease is attributed to the increased stress concentrations on the carbon fibres (see "5.2 Stress redistribution around fibre breaks").

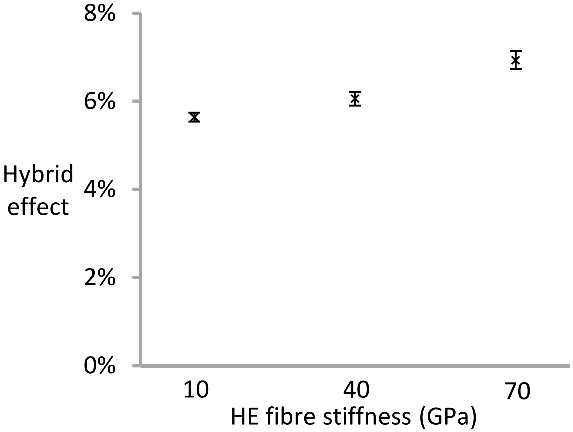

Figure 5-33: The effect of HE fibre stiffness on the hybrid effect in 50/50 carbon/HE hybrid composites. The overall V_f was 50%.

5.4.5 Conclusion

An extensive parametric study of the hybrid effect has been performed. This leads to vital conclusions on how the hybrid effect can be maximised:

- A higher hybrid volume fractions leads to a larger hybrid effect. This is an efficient way to delay break-cluster development.
- An increased fibre dispersion helps to increase the hybrid effect by reducing the number of paths for cluster growth. Very thin carbon fibre layers are the optimal configuration in most cases, apart from at very high hybrid volume fractions. In that case, the optimal configuration is to completely isolate the carbon fibres from each other.
- A carbon fibre type with more strength scatter or smaller Weibull modulus has more potential for large hybrid effects.
- An increased failure strain ratio increases the hybrid effect, but ratios above two do not yield any additional benefit.
- A higher HE fibre stiffness will have a small but positive influence on the hybrid effect.

With respect to hybrid composites of carbon and PP fibres, the following conclusions can be drawn:

- The high failure strain of the PP fibres does not have any additional benefit for the hybrid effect.
- The low stiffness of the PP fibres compared to glass fibres will slightly reduce the hybrid effect compared to carbon/glass hybrids.

The increase in the ultimate failure strain is therefore expected to be the main advantage of PP fibres over glass fibres. This increase has indeed been observed in "Chapter 3: Hybrid self-reinforced composites" and increases the potential to achieve large pseudo-ductile effects.

5.5 Experimental validation

As mentioned in section "3.1 State of the art", many authors have reported hybrid effects in carbon/glass hybrid composites. The main difficulty is to establish an accurate baseline failure strain for the carbon fibre composite. Unidirectional carbon fibre composites often fail due to the stress concentrations near the grips, yielding an underestimation of the baseline failure strain. This causes overestimations of the hybrid effect and should therefore be avoided.

A better approach for measuring the failure strain of carbon fibre composites is to sandwich them in between glass fibre layers. Czél and Wisnom [122] pointed out that the glass fibre layers protect the carbon fibre layers against stress concentrations near the grips. Failure near the grips, which is typically found in tensile testing of UD carbon fibre composites, can be avoided in this manner. This approach inherently assumes that the carbon fibre layers are sufficiently thick to avoid any hybrid effect. This assumption needs to be validated by applying a strength model for hybrid composites.

This section has two objectives. Firstly, a new methodology for accurately measuring the hybrid effect will be proposed. Secondly, the developed strength model for hybrid composites will be validated against experimental results. This will highlight the vital synergy between models and experiments.

5.5.1 Materials

The material input data were kindly provided by Gergely Czél from the University of Bristol. The hybrid composites and their properties have been partially described in Czél and Wisnom [122]. The carbon/glass interlayer hybrid composites were made using UD epoxy prepregs. The carbon fibre prepregs were SkyFlex USN020A from SK Chemicals. These plies contain TR30 carbon fibres from Mitsubishi Rayon with a 234 GPa stiffness. The fibre radius was 3.5 µm. The matrix was a K50 epoxy from SK Chemicals with an unspecified stiffness. The measured areal density was 42.6 ± 1.1

g/m², of which 21.1 ± 0.8 g/m² comes from the fibres. The fibre volume fraction was measured to be 41%.

HexPly® glass fibre prepregs were sourced from Hexcel. These prepregs contain S-glass fibres with a stiffness of 88 GPa. The nominal areal density is 560 g/m², of which 190 g/m² comes from the fibres. The fibre volume fraction was estimated to be 51%, which is higher than for the carbon fibre plies. The fibre radius was 4.5 µm. The matrix was HexPly® 913 epoxy with a 3.4 GPa stiffness.

Two different lay-ups were made: $G_1C_1G_1$ and $G_2C_4G_2$, where G stands for a glass fibre ply and C for a carbon fibre ply. These lay-ups are labelled "1 carbon ply hybrid" and "4 carbon ply hybrid" respectively. Their nominal hybrid volume fractions are 93.9% and 88.5% respectively.

The lay-ups were cured in an autoclave. The cure cycle happened to be the same for both prepregs: 60 min at 125°C and 7 bar pressure. The resins in both prepregs were found to be compatible, meaning that the plies were well bonded and phase separation did not occur. The sample thicknesses were 0.347 ± 0.005 mm and 0.685 ± 0.005 mm for the 1 and 4 carbon ply hybrids, respectively.

The residual strains in hybrid composites were calculated assuming a thermal expansion coefficient of $-0,5.10^{-6}$ K^{-1}, $1,6.10^{-6}$ K^{-1} and 55.10^{-6} K^{-1} for carbon fibre, glass fibre and epoxy, respectively [137,139,410]. The value for the glass fibre may seem lower than the usual 5.10^{-6} K^{-1}, which is the typical value for E-glass. S-glass fibres however, have a lower thermal expansion coefficient [410]. Interestingly, this also means that E-glass fibres yield a slightly larger hybrid effects than S-glass fibres.

The thermal expansion coefficients of the carbon and glass plies were calculated using a rule of mixtures [411]. The classical laminate theory was then used to predict a compressive residual strain of 0.024% and 0.016% on the carbon ply in the 1 and 4 ply carbon hybrid, respectively. These residual strains were not taken into account in the strength model, but do help in the interpretation of the results.

5.5.2 Tensile testing

Samples were cut using a diamond cutting wheel. The samples had a size of 260 x 20 mm and were tested at a gauge length of 160 mm. The crosshead speed was set to 2 mm/min. At least five samples were tested for each configuration. The strain was measured using an Imetrum video gauge system with a 140 mm target distance.

Czél and Wisnom [122] determined two points from the obtained stress-strain diagrams: the yield point and ultimate failure. The ultimate failure is irrelevant for the present purposes, as the hybrid effect deals with the initial carbon fibre failure. The yield point was defined as the point where the curves deviate from linearity. This point is also not relevant, as yielding corresponds to fragmentation or multiple cracks in the carbon fibre layer. The point required for the present analysis is the point at first fracture of the carbon fibre layer. Therefore, Gergely Czél analysed their results in more detail and kindly provided the initial failure strains of the carbon fibre layers in the hybrid composites. In both hybrid composites, this initial failure occurred sufficiently far away from the stress concentrations near the grips. This is hence a reliable measure for the failure strain of the carbon fibre layer.

5.5.3 Model parameters

The very local load sharing model is used, as this facilitates the generation of layered hybrid packings. Figure 5-17 proved that the predictions from this model are similar to the ones from the more refined local load sharing model.

While the V_f was different in the carbon (41%) and glass (51%) layers, such a difference in V_f is difficult to work with in a hexagonal packing. These different fractions would cause changes in the fibre spacing at the interface between dissimilar layers. Therefore, an overall volume fraction of 50% was chosen. Subsection “4.4.5 Fibre volume fraction” already proved that the fibre volume fraction only has a minor influence on the failure development in non-hybrid composites.

The longitudinal fibre stiffnesses in “5.5.1 Materials” were used to calculate the ineffective length. The other engineering constants of the carbon fibre were the same as before. The S-glass fibre is assumed to have a Poisson’s ratio of 0.22, which leads to a shear modulus of 36 GPa. The matrix was assumed to be well-bonded and linear elastic with a stiffness of 3.4 GPa and Poisson’s ratio of 0.4. FE models with a hexagonal packing and 50% fibre volume fraction were used to calculate the ineffective length. The strength model again only uses the longitudinal stiffness of the fibres.

Optical microscopy images were provided by Gergely Czél to allow an optimal choice of the modelling strategy (see Figure 5-34). Accurately measuring the layer thickness in the 1 carbon ply hybrid is difficult as the boundary between the layers is not clearly defined. Therefore, measurements were performed on hybrid composites with the number of carbon fibre plies varying from 1 to 4. This leads to an average layer thickness of 25 μm. In a hexagonal packing with a V_f of 50%, this corresponds to a layer of about three fibres thick. Similarly, the average layer thickness of the glass fibre plies was determined to be 155 μm.

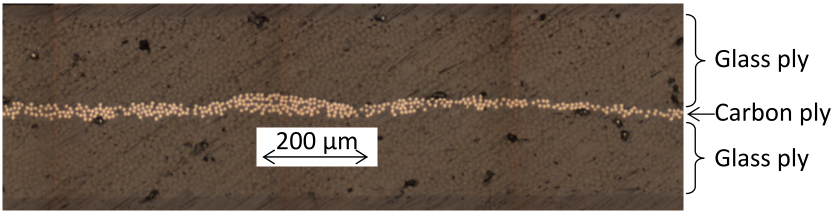

Figure 5-34: Cross-sectional image of the 1 ply carbon hybrid, showing the variation in carbon fibre ply thickness.

The variation in layer thickness leads to an increase in the fibre dispersion. This variation needs to be taken into account, as the subsection “5.4.2 Fibre dispersion” proved that dispersion is a vital parameter for the hybrid effect. Therefore, the layer thickness of the 1 ply carbon hybrid was varied between 1 and 5 fibres thick (see Figure 5-35a). For the 4 ply carbon hybrid, the thickness was randomly varied between 11 and 15 fibres (see Figure 5-35b). A 1 carbon ply with a constant thickness of three fibres was also modelled to gauge the importance of the variation in layer thickness.

The glass fibre layers above and below the carbon layer were at least three fibres thick all along the width of the model. These layers are thicker in reality, but their thickness does not affect the modelling predictions. This hypothesis is based on Figure 5-32, which implies that the glass fibre breaks only have a negligible influence on the development of carbon fibre breaks. The hypothesis will be double-checked by running models with thicker glass fibre layers as well.

The modelled width was 2 mm, while the fibre length was 10 mm. The number of fibres was 2337 for the 1 ply carbon hybrid and 4463 for the 4 ply carbon hybrid.

Boundary fibres were added to the model to make it more representative of larger sample sizes (see subsection “4.4.3 Boundary effects and size scaling”). Their absence could make a small difference at the left and right edges of the model (see Figure 5-35). Adding boundary fibres on the top and bottom, however, would not make a difference as the critical cluster will not develop in the glass fibre layers.

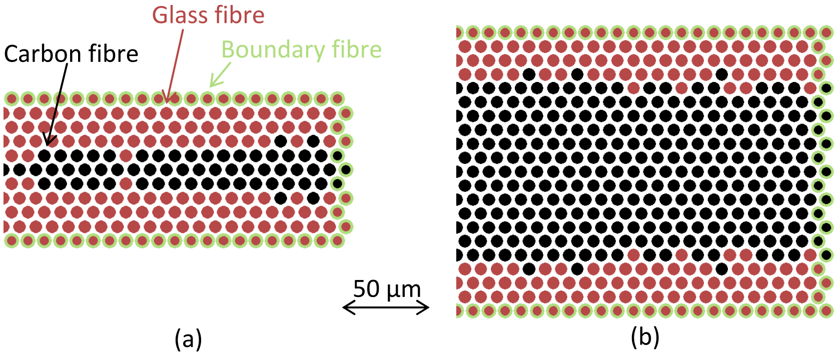

Figure 5-35: Modelling geometry of the carbon/glass hybrid composites: (a) 1 ply carbon hybrid, and (b) 4 ply carbon hybrid. The width corresponds to 200 µm out of the 2 mm in total.

The Weibull distributions for both fibre types are unknown. Therefore, the following strategy was used to set up the parameters of a unimodal Weibull distribution with $\alpha = 1$ (see equation 4-1). The carbon fibre Weibull modulus m was set to 6, which is a reasonable value for this carbon fibre type [286,412]. The gauge length L_0 was set to 10 mm, which corresponds to the actual length of the model. The Weibull scale parameter σ_0 was chosen in such a way that the predicted failure strain of the 4 ply carbon hybrid corresponded to the experimental value of 1.93%. This was achieved by setting σ_0 equal to 3577 MPa.

From experiments, the failure strain of all-glass fibre composites is known to be at least 4%, as they failed near the grips at this strain. The data sheet value of 5.5% is only valid for pristine glass fibres, and is hence an overestimate. Therefore, a similar approach as for the carbon fibres was used. The Weibull modulus was set to 4, as that is a reasonable value for glass fibres [282]. The other Weibull parameters were chosen to yield a reasonable failure strain. Therefore, σ_0 and L_0 were set to 2000 MPa and 50 mm respectively. The exact value of the failure strain of the glass fibres has no significant effect on the hybrid effect, as the failure strain ratio is larger than two (see “5.4.4 HE fibre properties”).

A total of 200 simulations was performed for every configuration. The failure strain of the reference all-carbon and all-glass composites was determined using a model with the same dimensions as the 4 ply carbon hybrid (see Figure 5-35). By using boundary fibres, the exact size of these reference composites will only have minor influence on their predicted failure strain.

5.5.4 Results

Reference composites

The carbon fibre reference composite had a predicted failure strain of 1.94% ± 0.04%. This is significantly higher than 1.5%, which was measured on samples that failed due to stress concentrations at the grips. This clearly proves that these measurements would have been an incorrect baseline for calculating the hybrid effect. It should be noted however that this reference failure strain may be lower if the model size was larger. By using boundary fibres however, this influence should be minimal.

The glass fibre reference composite had a predicted failure strain of 5.25% ± 0.12%. This yields a glass/carbon failure strain ratio of 2.7. As shown in "5.4.4 HE fibre properties", the exact failure strain ratio does not influence the hybrid effect anymore when this ratio is above two.

Hybrid composites

The 4 carbon ply hybrid had an average predicted failure strain of 1.93% ± 0.04%. This value lies in the middle of the experimental range of 1.93% ± 0.11%. This is not surprising as σ_0 was adapted to achieve this failure strain in the model. The predicted range also corresponds well to the failure strain of the carbon fibre reference composite, indicating that the hybrid effect in the 4 carbon ply hybrid can be neglected. This is important, as it proves that a layer thickness of only 100 μm is enough to avoid a hybrid effect. Simultaneously, it also means that the layers must be thinner than 100 μm to realise a hybrid effect. This may be an important implication for other researchers.

Next, the 1 carbon ply hybrids were modelled. With the varying layer thickness model, this yielded a predicted failure strain of 2.13% ± 0.04%. This agrees reasonably well with 2.19% ± 0.06% found in the experiments. If the layer thickness was constant, then the failure strain reduced slightly to 2.10% ± 0.03%. This shows that incorporating some degree of layer thickness variation brings the modelling predictions closer to the experimental results.

Based on the baseline failure strain of the all-carbon fibre composite, the modelled and measured hybrid effects for the 1 carbon ply hybrids can be compared (see Figure 5-36). The results agree reasonably well, even though the differences between model and experiments are statistically significant.

The small discrepancy between experiments and modelling predictions may be explained by residual strains in the plies. The model neglects the residual compressive strain of 0.024% in the carbon fibre ply of the 1 carbon ply hybrid. If this is taken into account, then the failure strain of the 1 carbon ply hybrid increases to 2.15% ± 0.04%. The hybrid effect then increases from 9.4% ± 2.1% to 10.7% ± 2.1%, which comes close to the experimental range of 12.9% ± 2.9%. Nevertheless, the difference is still statistically significant with a p-value of 1.5%.

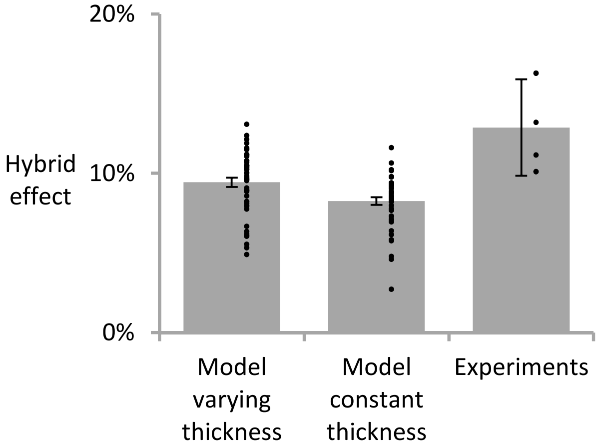

Figure 5-36: Comparison of the hybrid effects for 1 carbon ply hybrids. The error bars represent the 95% confidence interval, whereas the dots represent the individual data points.

Sensitivity analysis

A sensitivity analysis was performed to validate some of the assumptions made in the model. The previously described models used boundary fibres to prevent preferential cluster formation at the edges and make the models more representative of the true size of the specimens. This was important for the reference carbon fibre composite, as the predicted failure strain was 1.84% ± 0.05% and 1.94% ± 0.04% for models without and with boundary fibres respectively. Not using the boundary fibres in the current model size would hence cause an overestimation of the hybrid effect. Using these boundary fibres would not matter anymore if the number of fibres were increased from 4463 to 1 million. This statement cannot be verified with the present model due to computational limitations.

The boundary fibres were also used in the hybrid composites. This is however not necessarily needed. The glass fibre layers actually act as boundary fibres, as their failure strain is much higher than that of the carbon fibres. The only region of the model where boundary fibres could make a difference is on the right and left hand side of the model, where the fibres on the edge are carbon fibres. This edge is however so small that it should not make a difference in the predicted failure strain. This was confirmed by modelling single ply carbon hybrids without boundary fibres. These models had a predicted failure strain of 2.12 ± 0.05%, which is nearly the same as 2.13% ± 0.04% for the same model with boundary fibres.

A final sensitivity analysis was performed by increasing the number of HE fibres in the single carbon ply hybrid. The number of fibres in the thickness direction was the same as in the four carbon ply hybrid (see Figure 5-35b), while the number of carbon fibres was the same as in the single carbon ply hybrid (see Figure 5-35a). This increases the average number of glass fibres in a layer from 4 to 9. This had a predicted failure strain of 2.12% ± 0.04%, which is statistically the same as 2.13% ± 0.04% for the default single carbon ply hybrid.

The main improvements to more accurately determine the hybrid effect would be to accurately measure the Weibull distribution and specifically the Weibull modulus. Unfortunately, this would require an enormous amount of experimental data. Another improvement is to use the local load sharing model and use the real microstructure in Figure 5-34. This would require some additional verification steps, especially with respect to the stress redistribution for fibre breaks near the boundary between carbon and glass layers.

5.5.5 Conclusion

The strength model for hybrid composites was experimentally validated for carbon/glass hybrids. A new approach was proposed that consists of four steps:

- Measure the carbon fibre failure strain in a hybrid composite with a thick carbon fibre layer in the middle.
- Fit a Weibull data set to correctly predict the measured failure strain.
- Apply the same Weibull data set to predict the failure strain of an all-carbon fibre composite.
- Apply the same Weibull data set to a hybrid composite with an arbitrary fibre dispersion and compare model results to experimental measurements.

The issues that typically occur in tensile tests on UD carbon fibre composites were avoided by using interlayer hybrid composites. By combining experimental data with modelling predictions, the hybrid effect could be accurately measured. The modelling predictions agreed excellent with the experimental results, especially when residual strains were taken into account.

This was the first time that such a good agreement between model predictions and experiments was found. The model only fitted σ_0 to achieve the correct failure strain of the 4 ply carbon hybrid. All the other input parameters were either measured or based on reasonable estimates from literature. The actual hybrid effect is calculated by comparing the 1 ply carbon hybrid with the all-carbon fibre composite, both of which required no fitting at all.

5.6 Conclusion

A novel strength model for UD hybrid composites was developed and validated. The analysis provides a deeper understanding of the failure development in hybrid composites. The main reason for the hybrid effect was found to be the delay in the onset of break-cluster development.

An extensive parametric study revealed that the hybrid effect can be maximised by:

- The carbon fibre should have a low Weibull modulus. This can be either a low-quality carbon fibre or a pitch-based carbon fibre. This conclusion is only valid if the reference carbon fibre composites have the same failure strain and strength, which may not be the case in practice.
- The HE fibre should have a high coefficient of thermal expansion, a failure strain ratio of at least two and a high stiffness.
- The fibres should be well dispersed. For most hybrid volume fractions, a configuration with carbon fibre layers that are only a single fibre thick is optimal. For very high hybrid volume fractions however, the carbon fibres should be isolated from each other as much as possible.
- The hybrid volume fraction should be as high as possible, provided the hybrid composites still meet the stiffness and strength requirements for the application.

The model predictions agreed well with experimental data, which proves that the model captures the main phenomena occurring in hybrid composites.

The model focused on the failure strain of the carbon fibres in the hybrid composites. A crucial next step would be to predict what happens to the glass fibres after the carbon fibres have failed. This will be vital in aiding the developments on pseudo-ductile hybrid composites, and in maximising the area underneath the stress-strain diagram. This area represents the energy absorbed in a tensile test, and maximising it may be an alternative reason for hybridisation.

Chapter 6:

Conclusion

The objectives of this thesis are stated again and compared to the presented results. A road map is presented that can be used to tailor hybrid SRCs to various application requirements. The main achievements and how they impact future research are highlighted. Finally, the limitations of this thesis are discussed and ideas for future research are presented.

6.1 General discussion and critical reflection

The overall research objective was to optimise the mechanical performance of hybrid SRCs. More specifically, the tensile stiffness and strength of SRCs should be improved without a large loss in toughness and impact resistance.

Improving the tensile stiffness and strength was successfully achieved, and mainly depended on the fraction of carbon fibre that was added. It was, however, found that the carbon fibre fraction of also affected the ultimate failure strain in tension. For high carbon fibre fractions, the intralayer bonding became too strong, which prevented the debonding of the CFRPP from growing and reduced the ultimate failure strain. In terms of impact resistance, the high carbon fibre fractions did present a significant loss. The main interest in this material is therefore at low carbon fibre fractions, where the increased stiffness and strength do not lead to large losses in ultimate failure strain. In this region, the combination of stiffness, strength and high failure strain is unique.

Another benefit of hybridising SRCs that was not discussed before, is the increase of the yield stress. The yield stress of SRCs is typically around 20 MPa. Hybridisation can easily increase this yield stress by a factor of 5 to 10. This may be a crucial benefit for applications that either require a certain load to be carried or where creep should be avoided.

The addition of carbon fibre to SRCs can impart excellent mechanical properties to SRCs, while keeping the density low. Hybrid SRCs have the additional advantage of having a low cycle time, making them a suitable material for the fast-growing market of automotive composites. The material cost is, however, the main stumbling block for using hybrid SRCs and other carbon fibre composites in automotive industry. Carbon fibre composites are more expensive, but become cost-competitive when the reduced fuel consumption over the lifetime of a car is taken into account [413,414]. Unfortunately, it is often the initial cost that is considered both by the manufacturers and the customers. This mindset is gradually changing as people become more environmentally conscious.

Attentive readers will have noticed that chapter 5 for modelling unidirectional hybrid composites was not directly linked to the experimental work on hybrid SRCs in chapter 3. There are three reasons for this:

- Modelling of hybrid composites is mainly concerned with well-dispersed UD hybrid composites. The current state of the art technologies however do not yet allow such high dispersions, which makes it difficult to directly feed modelling results into the experimental work.
- Producing UD hybrid SRCs is challenging due to the shrinkage of the oriented polymer tapes. This is not an issue for woven architectures, but modelling attempts for multidirectional hybrid composites are unfortunately still rare.

- Predicting what happens after the carbon fibre failure is challenging, and the model is currently not capable of doing this. This will be discussed in more detail in “6.4 Limitations and future developments”

Nevertheless, the modelling conclusions from chapter 5 provide vital information for future developments. In recent years, new processing technologies have been developed that allow previously unseen degrees of dispersion:

- Thin ply technology has gradually reduced the ply thickness and is now able to produce layers that are only three fibres thick [122]. The presented results proved that thin interlayer hybrids are a promising strategy for achieving large hybrid effects. An even better strategy would be to spread out two fibre types simultaneously. This should lead to a better dispersion than for thin ply interlayer hybrids, but requires some process optimisation.
- Well-dispersed tows of discontinuous fibres with an excellent alignment can now be produced with a recently developed technology [204,415]. Once this process has been optimised and scaled up, it has potential to create well-dispersed hybrid yarns.

Chapter 3 on hybrid SRCs did use two models that were directly applicable to the experimental work. This was the delamination growth model and the equation to predict the critical layer thickness. Both models may be combined and extended to fully predict the stress-strain diagrams of hybrid SRCs without any fitting parameters.

The advantage of the modelling work is its applicability to other types of hybrid composites. The modelling evidence in this thesis has clearly proven that there are potential benefits associated with hybrid composites. This should provide a driving force for future improvements in processing technology.

6.2 Road map

A composite that is optimal for all possible applications does not exist. This is especially true for hybrid self-reinforced composites, where one property is often improved at the cost of another. Therefore, the experimental and modelling results were used to set up a road map for optimising hybrid SRCs (see Table 6-1).

Table 6-1: Road map for optimising the mechanical properties of hybrid SRCs.

Property goal	Can be achieved by
High tensile modulus	- Adding a large amount of carbon fibres - Selecting a high modulus carbon fibre - Orienting carbon and polymer fibres in the loading direction - Ensuring a strong intralayer bonding to avoid undulations
High tensile strength	- Dispersing the fibres well - Adding a large amount of carbon fibres - Selecting a high strength carbon fibre - Orienting carbon and polymer fibres in the loading direction, but only if carbon fibre undulations can be avoided
Improved carbon fibre failure strain	- Dispersing the fibres well - Adding a small amount of carbon fibres - Selecting a carbon fibre with a low Weibull modulus
High ultimate failure strain	- Ensuring a weak intralayer bonding - Adding a limited amount of carbon fibres - Using UD CFRPP prepregs instead of woven prepregs - Selecting an SRC with a high failure strain
High flexural modulus	- Adding a large amount of carbon fibres - Selecting a high modulus carbon fibre - Orienting carbon and polymer fibres in the loading direction, but only if carbon fibre undulations can be avoided - Placing high V_f layers on the outside and low V_f layers in the middle - Ensuring a strong intralayer bonding to avoid undulations
High flexural strength	- Adding a large amount of carbon fibres - Ensuring a strong intralayer bonding to avoid undulations - Using a matrix with strong adhesion to carbon fibre
High penetration impact resistance	- Adding a small amount of carbon fibres - Using a matrix with poor adhesion to carbon fibre
Small indentation depth	- Adding a large amount of carbon fibre - Using a matrix with strong adhesion to carbon

The road map contains a number of requirements that may seem to conflict. These requirements are, however, not necessarily conflicting, as each application has different property requirements. For example, the flexural modulus and penetration impact resistance may be important for a hybrid SRC suitcase. This combination can be achieved by placing high V_f layers on the outside and low V_f layers on the inside. The outer layers increase the flexural modulus, while the inner layers ensure a high penetration impact resistance.

6.3 Main achievements and impact

Self-reinforced composites

- The process parameters of hot compaction were optimised and their influence on tensile and impact properties were revealed. This allows other researchers to tailor self-reinforced composites to specific application requirements.
- The possible issues encountered in penetration impact testing of self-reinforced composites were highlighted. Recommendations were made for the types of damage that should be avoided to have reliable penetration impact values when testing ductile fibre composites.
- The transmitted light imaging technique was proposed as a new methodology for investigating the non-penetration impact resistance of translucent composites. This technique provides more information on the damage mechanisms than ultrasonic C-scans. This will lead to a better understanding of these damage mechanisms and prove itself useful for future developments of improved SRCs.
- The weave architecture was found to be an additional parameter that can help to widen the processing window for hot compaction. Flat weaves without folded tapes and with a low crimp can be hot compacted at lower temperatures. This can improve the robustness of hot compaction at both the lab and industrial scale.

Hybrid self-reinforced composites

- The developed hybrid SRC possesses a unique combination of stiffness, strength and toughness. Since this composite is also suitable for high volume applications, it has potential to be used in the automotive industry.
- A patent on “Hybrid self-reinforced composites material” with publication number WO/2013/190149 has been granted. Several follow-up patents have been filed in collaboration with a major industrial organisation in the field of composites. This proves the industrial relevance of this thesis.

- The state of the art section has also been published as a review paper. This paper provides a uniform definition for the hybrid effect and emphasises the importance of an accurate failure strain of the reference carbon fibre composite. This should raise awareness of potential issues that may arise in determining the hybrid effect.
- The damage mechanisms in interlayer hybrid composites were investigated and it was revealed how they can be controlled. This provides guidelines for achieving pseudo-ductility through hybridisation.
- The co-weaving of cloths of PP tapes and CFRPP prepregs has been optimised and scaled up to pilot size. This significantly reduces the time required to put these novel hybrid composites on the market.
- The influence of the CFRPP prepreg type and thickness on the mechanical properties and surface quality of hybrid SRCs were revealed. This provides guidance for selecting the optimal prepreg, depending on the requirements of the targeted application.
- The importance of the inter- and intralayer bonding in hybrid SRCs was highlighted. This is the main parameter for optimising the performance in terms of tensile, flexural and impact performance.
- The most important parameters for optimising hybrid SRPP have been investigated. This led to the development of a road map (see Table 6-1), which can be used to optimise other hybrid SRCs.

Strength model for UD non-hybrid composites

- The developed strength model is a novel and versatile approach for predicting the strength of UD composites. The versatility makes it intrinsically suitable to be extended to a wide variety of problems in UD composites, such as matrix plasticity, time-dependent effects and dynamic stress concentrations.
- The presence of matrix cracks around fibre breaks was found to have a large influence on the stress redistribution and damage development. These cracks are neglected by most state-of-the-art models even though they are known to occur in practice, albeit not always.
- The experimental determination of reliable Weibull distributions for fibre strength was proven to require a large number of tests. Improved methodologies should be developed to more accurately measure this crucial parameter for strength models.
- The fibre packing type was proven to have only a minor influence on the results of strength models with the current assumptions. From now on, other strength models can therefore assume regular packings with confidence.
- The strength model was validated by an in-depth comparison with experiments. The observed discrepancies in break-cluster development provide vital recommendations for future research.

Strength model for UD hybrid composites

- The gap between the state-of-the-art models for UD non-hybrid and hybrid composites has been closed. The failure development of hybrid composites can now be studied in as much detail as was already the case for non-hybrid composites.
- The extensive parametric study highlighted the importance of various parameters influencing the hybrid effect. This sheds new light on how the hybrid effect can be maximised.
- The model predicted that the largest hybrid effect in a 50/50 carbon/glass hybrid can be achieved in a layer-by-layer configuration. This sheds new light on how the hybrid effect can be maximised, especially given the recent developments of ultrathin plies.
- The use of interlayer hybrid composites was shown to be a new methodology for measuring the failure strain of UD carbon fibre composites. This methodology avoids the difficult and time-consuming sample preparation and provides a more reliable measure for the failure strain.
- The experimentally observed hybrid effects agreed well with the modelling predictions. This is the first time that such a good agreement was found, which proves that the model is capable of capturing the main phenomena in hybrid composites.

6.4 Limitations and future developments

Self-reinforced composites

The field of self-reinforced composites is well-established and many of the aspects have already been covered. Most developments in this field focus on developing SRCs with new polymers. Many of these developments are still based on trial-and-error to find the optimal polymer grade and processing parameters. A general framework for the optimisation of self-reinforced composites would speed up these new developments. This framework would use DSC thermograms, molecular weight distributions and draw ratios to predict the optimal process conditions without extensive experimental work. More fundamental research is needed before such an ambitious framework can be set up. The framework would also require a fundamental understanding of the interactions between pressure and temperature for melting of oriented polymers. Such understanding is currently not available in literature.

Transmitted light imaging was developed as a powerful technique to reveal the damage in translucent composites. Its disadvantage compared to ultrasonic C-scans is the lack of quantitative data. An image processing methodology is currently being set up that would allow the definition of a damaged area. Since transmitted light imaging yields more data than ultrasonic C-scans, it may be possible to develop an approach that does not require an arbitrary threshold.

Most of the current commercial applications of SRPP exploit its excellent impact resistance. Nevertheless, the amount of research performed to explore its impact resistance is relatively limited. Many of the studies focus only on penetration impact resistance, while non-penetration impact resistance has received little attention. From a practical point of view however, the non-penetration impact resistance may be more important. More work is needed to clarify which types of damage are introduced into SRPP when it is impacted. Residual properties after such an impact event are also an important aspect but they have received hardly any attention in literature.

Hybrid self-reinforced composites

The inter- and intralayer bonding was a crucial parameter for the mechanical performance of hybrid SRCs. While various strategies for changing this bonding were presented, one strategy was not tested yet. Chapter 2 revealed that an increased compaction temperature creates more matrix in SRCs. Since this is known to improve the inter- and intralayer bonding, the processing temperature should also affect the performance of hybrid SRCs. Some hybrid SRCs therefore may benefit from a lower compaction temperature. This lower temperature could counteract the increased inter- and intralayer bonding due to a high CFRPP fraction, hence avoiding a possible reduction in ultimate failure strain.

Using the ultrathin prepregs with MAPP solved the surface quality issues encountered in the other intralayer hybrids. Insufficient data are available to conclude whether this was due to the reduced thickness difference with the PP tapes or due to the improved adhesion between carbon fibre and PP. The first steps have been taken to source ultrathin prepregs with PP grafted with a lower percentage of maleic anhydride.

While the non-penetration impact resistance of hybrid SRCs was studied, it was not yet studied in great detail. This was due to the lack of suitable testing methodologies to assess the damage in these hybrid composites. Ultrasonic C-scans were found to be unsuitable, presumably because the CFRPP-SRPP interface caused too many reflections. The indentation depth did provide some information, but the interpretation was hampered by the thickness differences of the samples. Other techniques, such as microCT or infrared thermography, should be used in the future.

Strength model for UD non-hybrid composites

Models for unidirectional composites have been studied for more than 60 years now. Most of the occurring phenomena have already been studied on their own. The true challenge lies in developing models that are capable of incorporating all these phenomena in a single model.

In clusters of multiple fibre breaks, the ineffective length should be longer than in a single fibre break [146,148]. The present model however assumes the ineffective length remains constant throughout each simulation. This leads to an overestimation of the composite failure strain. The model currently neglects this, but is intrinsically capable of incorporating this feature.

The damage development was analysed based on the development of break-clusters. The criterion for a break-cluster was based on a maximum lateral and axial distance from the fibre break. These distances were the same for all models to facilitate comparisons between the different results. It would however be better to let both distances depend on the length over which the SCFs are significant. This length can vary significantly depending on the modelling assumptions, as was for example shown for matrix cracks (see subsection "4.2.2 Stress redistribution for non-interacting fibre breaks"). A further refinement would also adapt the criterion to the size of the break-cluster during a simulation, as indicated in the previous paragraph.

While carbon fibres are often assumed to be linearly elastic, they are known to exhibit a significant stiffening effect [253,254]. This is mainly caused by an increased orientation of the crystallites [416]. Since Weibull distributions are measured in terms of strength, the non-linearity will only affect the predicted failure strain but not the strength. Since the carbon fibre stiffness is assumed to increase by 20% for every 1% strain [253,254], this neglect can lead to large overestimations of the failure strain.

The model currently neglects local variations in packings. For low fibre volume fractions, these variations may play an important role (see subsection "4.4.5 Fibre volume fraction"). Before a solution can be implemented in the strength model, further FE studies are required to understand how stresses redistribute near these local variations.

The presented model neglects the dynamic stress concentrations that occur when a fibre breaks and springs back. All other state-of-the-art strength models also ignore this, either because their models are not capable of incorporating it or because the necessary input data are not available. The experimental validation part however highlighted these dynamic effects as one of the main reasons for the observed discrepancies. The presented model is one of the few approaches with the intrinsic capacity to incorporate these effects. The main challenge therefore lies in developing suitable FE models that can predict these dynamic effects.

All presented results assumed a linear elastic matrix that is well bonded to the fibres. While the reported values may be affected by these assumptions, their interpretation is unlikely to change. A major issue is obtaining correct and reliable input data for matrix plasticity and fibre-matrix debonding. Experiments are challenging due to the small scale at which they should ideally be measured.

The model currently predicts stress-strain diagrams that are completely linear. In principle, some limited stiffness reduction should be present due to the gradually developing damage in the material. Regions that contain significantly more fibre breaks than others should be more compliant and cause this stiffness reduction. This deficiency could be resolved by considering the changes in element length, which are currently neglected in the model. This neglect is a reasonable approximation for continuous fibre-reinforced composites, as the stiffness reduction is expected to be small. The model should however be able to predict this stiffness reduction if the aim is to model short fibre composites.

Many models for UD non-hybrid composites are available in literature and all of them use different approaches and assumptions. Currently, it is nearly impossible to compare different models with each other. Another remarkable feature in literature is that most models seem to result in a slight overprediction of the strength by 10-20%. This consistency and accuracy is surprising for many reasons:

- The Weibull distributions found in literature show large differences even though they were measured on the same fibre type (see Figure 4-3).
- The number of tests that are typically used to measure the Weibull distribution was found to be insufficient to expect such accuracies.
- Several features such as matrix plasticity, fibre-matrix debonding and matrix cracking, are known to have an effect on the modelling predictions. Despite the fact that some models include them while others do not, most predictions are similar.
- Most models use the macroscopic behaviour of the matrix, while it is known that the microscopic strength can be up to three times higher than the macroscopic strength [371].
- None of the models include the non-linear elasticity of carbon fibre.
- None of the models include dynamic effects, while the presented experimental validation indicated that this was a vital aspect.

Therefore, we are currently leading a benchmarking exercise to compare various state-of-the-art models. This exercise includes leading experts from all over the world: William Curtin (EPFL, Switzerland), Anthony Bunsell, Alain Thionnet and Sébastien Joannès (Mines ParisTech, France), Tomonaga Okabe (Tohoku University, Japan), Neil McCartney (National Physical Laboratory, UK), Soraia Pimenta (Imperial College London, UK), Hannah Morton and Mark Spearing (University of Southampton, UK) and Ichiro Taketa (Toray Industries, Japan). By including a blind prediction for an imaginary material, the reliability of strength models in general can be assessed. This will be the first time that strength models for UD composites are benchmarked.

Strength model for UD hybrid composites

The limitations and future developments for non-hybrid composites also apply to hybrid composites. There are however some additional features that require more attention.

Dynamic stress concentrations have been indicated to be lower in hybrid composites than in non-hybrid composites [155]. This should in principle contribute to a positive hybrid effect for failure strain, but this has never been modelled before.

The model is currently not capable of predicting what happens after failure of the carbon fibres. In hybrid composites with poor dispersion, the carbon fibre bundles may debond from the glass fibres. The glass fibre bundles can then continue to carry load. Implementing this in the model would require a criterion for debonding of the carbon fibre bundles. Once this is implemented, it would allow a study of the ultimate failure strain of hybrid composites and perhaps also provide new insights for the development of pseudo-ductile hybrid composites. The main limitation is however to achieve a reliable criterion for debonding, which is supported by experimental measurements.

The influence of model size has been extensively studied for non-hybrid composites. The results in this thesis also revealed this as an important parameter. Size scaling of strength of non-hybrid composites intrinsically stems from the distribution of flaws throughout the composite. Since the hybrid effect is a way of making these flaws less critical, the model size may have an influence on the hybrid effect as well.

Chapter 7:

References

This chapter lists all references in order of appearance.

[1] *Growth opportunities in global composites industry*, www.lucintel.com/lucintelbrief/opportunitiesinglobalcompositesmarket-final.pdf, March 2011.
[2] Phillips NL. *Improving racing-car bodies*. Composites. **1969**;1:50-51.
[3] Hsiu-Ying H, Chung-Che Y. *Light weight design for a concept sports car using composite material*. Appl Mech Mater. **2013**;284-287:608-612.
[4] Hibbert L. *Supercarbon McLaren sportscar*. Prof Eng. **2010**;23(7):16-17.
[5] Beckwith SW. *Thermoplastics and carbon fiber technologies for high volume production and automotive*. Sampe J. **2014**;50(3):5-5.
[6] Davey S, Das R, Cantwell WJ, Kalyanasundaram S. *Forming studies of carbon fibre composite sheets in dome forming processes*. Composite Structures. **2013**;97(0):310-316.
[7] Bullis K. *Tesla Roadster*. Technol Rev. **2008**;111(5):102-103.
[8] Rako P. *The Tesla Roadster: sporty and electric*. Edn. **2008**;53(10):30-30.
[9] Ramsbrock J, Vilimek R, Weber J. *Exploring Electric Driving Pleasure – The BMW EV Pilot Projects*. In: Kurosu M, editor. Human-Computer Interaction Applications and Services, vol. 8005: Springer Berlin Heidelberg; **2013**. p. 621-630.
[10] Rodgers S. *I'll Second That E(V)Motion*. Sampe J. **2013**;49(2):28-29.
[11] Kambly KR, Bradley TH. *Estimating the HVAC energy consumption of plug-in electric vehicles*. Journal of Power Sources. **2014**;259:117-124.
[12] Liu Q, Lin Y, Zong Z, Sun G, Li Q. *Lightweight design of carbon twill weave fabric composite body structure for electric vehicle*. Composite Structures. **2013**;97(0):231-238.
[13] *Body work of a BMW i3*, www.motortrend.com, July 2014.
[14] Beckwith SW. *Thermoset Composite Resin Matrices*. Sampe J. **2012**;48(6):42-43.
[15] Paris C, Bernhart G, De Almeida O. *Influence of fast curing cycles on aeronautical prepreg M21/T700: polymerization control and mechanical properties*. Mater Tech. **2012**;100(6-7):611-622.
[16] Zhang KM, Gu YZ, Li M, Zhang ZG. *Effect of rapid curing process on the properties of carbon fiber/epoxy composite fabricated using vacuum assisted resin infusion molding*. Materials & Design. **2014**;54:624-631.
[17] Khan LA, Kausar A, Hussain ST, Iqbal Z, Day RJ, Syed AS, et al. *Cure Characterization of Cycom 977-2A Carbon/Epoxy Composites for Quickstep Processing*. Polymer Engineering and Science. **2014**;54(4):887-898.
[18] Vieille B, Albouy W, Chevalier L, Taleb L. *About the influence of stamping on thermoplastic-based composites for aeronautical applications*. Composites Part B: Engineering. **2013**;45(1):821-834.
[19] Harbers T, Ebel C, Drechsler K, Endres A, Mueller G. *Highly Efficient Production and Characterization of CFRP Made from Recycled Carbon Fibers*. Sampe J. **2014**;50(3):7-13.
[20] Lefebure P, Soccard E, Piana M, Guimard JM. *Thermoplastic Composites Technologies for Manufacturing Nose Fuselage Structures*. Sampe J. **2013**;49(5):32-41.
[21] Verrey J, Wakeman MD, Michaud V, Manson JAE. *Manufacturing cost comparison of thermoplastic and thermoset RTM for an automotive floor pan*. Composites Part A-Applied Science and Manufacturing. **2006**;37(1):9-22.
[22] Uematsu Y, Kitamura T, Ohtani R. *Delamination behavior of a carbon-fibre-reinforced thermoplastic polymer at high temperatures*. Composites Science and Technology. **1995**;53(3):333-341.
[23] Carnevale P, Rasool S, Bersee HEN. *Fibre-matrix interfaces in carbon fibre reinforced PPS composites: damage initiation and propagation in tensile tests*. Composite Interfaces. **2014**;21(4):337-352.
[24] Kobayashi S, Tanaka A. *Resin Impregnation Behavior in Processing of Unidirectional Carbon Fiber Reinforced Thermoplastic Composites*. J Jap Soc Compos Mater. **2012**;38(2):51-57.
[25] Jespersen ST, Wakeman MD, Michaud V, Cramer D, Månson JAE. *Film stacking impregnation model for a novel net shape thermoplastic composite preforming process*. Composites Science and Technology. **2008**;68(7–8):1822-1830.
[26] Bogoeva-Gaceva G, Mader E, Queck H. *Properties of Glass Fiber Polypropylene Composites Produced from Split-Warp-Knit Textile Preforms*. Journal of Thermoplastic Composite Materials. **2000**;13(5):363-377.
[27] De Greef N, Gorbatikh L, Godara A, Mezzo L, Lomov SV, Verpoest I. *The effect of carbon nanotubes on the damage development in carbon fiber/epoxy composites*. Carbon. **2011**;49(14):4650-4664.
[28] Capiati NJ, Porter RS. *The concept of one polymer composites modelled with high density polyethylene*. Journal of Materials Science. **1975**;10(10):1671-1677.

[29] Alcock B, Cabrera NO, Barkoula NM, Loos J, Peijs T. *Interfacial properties of highly oriented coextruded polypropylene tapes for the creation of recyclable all-polypropylene composites*. Journal of Applied Polymer Science. **2007**;104(1):118-129.
[30] *Material properties for PP-based composites*, www.matweb.com, April 2014.
[31] Jones RS, Riley DE *A new self-reinforced polypropylene composite*. Proceedings of the 2nd annual conference of Society of Plastics Engineers, Automotive and Composites Division, Michigan, USA, **2002**.
[32] Ward IM, Hine PJ. *The science and technology of hot compaction*. Polymer. **2004**;45(5):1413-1427.
[33] Ward IM, Hine PJ. *Novel composites by hot compaction of fibers*. Polymer Engineering and Science. **1997**;37(11):1809-1814.
[34] Hine PJ, Ward IM. *Hot compaction of woven nylon 6,6 multifilaments*. Journal of Applied Polymer Science. **2006**;101(2):991-997.
[35] Karger-Kocsis J, Bárány T. *Single-polymer composites (SPCs): Status and future trends*. Composites Science and Technology. **2014**;92(0):77-94.
[36] Alcock B, Peijs T. *Technology and development of self-reinforced polymer composites*. In: Abe A, Kausch HH, Moller M, Pasch H, editors. Polymer composites - polyolefin fractionation - polymeric peptidomimetics - collagens, vol. 251 Berlin: Springer-Verlag; **2013**. p. 1-76.
[37] Fratzl P. *Collagen: structure and mechanics*. New York, USA: Springer Science+Business Media, LLC; **2008**.
[38] Bouville F, Maire E, Meille S, Van de Moortele B, Stevenson AJ, Deville S. *Strong, tough and stiff bioinspired ceramics from brittle constituents*. Nature Materials. **2014**;13(5):508-514.
[39] Ko KK, Kawabata S, Inoue M, Niwa M, Fossey S, Song JW. *Engineering properties of spider silk*. In: Wallenberger FT, Weston NE, Ford R, Wool RP, Chawla K, editors. Advanced Fibers, Plastics, Laminates and Composites, vol. 702**2002**. p. 17-23.
[40] Launey ME, Ritchie RO. *On the Fracture Toughness of Advanced Materials*. Advanced Materials. **2009**;21(20):2103-2110.
[41] Jelf PM, Fleck NA. *Compression failure mechanisms in unidirectional composites*. Journal of Composite Materials. **1992**;26(18):2706-2726.
[42] Dai Z, Shi F, Zhang B, Li M, Zhang Z. *Effect of sizing on carbon fiber surface properties and fibers/epoxy interfacial adhesion*. Applied Surface Science. **2011**;257(15):6980-6985.
[43] Li P, Hu L, McGaughey AJH, Shen S. *Crystalline Polyethylene Nanofibers with the Theoretical Limit of Young's Modulus*. Advanced Materials. **2014**;26(7):1065-1070.
[44] Choy CL, Wong YW, Yang GW, Kanamoto T. *Elastic modulus and thermal conductivity of ultradrawn polyethylene*. Journal of Polymer Science Part B: Polymer Physics. **1999**;37(23):3359-3367.
[45] Hine PJ, Ward IM, Olley RH, Bassett DC. *The hot compaction of high modulus melt-spun polyethylene fibers*. Journal of Materials Science. **1993**;28(2):316-324.
[46] El Maaty MIA, Bassett DC, Olley RH, Hine PJ, Ward IM. *The hot compaction of polypropylene fibres*. Journal of Materials Science. **1996**;31(5):1157-1163.
[47] Hine PJ, Ward IM, Teckoe J. *The hot compaction of woven polypropylene tapes*. Journal of Materials Science. **1998**;33(11):2725-2733.
[48] Hine PJ, Bonner M, Brew B, Ward IM. *Hot compacted polypropylene sheet*. Plastics Rubber and Composites Processing and Applications. **1998**;27(4):167-171.
[49] Teckoe J, Olley RH, Bassett DC, Hine PJ, Ward IM. *The morphology of woven polypropylene tapes compacted at temperatures above and below optimum*. Journal of Materials Science. **1999**;34(9):2065-2073.
[50] Rasburn J, Hine PJ, Ward IM, Olley RH, Bassett DC, Kabeel MA. *The hot compaction of polyethylene terephthalate*. Journal of Materials Science. **1995**;30(3):615-622.
[51] Hine PJ, Ward IM. *Hot compaction of woven poly(ethylene terephthalate) multifilaments*. Journal of Applied Polymer Science. **2004**;91(4):2223-2233.
[52] Schneider C, Kazemahvazi S, Åkermo M, Zenkert D. *Compression and tensile properties of self-reinforced poly(ethylene terephthalate)–Composites*. Polymer Testing. **2012**(0).
[53] Bhattacharyya D, Maitrot P, Fakirov S. *Polyamide 6 single polymer composites*. Express Polymer Letters. **2009**;3(8):525-532.
[54] Matabola KP, de Vries AR, Luyt AS, Kumar R. *Studies on single polymer composites of poly(methyl methacrylate) reinforced with electrospun nanofibers with a focus on their dynamic mechanical properties*. Express Polymer Letters. **2011**;5(7):635-642.
[55] Wright-Charlesworth DD, Lautenschlager EP, Gilbert JL. *Hot compaction of poly(methyl methacrylate) composites based on fiber shrinkage results*. Journal of Materials Science-Materials in Medicine. **2005**;16(10):967-975.

[56] Gilbert JL, Ney DS, Lautenschlager EP. *Self-reinforced composite poly(methyl methacrylate): static and fatigue properties*. Biomaterials. **1995**;16(14):1043-1055.
[57] Dorigato A, Pegoretti A. *Biodegradable single-polymer composites from polyvinyl alcohol*. Colloid and Polymer Science. **2012**;290(4):359-370.
[58] Li RH, Yao DG. *Preparation of single poly(lactic acid) composites*. Journal of Applied Polymer Science. **2008**;107(5):2909-2916.
[59] Olley RH, Bassett DC, Hine PJ, Ward IM. *Morphology of compacted polyethylene fibers*. Journal of Materials Science. **1993**;28(4):1107-1112.
[60] Alcock B, Cabrera NO, Barkoula NM, Peijs T. *Low velocity impact performance of recyclable all-polypropylene composites*. Composites Science and Technology. **2006**;66(11-12):1724-1737.
[61] Alcock B, Cabrera N, Barkoula N, Spoelstra A, Loos J, Peijs T. *The mechanical properties of woven tape all-polypropylene composites*. Composites Part A: Applied Science and Manufacturing. **2007**;38(1):147-161.
[62] Alcock B, Cabrera NO, Barkoula NM, Wang Z, Peijs T. *The effect of temperature and strain rate on the impact performance of recyclable all-polypropylene composites*. Composites Part B: Engineering. **2008**;39(3):537-547.
[63] Mead WT, Porter RS. *The preparation and tensile properties of polyethylene composites*. Journal of Applied Polymer Science. **1978**;22(11):3249-3265.
[64] Zhang JM, Reynolds CT, Peijs T. *All-poly(ethylene terephthalate) composites by film stacking of oriented tapes*. Composites Part A: Applied Science and Manufacturing. **2009**;40(11):1747-1755.
[65] Izer A, Bárány T, Varga J. *Development of woven fabric reinforced all-polypropylene composites with beta nucleated homo- and copolymer matrices*. Composites Science and Technology. **2009**;69(13):2185-2192.
[66] Bárány T, Izer A, Karger-Kocsis J. *Impact resistance of all-polypropylene composites composed of alpha and beta modifications*. Polymer Testing. **2009**;28(2):176-182.
[67] Lacroix F, Lu HQ, Schulte K. *Wet powder impregnation for polyethylene composites: preparation and mechanical properties*. Composites Part A: Applied Science and Manufacturing. **1999**;30(3):369-373.
[68] Peterlin A. *Molecular model of drawing polyethylene and polypropylene*. Journal of Materials Science. **1971**;6(6):490-508.
[69] Ward IM. *Structure and properties of oriented polymers*. Dordrecht, Netherlands: Springe Science+Business Media; **1997**.
[70] Kmetty Á, Bárány T, Karger-Kocsis J. *Self-reinforced polymeric materials: A review*. Progress in Polymer Science. **2010**;35(10):1288-1310.
[71] Yamada K, Kamezawa M, Takayanagi M. *Relationship between orientation of amorphous chains and modulus in highly oriented polypropylene*. Journal of Applied Polymer Science. **1981**;26(1):49-60.
[72] Alcock B, Cabrera NO, Barkoula NM, Peijs T. *The effect of processing conditions on the mechanical properties and thermal stability of highly oriented PP tapes*. European Polymer Journal. **2009**;45(10):2878-2894.
[73] Schimanski T, Peijs T, Lemstra PJ, Loos J. *Influence of postdrawing temperature on mechanical properties of melt-spun isotactic polypropylene*. Macromolecules. **2004**;37(5):1810-1815.
[74] Smith P, Matheson RR, Irvine PA. *Extension ratios of polymer molecules*. Polymer Communications. **1984**;25(10):294-297.
[75] Schimanski T. *High-performance polypropylene structures for eco-friendly, fully recyclable composite*. Technische Universiteit Eindhoven, **2002**.
[76] Pae KD, Chu HC, Lee JK, Kim JH. *Healing of stress-whitening in polyethylene and polypropylene at or below room temperature*. Polymer Engineering and Science. **2000**;40(8):1783-1795.
[77] Schimanski T, Loos J, Peijs T, Alcock B, Lemstra PJ. *On the overdrawing of melt-spun isotactic polypropylene tapes*. Journal of Applied Polymer Science. **2007**;103(5):2920-2931.
[78] El Maaty MIA, Bassett DC, Olley RH, Dobb MG, Tomka JG, Wang IC. *On the formation of defects in drawn polypropylene fibres*. Polymer. **1996**;37(2):213-218.
[79] Flood JE, Nulf SA. *How molecular weight distribution and drawing temperature affect polypropylene physical properties and morphology*. Polymer Engineering and Science. **1990**;30(23):1504-1512.
[80] Abraham TN, Wanjale SD, Bárány T, Karger-Kocsis J. *Tensile mechanical and perforation impact behavior of all-PP composites containing random PP copolymer as matrix and stretched*

PP homopolymer as reinforcement: Effect of β nucleation of the matrix. Composites Part A: Applied Science and Manufacturing. **2009**;40(5):662-668.

[81] Hine P, Olley R, Ward I. *The use of interleaved films for optimising the production and properties of hot compacted, self reinforced polymer composites*. Composites Science and Technology. **2008**;68(6):1413-1421.

[82] Hine PJ, Ward IM, Jordan ND, Olley R, Bassett DC. *The hot compaction behaviour of woven oriented polypropylene fibres and tapes. I. Mechanical properties*. Polymer. **2003**;44(4):1117-1131.

[83] Pinxten W. *De invloed van het visco-elastisch gedrag van vertrekt polypropyleen op het krimpgedrag van polypropyleencomposieten* Master thesis. KU Leuven, KU Leuven, **2005**.

[84] Cabrera N, Alcock B, Loos J, Peijs T. *Processing of all-polypropylene composites for ultimate recyclability*. Proceedings of the Institution of Mechanical Engineers Part L-Journal of Materials-Design and Applications. **2004**;218(L2):145-155.

[85] Jordan ND, Bassett DC, Olley RH, Hine PJ, Ward IM. *The hot compaction behaviour of woven oriented polypropylene fibres and tapes. II. Morphology of cloths before and after compaction*. Polymer. **2003**;44(4):1133-1143.

[86] Foster RJ, Bonner MJ, Ward IM. *The use of nano and micron-sized particles to enhance the interlayer adhesion in self-reinforced, single-polymer composites*. Composites Science and Technology. **2011**;71(4):461-465.

[87] Alcock B, Cabrera NO, Barkoula NM, Peijs T. *Direct Forming of All-Polypropylene Composites Products from Fabrics made of Co-Extruded Tapes*. Applied Composite Materials. **2009**;16(2):117-134.

[88] *Manufacturer's data sheet for PURE®*, www.pure-composites.com, May 2014.

[89] *Manufacturer's data sheet for CURV®*, www.curvonline.com, May 2014.

[90] Hine P, Broome V, Ward I. *The incorporation of carbon nanofibres to enhance the properties of self reinforced, single polymer composites*. Polymer. **2005**;46(24):10936-10944.

[91] Aurrekoetxea J, Sarrionandia M, Mateos M, Aretxabaleta L. *Repeated low energy impact behaviour of self-reinforced polypropylene composites*. Polymer Testing. **2011**;30(2):216-221.

[92] Bastiaansen CWM, Lemstra PJ. *Melting behaviour of gelspun/drawn polyolefins*. Makromolekulare Chemie Macromolecular Symposia. **1989**;28(1):73-84.

[93] Rein DM, Vaykhansky L, Khalfin RL, Cohen Y. *Controlling the properties of single-polymer composites by surface melting of the reinforcing fibers*. Polymers for Advanced Technologies. **2002**;13(10-12):1046-1054.

[94] Barkoula NM, Peijs T, Schimanski T, Loos J. *Processing of single polymer composites using the concept of constrained fibers*. Polymer Composites. **2005**;26(1):114-120.

[95] Loos J, Schimanski T, Hofman J, Peijs T, Lemstra PJ. *Morphological investigations of polypropylene single-fibre reinforced polypropylene model composites*. Polymer. **2001**;42(8):3827-3834.

[96] Yadav YS, Jain PC. *Melting behaviour of oriented isotactic polypropylene*. Thermochimica Acta. **1987**;117:97-103.

[97] Alcock B, Cabrera NO, Barkoula NM, Loos J, Peijs T. *The mechanical properties of unidirectional all-polypropylene composites*. Composites Part A: Applied Science and Manufacturing. **2006**;37(5):716-726.

[98] Fabich B, Taketa I, Gorbatikh L, Lomov SV, Janetzko S, Gries T, et al. *Toughness improvement in hybrid composites made of carbon fibre reinforced polypropylene and self-reinforced polypropylene*. Lancaster: Destech Publications, Inc; **2010**.

[99] Dasdemir M, Maze B, Anantharamaiah N, Pourdeyhimi B. *Formation of novel thermoplastic composites using bicomponent nonwovens as a precursor*. Journal of Materials Science. **2011**;46(10):3269-3281.

[100] Hine PJ, Unwin AP, Ward IM. *The use of an interleaved film for optimising the properties of hot compacted polyethylene single polymer composites*. Polymer. **2011**;52(13):2891-2898.

[101] Amer MS, Ganapathiraju S. *Effects of processing parameters on axial stiffness of self-reinforced polyethylene composites*. Journal of Applied Polymer Science. **2001**;81(5):1136-1141.

[102] Hine PJ, Ward IM, Jordan ND, Olley RH, Bassett DC. *A comparison of the hot-compaction behavior of oriented, high-modulus, polyethylene fibers and tapes*. Journal of Macromolecular Science, Part B: Physics. **2001**;B40(5):959-989.

[103] Houshyar S, Shanks RA, Hodzic A. *Influence of Different Woven Geometry in Poly(propylene) Woven Composites*. Macromolecular Materials and Engineering. **2005**;290(1):45-52.

[104] Amornsakchai T, Bassett DC, Olley RH, Hine PJ, Ward IM. *On morphologies developed during two-dimensional compaction of woven polypropylene tapes*. Journal of Applied Polymer Science. **2000**;78(4):787-793.

[105] Shahin MM, Olley RH, Bassett DC, Maxwell AS, Unwin AP, Ward IM. *Morphological changes in pressure annealed polyethylene*. Journal of Materials Science. **1996**;31(20):5541-5549.

[106] Olley RH, Hosier IL, Bassett DC, Smith NG. *On morphology of consolidated UHMWPE resin in hip cups*. Biomaterials. **1999**;20(21):2037-2046.

[107] Bonner M, Elfering B, Ward IM. *The mechanical properties of high stiffness hot-compacted polypropylene: a new development*. Journal of Materials Science. **2014**;49(4):1606-1611.

[108] Kmetty Á, Bárány T, Karger-Kocsis J. *Injection moulded all-polypropylene composites composed of polypropylene fibre and polypropylene based thermoplastic elastomer*. Composites Science and Technology. **2012**;73(0):72-80.

[109] Bárány T, Karger-Kocsis J, Czigány T. *Development and characterization of self-reinforced poly(propylene) composites: carded mat reinforcement*. Polymers for Advanced Technologies. **2006**;17(9-10):818-824.

[110] Hine PJ, Ward IM, El Matty MIA, Olley RH, Bassett DC. *The hot compaction of 2-dimensional woven melt spun high modulus polyethylene fibres*. Journal of Materials Science. **2000**;35(20):5091-5099.

[111] Deng H, Reynolds CT, Cabrera NO, Barkoula NM, Alcock B, Peijs T. *The water absorption behaviour of all-polypropylene composites and its effect on mechanical properties*. Composites Part B: Engineering. **2010**;41(4):268-275.

[112] Kim KJ, Yu WR, Harrison P. *Optimum consolidation of self-reinforced polypropylene composite and its time-dependent deformation behavior*. Composites Part A: Applied Science and Manufacturing. **2008**;39(10):1597-1605.

[113] Swolfs Y, Van den fonteyne W, Baets J, Verpoest I. *Failure behaviour of self-reinforced polypropylene at and below room temperature*. Composites Part A: Applied Science and Manufacturing. **2014**;65:100-107.

[114] Samuels RJ. *High strength elastic polypropylene*. Journal of Polymer Science Part B: Polymer Physics. **1979**;17(4):535-568.

[115] Kalantar J, Drzal LT. *The bonding mechanism of aramid fibres to epoxy matrices*. Journal of Materials Science. **1990**;25(10):4186-4193.

[116] Hine PJ, Bonner M, Ward IM, Swolfs Y, Verpoest I, Mierzwa A. *Hybrid carbon fibre/nylon 12 single polymer composites*. Composites Part A: Applied Science and Manufacturing. **2014**;65:19-26.

[117] Shindo A. *On the carbonization of polyacrylonitrile fiber*. Carbon. **1964**;1(3):391-392.

[118] Tang MM, Bacon R. *Carbonization of cellulose fibers - 1. Low temperature pyrolysis*. Carbon. **1964**;2(3):211-220.

[119] Fitzer E. *PAN-based carbon fibers - present state and trend of the technology from the viewpoint of possibilities and limits to influence and to control the fiber properties by the process parameters*. Carbon. **1989**;27(5):621-645.

[120] Kretsis G. *A review of the tensile, compressive, flexural and shear properties of hybrid fibre-reinforced plastics*. Composites. **1987**;18(1):13-23.

[121] Wu ZS, Yang CQ, Tobe YH, Ye LP, Harada T. *Electrical and mechanical characterization of hybrid CFRP sheets*. Journal of Composite Materials. **2006**;40(3):227-244.

[122] Czél G, Wisnom MR. *Demonstration of pseudo-ductility in high performance glass/epoxy composites by hybridisation with thin-ply carbon prepreg*. Composites Part A: Applied Science and Manufacturing. **2013**;52:23-30.

[123] Manders PW, Bader MG. *The strength of hybrid glass/carbon fibre composites Part 1 Failure strain enhancement and failure mode*. Journal of Materials Science. **1981**;16(8):2233-2245.

[124] Hayashi T. *On the improvement of mechanical properties of composites by hybrid composition*. Proc 8th Intl Reinforced Plastics Conference. **1972**:149-152.

[125] Marom G, Fischer S, Tuler FR, Wagner HD. *Hybrid effects in composites: conditions for positive or negative effects versus rule-of-mixtures behavior*. Journal of Materials Science. **1978**;13(7):1419-1426.

[126] Summerscales J, Short D. *Carbon fiber and glass fibre hybrid reinforced plastics*. Composites. **1978**;9(3):157-166.

[127] Phillips MG. *Composition parameters for hybrid composite materials*. Composites. **1981**;12(2):113-116.

[128] Phillips MG. *On composition parameters for hybrid composite materials*. Composites. **1982**;13(1):18-20.

[129] Phillips LN. *The hybrid effect - does it exist?* Composites. **1976**;7(1):7-8.

[130] Harris B, Bunsell AR. *Impact properties of glass fibre/carbon fibre hybrid composites*. Composites. **1975**;6(5):197-201.

[131] Qiu YP, Schwartz P. *Micromechanical behavior of Kevlar-149/S-glass hybrid 7-fiber microcomposites: II. Stochastic modeling of stress-rupture of hybrid composites*. Composites Science and Technology. **1993**;47(3):303-315.

[132] Aveston J, Sillwood JM. *Synergistic fiber strengthening in hybrid composites*. Journal of Materials Science. **1976**;11(10):1877-1883.

[133] Zweben C. *Tensile strength of hybrid composites*. Journal of Materials Science. **1977**;12(7):1325-1337.

[134] Fukuda H, Chou TW. *Stress concentrations in a hybrid composite sheet*. Journal of Applied Mechanics - Transactions of the ASME. **1983**;50(4A):845-848.

[135] Harlow DG. *Statistical properties of hybrid composites. I. Recursion analysis*. Proceedings of the Royal Society of London Series A: Mathematical Physical and Engineering Sciences. **1983**;389(1796):67-100.

[136] Zeng QD, Fan FQ, Zhang YY. *A random critical-core theory of microdamage in interply hybrid composites 1. First failure strain and hybrid effect*. Composites Science and Technology. **1993**;49(4):341-348.

[137] Kulkarni R, Ochoa O. *Transverse and longitudinal CTE measurements of carbon fibers and their impact on interfacial residual stresses in composites*. Journal of Composite Materials. **2006**;40(8):733-754.

[138] Dong CS. *Development of a Model for Predicting the Transverse Coefficients of Thermal Expansion of Unidirectional Carbon Fibre Reinforced Composites*. Applied Composite Materials. **2008**;15(3):171-182.

[139] Motoc DL, Ivens J, Dadirlat N. *Coefficient of thermal expansion evolution for cryogenic preconditioned hybrid carbon fiber/glass fiber-reinforced polymeric composite materials*. Journal of Thermal Analysis and Calorimetry. **2013**;112(3):1245-1251.

[140] Bunsell AR, Harris B. *Hybrid carbon and glass fibre composites*. Composites. **1974**;5(4):157-164.

[141] Manders PW, Bader MG. *The strength of hybrid glass/carbon fibre composites Part 2 A statistical model*. Journal of Materials Science. **1981**;16(8):2246-2256.

[142] Rosen BW. *Tensile failure of fibrous composites*. AIAA Journal. **1964**;2(11):1985-1991.

[143] Hedgepeth JM, Van Dyke P. *Local stress concentrations in imperfect filamentary composite materials*. Journal of Composite Materials. **1967**;1(3):294-309.

[144] Landis CM, McMeeking RM. *Stress concentrations in composites with interface sliding, matrix stiffness and uneven fiber spacing using shear lag theory*. International Journal of Solids and Structures. **1999**;36(28):4333-4361.

[145] Nedele MR, Wisnom MR. *Stress-Concentration Factors around a Broken Fiber in a Unidirectional Carbon-Fiber-Reinforced Epoxy*. Composites. **1994**;25(7):549-557.

[146] Behzadi S, Curtis PT, Jones FR. *Improving the prediction of tensile failure in unidirectional fibre composites by introducing matrix shear yielding*. Composites Science and Technology. **2009**;69(14):2421-2427.

[147] Scott AE, Mavrogordato M, Wright P, Sinclair I, Spearing SM. *In situ fibre fracture measurement in carbon-epoxy laminates using high resolution computed tomography*. Composites Science and Technology. **2011**;71:1471-1477.

[148] Pimenta S, Pinho ST. *Hierarchical scaling law for the strength of composite fibre bundles*. Journal of the Mechanics and Physics of Solids. **2013**;61(6):1337-1356.

[149] Phillips LN *On the usefulness of glass-fibre-carbon hybrids*. British Plastics Federation Congress, Brighton, United Kingdom, **1976**.

[150] Curtin WA. *Dimensionality and size effects on the strength of fiber-reinforced composites*. Composites Science and Technology. **2000**;60(4):543-551.

[151] Wisnom MR, Khan B, Hallett SR. *Size effects in unnotched tensile strength of unidirectional and quasi-isotropic carbon/epoxy composites*. Composite Structures. **2008**;84(1):21-28.

[152] Hedgepeth JM. *Stress concentrations in filamentary structures*. NASA TN. **1961**;D-882( ):1-36.

[153] Ji X, Liu XR, Chou TW. *Dynamic stress concentration factors in unidirectional composites*. Journal of Composite Materials. **1985**;19(3):269-275.

[154] Xia Y, Ruiz C. *Analysis of damage in stress wave loaded unidirectional composites*. Computers & Structures. **1991**;38(3):251-258.
[155] Xing J, Hsiao GC, Chou TW. *A dynamic explanation of the hybrid effect*. Journal of Composite Materials. **1981**;15(SEP):443-461.
[156] Zhang Y, Li Y, Ma H, Yu T. *Tensile and interfacial properties of unidirectional flax/glass fiber reinforced hybrid composites*. Composites Science and Technology. **2013**;88(0):172-177.
[157] Ren PG, Zhang ZP, Xie L, Ren F, Jin YL, Di YY, et al. *Hybrid Effect on Mechanical Properties of M40-T300 Carbon Fiber Reinforced Bisphenol A Dicyanate Ester Composites*. Polymer Composites. **2010**;31(12):2129-2137.
[158] Taketa I. *Analysis of failure mechanisms and hybrid effects in carbon fibre reinforced thermoplastic composites* PhD. thesis. KU Leuven, Department of Materials Engineering, **2011**.
[159] Perry JL, Adams DF. *Charpy impact experiments on graphite/epoxy hybrid composites*. Composites. **1975**;6(4):166-172.
[160] Peijs A, Catsman P, Govaert LE, Lemstra PJ. *Hybrid composites based on polyethylene and carbon fibres Part 2: Influence of composition and adhesion level of polyethylene fibers on mechanical properties*. Composites. **1990**;21(6):513-521.
[161] Taketa I, Ustarroz J, Gorbatikh L, Lomov SV, Verpoest I. *Interply hybrid composites with carbon fiber reinforced polypropylene and self-reinforced polypropylene*. Composites Part A: Applied Science and Manufacturing. **2010**;41(8):927-932.
[162] Diao H, Bismarck A, Robinson P, Wisnom MR *Pseudo-ductile behaviour of unidirectional fibre reinforced polyamide 12 composite by intra-tow hybridization*. Proceedings of the 15th European Conference on Composite Materials, Venice, **2012**.
[163] You YJ, Park YH, Kim HY, Park JS. *Hybrid effect on tensile properties of FRP rods with various material compositions*. Composite Structures. **2007**;80(1):117-122.
[164] Pandya KS, Veerraju C, Naik NK. *Hybrid composites made of carbon and glass woven fabrics under quasi-static loading*. Materials & Design. **2011**;32(7):4094-4099.
[165] Zhang J, Chaisombat K, He S, Wang CH. *Hybrid composite laminates reinforced with glass/carbon woven fabrics for lightweight load bearing structures*. Materials & Design. **2012**;36:75-80.
[166] Chamis CC, Lark RF, Sinclair JH. *Mechanical property characterisation of intraply hybrid composites*. In: Chamis CC, editor. Test methods and design allowables for fibrous composites, vol. STP 734: ASTM; **1981**. p. 261-280.
[167] Chou TW, Kelly A. *Mechanical properties of composites*. Annual Review of Materials Science. **1980**;10:229-259.
[168] Aveston J, Kelly A. *Tensile first cracking strain and strength of hybrid composites and laminates*. Philosophical Transactions of the Royal Society of London Series a-Mathematical Physical and Engineering Sciences. **1980**;294(1411):519-534.
[169] Shan Y, Liao K. *Environmental fatigue behavior and life prediction of unidirectional glass–carbon/epoxy hybrid composites*. International Journal of Fatigue. **2002**;24(8):847-859.
[170] Wonderly C, Grenestedt J, Fernlund G, Cĕpus E. *Comparison of mechanical properties of glass fiber/vinyl ester and carbon fiber/vinyl ester composites*. Composites Part B: Engineering. **2005**;36(5):417-426.
[171] Tanaka F, Okabe T, Okuda H, Kinloch IA, Young RJ. *The effect of nanostructure upon the compressive strength of carbon fibres*. Journal of Materials Science. **2013**;48(5):2104-2110.
[172] Choi SR. *Free-Roller Versus Fixed-Roller Fixtures in Flexure Testing of Advanced Ceramic Materials*. Proceedings of the 20th Annual Conference on Composites, Advanced Ceramics, Materials, and Structures—A: Ceramic Engineering and Science Proceedings: John Wiley & Sons, Inc.; **2008**. p. 69-77.
[173] Davidson BD, Sun X. *Effects of Friction, Geometry, and Fixture Compliance on the Perceived Toughness from Three-and Four-Point Bend End-Notched Flexure Tests*. Journal of Reinforced Plastics and Composites. **2005**;24(15):1611-1628.
[174] Wisnom MR, Atkinson JW, Jones MI. *Reduction in compressive strain to failure with increasing specimen size in pin-ended buckling tests*. Composites Science and Technology. **1997**;57(9–10):1303-1308.
[175] Wisnom MR. *The effect of specimen size on the bending strength of unidirectional carbon fibre-epoxy*. Composite Structures. **1991**;18(1):47-63.
[176] Dong CS, Duong J, Davies IJ. *Flexural properties of S-2 glass and TR30S carbon fiber-reinforced epoxy hybrid composites*. Polymer Composites. **2012**;33(5):773-781.
[177] Giancaspro JW, Papakonstantinou CG, Balaguru PN. *Flexural Response of Inorganic Hybrid Composites With E-Glass and Carbon Fibers*. Journal of Engineering Materials and Technology. **2010**;132(2):1-8.

[178] Davies IJ, Hamada H. *Flexural properties of a hybrid polymer matrix composite containing carbon and silicon carbide fibres*. Advanced Composite Materials. **2001**;10(1):77-96.
[179] Dong C, Davies IJ. *Optimal design for the flexural behaviour of glass and carbon fibre reinforced polymer hybrid composites*. Materials & Design. **2012**;37:450-457.
[180] Petrucci R, Santulli C, Puglia D, Sarasini F, Torre L, Kenny JM. *Mechanical Characterisation of Hybrid Composite Laminates Based On Basalt Fibres in Combination with Flax, Hemp and Glass Fibres Manufactured By Vacuum Infusion*. Materials & Design. **2013**.
[181] Boopalan M, Niranjanaa M, Umapathy MJ. *Study on the mechanical properties and thermal properties of jute and banana fiber reinforced epoxy hybrid composites*. Composites Part B: Engineering. **2013**;51(0):54-57.
[182] Khanam PN, Reddy GR, Raghu K, Naidu SV. *Tensile, Flexural, and Compressive Properties of Coir/Silk Fiber-reinforced Hybrid Composites*. Journal of Reinforced Plastics and Composites. **2010**;29(14):2124-2127.
[183] Haneefa A, Bindu P, Aravind I, Thomas S. *Studies on tensile and flexural properties of short banana/glass hybrid fiber reinforced polystyrene composites*. Journal of Composite Materials. **2008**;42(15):1471-1489.
[184] Kowsika MV, Mantena PR. *Static and low-velocity impact response characteristics of pultruded hybrid glass-graphite/epoxy composite beams*. Journal of Thermoplastic Composite Materials. **1999**;12(2):121-132.
[185] Naik NK, Ramasimha R, Arya H, Prabhu SV, ShamaRao N. *Impact response and damage tolerance characteristics of glass–carbon/epoxy hybrid composite plates*. Composites Part B: Engineering. **2001**;32(7):565-574.
[186] Sevkat E, Liaw B, Delale F, Raju BB. *Drop-weight impact of plain-woven hybrid glass–graphite/toughened epoxy composites*. Composites Part A: Applied Science and Manufacturing. **2009**;40(8):1090-1110.
[187] Sevkat E, Liaw B, Delale F, Raju BB. *Effect of repeated impacts on the response of plain-woven hybrid composites*. Composites Part B: Engineering. **2010**;41(5):403-413.
[188] Enfedaque A, Molina-Aldareguia JM, Galvez F, Gonzalez C, Llorca J. *Effect of Glass Fiber Hybridization on the Behavior Under Impact of Woven Carbon Fiber/Epoxy Laminates*. Journal of Composite Materials. **2010**;44(25):3051-3068.
[189] González EV, Maimí P, Sainz de Aja JR, Cruz P, Camanho PP. *Effects of interply hybridization on the damage resistance and tolerance of composite laminates*. Composite Structures. **2014**;108:319-331.
[190] Jang BZ, Chen LC, Wang CZ, Lin HT, Zee RH. *Impact resistance and energy-absorption mechanisms in hybrid composites*. Composites Science and Technology. **1989**;34(4):305-335.
[191] Park R, Jang JS. *Impact behavior of aramid fiber glass fiber hybrid composite: Evaluation of four-layer hybrid composites*. Journal of Materials Science. **2001**;36(9):2359-2367.
[192] Onal L, Adanur S. *Effect of Stacking Sequence on the mechanical properties of glass-carbon hybrid composites before and after impact*. Journal of Industrial Textiles. **2002**;31(4):255-271.
[193] Sayer M, Bektasc NB, Sayman O. *An experimental investigation on the impact behavior of hybrid composite plates*. Composite Structures. **2010**:1256-1262.
[194] De Cuyper P. *Interlayer hybridisation of steel fibre and self-reinforced composites* Master thesis. KU Leuven, Metallurgy and Materials Engineering, **2012**.
[195] Pavithran C, Mukherjee PS, Brahmakumar M, Damodaran AD. *Impact properties of sisal-glass hybrid laminates*. Journal of Materials Science. **1991**;26(2):455-459.
[196] De Rosa IM, Marra F, Pulci G, Santulli C, Sarasini F, Tirillo J, et al. *Post-impact mechanical characterisation of E-glass/basalt woven fabric interply hybrid laminates*. Express Polymer Letters. **2011**;5(5):449-459.
[197] Sarasini F, Tirillò J, Valente M, Valente T, Cioffi S, Iannace S, et al. *Effect of Basalt Fibre Hybridization on The Impact Behaviour Under Low Impact Velocity of Glass/Basalt Woven Fabric/Epoxy Resin Composites*. Composites Part A: Applied Science and Manufacturing. **2013**;47:109-123.
[198] Sarasini F, Tirillò J, Valente M, Ferrante L, Cioffi S, Iannace S, et al. *Hybrid composites based on aramid and basalt woven fabrics: Impact damage modes and residual flexural properties*. Materials & Design. **2013**;49(0):290-302.
[199] Park R, Jang J. *Effect of laminate geometry on impact performance of aramid fiber/polyethylene fiber hybrid composites*. Journal of Applied Polymer Science. **2000**;75(7):952-959.

[200] Peijs A, Venderbosch RW. *Hybrid composites based on polyethylene and carbon fibres Part 4: Influence of hybrid design on impact strength*. Journal of Materials Science Letters. **1991**;10(19):1122-1124.

[201] El-Dessouky HM, Lawrence CA. *Ultra-lightweight carbon fibre/thermoplastic composite material using spread tow technology*. Composites Part B: Engineering. **2013**.

[202] Yokozeki T, Kuroda A, Yoshimura A, Ogasawara T, Aoki T. *Damage characterization in thin-ply composite laminates under out-of-plane transverse loadings*. Composite Structures. **2010**;93(1):49-57.

[203] Saito H, Morita M, Kawabe K, Kanesaki M, Takeuchi H, Tanaka M, et al. *Effect of ply-thickness on impact damage morphology in CFRP laminates*. Journal of Reinforced Plastics and Composites. **2011**;30(13):1097-1106.

[204] Yu H, Potter KD, Wisnom MR *Aligned short fibre composites with high performance*. 19th International Conference on Composites Materials, Montreal, Canada, **2013**.

[205] Czél G, Wisnom MR *Study of non-linear tensile behaviour of discontinuous carbon-epoxy prepreg composites*. 19th International Conference on Composite Materials, Montreal, Canada, **2013**.

[206] Jalalvand M, Czél G, Wisnom MR. *Numerical modelling of the damage modes in UD thin carbon/glass hybrid laminates*. Composites Science and Technology. **2014**;94:39-47.

[207] Jones KD, Dibenedetto AT. *Fiber fracture in hybrid composite systems*. Composites Science and Technology. **1994**;51(1):53-62.

[208] Bakis CE, Nanni A, Terosky JA, Koehler SW. *Self-monitoring, pseudo-ductile, hybrid FRP reinforcement rods for concrete applications*. Composites Science and Technology. **2001**;61(6):815-823.

[209] Somboonsong W, Ko FK, Harris HG. *Ductile hybrid fiber reinforced plastic reinforcing bar for concrete structures: Design methodology*. ACI Materials Journal. **1998**;95(6):655-666.

[210] Liang Y, Sun C, Ansari F. *Acoustic emission characterization of damage in hybrid fiber-reinforced polymer rods*. Journal of Composites for Construction. **2004**;8(1):70-78.

[211] Callens MG, Gorbatikh L, Verpoest I. *Ductile steel fibre composites with brittle and ductile matrices*. Composites Part A: Applied Science and Manufacturing. **2014**;61:235-244.

[212] Thysen S. *Mechanical behavior of hybrid steel and glass fibre composites* Master thesis. KU Leuven, Metallurgy and Materials Engineering, **2013**.

[213] Peijs A, Venderbosch RW, Lemstra PJ. *Hybrid composites based on polyethylene and carbon fibres Part 3: Impact resistant structural composites through damage management*. Composites. **1990**;21(6):522-530.

[214] Dehkordi MT, Nosraty H, Shokrieh MM, Minak G, Ghelli D. *Low velocity impact properties of intra-ply hybrid composites based on basalt and nylon woven fabrics*. Materials & Design. **2010**;31(8):3835-3844.

[215] Pegoretti A, Fabbri E, Migliaresi C, Pilati F. *Intraply and interply hybrid composites based on E-glass and poly(vinyl alcohol) woven fabrics: tensile and impact properties*. Polymer International. **2004**;53(9):1290-1297.

[216] Jayabal S, Natarajan U, Sathiyamurthy S. *Effect of glass hybridization and staking sequence on mechanical behaviour of interply coir-glass hybrid laminate*. Bulletin of Materials Science. **2011**;34(2):293-298.

[217] Pavithran C, Mukherjee PS, Brahmakumar M. *Coir-glass intermingled fibre hybrid composites*. Journal of Reinforced Plastics and Composites. **1991**;10(1):91-101.

[218] Tran LQN, Fuentes CA, Dupont-Gillain C, Van Vuure AW, Verpoest I. *Understanding the interfacial compatibility and adhesion of natural coir fibre thermoplastic composites*. Composites Science and Technology. **2013**;80:23-30.

[219] Jawaid M, Khalil H. *Cellulosic/synthetic fibre reinforced polymer hybrid composites: A review*. Carbohydr Polym. **2011**;86(1):1-18.

[220] Nunna S, Chandra PR, Shrivastava S, Jalan AK. *A review on mechanical behavior of natural fiber based hybrid composites*. Journal of Reinforced Plastics and Composites. **2012**;31(11):759-769.

[221] Jawaid M, Khalil HPSA, Abu Bakar A. *Woven hybrid composites: Tensile and flexural properties of oil palm-woven jute fibres based epoxy composites*. Materials Science and Engineering A. **2011**;528(15):5190-5195.

[222] Venkateshwaran N, Elayaperumal A, Sathiya GK. *Prediction of tensile properties of hybrid-natural fiber composites*. Composites Part B: Engineering. **2012**;43(2):793-796.

[223] Idicula M, Joseph K, Thomas S. *Mechanical Performance of Short Banana/Sisal Hybrid Fiber Reinforced Polyester Composites*. Journal of Reinforced Plastics and Composites. **2010**;29(1):12-29.

[224] De Rosa IM, Santulli C, Sarasini F, Valente M. *Effect of Loading-Unloading Cycles on Impact-Damaged Jute/Glass Hybrid Laminates*. Polymer Composites. **2009**;30(12):1879-1887.
[225] De Rosa IM, Santulli C, Sarasini F, Valente M. *Post-impact damage characterization of hybrid configurations of jute/glass polyester laminates using acoustic emission and IR thermography*. Composites Science and Technology. **2009**;69(7-8):1142-1150.
[226] Almeida Jr JHS, Amico SC, Botelho EC, Amado FDR. *Hybridization effect on the mechanical properties of curaua/glass fiber composites*. Composites Part B: Engineering. **2013**;55(0):492-497.
[227] Devi LU, Bhagawan SS, Thomas S. *Dynamic Mechanical Analysis of Pineapple Leaf/Glass Hybrid Fiber Reinforced Polyester Composites*. Polymer Composites. **2010**;31(6):956-965.
[228] Santulli C, Janssen M, Jeronimidis G. *Partial replacement of E-glass fibers with flax fibers in composites and effect on falling weight impact performance*. Journal of Materials Science. **2005**;40(13):3581-3585.
[229] Sreekala MS, George J, Kumaran MG, Thomas S. *The mechanical performance of hybrid phenol-formaldehyde-based composites reinforced with glass and oil palm fibres*. Composites Science and Technology. **2002**;62(3):339-353.
[230] John K, Naidu SV. *Tensile properties of unsaturated polyester-based sisal fiber-glass fiber hybrid composites*. Journal of Reinforced Plastics and Composites. **2004**;23(17):1815-1819.
[231] Sabeel Ahmed K, Vijayarangan S. *Tensile, flexural and interlaminar shear properties of woven jute and jute-glass fabric reinforced polyester composites*. Journal of Materials Processing Technology. **2008**;207(1-3):330-335.
[232] Amico SC, Angrizani CC, Drummond ML. *Influence of the Stacking Sequence on the Mechanical Properties of Glass/Sisal Hybrid Composites*. Journal of Reinforced Plastics and Composites. **2010**;29(2):179-189.
[233] Khalil HPSA, Kang CW, Khairul A, Ridzuan R, Adawi TO. *The Effect of Different Laminations on Mechanical and Physical Properties of Hybrid Composites*. Journal of Reinforced Plastics and Composites. **2009**;28(9):1123-1137.
[234] Khanam PN, Khalil HPSA, Jawaid M, Reddy GR, Narayana CS, Naidu SV. *Sisal/Carbon Fibre Reinforced Hybrid Composites: Tensile, Flexural and Chemical Resistance Properties*. Journal of Polymers and the Environment. **2010**;18(4):727-733.
[235] Patel VA, Bhuva BD, Parsania PH. *Performance Evaluation of Treated-Untreated Jute-Carbon and Glass-Carbon Hybrid Composites of Bisphenol-C based Mixed Epoxy-Phenolic Resins*. Journal of Reinforced Plastics and Composites. **2009**;28(20):2549-2556.
[236] Atiqah A, Maleque MA, Jawaid M, Iqbal M. *Development of kenaf-glass reinforced unsaturated polyester hybrid composite for structural applications*. Composites Part B: Engineering. **2014**;56(0):68-73.
[237] Karsli NG, Aytac A. *Effects of maleated polypropylene on the morphology, thermal and mechanical properties of short carbon fiber reinforced polypropylene composites*. Materials & Design. **2011**;32(7):4069-4073.
[238] Van den fonteyne W. *Falingsgedrag van zelfversterkt polypropyleen* Master thesis. KU Leuven, Materials Engineering, **2012**.
[239] Foster RJ, Hine PJ, Ward IM. *The incorporation of carbon nanofibres to enhance the interlayer adhesion of hot compacted single-polymer polypropylene composites*. Polymer. **2010**;51(5):1140-1146.
[240] Chamis CC. *Simplified Composite Micromechanics Equations for Hygral, Thermal and Mechanical Properties*. NASA Technical Memorandum 88320, Houston, United States: NASA; **1983**.
[241] Searles K, Odegard G, Kumosa M. *Micro- and mesomechanics of 8-harness satin woven fabric composites: I - evaluation of elastic behavior*. Composites Part A-Applied Science and Manufacturing. **2001**;32(11):1627-1655.
[242] Shindo A. *Polyacrylonitrile (PAN)-based carbon fibers*. In: Kelly A, Zweben C, Chou TW, editors. Comprehensive composite materials, vol. 1.01 Amsterdam: Elsevier; **2000**. p. 1-33.
[243] Ward IM, Sweeney J. *Mechanical properties of solid polymers*. 3rd ed. Chichester, United Kingdom: John Wiley & Sons; **2012**.
[244] Li VC. *Can Concrete Be Bendable? The notoriously brittle building material may yet stretch instead of breaking*. American Scientist. **2012**;100(6):484-493.
[245] Li VC, Wang S, Wu C. *Tensile strain-hardening behavior of PVA-ECC*. ACI Materials Journal. **2001**;98(6):483-492.
[246] Ebacher V, Wang R. *A Unique Microcracking Process Associated with the Inelastic Deformation of Haversian Bone*. Advanced Functional Materials. **2009**;19(1):57-66.

[247] Barthelat F, Espinosa HD. *An experimental investigation of deformation and fracture of nacre-mother of pearl*. Experimental Mechanics. **2007**;47(3):311-324.

[248] Rim JE, Zavattieri P, Juster A, Espinosa HD. *Dimensional analysis and parametric studies for designing artificial nacre*. Journal of the Mechanical Behavior of Biomedical Materials. **2011**;4(2):190-211.

[249] Le Bozec Y, Kaang S, Hine PJ, Ward IM. *The thermal-expansion behaviour of hot-compacted polypropylene and polyethylene composites*. Composites Science and Technology. **2000**;60(3):333-344.

[250] Kim J-K, Sham M-L. *Impact and delamination failure of woven-fabric composites*. Composites Science and Technology. **2000**;60(5):745-761.

[251] Hu Y. *Micromechanics of chopped fiber composites using carbon fiber and thermoplastic matrix* Master thesis. KU Leuven, Department of Materials Engineering, **2010**.

[252] Compston P, Jar PYB. *Comparison of Interlaminar Fracture Toughness in Unidirectional and Woven Roving Marine Composites*. Applied Composite Materials. **1998**;5(3):189-206.

[253] Nukushina Y, Matsui J, Itoh M. *On the Tensile Load to Elongation Response of Carbon Fibre Single Filament Samples*. J Jap Soc Compos Mater. **1989**;15(5):210-221.

[254] Toyama N, Takatsubo J. *An investigation of non-linear elastic behavior of CFRP laminates and strain measurement using Lamb waves*. Composites Science and Technology. **2004**;64(16):2509-2516.

[255] Ghaseminejhad MN, Parvizi-Majidi A. *Impact behaviour and damage tolerance of woven carbon fibre-reinforced thermoplastic composites*. Composites. **1990**;21(2):155-168.

[256] Meerten Y. *Impact resistance of interlayer hybrid composites of self-reinforced polypropylene and carbon fibres* Master thesis. KU Leuven, Materials Engineering, **2013**.

[257] Olave M, Vanaerschot A, Lomov SV, Vandepitte D. *Internal geometry variability of two woven composites and related variability of the stiffness*. Polymer Composites. **2012**;33(8):1335-1350.

[258] Hinton MJ, Kaddour AS, Soden PD. *Evaluation of failure prediction in composite laminates: background to 'part C' of the exercise*. Composites Science and Technology. **2004**;64(3–4):321-327.

[259] Kaddour AS, Hinton MJ. *Maturity of 3D failure criteria for fibre-reinforced composites: Comparison between theories and experiments: Part B of WWFE-II*. Journal of Composite Materials. **2013**;47(6-7):925-966.

[260] Hinton MJ, Soden PD. *Predicting failure in composite laminates: the background to the exercise*. Composites Science and Technology. **1998**;58(7):1001-1010.

[261] Weibull W. *A statistical distribution function of wide applicability*. Journal of Applied Mechanics - Transactions of the ASME. **1951**;18(3):293-297.

[262] Swolfs Y, Gorbatikh L, Romanov V, Orlova S, Lomov SV, Verpoest I. *Stress concentrations in an impregnated fibre bundle with random fibre packing*. Composites Science and Technology. **2013**;74:113-120.

[263] Nedele MR, Wisnom MR. *Three-dimensional finite element analysis of the stress concentration at a single fibre break*. Composites Science and Technology. **1994**;51(4):517-524.

[264] Behzadi S, Jones FR. *The effect of temperature on stress transfer between a broken fibre and the adjacent fibres in unidirectional fibre composites*. Composites Science and Technology. **2008**;68(13):2690-2696.

[265] Scott AE, Sinclair I, Spearing SM, Thionnet A, Bunsell AR. *Damage accumulation in a carbon/epoxy composite: Comparison between a multiscale model and computed tomography experimental results*. Composites Part A: Applied Science and Manufacturing. **2012**;43(9):1514-1522.

[266] Thionnet A, Chou HY, Bunsell A. *Fibre break processes in unidirectional composites*. Composites Part A: Applied Science and Manufacturing. **2014**;65:148-160.

[267] Asloun EM, Donnet JB, Guilpain G, Nardin M, Schultz J. *On the estimation of the tensile strength of carbon fibres at short lengths*. Journal of Materials Science. **1989**;24(10):3504-3510.

[268] Gulino R, Phoenix SL. *Weibull strength statistics for graphite fibres measured from the break progression in a model graphite/glass/epoxy composite*. Journal of Materials Science. **1991**;26(11):3107-3118.

[269] Beyerlein IJ, Phoenix SL. *Statistics for the strength and size effects of microcomposites with four carbon fibers in epoxy resin*. Composites Science and Technology. **1996**;56(1):75-92.

[270] Watson AS, Smith RL. *An examination of statistical theories for fibrous materials in the light of experimental data*. Journal of Materials Science. **1985**;20(9):3260-3270.

[271] Phoenix SL, Schwartz P, Robinson HH. *Statistics for the strength and lifetime in creep-rupture of model carbon/epoxy composites*. Composites Science and Technology. **1988**;32(2):81-120.

[272] Berger MH, Jeulin D. *Statistical analysis of the failure stresses of ceramic fibres: Dependence of the Weibull parameters on the gauge length, diameter variation and fluctuation of defect density*. Journal of Materials Science. **2003**;38(13):2913-2923.

[273] Curtin WA. *Tensile strength of fiber-reinforced composites: III. Beyond the traditional Weibull model for fiber strengths*. Journal of Composite Materials. **2000**;34(15):1301-1332.

[274] Andersons J, Joffe R, Hojo M, Ochiai S. *Glass fibre strength distribution determined by common experimental methods*. Composites Science and Technology. **2002**;62(1):131-145.

[275] Watanabe J, Tanaka F, Okabe T *The tensile strength distribution of carbon fibers at short gauge length*. 38th Conference of the Japan Society for Composite Materials, **2013**.

[276] Okabe T, Takeda N. *Size effect on tensile strength of unidirectional CFRP composites - experiment and simulation*. Composites Science and Technology. **2002**;62(15):2053-2064.

[277] Loidl D, Paris O, Rennhofer H, Mueller M, Peterlik H. *Skin-core structure and bimodal Weibull distribution of the strength of carbon fibers*. Carbon. **2007**;45(14):2801-2805.

[278] Peterlik H, Loidl D. *Bimodal strength distributions and flaw populations of ceramics and fibres*. Engineering Fracture Mechanics. **2001**;68(3):253-261.

[279] Zinck P, Pays MF, Rezakhanlou R, Gerard JF. *Extrapolation techniques at short gauge lengths based on the weakest link concept for fibres exhibiting multiple failure modes*. Philosophical Magazine a-Physics of Condensed Matter Structure Defects and Mechanical Properties. **1999**;79(9):2103-2122.

[280] Beetz CP. *The analysis of carbon fibre strength distributions exhibiting multiple modes of failure*. Fibre Science & Technology. **1982**;16(1):45-59.

[281] Stoner EG, Edie DD, Durham SD. *An end-effect model for the single-filament tensile test*. Journal of Materials Science. **1994**;29(24):6561-6574.

[282] Thomason JL. *On the application of Weibull analysis to experimentally determined single fibre strength distributions*. Composites Science and Technology. **2013**;77:74-80.

[283] Yang L, Thomason JL. *Effect of silane coupling agent on mechanical performance of glass fibre*. Journal of Materials Science. **2013**;48(5):1947-1954.

[284] Bader MG, Priest AM *Statistical aspects of fibre and bundle strength*. Fourth International Conference on Composite Materials, Tokyo, Japan, **1982**.

[285] Zinck P, Mader E, Gerard JF. *Role of silane coupling agent and polymeric film former for tailoring glass fiber sizings from tensile strength measurements*. Journal of Materials Science. **2001**;36(21):5245-5252.

[286] Naito K, Yang JM, Tanaka Y, Kagawa Y. *The effect of gauge length on tensile strength and Weibull modulus of polyacrylonitrile (PAN)- and pitch-based carbon fibers*. Journal of Materials Science. **2012**;47(2):632-642.

[287] Phoenix SL, Sexsmith RG. *Clamp effects in fiber testing*. Journal of Composite Materials. **1972**;6(JUL):322-337.

[288] Tanaka F, Okabe T, Okuda H, Kinloch IA, Young RJ. *Factors Controlling the Strength of Carbon Fibres in Tension*. Composites Part A: Applied Science and Manufacturing. **2014**;57:88-94.

[289] Jimenez FL, Pellegrino S. *Failure of Carbon Fibers at a Crease in a Fiber-Reinforced Silicone Sheet*. Journal of Applied Mechanics - Transactions of the ASME. **2013**;80(1):8.

[290] Cox HL. *The elasticity and strength of paper and other fibrous materials*. British Journal of Applied Physics. **1952**;3(3):72-79.

[291] Ochiai S, Hojo M, Osamura K. *General expression of the shear lag analysis for unidirectional elastic fiber-elastic matrix composites*. Zeitschrift Fur Metallkunde. **1993**;84(11):796-801.

[292] Zeng QD, Wang ZL, Ling L. *A study of the influence of interfacial damage on stress concentrations in unidirectional composites*. Composites Science and Technology. **1997**;57(1):129-135.

[293] Okabe T, Takeda N, Kamoshida Y, Shimizu M, Curtin WA. *A 3D shear-lag model considering micro-damage and statistical strength prediction of unidirectional fiber-reinforced composites*. Composites Science and Technology. **2001**;61(12):1773-1787.

[294] Beyerlein IJ, Landis CM. *Shear-lag model for failure simulations of unidirectional fiber composites including matrix stiffness*. Mechanics of Materials. **1999**;31(5):331-350.

[295] de Morais AB. *Prediction of the longitudinal tensile strength of polymer matrix composites*. Composites Science and Technology. **2006**;66(15):2990-2996.

[296] Mishnaevsky Jr L, Brøndsted P. *Micromechanisms of damage in unidirectional fiber reinforced composites: 3D computational analysis*. Composites Science and Technology. **2009**;69(7-8):1036-1044.
[297] Xia Z, Curtin WA, Peters PWM. *Multiscale modeling of failure in metal matrix composites*. Acta Materialia. **2001**;49(2):273-287.
[298] Xia Z, Okabe T, Curtin WA. *Shear-lag versus finite element models for stress transfer in fiber-reinforced composites*. Composites Science and Technology. **2002**;62(9):1141-1149.
[299] van den Heuvel PWJ, Wubbolts MK, Young RJ, Peijs T. *Failure phenomena in two-dimensional multi-fibre model composites: 5. A finite element study*. Composites Part A-Applied Science and Manufacturing. **1998**;29(9-10):1121-1135.
[300] Wagner HD, Eitan A. *Stress concentration factors in two-dimensional composites: effects of material and geometrical parameters*. Composites Science and Technology. **1993**;46(4):353-362.
[301] Smith RL, Phoenix SL, Greenfield MR, Henstenburg RB, Pitt RE. *Lower-tail approximations for the probability of failure of three-dimensional fibrous composites with hexagonal geometry* Proceedings of the Royal Society of London Series A: Mathematical Physical and Engineering Sciences. **1983**;388(1795):353-391.
[302] Batdorf SB, Ghaffarian R. *Size effect and strength variability of unidirectional composites*. International Journal of Fracture. **1984**;26(2):113-123.
[303] Oh JH, Jin KK, Ha SK. *Interfacial strain distribution of a unidirectional composite with randomly distributed fibers under transverse loading*. Journal of Composite Materials. **2006**;40(9):759-778.
[304] Wongsto A, Li S. *Micromechanical FE analysis of UD fibre-reinforced composites with fibres distributed at random over the transverse cross-section*. Composites Part A: Applied Science and Manufacturing. **2005**;36(9):1246-1266.
[305] Jodrey WS, Tory EM. *Computer simulation of close random packing of equal spheres*. Physical Review A. **1985**;32(4):2347-2351.
[306] van den Heuvel PWJ, Peijs T, Young RJ. *Failure phenomena in two-dimensional multi-fibre microcomposites .2. A Raman spectroscopic study of the influence of inter-fibre spacing on stress concentrations*. Composites Science and Technology. **1997**;57(8):899-911.
[307] Wagner HD, Amer MS, Schadler LS. *Fibre interactions in two-dimensional composites by micro-Raman spectroscopy*. Journal of Materials Science. **1996**;31(5):1165-1173.
[308] Beyerlein IJ, Amer MS, Schadler LS, Phoenix SL. *New methodology for determining in situ fiber, matrix and interface stresses in damaged multifiber composites*. Science and Engineering of Composite Materials. **1998**;7(1-2):151-204.
[309] He J, Beyerlein IJ, Clarke DR. *Load transfer from broken fibers in continuous fiber Al2O3-A1 composites and dependence on local volume fraction*. Journal of the Mechanics and Physics of Solids. **1999**;47(3):465-502.
[310] Ochiai S, Schulte K, Peters PWM. *Strain concentration factors for fibers and matrix in unidirectional composites*. Composites Science and Technology. **1991**;41(3):237-256.
[311] de Morais AB. *Stress distribution along broken fibres in polymer-matrix composites*. Composites Science and Technology. **2001**;61(11):1571-1580.
[312] Landis CM, McMeeking RM. *A shear-lag model for a broken fiber embedded in a composite with a ductile matrix*. Composites Science and Technology. **1999**;59(3):447-457.
[313] Beyerlein IJ, Phoenix SL. *Stress concentrations around multiple fiber breaks in an elastic matrix with local yielding or debonding using quadratic influence superposition*. Journal of the Mechanics and Physics of Solids. **1996**;44(12):1997-2039.
[314] Blassiau S, Thionnet A, Bunsell AR. *Micromechanisms of load transfer in a unidirectional carbon fibre-reinforced epoxy composite due to fibre failures. Part 2: Influence of viscoelastic and plastic matrices on the mechanisms of load transfer*. Composite Structures. **2006**;74(3):319-331.
[315] Goree JG, Gross RS. *Analysis of a unidirectional composite containing broken fibers and matrix damage*. Engineering Fracture Mechanics. **1980**;13(3):563-578.
[316] Ohno N, Okabe S, Okabe T. *Stress concentrations near a fiber break in unidirectional composites with interfacial slip and matrix yielding*. International Journal of Solids and Structures. **2004**;41(16-17):4263-4277.
[317] Zhao FM, Takeda N. *Effect of interfacial adhesion and statistical fiber strength on tensile strength of unidirectional glass fiber/epoxy composites. Part I: experiment results*. Composites Part A-Applied Science and Manufacturing. **2000**;31(11):1203-1214.
[318] Pegoretti A, Accorsi ML, Dibenedetto AT. *Fracture toughness of the fibre-matrix interface in glass-epoxy composites*. Journal of Materials Science. **1996**;31(23):6145-6153.

[319] Johnson AC, Zhao FM, Hayes SA, Jones FR. *Influence of a matrix crack on stress transfer to an alpha-alumina fibre in epoxy resin using FEA and photoelasticity*. Composites Science and Technology. **2006**;66(13):2023-2029.

[320] van den Heuvel PWJ, Peijs T, Young RJ. *Failure phenomena in two-dimensional multi-fibre microcomposites. Part 4: a Raman spectroscopic study on the influence of the matrix yield stress on stress concentrations*. Composites Part A: Applied Science and Manufacturing. **2000**;31(2):165-171.

[321] van den Heuvel PWJ, vanderBruggen YJW, Peijs T. *Failure phenomena in multi-fibre model composites .1. An experimental investigation into the influence of fibre spacing and fibre-matrix adhesion*. Composites Part A: Applied Science and Manufacturing. **1996**;27(9):855-859.

[322] Zeng QD. *A statistical analysis of the tensile failure and hybrid effect of an intraply hybrid composite*. International Journal of Fracture. **1994**;68(4):351-362.

[323] Wagner HD, Wiesel E, Green AK. *Evidence of dynamic effects in the fragmentation of optical fibers in epoxy*. Composites Part A: Applied Science and Manufacturing. **1998**;29(8):989-991.

[324] Netravali AN, Henstenburg RB, Phoenix SL, Schwartz P. *Interfacial shear strength studies using the single-filament-composite test. 1. Experiments on graphite fibers in epoxy*. Polymer Composites. **1989**;10(4):226-241.

[325] Li H, Jia Y, Mamtimin G, Jiang W, An L. *Stress transfer and damage evolution simulations of fiber-reinforced polymer-matrix composites*. Materials Science and Engineering A. **2006**;425(1-2):178-184.

[326] Sakharova EN, Ovchinskii AS. *Influence of dynamic effects accompanying rupture of fibers and separation of fibers from the matrix on interaction between failure micromechanisms of composite materials*. Mech Compos Mater. **1984**;20(3):323-327.

[327] Sakharova EN, Ovchinskii AS. *Dynamics of stress redistribution in fiber fracture in composites*. Mech Compos Mater. **1980**;16(4):417-422.

[328] Sastry AM, Phoenix SL. *Load redistribution near non-aligned fiber breaks in a 2-dimensional unidirectional composite using break-influence superposition*. Journal of Materials Science Letters. **1993**;12(20):1596-1599.

[329] Beyerlein IJ, Phoenix SL, Sastry AM. *Comparison of shear-lag theory and continuum fracture mechanics for modeling fiber and matrix stresses in an elastic cracked composite lamina*. International Journal of Solids and Structures. **1996**;33(18):2543-2574.

[330] Kachanov M. *A simple technique of stress analysis in elastic solids with many cracks*. International Journal of Fracture. **1985**;28(1):R11-R19.

[331] Landis CM, Beyerlein IJ, McMeeking RM. *Micromechanical simulation of the failure of fiber reinforced composites*. Journal of the Mechanics and Physics of Solids. **2000**;48(3):621-648.

[332] Ibnabdeljalil M, Curtin WA. *Strength and reliability of fiber-reinforced composites: Localized load-sharing and associated size effects*. International Journal of Solids and Structures. **1997**;34(21):2649-2668.

[333] Ibnabdeljalil M, Curtin WA. *Strength and reliability of notched fiber-reinforced composites*. Acta Materialia. **1997**;45(9):3641-3652.

[334] Zhou SJ, Curtin WA. *Failure of fiber composites: a lattice green function model*. Acta Metallurgica Et Materialia. **1995**;43(8):3093-3104.

[335] Xia Z, Curtin WA, Okabe T. *Green's function vs. shear-lag models of damage and failure in fiber composites*. Composites Science and Technology. **2002**;62(10-11):1279-1288.

[336] Mishnaevskyjr L, Brondsted P. *Micromechanical modeling of damage and fracture of unidirectional fiber reinforced composites: A review*. Computational Materials Science. **2009**;44(4):1351-1359.

[337] Mahesh S, Phoenix SL, Beyerlein IJ. *Strength distributions and size effects for 2D and 3D composites with Weibull fibers in an elastic matrix*. International Journal of Fracture. **2002**;115(1):41-85.

[338] Curtin WA. *The "tough" to brittle transition in brittle matrix composites*. Journal of the Mechanics and Physics of Solids. **1993**;41(2):217-245.

[339] Neumeister JM. *A constitutive law for continuous fiber reinforced brittle matrix composites with fiber fragmentation and stress recovery*. Journal of the Mechanics and Physics of Solids. **1993**;41(8):1383-1404.

[340] Neumeister JM. *Bundle pullout—a failure mechanism limiting the tensile strength of continuous fiber reinforced brittle matrix composites— and its implications for strength dependence on volume and type of loading*. Journal of the Mechanics and Physics of Solids. **1993**;41(8):1405-1424.

[341] Hui CY, Phoenix SL, Ibnabdeljalil M, Smith RL. *An exact closed form solution for fragmentation of Weibull fibers in a single filament composite with applications to fiber-reinforced ceramics*. Journal of the Mechanics and Physics of Solids. **1995**;43(10):1551-1585.

[342] Rajan VP, Zok FW. *Effects of non-uniform strains on tensile fracture of fiber-reinforced ceramic composites*. Journal of the Mechanics and Physics of Solids. **2012**;60(12):2003-2018.

[343] Zhou XF, Wagner HD. *Stress concentrations caused by fiber failure in two-dimensional composites*. Composites Science and Technology. **1999**;59(7):1063-1071.

[344] Curtin WA. *Theory of mechanical properties of ceramic-matrix composites*. Journal of the American Ceramic Society. **1991**;74(11):2837-2845.

[345] Curtin WA. *Exact theory of fibre fragmentation in a single-filament composite*. Journal of Materials Science. **1991**;26(19):5239-5253.

[346] Harlow DG, Phoenix SL. *The chain-of-bundles probability model for the strength of fibrous materials I: Analysis and conjectures*. Journal of Composite Materials. **1978**;12(APR):195-214.

[347] Harlow DG, Phoenix SL. *The chain-of-bundles probability model for the strength of fibrous materials II: Numerical study of convergence*. Journal of Composite Materials. **1978**;12(JUL):314-334.

[348] Harlow DG, Phoenix SL. *Probability distributions for the strength of composite materials I: two-level bounds*. International Journal of Fracture. **1981**;17(4):347-372.

[349] Harlow DG, Phoenix SL. *Probability distributions for the strength of composite materials II: A convergent sequence of tight bounds*. International Journal of Fracture. **1981**;17(6):601-630.

[350] Pitt RE, Phoenix SL. *Probability distributions for the strength of composite materials. III: The effect of fiber arrangement*. International Journal of Fracture. **1982**;20(4):291-311.

[351] Smith RL. *Limit theorems and approximations for the reliability of load-sharing systems*. Advances in Applied Probability. **1983**;15(2):304-330.

[352] Duxbury PM, Leath PL. *Exactly solvable models of material breakdown*. Physical Review B. **1994**;49(18):12676-12687.

[353] Foreman JP, Behzadi S, Tsampas SA, Porter D, Curtis PT, Jones FR. *Rate dependent multiscale modelling of fibre reinforced composites*. Plast Rubber Compos. **2009**;38(2-4):67-71.

[354] Foreman JP, Behzadi S, Porter D, Jones FR. *Multi-scale modelling of the effect of a viscoelastic matrix on the strength of a carbon fibre composite*. Philosophical Magazine. **2010**;90(31-32):4227-4244.

[355] Blassiau S, Bunsell AR, Thionnet A. *Damage accumulation processes and life prediction in unidirectional composites*. Proceedings of the Royal Society of London Series A: Mathematical Physical and Engineering Sciences. **2007**;463(2080):1135-1152.

[356] Blassiau S, Thionnet A, Bunsell AR. *Micromechanisms of load transfer in a unidirectional carbon fibre-reinforced epoxy composite due to fibre failures: Part 3. Multiscale reconstruction of composite behaviour*. Composite Structures. **2008**;83(3):312-323.

[357] Okabe T, Sekine H, Ishii K, Nishikawa M, Takeda N. *Numerical method for failure simulation of unidirectional fiber-reinforced composites with spring element model*. Composites Science and Technology. **2005**;65(6):921-933.

[358] Okabe T, Ishii K, Nishikawa M, Takeda N. *Prediction of Tensile Strength of Unidirectional CFRP Composites*. Advanced Composite Materials. **2010**;19(3):229-241.

[359] Chiang M, Wang X, Schultheisz C, He J. *Prediction and three-dimensional Monte-Carlo simulation for tensile properties of unidirectional hybrid composites*. Composites Science and Technology. **2005**;65(11-12):1719-1727.

[360] Okabe T, Nishikawa M, Takeda N, Sekine H. *Effect of matrix hardening on the tensile strength of alumina fiber-reinforced aluminum matrix composites*. Acta Materialia. **2006**;54(9):2557-2566.

[361] Mishnaevsky Jr L, Dai G. *Hybrid carbon/glass fiber composites: Micromechanical analysis of structure–damage resistance relationships*. Computational Materials Science. **2014**;81:630-640.

[362] Dai G, Mishnaevsky Jr L. *Fatigue of hybrid glass/carbon composites: 3D computational studies*. Composites Science and Technology. **2014**;94:71-79.

[363] Wang F, Chen ZQ, Wei YQ, Zeng XG. *Numerical Modeling of Tensile Behavior of Fiber-reinforced Polymer Composites*. Journal of Composite Materials. **2010**;44(19):2325-2340.

[364] Peirce FT. *Tensile tests for cotton yarns: V - 'the weakest link' - Theorems on the strength of long and short composite specimens*. Journal of the Textile Institute. **1926**;17:355-368.

[365] Daniels HE. *The statistical theory of strength of bundles of threads. I.* Proceedings of the Royal Society of London Series A: Mathematical Physical and Engineering Sciences. **1945**;183(995):405-435.

[366] Curtis PT. *A computer model of the tensile failure process in unidirectional fibre composites*. Composites Science and Technology. **1986**;27(1):63-86.

[367] Blassiau S, Thionnet A, Bunsell AR. *Micromechanisms of load transfer in a unidirectional carbon fibre-reinforced epoxy composite due to fibre failures. Part 1: Micromechanisms and 3D analysis of load transfer: The elastic case*. Composite Structures. **2006**;74(3):303-318.

[368] Blassiau S, Thionnet A, Bunsell AR. *Three-dimensional analysis of load transfer micro-mechanisms in fibre/matrix composites*. Composites Science and Technology. **2009**;69(1):33-37.

[369] Wisnom MR, Green D. *Tensile failure due to interaction between fibre breaks*. Composites. **1995**;26(7):499-508.

[370] Gulino R, Schwartz P, Phoenix SL. *Experiments on shear deformation, debonding and local load transfer in a model graphite/glass/epoxy microcomposite*. Journal of Materials Science. **1991**;26(24):6655-6672.

[371] Hobbiebrunken T, Fiedler B, Hojo M, Tanaka M. *Experimental determination of the true epoxy resin strength using micro-scaled specimens*. Composites Part A: Applied Science and Manufacturing. **2007**;38(3):814-818.

[372] Ohnami M. *Fracture and society*. Tokyo, Japan: Ohmsha Ltd; **1992**.

[373] Zweben C. *Is there a size effect in composites?* Composites. **1994**;25(6):451-454.

[374] Wisnom MR. *Size effects in the testing of fibre-composite materials*. Composites Science and Technology. **1999**;59(13):1937-1957.

[375] Wisnom MR, Hallett SR, Soutis C. *Scaling Effects in Notched Composites*. Journal of Composite Materials. **2010**;44(2):195-210.

[376] Bazant ZP, Daniel IM, Li ZZ. *Size effect and fracture characteristics of composite laminates*. Journal of Engineering Materials and Technology-Transactions of the ASME. **1996**;118(3):317-324.

[377] Gurvich MR, Pipes RB. *Strength size effect of laminated composites*. Composites Science and Technology. **1995**;55(1):93-105.

[378] Mahesh S, Beyerlein IJ, Phoenix SL. *Size and heterogeneity effects on the strength of fibrous composites*. Physica D. **1999**;133(1-4):371-389.

[379] Camanho PP, Maimi P, Davila CG. *Prediction of size effects in notched laminates using continuum damage mechanics*. Composites science and technology. **2007**;67(13):2715-2727.

[380] Naito K, Tanaka Y, Yang J-M, Kagawa Y. *Tensile properties of ultrahigh strength PAN-based, ultrahigh modulus pitch-based and high ductility pitch-based carbon fibers*. Carbon. **2008**;46(2):189-195.

[381] Zhang F, Lisle T, Curtin WA, Xia Z. *Multiscale modeling of ductile-fiber-reinforced composites*. Composites Science and Technology. **2009**;69(11-12):1887-1895.

[382] Aroush DRB, Maire E, Gauthier C, Youssef S, Cloetens P, Wagner HD. *A study of fracture of unidirectional composites using in situ high-resolution synchrotron X-ray microtomography*. Composites Science and Technology. **2006**;66(10):1348-1353.

[383] Zhao FM, Takeda N. *Effect of interfacial adhesion and statistical fiber strength on tensile strength of unidirectional glass fiber/epoxy composites. Part. II: comparison with prediction*. Composites Part A-Applied Science and Manufacturing. **2000**;31(11):1215-1224.

[384] Melro AR, Camanho PP, Pinho ST. *Generation of random distribution of fibres in long-fibre reinforced composites*. Composites Science and Technology. **2008**;68(9):2092-2102.

[385] Romanov V, Lomov SL, Gorbatikh L, Verpoest I *Validation of a heuristic fibre placement algorithm: statistical analysis of real and simulated fibre arrangements*. XVII International conference on Mechanics of Composite Materials, Book of abstracts, Riga, Latvia **2012**.

[386] Fukuda H. *Stress concentration factors in unidirectional composites with random fiber spacing*. Composites Science and Technology. **1985**;22(2):153-163.

[387] Karahan M, Lomov SV, Bogdanovich AE, Mungalov D, Verpoest I. *Internal geometry evaluation of non-crimp 3D orthogonal woven carbon fabric composite*. Composites Part A: Applied Science and Manufacturing. **2010**;41(9):1301-1311.

[388] Guild FJ, Vlattas C, Galiotis C. *Modelling of stress transfer in fibre composites*. Composites Science and Technology. **1994**;50(3):319-332.

[389] *T700S carbon fibre data sheet*, www.toraycfa.com, June 2014.

[390] Curtin WA. *Size scaling of strength in heterogeneous materials*. Physical Review Letters. **1998**;80(7):1445-1448.

[391] Trias D, Costa J, Mayugo JA, Hurtado JE. *Random models versus periodic models for fibre reinforced composites*. Computational Materials Science. **2006**;38(2):316-324.

[392] *T600S carbon fibre data sheet*, www.toraycfa.com, June 2014.

[393] Wright P, Moffat A, Sinclair I, Spearing SM. *High resolution tomographic imaging and modelling of notch tip damage in a laminated composite*. Composites science and technology. **2010**;70(10):1444-1452.

[394] Fukuda H. *An advanced theory of the strength of hybrid composites*. Journal of Materials Science. **1984**;19(3):974-982.

[395] Fariborz SJ, Yang CL, Harlow DG. *The tensile behavior of intraply hybrid composites I: Model and simulation*. Journal of Composite Materials. **1985**;19(4):334-354.

[396] Kobelev VV. *Explicit crack problem solutions of hybrid composites*. International Journal of Solids and Structures. **1993**;30(3):413-426.

[397] Fukunaga H, Chou TW, Fukuda H. *Probabilistic strength analyses of interlaminated hybrid composites*. Composites Science and Technology. **1989**;35(4):331-345.

[398] Zweben C. *An approximate method of analysis for notched unidirectional composites*. Engineering Fracture Mechanics. **1974**;6(1):1-10.

[399] Fukunaga H, Tsu-Wei C, Fukuda H. *Strength of intermingled hybrid composites*. Journal of Reinforced Plastics and Composites. **1984**;3(2):145-160.

[400] Fukuda H, Chou TW. *Monte Carlo simulation of the strength of hybrid composites*. Journal of Composite Materials. **1982**;16(SEP):371-385.

[401] Pimenta S, Robinson P *Modelling the tensile response of unidirectional hybrid composites*. Proceedings of the 16th European Conference on Composite Materials, Seville, Spain, **2014**.

[402] Pan N, Postle R. *The tensile strength of hybrid fibre composites: A probabilistic analysis of the hybrid effects*. Philosophical Transactions of the Royal Society of London Series a-Mathematical Physical and Engineering Sciences. **1996**;354(1714):1875-1897.

[403] Fariborz SJ, Harlow DG. *The tensile behavior of intraply hybrid composites II: Micromechanical model*. Journal of Composite Materials. **1987**;21(9):856-875.

[404] Harlow DG. *Statistical properties of hybrid composites: Asymptotic distributions for strain*. Reliability Engineering & System Safety. **1997**;56(3):197-208.

[405] Manders PW. *The strength of mixed fibre composites* PhD. thesis. University of Surrey, University of Surrey, **1979**.

[406] Swolfs Y, Gorbatikh L, Verpoest I. *Stress concentrations in hybrid unidirectional fibre-reinforced composites with random fibre packings*. Composites Science and Technology. **2013**;85:10-16.

[407] Peijs A, Dekok JMM. *Hybrid composites based on polyethylene and carbon fibres Part 6: Tensile and fatigue behavior*. Composites. **1993**;24(1):19-32.

[408] Pitkethly MJ, Bader MG. *Failure modes of hybrid composites consisting of carbon fibre bundles dispersed in a glass fibre epoxy resin matrix*. Journal of Physics D-Applied Physics. **1987**;20(3):315-322.

[409] Kelly A, Tyson WR. *Tensile properties of fibre-reinforced metals - copper/tungsten and copper/molybdenum*. Journal of the Mechanics and Physics of Solids. **1965**;13(6):329-350.

[410] Dwight DW. *Glass fiber reinforcements*. In: Kelly A, Zweben C, Chou TW, editors. Comprehensive composite materials, vol. 1.08 Amsterdam: Elsevier; **2000**. p. 1-31.

[411] Zhiguo R, Ying Y, Jianfeng L, Zhongxing Q, Lei Y. *Determination of thermal expansion coefficients for unidirectional fiber-reinforced composites*. Chinese Journal of Aeronautics, In press. **2014**.

[412] Naito K, Yang J-M, Kagawa Y. *Tensile properties of high strength polyacrylonitrile (PAN)-based and high modulus pitch-based hybrid carbon fibers-reinforced epoxy matrix composite*. Journal of Materials Science. **2012**;47(6):2743-2751.

[413] Witik RA, Payet J, Michaud V, Ludwig C, Månson J-AE. *Assessing the life cycle costs and environmental performance of lightweight materials in automobile applications*. Composites Part A: Applied Science and Manufacturing. **2011**;42(11):1694-1709.

[414] Duflou JR, De Moor J, Verpoest I, Dewulf W. *Environmental impact analysis of composite use in car manufacturing*. CIRP Annals - Manufacturing Technology. **2009**;58(1):9-12.

[415] Yu H, Potter KD, Wisnom MR. *A novel manufacturing method for aligned discontinuous fibre composites (High Performance-Discontinuous Fibre method)*. Composites Part A: Applied Science and Manufacturing. **2014**;65(0):175-185.

[416] Shioya M, Takaku A. *Rotation and extension of crystallites in carbon fibers by tensile stress*. Carbon. **1994**;32(4):615-619.

Chapter 8:

Publications

This chapter lists all journal and conference publications related to this thesis. The supervised master theses are listed, and their contribution to this PhD thesis is highlighted.

8.1 Journal papers

Published

1. Swolfs Y, Gorbatikh L, Romanov V, Orlova S, Lomov SV, Verpoest I, *Stress concentrations in an impregnated fibre bundle with random fibre packing*, Composite Science and Technology 74 (2013) p. 113-120.
2. Swolfs Y, Gorbatikh L, Verpoest I, *Stress concentrations in hybrid unidirectional fibre-reinforced composites with random fibre packings*, Composite Science and Technology 85 (2013) p. 10-16.
3. Swolfs Y, Crauwels L, Gorbatikh L, Verpoest I, *The influence of weave architecture on the mechanical properties of self-reinforced polypropylene*, Composites Part A: Applied Science and Manufacturing 53 (2013) p. 129-136.
4. Romanov V, Lomov SV, Swolfs Y, Orlova S, Gorbatikh L, Verpoest I, *Statistical analysis of real and simulated fibre arrangements in unidirectional composites*, Composites Science and Technology 87 (2013) p. 126-134.
5. Swolfs Y, Crauwels L, Van Breda E, Gorbatikh L, Hine PJ, Ward IM, Verpoest I, *Tensile behaviour of intralayer hybrid composites of carbon fibre and self-reinforced polypropylene*, Composites Part A: Applied Science and Manufacturing 59 (2014) p. 78-84.
6. Verpoest I, Lomov SV, Swolfs Y, Jacquet P, Michaud V, Manson J-A, Hobdell J, Hine PJ, Marquette P, Herten H, Vasiliadis H, *Advanced materials enabling high-volume road transport applications of lightweight structural composite parts*, SAMPE Journal 50 (2014) p. 30-37.
7. Hine PJ, Bonner MJ, Ward IM, Swolfs Y, Verpoest I, Mierzwa A, *Hybrid carbon fibre/nylon 12 single polymer composites*, Composites Part A: Applied Science and Manufacturing 65 (2014) p. 19-26.
8. Swolfs Y, Zhang Q, Baets J, Verpoest I, *The influence of process parameters on the properties of hot compacted self-reinforced polypropylene composites*, Composites Part A: Applied Science and Manufacturing 65 (2014) p. 38-46.
9. Swolfs Y, Van den fonteyne W, Baets J, Verpoest I, *Failure behaviour of self-reinforced polypropylene at and below room temperature*, Composites Part A: Applied Science and Manufacturing 65 (2014) p. 100-107.
10. Swolfs Y, Gorbatikh L, Verpoest I, *Fibre hybridisation in polymer composites: a review*, Composites Part A: Applied Science and Manufacturing 67 (2014) p. 181-200.
11. Meerten Y, Swolfs Y, Baets Y, Gorbatikh L, Verpoest I, *Penetration impact testing of self-reinforced composites*, Composites Part A: Applied Science and Manufacturing 68 (2015) p. 289-295.
12. Swolfs Y, McMeeking RM, Verpoest I, Gorbatikh L, *The effect of fibre dispersion on initial failure strain and cluster development in unidirectional carbon/glass hybrid composites*, Composites Part A:

Applied Science and Manufacturing, DOI: 10.1016/j.compositesa.2014.12.001.

Accepted with revisions

13. Swolfs Y, McMeeking RM, Verpoest I, Gorbatikh L, *Matrix cracks around fibre breaks and their effect on stress redistribution and failure development in unidirectional composites*, Composites Science and Technology, accepted.
14. Swolfs Y, McMeeking RM, Rajan VP, Zok FW, Verpoest I, Gorbatikh L, *Global load-sharing model for unidirectional hybrid fibre-reinforced composites*, Journal of the Mechanics and Physics of Solids, accepted.
15. Swolfs Y, Verpoest I, Gorbatikh L, *Issues in strength models for unidirectional fibre-reinforced composites*, Composites Science and Technology, accepted.

Submitted

16. Li L, Swolfs Y, Straumit I, Yan X, Lomov SV, *Cluster analysis of acoustic emission signals for 2D and 3D woven carbon fiber/epoxy composites*, submitted to Journal of Composite Materials.
17. Swolfs Y, Morton H, Scott AE, Gorbatikh L, Reed PAS, Sinclair I, Spearing SM, Verpoest I, *Synchrotron radiation computed tomography for experimental validation of a tensile strength model for unidirectional fibre-reinforced composites*, submitted to Composites Part A: Applied Science and Manufacturing.

It should be noted that not all journal papers ended up in this thesis. More specifically, papers 4, 6, 7, 9, 12 and 15 were left out as they did not entirely fit the storyline of this thesis. Some sections of this thesis have not been published yet, but will be in the near future.

8.2 Conference papers

1. Swolfs Y, Gorbatikh L, Verpoest I, *Stress concentrations in hybrid unidirectional fibre-reinforced composites*, 10th International conference on durability of composite systems (Duracosys), September 17-19 2012, Brussels, Belgium.
2. Swolfs Y, Sun X, Gorbatikh L, Verpoest I, Hine PJ, Bonner MJ, Ward IM, *Interlayer hybridization of unidirectional glass fibre composites with self-reinforced polypropylene*, Proceedings of the 15th European Conference on Composite Materials (ECCM), June 24-28 2012, Venice, Italy.
3. Swolfs Y, Gorbatikh L, Verpoest I, *A 3D finite element analysis of static stress concentrations around a broken fibre*, Proceedings of the

15th European Conference on Composite Materials (ECCM), June 24-28 2012, Venice, Italy.

4. Hine PJ, Bonner MJ, Ward IM, Crauwels L, Swolfs Y, Verpoest I, *Developing the next generation of single polymer/carbon fibre hybrid composite materials for automotive use - HIVOCOMP*, Proceedings of the 15th European Conference on Composite Materials (ECCM), June 24-28 2012, Venice, Italy.
5. Swolfs Y, Gorbatikh L, Hine PJ, Ward IM, Verpoest I, *Toughening of carbon fibre composites by hybridisation with self-reinforced polypropylene*, 9th International Conference on Composite Science and Technology (ICCST), April 24-26 2013, Sorrento, Italy.
6. Callens MG, De Cuyper P, Swolfs Y, Gorbatikh L, Verpoest I, *Hybridization of ductile steel fibre and self-reinforced composites*, 9th International Conference on Composite Science and Technology (ICCST), April 24-26 2013, Sorrento, Italy.
7. Swolfs Y, Crauwels L, Gorbatikh L, Hine PJ, Ward IM, Verpoest I, *Tensile behaviour of carbon fibre composites hybridised with self-reinforced polypropylene*, 19th International Conference on Composite Materials (ICCM), July 28-August 2 2013, Montréal, Canada.
8. Swolfs Y, Gorbatikh L, Verpoest I, *A novel strength model for unidirectional fibre-reinforced composites with realistic fibre packings*, 19th International Conference on Composite Materials (ICCM), July 28-August 2 2013, Montréal, Canada.
9. Hine PJ, Bonner MJ, Ward IM, Swolfs Y, Verpoest I, Mierzwa A, *The HIVOCOMP project: carbon fibre/PA12 hybrid single polymer composites*, 19th International Conference on Composite Materials (ICCM), July 28-August 2 2013, Montréal, Canada.
10. Swolfs Y, Gorbatikh L, Verpoest I, *Stress concentrations around multiple fibre breakages: the validity of linear superposition*, 4th ECCOMAS Thematic Conference on Mechanical Response of Composites, September 25-27 2013, Ponta Delgada, Portugal.
11. Swolfs Y, Gorbatikh L, Hine PJ, Ward IM, Verpoest I, *Tough carbon fiber composites by hybridization with self-reinforced composites*, Sampe Seico 14, March 10-11, Paris, France.
12. Swolfs Y, McMeeking RM, Gorbatikh L, Verpoest I, *Parametric study of the tensile behaviour of unidirectional hybrid carbon/glass composites*, 16th European Conference on Composite Materials, June 22-26 2014, Seville, Spain.
13. Hine PJ, Bonner MJ, Ward IM, Swolfs Y, Verpoest I, *Self reinforced polyamide 12/carbon fibre hybrid composites*, 16th European Conference on Composite Materials, June 22-26 2014, Seville, Spain.
14. Swolfs Y, McMeeking RM, Verpoest I, Gorbatikh L, *A novel strength model with increased flexibility for predicting failure of unidirectional fiber-reinforced composites*, 29th American Society for Composites (ASC) Technical Conference, September 8-10 2014, San Diego, USA.

8.3 Patents

A patent on “Hybrid self-reinforced composites” with publication number WO/2013/190149 has been granted. Several follow-up patents have been filed in collaboration with a major industrial organisation in the field of composites.

8.4 Master theses

Over the course of four years, a total of 12 master thesis students were supervised. Two additional master thesis students have been started this academic year.

1. Xiaoming Sun (2010-2011): *Hybridization of unidirectional self-reinforced polypropylene with glass fiber polypropylene*
2. Pieter Decuyper (2011-2012): *Interlaag hybridisatie van staalvezel en zelf-versterkte composieten* (English: *Interlayer hybridisation of steel fibre and self-reinforced composites*)
3. Winke van den Fonteyne (2011-2012): *Falingsgedrag van zelfversterkt polypropyleen* (English: *Failure behaviour of self-reinforced polypropylene*)
4. Liesbet Crauwels (2011-2012): *Intralayer hybridization of self-reinforced composites*
5. Hans Van Der Velpen (2011-2012): *Interlaag hybridisatie van zelfversterkte compositen met unidirectionele glasvezel composieten* (English: *Interlayer hybridisation of self-reinforced composites with unidirectional glass fibre composites*)
6. Eline Van Breda (2012-2013): *Damage evolution in hybrid self-reinforced composites*
7. Yannick Meerten (2012-2013): *Impact resistance of hybrid self-reinforced composites*
8. Qingcheng Zhang (2012-2013): *Optimization of the process parameters for self-reinforced composites*
9. Jia Shi (2013-2014): *Impact resistance of hybrid self-reinforced composites*
10. Koen Michielsen (2013-2014): *Introducing discontinuous reinforcements in hybrid self-reinforced composites*
11. Haoran Wu (2013-2014): *Full field stress/strain analysis of the hybridized SRPP/CFPP composites via FEM and experiment*
12. Xiaoshi Jia (2013-2014): *Numerical and experimental analysis of the inter-layer hybridization effect on failure strain of SRPP and CFPP laminates*
13. Gilles Cleeren (2014-…): *Setting up an experimental test methodology for measuring the resin properties at the microscale*

14. Mengdie Zhang (2014-…): *Pseudo-ductility in hybrid self-reinforced composites*

Some results of these master theses were used at various points in this thesis. Below is an overview of how these master thesis students contributed to this this PhD thesis:

- Liesbet Crauwels:
    - Performing the initial work and setting up the methodology for section "2.5 Influence of weave architecture".
    - Production and testing of the materials for subsection "3.4.1 Tensile behaviour".
- Eline Van Breda:
    - Setting up the model for delamination growth in subsection "3.4.1 Tensile behaviour".
- Yannick Meerten:
    - Setting up the optimal methodology for testing self-reinforced composites in penetration impact and providing the results in subsection "2.4.1 Penetration impact resistance".
- Qingcheng Zhang:
    - Production and testing of the materials for optimising the process parameters of hot compaction in sections "2.3 Optimisation of process parameters" and "2.4 Impact resistance".
- Jia Shi
    - Setting up testing methodologies for non-penetration impact on SRCs, see subsection "2.4.2 Non-penetration impact resistance".
    - Doing the initial work on producing and testing the 160 µm prepreg hybrids. Although her results did not end up in this thesis, they laid the foundation for the results that were shown in subsection "3.4.2 Effect of carbon fibre volume fraction".

Chapter 9:

Curriculum vitae

Yentl Swolfs
Birthday: 31 August 1987
Nationality: Belgian

Home address
Venhoefweg 1A
2322 Hoogstraten
Belgium

Work information
Kasteelpark Arenberg 44 bus 2450
3001 Heverlee
Belgium
Phone: 0032/16 36 37 16
E-mail: yentl.swolfs@mtm.kuleuven.be
URL: www.composites-kuleuven.be/people/YentlSwolfs/YentlSwolfs

Education
2005 - 2008
Bachelor in Materials Engineering, cum laude
Department of Materials Engineering, KU Leuven

2008 - 2010
Master in Materials Engineering, cum laude
Department of Materials Engineering, KU Leuven

Research stays
January - February 2012
1-month stay with Prof. Ian Ward and dr. Peter Hine
University of Leeds

October 2013 - January 2014
4-month stay with Prof. Robert McMeeking and Prof. Frank Zok
University of California, Santa Barbara

Awards
IWT grant for 4 years of PhD research (2010-2014)

Winner of the Sampe Benelux students meeting (January 2013)

FWO grant for a 4-month research stay at the University of California, Santa Barbara (October 2013 - January 2014)

Patents
"Hybrid self-reinforced composites material" (n° WO/2013/190149)